Doctoral Dissertation
博士論文

$\mathbf{U(1)_{\mu-\tau}}$ gauge symmetry and its phenomenology

($\mathrm{U}(1)_{\mu-\tau}$ ゲージ対称性と現象論)

A Dissertation Submitted for the Degree of Doctor of Philosophy
December 2020
令和2年12月　博士 (理学) 申請

Department of Physics, Graduate School of Science,
The University of Tokyo
東京大学大学院理学系研究科
物理学専攻

Kento Asai
浅井　健人

Abstract

$U(1)_{L_\mu - L_\tau}$ gauge symmetry is one of the possibilities of the extension of the Standard Model (SM). Models extended by the $U(1)_{L_\mu - L_\tau}$ gauge symmetry contain a corresponding new gauge boson and have often been discussed in the context of the muon anomalous magnetic moment (muon $g-2$). However, the $U(1)_{L_\mu - L_\tau}$ gauge symmetry can play other important roles and is attractive even without the muon $g-2$. In this thesis, we focus on both the $U(1)_{L_\mu - L_\tau}$ gauge boson and the $U(1)_{L_\mu - L_\tau}$ gauge symmetry itself and discuss how they affect the neutrino and dark matter (DM) sectors. First, we discuss relations between neutrino parameters and structure of the neutrino mass matrices derived from the $U(1)_{L_\mu - L_\tau}$ gauge symmetry in the minimal gauged $U(1)_{L_\mu - L_\tau}$ model, and find that the neutrino CP phases and the sum of the neutrino masses are determined as functions of the neutrino oscillation parameters, regardless of the $U(1)_{L_\mu - L_\tau}$-breaking and Majorana mass scales. Second, using the above results, we point out that the successful non-thermal leptogenesis and inflation can be realized simultaneously in the minimal model. Third, we find that if the $U(1)_{L_\mu - L_\tau}$ gauge symmetry is broken at the electroweak scale, the $U(1)_{L_\mu - L_\tau}$ gauge boson can successfully contribute to the muon $g-2$ and determination of the light DM abundance simultaneously. Moreover, we explore the indirect detection of such a light DM by neutrino observations and obtain the upper limits from the future HyperKamiokande (HK) sensitivity to the DM annihilation cross section.

Acknowledgment

I would like to express my utmost gratitude to my supervisor Koichi Hamaguchi for countless support to me during my graduate course. He always guides me educationally and patiently and encourages me to grow up as a researcher. If he had not been my supervisor, I would never have gone on to the Ph.D. course, much less decided to be a researcher. Meeting him is an irreplaceable and precious thing to me, and I am delighted to have spent years of my graduate course as his student.

I would also like to express my sincere gratitude to Natsumi Nagata for various instructive advice and suggestions. I have learned a lot of knowledge and attitude necessary for a researcher.

I am also grateful to all my collaborators. I am happy that I was able to develop an understanding of physics through the discussions and work with them.

I would like to thank all the members of high energy physics theory group at the University of Tokyo for a variety of discussions and conversations relating to and not relating to physics. The interaction with them has enriched my laboratory life.

Lastly, I would like to express my gratitude to my family for their hospitality and nontrivial supports. Their consideration and thoughtfulness have been essential for me to continue study and research during my graduate course.

The works on which this dissertation bases were supported by JSPS KAKENHI Grant Number JP19J13812.

Contents

Notation and units

Notation

In this thesis, we use Greek indices of vectors and tensors as four dimension space-time coordinates, and Latin ones as three dimension spatial coordinates as follows :

$$\mu, \nu, \rho, ... = 0, 1, 2, 3 \ ,$$
$$i, j, k, ... = 1, 2, 3 \ .$$

Moreover, we use the following Greek indices of matrices and fields to distinguish flavors as follows :

$$\alpha, \beta, ... = e, \mu, \tau \ .$$

As the metric of the flat Minkowski space, we apply the time-like convention :

$$\eta^{\mu\nu} = (+1, -1, -1, -1) \ .$$

Units

Unless noted otherwise, we use the natural units for the physical units of measurement. In the natural units, the speed of light c, reduced Planck constant $\hbar$, and Boltzmann constant k_B are set equal to unity :

$$c = \hbar = k_B = 1 \ .$$

Chapter 1

Introduction

The Standard Model (SM) of particle physics is a successful model that has been verified by a lot of experiments and eventually established by the discovery of the Higgs boson at the Large Hadron Collider (LHC) in 2012. Although the SM provides explanations to a lot of phenomena related to particle physics, there are unsolved problems. One of them is the muon anomalous magnetic moment (muon $g-2$). Generally, charged particles have magnetic dipole moment $\vec{\mu}$ which is the physical value defined in terms of its spin $\vec{s}$ as follows:

$$\vec{\mu} = g\left(\frac{q}{2m}\right)\vec{s}\,, \tag{1.1}$$

where g is the gyromagnetic ratio called g-factor, and m and $q = \pm e$ is the mass and electric charge of the given charged particle, respectively. From the classical Dirac equation, the g-factor is exactly 2. However, quantum loop corrections deviate the g-factor from 2, and this deviation is represented by the parameter $a_\ell = (g-2)/2$ and called anomalous magnetic moment. The muon $g-2$ has been precisely measured by several experiments for over half a century, and the Brookhaven E821 experiment has given the experimental value [1–3]. On the other hand, theoretical prediction from the SM has also been calculated vigorously [4–15] (see also Ref. [16]), and it is known that there is the existence of the long-standing discrepancy between the experimental and SM predicted values at more than 3σ level.

To explain this discrepancy, a lot of extensions of the SM have been proposed. One promising solution of them is an extension of the SM gauge sector by an Abelian $\mathrm{U}(1)_{L_\mu - L_\tau}$ gauge symmetry. In models with $\mathrm{U}(1)_{L_\mu - L_\tau}$ gauge symmetry, muon (tau particle) and mu (tau)-type neutrino have $\mathrm{U}(1)_{L_\mu - L_\tau}$ charge $+1(-1)$, and the other SM particles have no charge. In this extended model, an extra $\mathrm{U}(1)_{L_\mu - L_\tau}$ gauge boson interacts with muon and contribute to the muon $g-2$ at one-loop level. If the mass of the $\mathrm{U}(1)_{L_\mu - L_\tau}$ gauge boson is $\mathcal{O}$(10-100) MeV and the gauge coupling constant is $\mathcal{O}(10^{-4})$, the discrepancy of the muon anomalous magnetic moment can be explained without conflicting severe experimental bounds. The review of the $\mathrm{U}(1)_{L_\mu - L_\tau}$ gauge symmetry and its gauge boson is shown in Section 2.1.

Besides the muon anomalous magnetic moment, the SM has long-standing unsolved problems. Representative examples of them are dark matter (DM) and the baryon asymmetry of the Universe (BAU). The existence of the DM is considered to be certain by various cosmological and astrophysical observations, such as those of the galaxy rotation curves [17–21] and cosmic microwave background (CMB) [22–26]. There are various candidates for the DM, including particles and non-particles. When the DM is elemental particle, it is required to have no electromagnetic charge and be non-relativistic to avoid experimental and observational constraints. Moreover, it should be stable or live longer than the age of the Universe in order not to decrease the abundance until the present. Because of the discovery of neutrino oscillation [27], it is known that neutrinos certainly have masses, and, comparing their masses and temperature estimated by that of the CMB, at least two of neutrino generations are non-relativistic. Then, among the SM particles, only neutrinos satisfy the above conditions. It is clear, however, that neutrinos can not be the candidate of DM because of the bounds on the sum of neutrino masses and failure of the structure formation of the Universe [28, 29]. Therefore, the SM has no candidate for DM and many new particles have been proposed as alternative candidates. One of the most promising and attractive candidates is Weakly Interacting Massive Particles (WIMPs). WIMPs appear in various motivated models, such as supersymmetric model [30], universal extra dimension model [31], and so on.

WIMPs are also attractive from the viewpoint of the DM production mechanism. WIMPs interact weakly with the SM particles and have been in thermal equilibrium in the early Universe. They are produced through interactions with the SM particles. With the cooling of the Universe, the ratio of the interaction rate to the Hubble expansion rate decreases, and then the interactions eventually freeze out. After that, with the expansion of the Universe, the DM number density decreases, and then the observed relic abundance of DM is realized. This kind of production scenario is called thermal freeze-out. When the DM mass is around the electroweak scale, the observed relic abundance indicates that the coupling strength between DM and SM particles is around the strength of the electroweak coupling. Such a realization of the DM relic abundance is called *WIMP miracle*. A lot of experiments have been performed to search WIMP DM with electroweak scale mass. However, there is no indication of DM detection, and for example, XENON1T experiment [32–34], which is one of the world's leading direct detection experiments, gives the most stringent constraint on the DM-nucleon scattering cross section. In order to avoid the severe constraints from direct detection experiments, alternative candidates of DM are explored.

$\mathrm{U}(1)_{L_\mu - L_\tau}$ gauge symmetry, described above, provides an escape route for DM from severe constraints from direct detection experiments. If DM has the $\mathrm{U}(1)_{L_\mu - L_\tau}$ charge, after breaking of the $\mathrm{U}(1)_{L_\mu - L_\tau}$ gauge symmetry, the remaining accidental global U(1) symmetry can warrant the DM stability, depending on the DM $\mathrm{U}(1)_{L_\mu - L_\tau}$ charge, as explained in section 7.2. Moreover,

DM can annihilate into the SM μ and τ-type particles through the $U(1)_{L_\mu - L_\tau}$ gauge boson, if kinematically allowed, and the observed relic abundance is realized. For direct detection experiments, because $U(1)_{L_\mu - L_\tau}$ gauge boson couple to neither nucleon nor electron at tree level, DM-nucleon and DM-electron scattering cross sections are suppressed, and severe constraints can be avoided. On the other hand, the DM annihilation into μ and τ-type SM particle, especially neutrinos is allowed, and thus there is a possibility of indirect detection by neutrino telescope, such as Superkamiokande. The feasibility of both DM relic abundance and muon $g-2$, and the bound on the DM annihilation cross section by the neutrino observations are discussed in Chapter 7, and this discussion is based on Ref. [35].

Baryon asymmetry of the Universe is also one of the unsolved puzzles. The SM includes both particles and antiparticles, and CPT invariance is conserved. Starting on the discovery of positron by C. D. Anderson in 1932, various antiparticles are observed. However, these particles are secondary cosmic rays and not primary ones which exist since the early Universe and come from outside the Earth's atmosphere. Standard big bang nucleosynthesis (BBN) scenario and observed abundance of light elements suggest baryon-antibaryon asymmetry in the Universe. The current observed value of the baryon asymmetry with 1σ error from the CMB observations by Planck satellite is given by [25]

$$\Omega_B h^2 = 0.02233 \pm 0.00015 \ , \tag{1.2}$$

where $\Omega_B = \rho_B/\rho_c$ is the density parameter of baryon, and ρ_B and ρ_c are the baryon energy density and critical density, respectively. h is the Hubble parameter expressed in units of 100 km/s/Mpc. If this baryon-antibaryon asymmetry has been generated before the inflation, it has been diluted with expanding the Universe, and the observed asymmetry cannot be obtained. Therefore the asymmetry should be generated after the inflation, and various scenarios that explain generations of the baryon-antibaryon asymmetry, called *baryogenesis*, are proposed.

Leptogenesis [36] is one of the promising baryogenesis scenarios. In this scenario, lepton-antilepton asymmetry is generated by some mechanism and converted into baryon-antibaryon one through sphaleron process [37]. So far many kinds of leptogenesis scenarios are proposed, and each scenario has its production mechanism of lepton asymmetry. The most well-known example is the generation of lepton asymmetry by decays of heavy right-handed neutrinos. Introducing right-handed neutrinos into the SM, neutrinos can form Dirac mass terms. Moreover, if right-handed neutrinos have much heavier Majorana masses than the Dirac masses, the lightness of neutrinos can be explained naturally by seesaw mechanism [38–41]. In this way, the right-handed neutrinos and their Majorana nature are attractive and searched for a long time.

$U(1)_{L_\mu - L_\tau}$ gauge symmetry also affects leptogenesis. In the minimal model extended by $U(1)_{L_\mu - L_\tau}$ gauge symmetry and right-handed neutrinos, matrices of neutrino Dirac and Majorana masses are severely restricted, and this restriction gives relations between parameters

relative to neutrinos. Therefore, this model can predict neutrino Dirac and Majorana CP phases with less ambiguity. Moreover, because of the restriction of neutrino parameters including Dirac and Majorana CP phases, there is the correlation between the Dirac CP phase and the sign of baryon asymmetry generated through leptogenesis scenario appears. We discuss the restrictions of neutrino parameters in Chapter 5 and the baryon asymmetry generated through leptogenesis scenario in Chapter 6, and these discussions are based on Refs. [42–45].

This thesis consists of two parts. Part I is the review part and consists of three chapters. In Chapter 2, we give reviews of theoretical foundation, such as right-handed neutrinos and its Majorana nature (Sec. 2.2) and $\mathrm{U}(1)_{L_\mu - L_\tau}$ gauge symmetry (Sec. 2.1). In Chapter 3, we give reviews about WIMP dark matter and thermal freeze-out mechanism. In Chapter 4, we summarize leptogenesis scenario. Part II consists of three chapters. In Chapter 5, the relations between the structure of the neutrino mass matrix and the neutrino parameters are discussed. In Chapter 6, non-thermal leptogenesis in the minimal gauged $\mathrm{U}(1)_{L_\mu - L_\tau}$ model is discussed, assuming an inflation model. In Chapter 7, the Dirac fermion DM in the $\mathrm{U}(1)_{L_\mu - L_\tau}$ model and indirect search by neutrino telescopes are discussed. Chapter 8 is lastly devoted to the summary and conclusion of this thesis. In Appendix, we collect some supplemental materials to support our understanding. In this thesis, Chapter 5, 6, and 7 are based on Refs. [42–44], [45], and [35], respectively.

Part I

Review Part

Chapter 2

Foundation

In this thesis, we discuss how $U(1)_{L_\mu - L_\tau}$ gauge symmetry affects dark matter and leptogenesis scenarios, following the author's works [35, 42–45]. In this chapter, we give the review of the $U(1)_{L_\mu - L_\tau}$ gauge symmetry and relation with the muon $g-2$, firstly. After that, we summarize the experimental constraints on the $U(1)_{L_\mu - L_\tau}$ gauge boson. Secondly, we review the right-handed neutrinos and Majorana natures.

2.1 $U(1)_{L_\mu - L_\tau}$ gauge symmetry

Extensions of the gauge sector in the SM have been tried, as one of physics beyond the SM, in various context for a long time (see Refs. [46–49] for early examples). $U(1)_{L_\mu - L_\tau}$ gauge symmetry is one of the examples and motivated by the discrepancy of the muon anomalous magnetic moment. Under this gauge symmetry, muon $\mu_{L,R}$ and mu-type neutrino ν_μ have the $U(1)_{L_\mu - L_\tau}$ charge $+1$, tau particle $\tau_{L,R}$ and tau-type neutrino ν_τ have the $U(1)_{L_\mu - L_\tau}$ charge -1, and the other SM particles have no $U(1)_{L_\mu - L_\tau}$ charge.

2.1.1 Gauge anomaly cancellation

When an extra gauge symmetry is added to the gauge sector of the SM, it is pretty important whether new symmetry causes gauge anomaly. The existence of the gauge anomaly destroys renormalizability and unitarity of S-matrix, and then it leads models to lose predictive power. The SM is the chiral gauge theory, and there is a danger that it includes the gauge anomaly in nature. But, in the SM, anomalies from the quark and lepton sectors, miraculously, cancel each other nontrivially. However, as we mentioned above, when $U(1)_{L_\mu - L_\tau}$ gauge symmetry is added to the SM gauge sector, we have to confirm the anomaly cancellation.

The SM is the chiral gauge theory, and the left and right-hand fermions transform differently

under the gauge transformation. For the $\mathrm{SU}(2)_L$ gauge transformation,

$$\Psi_L(x) \to \Psi'_L(x) = U(x)\Psi_L(x), \quad \Psi_R(x) \to \Psi'_R(x) = \Psi_R(x) \ , \tag{2.1}$$

where $\Psi_{L(R)}$ is the $\mathrm{SU}(2)_L$ doublet (singlet) of the SM left (right)-handed fermion, and $U(x) = \exp[ig\zeta^a(x)T^a]$ is the Hermitian matrix of the SU(2) gauge transformation with the gauge coupling constant, g, parameter of the transformation, $\zeta^a(x)$, and generator matrices of the $\mathrm{SU}(2)_L$, T^a. In the classical theory, the action is invariant under the above transformation. However, at the quantum level, the effective action included in the one-loop contribution of fermions is not necessarily invariant under the chiral gauge transformation. In fact, the gauge invariance is violated by the triangle diagram of fermions at the one-loop level. This violation of the gauge invariance is intrinsic and cannot be removed by adding local counterterms to the action. This kind of violation is called gauge anomalies. For the above triangle diagram, the gauge anomaly is given by

$$\mathcal{A}^{abc} = \sum_{f_L} \mathrm{tr}\left(t^a\left\{t^b, t^c\right\}\right) - \sum_{f_R} \mathrm{tr}\left(t^a\left\{t^b, t^c\right\}\right) \equiv \ \mathcal{A}_L^{abc} - \mathcal{A}_R^{abc}, \tag{2.2}$$

where $f_{L(R)}$ is the SM left (right)-handed fermion, t^a is the generator matrix associated with the gauge boson which couples to fermions at an apex of the triangle, and we omit the coefficient in Eq. (2.2). When left and right-handed fermions have the same charges, $\mathcal{A}_L^{abc} = \mathcal{A}_R^{abc}$, and then the anomalies are canceled.

The left and right-handed fermions transform in the same way under the $\mathrm{U}(1)_{L_\mu - L_\tau}$ gauge transformation when the right-handed neutrinos with three lepton flavors, $\nu_{R,\alpha}$, are introduced, and then there are five triangle diagrams which we have to confirm the anomaly cancellation as follows :

(i) $\mathrm{U}(1)_{L_\mu - L_\tau}$ - gravity - gravity (ii) $\mathrm{U}(1)_{L_\mu - L_\tau}$ - $\mathrm{U}(1)_{L_\mu - L_\tau}$ - $\mathrm{U}(1)_{L_\mu - L_\tau}$

(iii) $\mathrm{U}(1)_{L_\mu - L_\tau}$ - $\mathrm{U}(1)_{L_\mu - L_\tau}$ - $\mathrm{U}(1)_Y$ (iv) $\mathrm{U}(1)_{L_\mu - L_\tau}$ - $\mathrm{U}(1)_Y$ - $\mathrm{U}(1)_Y$

(v) $\mathrm{SU}(2)_L$ - $\mathrm{SU}(2)_L$ - $\mathrm{U}(1)_{L_\mu - L_\tau}$

In (i) $\sim$ (v) cases, the gauge anomalies are given by

$$\text{(i)} \quad \sum_{\alpha=e,\mu,\tau} \left[-Y'(e_{L,\alpha}) + Y'(e_{R,\alpha}) - Y'(\nu_{L,\alpha}) + Y'(\nu_{R,\alpha})\right] = 0 \ , \tag{2.3}$$

$$\text{(ii)} \quad \sum_{\alpha=e,\mu,\tau} \left[-Y'(e_{L,\alpha})^3 + Y'(e_{R,\alpha})^3 - Y'(\nu_{L,\alpha})^3 + Y'(\nu_{R,\alpha})^3\right] = 0 \ , \tag{2.4}$$

$$\text{(iii)} \quad \sum_{\alpha=e,\mu,\tau} \left[-\left(-\frac{1}{2}\right) Y'(e_{L,\alpha})^2 + (-1)Y'(e_{R,\alpha})^2 - \left(-\frac{1}{2}\right) Y'(\nu_{L,\alpha})^2 + 0 \times Y'(\nu_{R,\alpha})^2\right] = 0 \ , \tag{2.5}$$

$$\text{(iv)} \quad \sum_{\alpha=e,\mu,\tau} \left[-\left(-\frac{1}{2}\right)^2 Y'(e_{L,\alpha}) + (-1)^2 Y'(e_{R,\alpha}) - \left(-\frac{1}{2}\right)^2 Y'(\nu_{L,\alpha}) + 0^2 \times Y'(\nu_{R,\alpha})\right] = 0 \ , \tag{2.6}$$

$$\text{(v)} \quad \sum_{\alpha=e,\mu,\tau} \left[-Y'(e_{L,\alpha}) - Y'(\nu_{L,\alpha})\right] = 0 \ , \tag{2.7}$$

where $Y'(f)$ is the $\mathrm{U}(1)_{L_\mu - L_\tau}$ charge of fermion f. Here, we should emphasize that the above gauge anomalies cancel even if the right-handed neutrinos are not introduced. Moreover, we note that, in Chapter 7, we consider the Dirac fermion DM with non-zero $\mathrm{U}(1)_{L_\mu - L_\tau}$ charge, and this DM transform vector-like under the $\mathrm{U}(1)_{L_\mu - L_\tau}$ gauge transformation for the anomaly cancellation.

2.1.2 Kinetic mixing

Here, we show the Lagrangian relative to the $\mathrm{U}(1)_{L_\mu - L_\tau}$ gauge boson X :

$$\mathcal{L}_{\rm int} = -g_X X_\lambda (\bar{\mu}\gamma^\lambda \mu - \bar{\tau}\gamma^\lambda \tau + \bar{\nu}_{L,\mu}\gamma^\lambda \nu_{L,\mu} - \bar{\nu}_{L,\tau}\gamma^\lambda \nu_{L,\tau}) \ , \tag{2.8}$$

$$\mathcal{L}_{\rm kin} = -\frac{1}{4} F_{\lambda\rho} F^{\lambda\rho} - \frac{1}{4} X_{\lambda\rho} X^{\lambda\rho} \ , \tag{2.9}$$

where $F^{\lambda\rho}$ and $X^{\lambda\rho}$ are the field strengths of the SM photon and $\mathrm{U}(1)_{L_\mu - L_\tau}$ gauge boson, respectively, and g_X is the gauge coupling constant of $\mathrm{U}(1)_{L_\mu - L_\tau}$. As mentioned in the former subsection, the electron and quarks have no $\mathrm{U}(1)_{L_\mu - L_\tau}$ charge, and therefore X does not interact with them directly. However, the muon and tau particle have both $\mathrm{U}(1)_{L_\mu - L_\tau}$ and SM electroweak charges in the gauged $\mathrm{U}(1)_{L_\mu - L_\tau}$ models. Therefore, the models have the gauge kinetic mixing ϵ of X and the SM photon γ at low scale, although we set ϵ to be zero at some high scale. As shown in Fig. 2.1, the gauge kinetic mixing is generated at one-loop level and is given by

$$\mathcal{L}_\epsilon = -\frac{\epsilon_A}{2} F_{\lambda\rho} X^{\lambda\rho} - \frac{\epsilon_Z}{2} Z_{\lambda\rho} X^{\lambda\rho} \ , \tag{2.10}$$

$$\epsilon_A = -\frac{e g_X}{12\pi^2} \ln\left(\frac{m_\tau^2}{m_\mu^2}\right) \ , \tag{2.11}$$

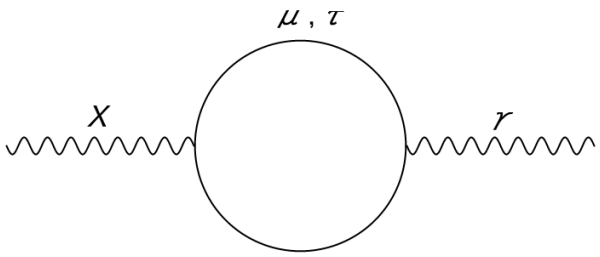

Figure 2.1: Kinetic mixing between the $\mathrm{U}(1)_{L_\mu - L_\tau}$ gauge boson and SM photon induced by muon and tau particle loop.

where $F^{\lambda\rho}$ and $Z^{\lambda\rho}$ denote the field strength for photon and Z boson, respectively. Besides, e is the electromagnetic charge, and $m_{\mu(\tau)}$ is the muon (tau particle) mass.

We will take into account this one-loop level mixing in this thesis. To get the canonically normalized gauge fields, we shift the photon field as $A_\mu \to A_\mu + \epsilon_A X_\mu$ for $|\epsilon_A| \ll 1$. This shift induces the interaction of X to the electromagnetic current $\epsilon_A e X_\mu J^\mu_{\mathrm{em}}$, which is crucial for DM direct detection. Similarly, the mixing with the Z boson is given by

$$\epsilon_Z = -\left(-\frac{1}{4} + \sin^2\theta_W\right) \frac{e g_X}{12\pi^2 \cos\theta_W \sin\theta_W} \ln\left(\frac{m_\tau^2}{m_\mu^2}\right) \ , \tag{2.12}$$

with the Weinberg angle θ_W. Shifting $Z_\mu \to Z_\mu - \epsilon_Z m_X^2/m_Z^2 X_\mu$ and $X_\mu \to X_\mu + \epsilon_Z Z_\mu$ to get the canonically normalized gauge fields, we find the Z boson couples to $L_\mu - L_\tau$ current and the X boson to the neutral current,

$$\mathcal{L}_{Z,L_\mu - L_\tau} = -g_X \epsilon_Z Z_\mu J^\mu_{L_\mu - L_\tau} \ , \tag{2.13}$$

$$\mathcal{L}_{X,\mathrm{NC}} = \frac{g}{\cos\theta_W} \epsilon_Z \frac{m_X^2}{m_Z^2} X_\mu J^\mu_{\mathrm{NC}} \ , \tag{2.14}$$

for $m_X \ll m_Z$. In Chapter 7, the $\mathrm{U}(1)_{L_\mu - L_\tau}$ gauge boson is assumed to be much lighter than the SM Z boson. Therefore, the effect of the mixing ϵ_Z is suppressed by m_X^2/m_Z^2, and thus we neglect it in the following discussion. In Appendix A.1, we show the detail about the gauge kinetic mixing and canonical normalization.

2.1.3 Muon anomalous magnetic moment

Muon anomalous magnetic moment is one of the most important motivations for the $\mathrm{U}(1)_{L_\mu - L_\tau}$ models. The latest experimental value of the muon $g-2$ is given by the Brookhaven E821 experiment [1–3]. On the other hand, the vigorous efforts have given the precise theoretical values, and the discrepancies of the muon $g-2$ between the experimental and theoretical values

are given by

$$\Delta a_\mu \equiv a_\mu^{\rm exp} - a_\mu^{\rm SM} = \begin{cases} (260 \pm 79) \times 10^{-11} & [11] \\ (280.2 \pm 73.7) \times 10^{-11} & [12] \\ (279 \pm 76) \times 10^{-11} & [16] \\ (261 \pm 79) \times 10^{-11} & [50] \end{cases} . \tag{2.15}$$

The differences among the above values in Eq. (2.15) are mainly derived from the estimations of the hadronic vacuum polarization.[1]

New physics can contribute to the muon $g-2$ and explain the long-standing deviation. To do so, new physics have to couple to muon. $\mathrm{U}(1)_{B-L}$, which is the well-known Abelian gauge group, is one example. However, the $\mathrm{U}(1)_{B-L}$ gauge boson has couplings with the electron and quarks, and then experimental constraints on the gauge coupling and gauge boson mass are much severe. Therefore, $\mathrm{U}(1)_{B-L}$ gauge boson can not explain the muon $g-2$ discrepancy without conflicting with the experiments (for example, see Ref. [52]). On the other hand, the $\mathrm{U}(1)_{L_\mu - L_\tau}$ gauge boson can avoid the constraints from the various experiments because it has no coupling with the electron and quarks. Therefore, the $\mathrm{U}(1)_{L_\mu - L_\tau}$ gauge boson can explain the muon $g-2$ discrepancy, avoiding the experimental constraints.

The $\mathrm{U}(1)_{L_\mu - L_\tau}$ gauge boson contributes to the muon $g-2$ through the one-loop diagram shown in Fig. 2.2. [2]

The one-loop contribution of the $\mathrm{U}(1)_{L_\mu - L_\tau}$ gauge boson is given by

$$\Delta a_\mu^X = \frac{g_X^2}{8\pi} \int_0^1 dx \frac{2m_\mu^2 x^2 (1-x)}{x^2 m_\mu^2 + (1-x) m_X^2} , \tag{2.16}$$

where g_X is the $\mathrm{U}(1)_{L_\mu - L_\tau}$ gauge coupling constant, and m_X is the mass of the $\mathrm{U}(1)_{L_\mu - L_\tau}$ gauge boson. In Fig. 2.3, the parameter region in the m_X-g_X plane which explains the muon $g-2$ anomaly is shown.

The dark (light) red area corresponds to the $1\sigma(2\sigma)$ favored region of the muon $g-2$ and realizes $\Delta a_\mu^X = (268 \pm 76) \times 10^{-11}$ [50]. The light brown area and dark brown dashed line correspond to the experimental constraints by CHARM-II and CCFR measurements of the neutrino trident production $\nu N \to \nu N \mu^+ \mu^-$ [53–55], respectively. The dark gray area corresponds to the

[1] The BMW Collaboration [51] gave the new result of the determination of the hadronic vacuum polarization, based on the lattice calculation, and its value is significantly larger than the above values on Eq. (2.15), based on the phenomenological input. If this value is adopted, the deviation between the experimental and SM values reduces.

[2] The $\mathrm{U}(1)_{L_\mu - L_\tau}$ gauge boson interacts with the SM muon and has a gauge mixing with the SM photon as shown in Fig. 2.1. However, there is no contribution to the muon $g-2$ by a tree diagram which is described by the gauge interaction and gauge kinetic mixing with the photon. This is because, as shown in Appendix A.1, the SM photon is defined as a massless eigenstate after redefining gauge bosons mixed with each other and removing the gauge kinetic mixing. Therefore, the SM photon has no mixing with a mass eigenstate X and the he $\mathrm{U}(1)_{L_\mu - L_\tau}$ gauge boson contributes to the muon $g-2$ at one-loop level.

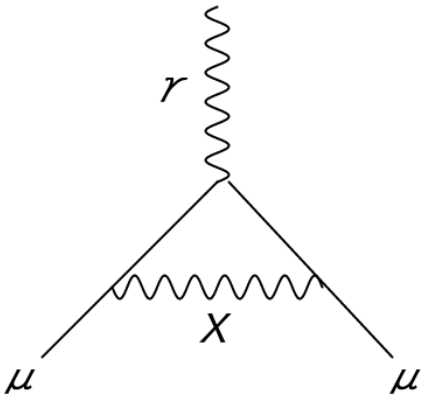

Figure 2.2: One-loop diagram which contributes the muon $g-2$. X denotes the $\mathrm{U}(1)_{L_\mu - L_\tau}$ gauge boson.

bound from Borexino measurement of the interaction rate of the mono-energetic 862 keV ^{7}Be solar neutrino [56–58]. The region above the solid blue line corresponds to the experimental constraints by BABAR search for $e^+e^- \to \mu^+\mu^- X$ with a subsequent decay $X \to \mu^+\mu^-$ [59]. Besides the experimental constraints, there are some astrophysical bounds on the $\mathrm{U}(1)_{L_\mu - L_\tau}$ gauge boson. The light gray area corresponds to the astrophysical constraint by the white dwarf (WD) cooling induced by the plasmon decay via the off-shell $\mathrm{U}(1)_{L_\mu - L_\tau}$ gauge boson [60, 61]. Lastly, the yellow area and dashed line correspond to the bound from the effective neutrino number N_{eff}. The X boson mainly decays into a pair of neutrinos for $m_X < 2m_\psi$. The lifetime is much shorter than the time scale ($\tau_{\mathrm{BBN}} \sim 1\,\mathrm{sec}$) of BBN in the parameter space that we are interested in. If the X boson is light enough, the X boson can be in equilibrium with the neutrinos after the neutrino decoupling ($T \sim 1\,\mathrm{MeV}$). Then, it is possible to increase the effective neutrino number N_{eff}. Since the X boson is already non-relativistic at the BBN, it does not contribute directly to N_{eff}. It can decay into neutrinos, however. The decay releases the energy into neutrinos, reheating the neutrino temperature. Following [62], we estimate the contribution to N_{eff} and obtain the lower mass bound $m_X \gtrsim 6\,\mathrm{MeV}$ for $\epsilon_A = 0$. When we include the effects of the non-vanishing kinetic mixing, the lower bound becomes 10 MeV for $\epsilon_A \simeq 7.2 \times 10^{-6}$ corresponding to $g_X = 5 \times 10^{-4}$. For further details of the contribution to N_{eff} and the cosmological implication of the light $\mathrm{U}(1)_{L_\mu - L_\tau}$ gauge boson, see *e.g.* Ref. [63]. We conservatively use $m_X \gtrsim 6\,\mathrm{MeV}$ as the lower mass bound in this thesis.

The allowed region which explains the muon $g-2$ discrepancy can be searched in future experiments. For example, the E949 [64, 65]-like experiment has a potential to test the above region by searches for single muon tracks from the decays of stopped charged kaon ($K^+ \to \mu^+ + \nu_\mu + X,\ X \to \nu\bar{\nu}$) [66]. Besides, NA64 experiment can probe the above region through $\mu + N \to \mu + N + X$, $X \to$ inv. process [67, 68]. Also, the Belle-II experiment [69] also does

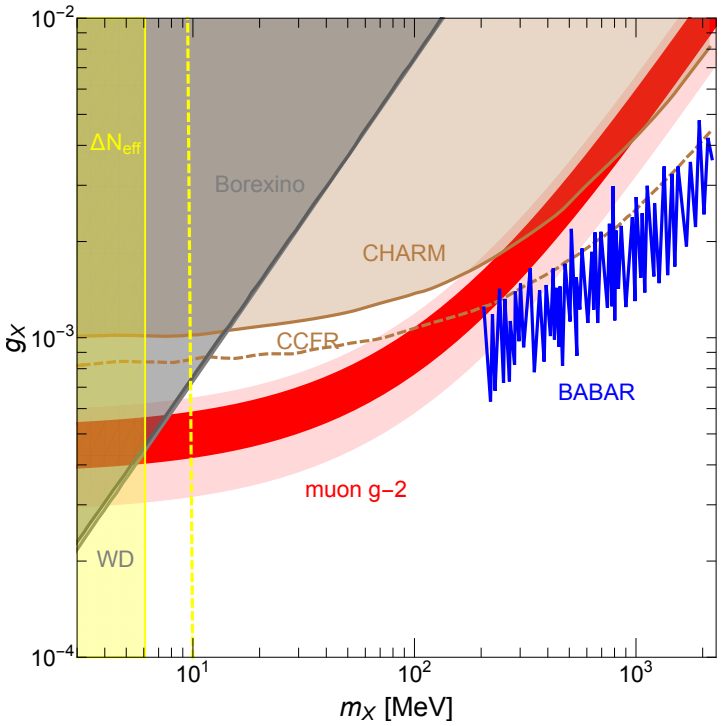

Figure 2.3: Constraints on the $U(1)_{L_\mu - L_\tau}$ boson and muon $g-2$ favored region. Dark (light) red area corresponds to the $1\sigma(2\sigma)$ favored region of the muon $g-2$, respectively.

by missing energy search from the mono-photon process ($e^+e^- \to \gamma X$, $X \to$ inv.) [70] and the X-bremsstrahlung one ($e^+e^- \to \mu^+\mu^- X$, $X \to$ inv.) [71]. Moreover, a new experiment carried out at the Fermilab [72, 73] is trying to measure the muon $g-2$ discrepancy precisely and reduce the experimental uncertainty. The J-PARK will also carry out another experiment using the newly developed novel technique [74, 75]. Lastly, we note that SHiP experiment at the CERN Beam Dump Facility [76, 77], which is one of future beam dump experiments, can also prove $U(1)_{L_\mu - L_\tau}$ gauge boson. However, the $U(1)_{L_\mu - L_\tau}$ gauge coupling constant which SHiP can search is much smaller that that which can explain the muon $g-2$ [52]. Also, the $U(1)_{L_\mu - L_\tau}$ gauge boson interacts with quarks through the gauge kinetic mixing. However, this interaction is quark flavor-diagonal and does not have a significant effect on B and K meson physics. Therefore, there is no substantial constraint on the $U(1)_{L_\mu - L_\tau}$ gauge boson. We note that, in Refs. [78, 79], $U(1)_{L_\mu - L_\tau}$-charged vector-like heavy quarks are introduced, and the relation between the $U(1)_{L_\mu - L_\tau}$ gauge boson and $B \to K^* \mu^+ \mu^-$ anomaly reported by LHCb [80].

2.2 Right-handed neutrinos and Majorana nature

Neutrino is one of the irregular particles in the SM matter contents. One major difference from the other SM fermions is the absence of the right-handed part. As a result, neutrinos cannot

have the Dirac mass terms and must be massless in the SM. However, starting with the report in Neturino 1998 that the neutrino oscillation has been observed by the Super-Kamiokande experiment [27], various experiments have observed the neutrino oscillation and it is clear that the neutrinos are massive. This fact indicates the necessity of extension of the SM in order to give masses to neutrinos. [3]

Right-handed neutrinos give a simple solution for the above problem of the neutrino masses. These particles beyond the SM are singlet fermions under the SM gauge group, $\mathrm{SU}(3)_c \times \mathrm{SU}(2)_L \times \mathrm{U}(1)_Y$. Therefore, they have no danger of the gauge anomaly. Moreover, the neutrinos are neutral fermion, and then there is a possibility that they are Majorana particles. If they are, these new particles may possibly solve various problems that the SM is facing. In this subsection, we give a brief review of the Majorana nature of the neutrinos and their effects on the beyond SM physics.

2.2.1 Majorana nature

Neutrinos have been discovered by F. Reines and C. L. Cowan in 1953 [81, 82]. After that, various experiments are trying to observe this particle. If neutrinos are Dirac fermion, the degree of freedom is four because there are neutrino and antineutrino, and left-handed and right-handed. However, currently, only left-handed neutrino and right-handed antineutrino have been observed, and therefore, we come across the possibility that neutrino and antineutrino are the same because neutrinos are neutral. Such particles, which are the same as their antiparticles, are called Majorana particles, and they have been proposed by E. Majorana [83]. In this subsection, we give a short review of Majorana particles and neutrinoless double beta decay, which is one of the phenomena specific to Majorana particles.

◯ Majorana particle and Majorana mass

Majorana particle is a particle that is identified with its antiparticle, that is, charge conjugate of the particle. Charge conjugation of particles ψ is given by

$$\psi = \begin{pmatrix} \xi_a \\ \eta^{\dot{a}} \end{pmatrix} \xrightarrow{\mathcal{C}} \psi^c = \begin{pmatrix} \eta^{*b}\epsilon_{ba} \\ \epsilon^{\dot{a}\dot{b}}\xi^*_{\dot{b}} \end{pmatrix} = i\gamma^2\psi^* \equiv \mathcal{C}\bar{\psi}^T \ , \tag{2.17}$$

where ϵ_{ba}, $\epsilon^{\dot{a}\dot{b}}$ are the completely antisymmetric tensors of rank 2 with $\epsilon_{12} = \epsilon^{12} = 1$, and ξ_α, $\eta^{\dot{\alpha}}$

[3] In the SM, the neutrino masses can be realized by the Weinberg operator $\mathcal{M}_\nu = c_{\alpha\beta}(\bar{L}_\alpha \cdot \tilde{H})(\tilde{H}^T \cdot L^c_\beta)/\Lambda$ with $c_{\alpha\beta}$ being a dimensionless constant, Λ the cutoff scale, and $\tilde{H} = i\sigma_2 H^*$. However, this operator is non-renormalizable, and the extensions of the SM are necessary to construct UV complete models.

are two-component spinors. γ^μ is the gamma matrix given by

$$\gamma^\mu = \begin{pmatrix} 0 & (\bar{\sigma}^\mu)_{\dot{a}b} \\ (\sigma^\mu)^{a\dot{b}} & 0 \end{pmatrix} , \tag{2.18}$$

with

$$\sigma^\mu = (1, -\sigma_1, -\sigma_2, -\sigma_3), \quad \bar{\sigma}^\mu = (1, \sigma_1, \sigma_2, \sigma_3) . \tag{2.19}$$

Matrices of dimension two, σ_i $(i = 1 \sim 3)$, are well-known Pauli matrices and given by

$$\sigma_1 = \begin{pmatrix} 0 & 1 \\ 1 & 0 \end{pmatrix}, \quad \sigma_2 = \begin{pmatrix} 0 & -i \\ i & 0 \end{pmatrix}, \quad \sigma_3 = \begin{pmatrix} 1 & 0 \\ 0 & -1 \end{pmatrix} . \tag{2.20}$$

$\mathcal{C}$ is the matrix of dimension four, which has the following characteristics :

$$C^{-1} = C^\dagger = C^T = -C, \tag{2.21}$$

$$[C, \gamma_5] = 0, \tag{2.22}$$

$$C\gamma_\mu^T C^{-1} = -\gamma_\mu , \tag{2.23}$$

with $\gamma_5 \equiv i\gamma^0\gamma^1\gamma^2\gamma^3$. Majorana particle satisfies $\psi = \psi^c$, and thus

$$\xi_a = \eta^{*b}\epsilon_{ba}, \ \eta^{\dot{a}} = \epsilon^{\dot{a}\dot{b}}\xi_{\dot{b}}^* \quad \Longrightarrow \quad \psi = \begin{pmatrix} \xi_a \\ \epsilon^{\dot{a}\dot{b}}\xi_{\dot{b}}^* \end{pmatrix} = \begin{pmatrix} \eta^{*b}\epsilon_{ba} \\ \eta^{\dot{a}} \end{pmatrix} \tag{2.24}$$

is given. When right-handed neutrinos are introduced, neutrinos also can have the Dirac mass terms. Moreover, if neutrinos are Majorana particles, the following Majorana mass terms can be formed

$$-\frac{1}{2}(\mathcal{M}_R)_{\alpha\beta}\bar{N}_\alpha^c N_\beta + h.c. = -\frac{1}{2}\left\{(\mathcal{M}_R)_{\alpha\beta}\xi_{\alpha,a}\epsilon^{ab}\xi_{\beta,b} - (\mathcal{M}_R)^*_{\alpha\beta}\xi_\alpha^{*\dot{a}}\epsilon_{\dot{a}\dot{b}}\xi_\beta^{*\dot{b}}\right\} , \tag{2.25}$$

where $\alpha, \beta = e, \mu, \tau$ are the index of lepton flavors, and $a, b = 1, 2$ is that of spinors.

○ Neutrinoless double beta decay

It is much important to confirm whether the neutrino is Majorana or Dirac fermion. This is because the neutrino sector perhaps can solve various problems that the SM is facing if the neutrino is Majorana fermion. Up to now, the most promising way to confirm it is the observation of the neutrinoless double beta decay.

It is known that some radioactive elements undergo beta decay through the weak interaction as follows :

$$\begin{aligned} (A, Z) &\longrightarrow (A, Z+1) + e^- + \bar{\nu}_e , \\ (d &\longrightarrow u + e^- + \bar{\nu}_e) \end{aligned} \tag{2.26}$$

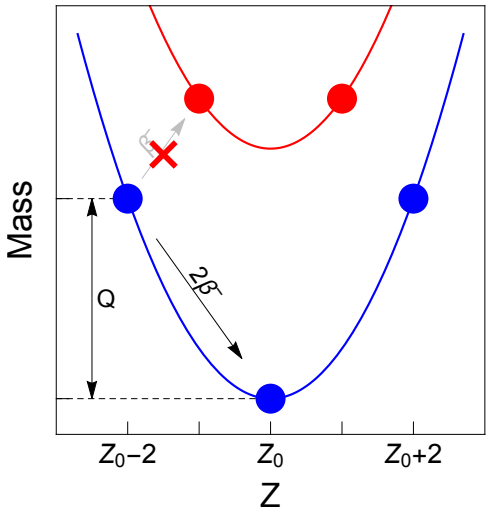

Figure 2.4: Relation between the atomic number Z and mass, based on the Bethe-Weizsäcker formula [84]. The blue (red) line corresponds to the case that both atomic and mass numbers are even (odd). In the setup of this figure, the element with $Z_0 - 1$ has smaller binding energy than that with $Z_0 - 2$. Therefore, the mass of the element with $Z_0 - 1$ is heavier than that of the element with $Z_0 - 2$, and the beta decay is prohibited. On the other hand, the element with Z_0 is lighter than that with $Z_0 - 2$, and therefore, the double beta decay can occur, and the difference of the binding energies Q is brought by emitted electron and neutrino.

where A and Z are mass and atomic numbers of the radioactive element, respectively.

However, among such radioactive elements whose mass and atomic numbers are even, some kinds of elements have higher binding energy than the daughter elements, as shown in Fig. 2.4, and therefore their masses are lighter than that of the daughter elements.[4] In this case, unstable elements with (A, Z) cannot undergo beta decay, which shifts atomic number by one. If the element with $(A, Z + 2)$ has larger biding energy and is lighter than that with (A, Z), as shown in Fig. 2.5a, double beta decay with neutrino emission ($2\nu\beta\beta$), which shifts the atomic number

[4]The Bethe-Weizsäcker formula [84] is based on the liquid drop model and describes binding energy between nucleons. For elements with $A \lesssim 30$, the binding energy $B(A, Z)$ is given accurately by five terms as follows :

$$B(A,Z) = a_V A - a_S A^{\frac{2}{3}} - a_C \frac{Z(Z-1)}{A^{\frac{1}{3}}} - a_A \frac{(A-2Z)^2}{A} + \delta(A,Z) \ . \tag{2.27}$$

In Eq. (2.27), the first term is known as volume term and comes from attractive forces by the strong interaction between neighboring nucleons. The second term is known as the surface term and corresponds to the correction due to the weakness of the binding energy of nucleons on the surface. This term is necessary because nucleons on the surface neighbor fewer nucleons than interior ones. The third term is known as the Coulomb term and comes from Coulomb repulsive force between protons.

Mass of nucleon is written in terms of the binding energy as follows :

$$m = Zm_p + (A - Z)m_n - B(A, Z) \ , \tag{2.28}$$

where m, m_p, and m_n are the nucleon, proton, and neutron mass, respectively.

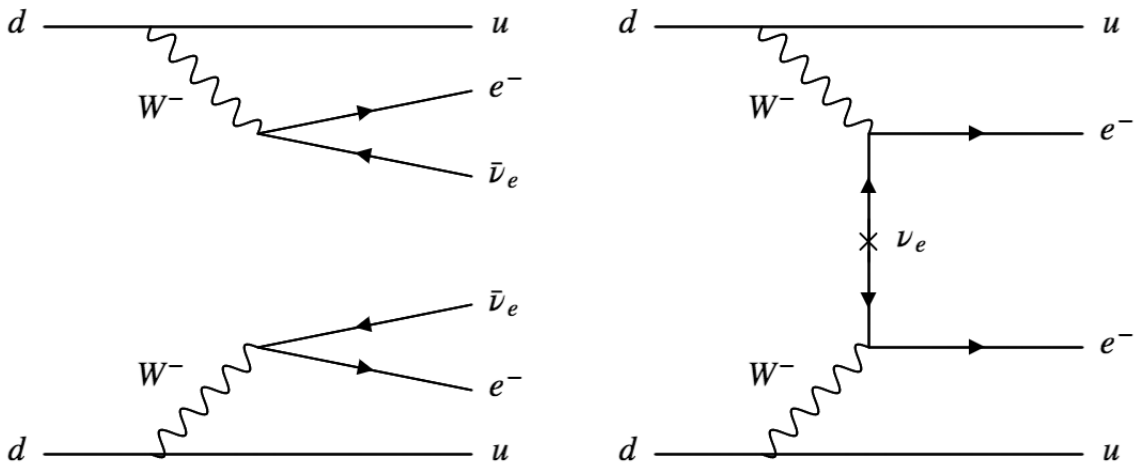

(a) Double beta decay with neutrino emission ($2\nu\beta\beta$) (b) Neutrinoless double beta decay ($0\nu\beta\beta$)

Figure 2.5: Feynman diagrams of two types of double beta decay. When neutrino is a Majorana particle, neutrinoless double beta decay can occur.

by two, can occur as follows :

$$(A, Z) \longrightarrow (A, Z+2) + 2e^- + 2\bar{\nu}_e \ . \tag{2.29}$$

This process is a second order process of the weak interaction, and the amplitude is suppressed by the Fermi constant, G_F, squared. As a consequence, the half-life is very long, and, for example, in ^{48}Ca case, is given by $T^{2\nu}_{1/2} = \left[6.4^{+0.7}_{-0.6}\ (\text{stat.})^{+1.2}_{-0.9}\ (\text{syst.})\right] \times 10^{19}$ yr [85].

Moreover, if neutrino is a Majorana particle, as shown in Fig. 2.5b, neutrinoless double beta decay ($0\nu\beta\beta$) can occur as follows :

$$(A, Z) \longrightarrow (A, Z+2) + 2e^- \ . \tag{2.30}$$

This process is not only second order of the weak interaction, but also suppressed by the interaction vertex, represented by a cross in Fig. 2.5b, $\langle m_{\beta\beta} \rangle / q \leq 1$ eV/100 MeV, where $\langle m_{\beta\beta} \rangle$ is the effective Majorana neutrino mass, and q is the typical scale of nuclear energy. On the other hand, in the $0\nu\beta\beta$ process, no neutrino is emitted, and therefore, the phase space factor is larger than the $2\nu\beta\beta$ process. The daughter elements are much heavier than emitted electrons and neutrinos, and then they are at rest. Thus the difference of the binding energy Q is distributed to the electrons and neutrinos. In the $2\nu\beta\beta$ process, the emitted neutrinos take away a part of "Q", and the energy spectrum of the emitted electrons is continuous, as shown in Fig. 2.6. On the other hand, in the ($0\nu\beta\beta$) process, neutrinos do not take away energy, and thus the energy spectrum has a sharp peak at $E = Q$. Therefore, by preparing a large number of radioactive

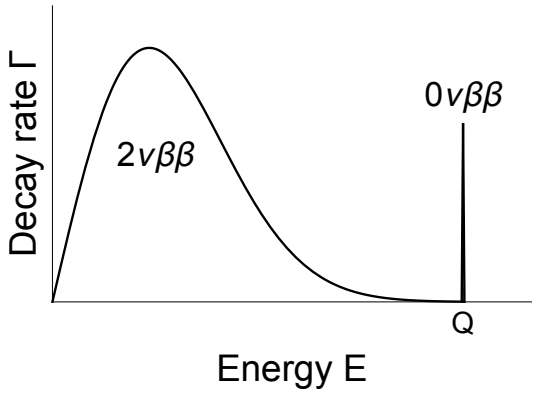

Figure 2.6: Energy spectra of emitted electrons in $2\nu\beta\beta$ and $0\nu\beta\beta$ processes. This figure shows the characteristic of the energy spectrum, and the scale of the vertical axis is not correct.

elements that are prohibited from undergoing the beta decay, and confirming whether there is a sharp peak at $E = Q$ in the energy spectrum of the emitted electrons, we can search for the Majorana nature of the neutrinos or, at least, the existence of new physics [86].

The effective Majorana neutrino mass $\langle m_{\beta\beta} \rangle$ is a parameter which characterizes the half-time of $0\nu\beta\beta$ process and given by

$$\langle m_{\beta\beta} \rangle \equiv |(\mathcal{M}_\nu)_{ee}| = \left| \sum_i m_i \left(U_{\rm PMNS}\right)_{ei}^2 \right| = \left| m_1 c_{13}^2 c_{12}^2 + m_2 c_{13}^2 s_{12}^2 e^{i\alpha_2} + m_3 s_{13}^2 e^{i(\alpha_3 - 2\delta)} \right| \ , \quad (2.31)$$

where $(\mathcal{M}_\nu)_{ee}$ is the (e, e) element of the mass matrix for the light neutrinos, and m_i $(i = 1, 2, 3)$ is the mass eigenvalues of the light neutrinos. As is described in detail in subsection 2.2.3, $U_{\rm PMNS}$ is the unitary matrix, so-called Pontecorvo–Maki–Nakagawa–Sakata matrix (PMNS matrix) [87, 88] and characterized by the mixing between three lepton flavors, $\sin\theta_{ij} \equiv s_{ij}$, $\cos\theta_{ij} \equiv c_{ij}$, one Dirac CP phase, δ, and two Majorana CP phases, $\alpha_{2,3}$.[5] Using the effective Majorana neutrino mass, the half-life of $(0\nu\beta\beta)$ process, $T_{1/2}^{0\nu}$, is given by [50]

$$\left(T_{1/2}^{0\nu}\right)^{-1} = G^{0\nu} \left| M_{\rm NM}^{0\nu} \right|^2 \frac{\langle m_{\beta\beta} \rangle^2}{m_e^2} \ , \quad (2.32)$$

where $G^{0\nu}$ is the phase space volume, and $M_{\rm NM}^{0\nu}$ is the nuclear matrix element. Among these parameters, the theoretical values of the nuclear matrix element have large uncertainties coming from the uncertainty in nuclear models.

Recently, various experiments are performing to observe the neutrinoless double beta decay, but they have not detected[6] , and then these experiments give severe bounds on the half-life and

[5] When neutrinos are Dirac particles, the Majorana CP phases do not exist. Moreover, even for the Majorana neutrinos, if two (not three) right-handed states are introduced, only one Majorana CP phase exists.

[6] The HEIDELBERG-MOSCOW experiment claimed that they had observed neutrinoless double beta decay [89–91]. The detail of their claim is that they detected $0\nu\beta\beta$ process of ^{76}Ge at the 6σ significance level and obtained $T_{1/2}^{0\nu}(^{76}\mathrm{Ge}) = \left(2.23^{+0.44}_{-0.31}\right) \times 10^{25}$ [year]. However, many researchers are doubtful about, for example, treatments of data [92–95], and there is no consensus on the discovery of the $0\nu\beta\beta$ process.

effective Majorana neutrino mass. In Tab. 2.1, we show the experiments which are performing and planning and their sensitivities. Moreover, for reference, the KamLAND-Zen experiment, which gives the most stringent bound, is also described at the bottom of the table.

Experiment	Isotope	Sensitivity of $\langle m_{\beta\beta} \rangle$ [meV]	Experimental period
KamLAND-ZEN 800 [96]	^{136}Xe	$40 \lesssim$	since 2019
KamLAND2-ZEN [97]	^{136}Xe	$20 \lesssim$	since 2027
SNO+ [98]	^{130}Te	55-133	for 5 years, since 2017
LEGEND-200 [99]	^{76}Ge	< 75	for 5 years, since 2021
LEGEND-1000 [99]	^{76}Ge	< 24	for 10 years
CUORE [100]	^{130}Te	50-130	$2017 \sim 2022$
CUPID [101]	^{130}Te	6-15	for 10 years
NEXT-100 [102, 103]	^{136}Xe	80-160	for 3 years, since 2021
SuperNEMO [104]	^{82}Se	50-100	for 5 years
nEXO [105]	^{136}Xe	5.7-17.7	for 10 years
KamLAND-ZEN [97, 106]	^{136}Xe	61-165	finished

Table 2.1: On-going and planned experiments and their sensitivities of the effective Majorana neutrino mass. The uncertainties of $\langle m_{\beta\beta} \rangle$ come from the uncertainties of the nuclear matrix elements.

2.2.2 Seesaw mechanism

There is no doubt that neutrinos are massive because of the observation of the neutrino oscillation. By the precise measurements of the neutrino oscillation, we know two neutrino mass squared differences, but do not know absolute values of the neutrino masses. The recent cosmological and astrophysical surveys give the severe constraint on the sum of the neutrino masses $\sum m_{\nu_i} < 0.15$ eV for normal ordering [107]. [7] These results indicate that neutrino masses are much smaller than the other SM fermions with $\mathcal{O}$(MeV-GeV) masses. If neutrinos are Dirac fermions and only renormalizable mass terms are considered, the neutrino masses are originated from the Dirac Yukawa terms, and this fact indicates the existence of a large hierarchy among the Yukawa coupling constants of the SM fermions.

Seesaw mechanism [38–41], discussed in this subsection, gives natural explanation for the mass hierarchy of the SM fermions. So far, various kinds of seesaw models have been proposed, and they are characterized by new fields introduced. In this subsection, we introduce the type-I

[7] The Planck Collaboration gives the stronger bound on the sum of the neutrino masses : $\sum m_{\nu_i} < 0.12$ eV (95% C.L.) [25]. To obtain this value, they assumed degeneracy of the neutrino masses. In Ref. [107], the neutrino mass squared differences are taken into account, and a more conservative bound is given.

seesaw model, which plays an important role in Chapter 6.

◯ Type-I seesaw model

In the type-I seesaw model, right-handed neutrinos are introduced, and neutrinos are assumed to be Majorana particles. The neutrino mass matrix is written by

$$\begin{aligned} -\mathcal{L}_{\nu,\mathrm{m}} &= \frac{1}{2}\left(\nu_L^T, (N^c)^T\right)\begin{pmatrix} 0 & \mathcal{M}_D \\ \mathcal{M}_D^T & \mathcal{M}_R \end{pmatrix}\begin{pmatrix} \nu_L \\ N^c \end{pmatrix} \\ &\equiv \frac{1}{2}\Psi_\nu^T \mathcal{M} \Psi_\nu \ , \end{aligned} \tag{2.33}$$

where $\nu_L^T = (\nu_{L,e}, \nu_{L,\mu}, \nu_{L,\tau})^T$ and $N^T = (N_e, N_\mu, N_\tau)^T$ are left-handed and right-handed neutrinos, respectively. $\mathcal{M}_D$ and $\mathcal{M}_R$ are the Dirac and Majorana mass term, respectively, and both are 3 by 3 matrices. Among them, the Majorana mass term, $(N^c)^T \mathcal{M}_R N^c$ is a lepton number violating operator ($\Delta L = 2$).

Here, we assume that the Majorana mass is much heavier than the Dirac mass, that is

$$(\Theta)_{\alpha\beta} \equiv (\mathcal{M}_D \mathcal{M}_R^{-1})_{\alpha\beta} \ll 1 \ , \tag{2.34}$$

where α, β are indices of flavors. Diagonalization of the neutrino mass matrix gives the mass eigenvalues for the active and heavy neutrinos. First, we block-diagonalize the neutrino mass matrix in terms of the left-handed and right-handed parts by a unitary transformation of Ψ. The block-diagonalization is realized by an approximate orthogonal matrix, $\mathcal{U}$, which satisfies $\mathcal{U}\mathcal{U}^T = \mathcal{U}^T\mathcal{U} = 1 + \mathcal{O}(\Theta^4)$, as follows :

$$\mathcal{U}^T \mathcal{M} \mathcal{U} = \begin{pmatrix} \mathcal{M}_{\nu_L} & 0_{3\times3} \\ 0_{3\times3} & \mathcal{M}_N \end{pmatrix} + \mathcal{O}(\Theta^3 \mathcal{M}_R) \ , \tag{2.35}$$

$$\mathcal{U} = \begin{pmatrix} 1_{3\times3} - \frac{1}{2}\Theta\Theta^T & \Theta \\ -\Theta^T & 1_{3\times3} - \frac{1}{2}\Theta^T\Theta \end{pmatrix} \ , \tag{2.36}$$

$$\mathcal{M}_{\nu_L} = -\mathcal{M}_D \mathcal{M}_R^{-1} \mathcal{M}_D^T \ , \tag{2.37}$$

$$\mathcal{M}_N = \mathcal{M}_R + \frac{1}{2}\left(\mathcal{M}_R\Theta^T\Theta + \Theta^T\Theta\mathcal{M}_R\right) \simeq \mathcal{M}_R \ , \tag{2.38}$$

where $\mathcal{M}_{\nu_L}$ and $\mathcal{M}_N$ are the mass matrices for the active and heavy neutrinos. As shown in Eq. (2.37), the mass matrix for the active neutrinos is suppressed by the inverse of the masses for the Majorana masses, and then the lightness of the masses for the active neutrinos can be realized without pretty small Dirac Yukawa couplings. This type-I seesaw model is represented by the Feynman diagram in Fig. 2.7.

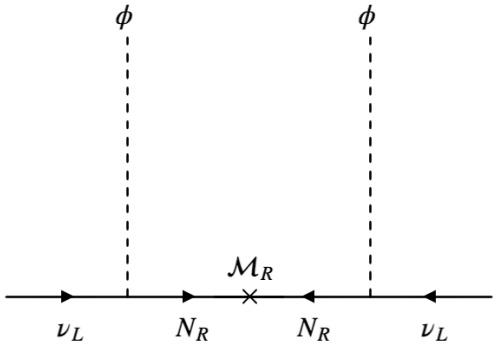

Figure 2.7: Feynman diagram which realizes lightness of the active neutrinos in the type-I seesaw model.

2.2.3 Flavor mixing and mass hierarchy of neutrinos

When the right-handed neutrinos are introduced in the SM, the neutrinos can form the Dirac mass terms and have masses. In general, the flavor eigenstates of the neutrinos and charged leptons are different from the mass eigenstates, and then the flavor mixing appears in the charged current of leptons, just like the flavor mixing in the quark sector. Moreover, by the observations of the neutrino oscillation, the mass squared differences of the neutrinos are measured precisely, but the absolute masses are unknown. In this subsection, we give a brief review of the flavor mixing in the lepton sector and mass ordering of the active neutrinos.[8]

◯ Mass hierarchy

The absolute masses of the neutrinos are bounded by astrophysical observations, but the precise value is unknown. On the other hand, the squared mass differences of the neutrinos are precisely measured by observations of neutrino oscillation. The observations of solar and atmospheric neutrinos imply the existence of three mass eigenstates of neutrinos. Among two eigenstates implied by the solar neutrinos, the mass of the lighter (heavier) is defined by $m_1(m_2)$, and the squared mass difference from the solar neutrinos is written as $\Delta m^2_{\rm sol} \equiv \Delta m^2_{21} = m_2^2 - m_1^2$. Moreover, a mass of third mass eigenstate is defined by m_3, and the squared mass difference from the atmospheric neutrinos is written by $\Delta m_{\rm atm} \equiv \Delta m^2_{32(31)} = m_3^2 - m^2_{2(1)}$. We know $\Delta m^2_{\rm sol} \ll |\Delta m^2_{\rm atm}|$, and the followng parameters, Δm^2 and δm^2 are often used :

$$\Delta m^2 \equiv \Delta m^2_{31} - \Delta m^2_{21}/2 = m_3^2 - (m_2^2 + m_1^2)/2 \ , \tag{2.39}$$

$$\delta m^2 \equiv \Delta m^2_{21} = m_2^2 - m_1^2 \ . \tag{2.40}$$

δm^2 is positive by definition of m_1 and m_2, and Δm^2 may be either positive or negative. As

[8] This kind of topic is written in detail in, for example, Refs .[50, 108].

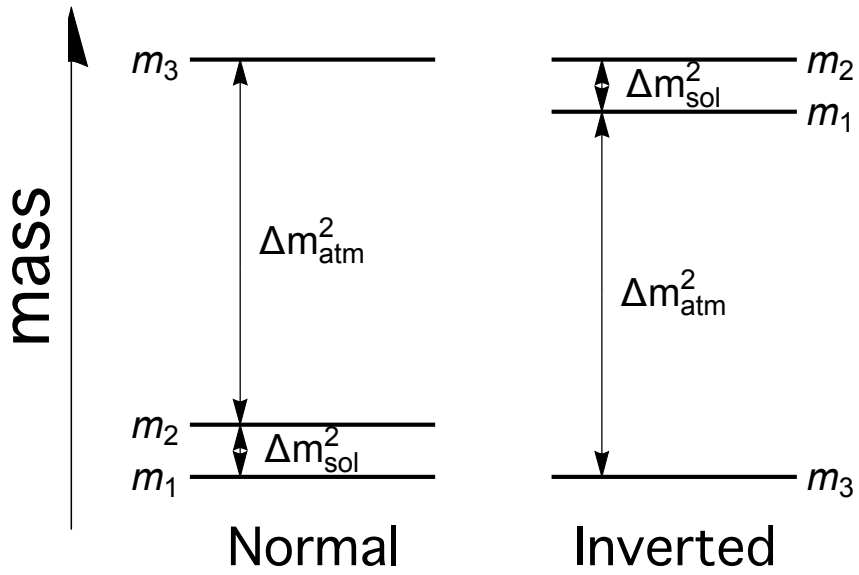

Figure 2.8: Mass hierarchy of neutrinos. The left shows the normal ordering (NO), and the right shows the inverted ordering (IO).

shown in Fig. 2.8, when $\Delta m^2 > 0$, namely $m_1 < m_2 < m_3$, such a mass hierarchy is called Normal Ordering (NO). On the other hand, when $\Delta m^2 < 0$, namely $m_3 < m_1 < m_2$, such is called Inverted Ordering (IO).

◯ Flavor mixing

Interactions between the SM gauge bosons and leptons come from the kinetic terms of the leptons as follows :

$$\mathcal{L}_{\text{Kinetic}} \supset -e j^{\mu}_{\gamma} A_{\mu} - \frac{g}{2\cos\theta_W} j^{\mu}_{\text{NC}} Z_{\mu} - \frac{g}{2\sqrt{2}} (j^{\mu\dagger}_{W} W^{+}_{\mu} + j^{\mu}_{\text{CC}} W^{-}_{\mu}) \ , \tag{2.41}$$

where j_γ, j_{NC}, and j_{CC} are the electromagnetic, neutral, and charged currents, respectively, and they are given by

$$j^{\mu}_{\gamma} = -\bar{e}\gamma^{\mu} e \ , \tag{2.42}$$

$$j^{\mu}_{\text{NC}} = \bar{\nu}\gamma^{\mu} P_L \nu + \bar{e}\gamma^{\mu}(2\sin\theta_W - P_L) e \ , \tag{2.43}$$

$$j^{\mu}_{\text{CC}} = 2\bar{e}\gamma^{\mu} P_L \nu \ , \tag{2.44}$$

with the elementary charge, e, the gauge coupling constant of $\text{SU}(2)_L$, g, and the Weinberg angle, θ_W. A^μ, Z^μ, and $W^{\pm\mu}$ denote the SM photon, Z boson, and W boson, respectively. In Eqs. (2.43) and (2.44), $P_{L/R} \equiv (1 \mp \gamma_5)/2$ is the projection operator which extracts left-handed element. In the above equations, $e^T = (e, \mu, \tau)^T$ and $\nu^T = (\nu_e, \nu_\mu, \nu_\tau)^T$. By the unitary

transformations of the leptons :

$$\begin{aligned} e'_L &= V_{e,L} e_L, \quad e'_R = V_{e,R} e_R, \\ \nu' &= V_{\nu,L} \nu_L, \quad N' = V_{\nu,R} N_R \ , \end{aligned} \tag{2.45}$$

the mass matrices for the leptons in the flavor basis can be diagonalized as follows :

$$V_{e,L}^\dagger \mathcal{M}_D^e V_{e,R} = \mathrm{diag}(m_e, m_\mu, m_\tau) \ , \tag{2.46}$$

$$V_{\nu,L}^T \mathcal{M}_{\nu_L} V_{\nu,L} = \mathrm{diag}(m_1, m_2, m_3) \ . \tag{2.47}$$

In Eqs. (2.45), fields with primes denote that they are mass eigenstates, while those without primes denote flavor eigenstates. Using the mass eigenstates, the charged current is rewritten as follows :

$$j_W^\mu = 2\bar{e}'_L V_{L,e}^\dagger V_{L,\nu} \gamma^\mu \nu' = 2\bar{e}'_L U_{\mathrm{PMNS}} \gamma^\mu \nu' \ , \tag{2.48}$$

where U_{PMNS} is the PMNS matrix [87, 88] and characterizes flavor mixing in the lepton sector. In the neutral current, because $V_{L,e}$ and $V_{L,\nu}$ are unitary matrices, no flavor mixing appears.

So far, we derived the PMNS matrix from general mass matrices for the leptons, and, from here, we consider the lepton mixing in the basis so that the mass matrix for the charged leptons is diagonal. On this basis, the relation between the flavor eigenstates, ν_α, and mass eigenstates, ν'_i, of the neutrinos is given by the PMNS matrix as follows :

$$\nu_{L,\alpha} = \sum_{i=1,2,3} (U_{\mathrm{PMNS}})_{\alpha i} \nu'_i \qquad (\alpha = e, \mu, \tau) \ . \tag{2.49}$$

The mass matrix for the active neutrinos is diagonalized by the PMNS matrix as follows :

$$U_{\mathrm{PMNS}}^T \mathcal{M}_{\nu_L} U_{\mathrm{PMNS}} = \mathrm{diag}(m_1, m_2, m_3) \ . \tag{2.50}$$

Next, we discuss the degree of freedom in the PMNS matrix. Generally speaking, when there are N generations, there are N^2 degrees of freedom in the PMNS matrix because the PMNS matrix is unitary. The breakdown of the degree of freedom is composed of $N(N-1)/2$ mixing angles and $N(N+1)/2$ phases. When the neutrinos are Dirac particles, $2N-1$ phases can be removed by phase redefinition of the lepton fields. Therefore, the PMNS matrix eventually has $N(N-1)/2$ mixing angles and $(N-1)(N-2)/2$ CP phases. On the other hand, when the neutrinos are Majorana particles, the Majorana mass terms are not invariant under the above phase redefinition. Thus, only the redefinition of the charged leptons is allowed, and N phases can be removed. There are $N(N-1)/2$ remaining phases, and therefore the PMNS matrix eventually has $N(N-1)/2$ mixing angles and $N(N-1)/2$ phases for the Majorana case. In the SM, there are three lepton generations, namely electron, muon, and tau particle, and the

parameter	mass ordering	Best fit	1σ	3σ
$\delta m^2/10^{-5}$ eV^2	NO,IO	7.39	7.19 $\to$ 7.60	6.79 $\to$ 8.01
$\lvert\Delta m^2/10^{-3}\rvert$ eV^2	NO	2.528	2.497 $\to$ 2.557	2.436 $\to$ 2.618
	IO	-2.510	-2.541 $\to$ -2.480	-2.601 $\to$ -2.419
$\sin^2\theta_{12}/10^{-1}$	NO,IO	3.10	2.981 $\to$ 3.230	2.75 $\to$ 3.50
$\sin^2\theta_{13}/10^{-2}$	NO	2.237	2.172 $\to$ 2.303	2.044 $\to$ 2.435
	IO	2.259	2.194 $\to$ 2.324	2.064 $\to$ 2.457
$\sin^2\theta_{23}/10^{-1}$	NO	5.63	5.39 $\to$ 5.81	4.33-6.09
	IO	5.65	5.43 $\to$ 5.82	4.36 $\to$ 6.10
$\delta/^\circ$	NO	221	193 $\to$ 260	144 $\to$ 357
	IO	282	257 $\to$ 305	205 $\to$ 348

Table 2.2: Values for the neutrino oscillation parameters we use in this paper. We take them from the NuFIT v4.1 result with the Super-Kamiokande atmospheric data [109, 110].

PMNS matrix has three mixing angles and three CP phases. Among three CP phases, the one CP phase which exists both in the Dirac and Majorana cases is called the Dirac CP phase. On the other hand, the two CP phases which are added in the Majorana case are called Majorana CP phases.

The PMNS matrix is characterized by the above mixing angles and CP phases and written as follows :

$$U_{PMNS} = \begin{cases} V & \text{(Dirac)} \\ VP & \text{(Majorana)} \end{cases} , \tag{2.51}$$

$$V \equiv \begin{pmatrix} c_{12}c_{13} & s_{12}c_{13} & s_{13}e^{-i\delta} \\ -s_{12}c_{23} - c_{12}s_{23}s_{13}e^{i\delta} & c_{12}c_{23} - s_{12}s_{23}s_{13}e^{i\delta} & s_{23}c_{13} \\ s_{12}s_{23} - c_{12}c_{23}s_{13}e^{i\delta} & -c_{12}s_{23} - s_{12}c_{23}s_{13}e^{i\delta} & c_{23}c_{13} \end{pmatrix} , \tag{2.52}$$

$$P \equiv \begin{pmatrix} 1 & & \\ & e^{i\frac{\alpha_2}{2}} & \\ & & e^{i\frac{\alpha_3}{2}} \end{pmatrix} , \tag{2.53}$$

where $s_{ij} \equiv \sin\theta_{ij}$ and $c_{ij} \equiv \cos\theta_{ij}$ with the mixing angle, θ_{12}, θ_{23}, and θ_{13}. δ and $\alpha_{2,3}$ are the Dirac and Majorana CP phases, respectively. In Eqs. (2.51)$\sim$(2.53), we follow the convention of the Particle Data Group [50], where $0 < \Delta m^2_{21} \ll |\Delta m^2_{31}|$ with $\Delta m^2_{ij} \equiv m^2_i - m^2_j$. In Tab. 2.2, we show the recent global fit, `NuFIT v4.1` [109, 110].

2.3 Standard Cosmology

The history of our Universe described by the standard cosmology is dynamic. The Universe is expanding since its birth, and the temperature is cooling with its expansion. Such behavior is described by general relativity (GR). In this section, we give a brief review of the standard cosmology that is one of the bases of Chapter 6 and 7.

2.3.1 Space-time of the Universe

The standard cosmology is based on the following fact :

- The Universe is spatially almost homogeneous and isotropic on large scales, and there is no special location and direction in the Universe.

This notion is called *cosmological principle* and confirmed by various observations. This principle is satisfied when we see at enough large scale. On the other hand, at the small scales, the Universe has various structures, for example, galaxies, stars, and so on.

Homogeneous and isotropic space-time is described by the Friedmann-Lemaître-Robertson-Walker metric (FLRW) metric. Hereafter, we apply the natural unit, and because the Universe has no special direction, we use the polar coordinates, $(x^0, x^1, x^2, x^3) = (t, r, \theta, \phi)$. The FLRW metric is given by

$$ds^2 = g_{\mu\nu} dx^\mu dx^\nu \ , \tag{2.54}$$

$$g_{00} = 1, \quad g_{11} = -\frac{a(t)^2}{1 - Kr^2}, \quad g_{22} = -a(t)^2 r^2, \quad g_{33} = -a(t)^2 r^2 \sin\theta^2, \quad g_{\mu\nu} = 0 \ (\mu \neq \nu), \tag{2.55}$$

where $a(t)$ is the so-called scale factor that depends on the time and characterizes the size of the Universe. K is the spatial curvature and can be taken to be $-1, 0$, and $+1$. When $K = +1(-1)$, the space-time of the Universe is non-Euclidean and has non-zero curvature. When $K = 0$, the space-time is flat, and the CMB observation indicates our Universe is $K \approx 1$ [25].

The space-time is characterized by the Christoffel symbols of the second kind, and they are defined by

$$\Gamma^\mu_{\nu\rho} \equiv \sum_\lambda \frac{1}{2} g^{\mu\lambda} \left(\frac{\partial g_{\rho\lambda}}{x^\nu} + \frac{\partial g_{\nu\lambda}}{x^\rho} - \frac{\partial g_{\nu\rho}}{x^\lambda} \right) \ , \tag{2.56}$$

Under the FLRW metric, the Christoffel symbols are calculated as

$$\begin{aligned} &\Gamma^0_{00} = \Gamma^0_{0i} = \Gamma^0_{i0} = \Gamma^i_{00} = 0, \quad \Gamma^0_{ij} = \frac{\dot{a}}{a} g_{ij} = H g_{ij}, \quad \Gamma^i_{j0} = \Gamma^i_{0j} = \frac{\dot{a}}{a} \delta_{ij} = H \delta_{ij} \ , \\ &\Gamma^i_{jk} = g^{ii} \left(\frac{\partial g_{ki}}{x^j} + \frac{\partial g_{ji}}{x^k} - \frac{\partial g_{jk}}{x^i} \right) \ , \end{aligned} \tag{2.57}$$

where $\dot{} \equiv d/dt$ is the time derivative of the scale factor, and δ_{ij} is the Kronecker delta. $H(t) \equiv \dot{a}(t)/a(t)$ is the Hubble parameter and characterizes the expansion rate of the Universe. The Hubble parameter depends on the time, and the present value of $H(t)$ is called the Hubble constant, H_0. The recent observations of the CMB [25] give

$$H_0 = 67.4 \pm 0.5 \text{ km s}^{-1} \text{ Mpc}^{-1} \ . \tag{2.58}$$

In terms of the Christoffel symbols, the Riemann curvature tensor, Ricci tensor, and Ricci scalar are defined by

$$R^{\lambda}_{\kappa\mu\nu} \equiv \frac{\partial \Gamma^{\lambda}_{\mu\nu}}{\partial x^{\kappa}} - \frac{\partial \Gamma^{\lambda}_{\kappa\nu}}{\partial x^{\mu}} + \sum_{\rho} \Gamma^{\lambda}_{\kappa\rho}\Gamma^{\rho}_{\mu\nu} - \sum_{\rho} \Gamma^{\lambda}_{\mu\rho}\Gamma^{\rho}_{\kappa\nu} \ , \tag{2.59}$$

$$R_{\mu\nu} = \sum_{\kappa} R^{\kappa}_{\kappa\mu\nu} \ , \tag{2.60}$$

$$\mathcal{R} = \sum_{\mu\nu} g^{\mu\nu} R_{\mu\nu} \ . \tag{2.61}$$

Using the results in Eqs (2.57), non-zero Ricci tensor and Ricci scalar are calculated as

$$R_{00} = -3\frac{\ddot{a}}{a}, \quad R_{ij} = -\left\{ \frac{\ddot{a}}{a} + 2\frac{\dot{a}^2}{a^2} + 2\frac{K}{a^2} \right\} \delta_{ij} \ , \tag{2.62}$$

$$\mathcal{R} = -6\left\{ \frac{\ddot{a}}{a} + \frac{\dot{a}^2}{a^2} + \frac{K}{a^2} \right\} \ . \tag{2.63}$$

Mass and energy distributions in the Universe are characterized by the energy-momentum tensor, $T^{\mu\nu}$. In the FLRW space-time, the Universe is homogeneous and isotropic, and then the energy-momentum tensor is described in terms of the energy density, ρ, and pressure, p, as follows :

$$T^{\mu}_{\ \nu} = \begin{pmatrix} \rho & 0 & 0 & 0 \\ 0 & -p & 0 & 0 \\ 0 & 0 & -p & 0 \\ 0 & 0 & 0 & -p \end{pmatrix} \ . \tag{2.64}$$

2.3.2 Evolution of the Universe

The evolution of the Universe is described by the Einstein equation :

$$R_{\mu\nu} - \frac{1}{2}\mathcal{R} g_{\mu\nu} - \Lambda g_{\mu\nu} = 8\pi G T_{\mu\nu} \ , \tag{2.65}$$

where G is the gravitational constant and $T_{\mu\nu}$ is the energy-momentum tensor. The third term in the left-hand side of Eq (2.65) is the cosmological constant term. From the $(0,0)$ component of Eq. (2.65), the Friedmann equation is obtained as

$$H^2 = \left(\frac{\dot{a}}{a}\right)^2 = \frac{8\pi G}{3}(\rho + \rho_{\Lambda}) - \frac{K}{a^2} \ , \tag{2.66}$$

where $\rho_\Lambda \equiv -\Lambda/8\pi G$ is the energy density originated from the cosmological constant. From the (i,j) component of Eq. (2.65), the following equation is obtained :

$$\frac{\ddot{a}}{a} = -\frac{4\pi G}{3}(\rho + 3p) \ . \tag{2.67}$$

These two equations originated from the Einstein equation determine the relationship between the dynamics of space-time and energy distribution. From Eq. (2.67) and the derivative of Eq. (2.66) with respect to time, t, we obtain

$$\dot{\rho} = -3H(\rho + p) \ , \tag{2.68}$$

and this relation is also derived from the time component of the conservation law of energy and momentum :

$$\nabla_\mu T^{\mu\nu} = 0 \ , \tag{2.69}$$

where ∇_μ is the covariant derivative and defined by

$$\nabla_\kappa X^{\lambda\mu} \equiv \frac{\partial X^{\lambda\mu}}{\partial x^\kappa} + \sum_\nu \left(\Gamma^\lambda_{\kappa\nu} X^{\nu\mu} + \Gamma^\mu_{\kappa\nu} X^{\nu\lambda} \right) \ . \tag{2.70}$$

In Eqs. (2.66) and (2.67), there are three independent variables, a, ρ, and p, and then it is impossible to solve these equations. By determining what occupies the energy density of the Universe, namely, giving the relation between the energy density and pressure, the above variable can be calculated. In the Universe, there are three kinds of energy component as follows :

◯ Radiation

Radiation is the relativistic component of particles in the Universe, and a representative example is a photon. The radiation satisfies the following equation of state (EOS)

$$p = \frac{1}{3}\rho \ . \tag{2.71}$$

From Eq. (2.69), the energy density of the radiation satisfies the following time evolution with the expansion of the Universe :

$$\rho_{\rm R} \propto a^{-4} \ . \tag{2.72}$$

◯ Matter

The matter is the non-relativistic component of particles in the Universe, and a representative example is a baryon in the present Universe. The matter satisfies the following EOS

$$p = 0 \ . \tag{2.73}$$

From Eq. (2.69), the energy density of the matter satisfies

$$\rho_{\mathrm{M}} \propto a^{-3} \ . \tag{2.74}$$

◯ Dark energy

Dark energy is a kind of energy components and contributes to the acceleration of the expansion of the Universe. The dark energy satisfies the following EOS

$$p = -\rho \ . \tag{2.75}$$

From Eq. (2.69), the energy density of the dark energy satisfies the following time evolution with the expansion of the Universe :

$$\rho_\Lambda = \text{const} \ . \tag{2.76}$$

Substituting the obtained energy density of each component for Eq. (2.66), the behavior of the scale parameter as a function of the time can be calculated as follows :

$$a(t) \propto \begin{cases} t^{\frac{1}{2}} & \text{[radiation dominant]} \\ t^{\frac{2}{3}} & \text{[matter dominant]} \\ \exp(H_0 t) & \text{[dark energy dominant]} \end{cases} \ . \tag{2.77}$$

The radiation, matter, and dark energy components of the energy coexist in the Universe. The fraction of these components is parametrized by the density parameters as

$$\Omega_i = \frac{\rho_i}{\rho_c} \qquad (i = r, m, \Lambda) \ , \tag{2.78}$$

where $\rho_c \equiv= 3H^2/8\pi G$ is called the critical density, and from Eq. (2.66), the density parameters satisfy

$$1 - (\Omega_r + \Omega_m + \Omega_\Lambda) = -\frac{K}{a^2 H^2} \ . \tag{2.79}$$

According to the recent result by the Planck collaboration [25], the non-relativistic matter and dark energy occupy about 68% and 32% of the energy density in the present Universe, respectively. The fraction of the relativistic radiations is $\mathcal{O}(10^{-5})$ and pretty small. This is because, as shown in Eqs. (2.72) and (2.74), the energy density of the radiation decreases more rapidly with the expansion of the Universe than that of the non-relativistic matter. The sum of Ω_r, Ω_m, and Ω_Λ is pretty close to one. Therefore, the curvature term is negligible, and the curvature of the Universe can be considered to be flat. Moreover, the above result of the energy components in the present Universe and time evolution of them imply the existence of the radiation and then matter dominant eras.

2.3.3 Early Universe and thermodynamics

In the previous subsection, we discuss the evolution of the Universe and confirm that the Universe expands with the time evolution, as shown in Eq. (2.77). Thus, the early Universe was much smaller and hotter than the previous one. Particles in the early Universe interact with each other, and the higher the temperature is, the more the interaction rate is. In the early radiation and matter dominant eras, the Hubble parameter also increases as going back in time. However, the former increases more rapidly and, at a certain time, exceeds the latter. Such a comparison between the Hubble parameter and interaction rate is important to judge whether a given particle interacts with other ones or not. Gamov's criterion gives one of the simplest standards for judgment of whether a given particle is decoupled or not as follows :

$$\begin{cases} \Gamma_{\rm int} > H & \text{in thermal equilibrium} \\ \Gamma_{\rm int} < H & \text{decoupled} \end{cases} . \tag{2.80}$$

From Gamov's criterion, it is certain that particles interact with each other and are in the thermal equilibrium in the early Universe.

Particles in the thermal equilibrium have a common parameter which characterizes their states, namely, temperature, T, and they obey the following Fermi-Dirac or Bose-Einstein distribution functions for the fermion or boson case, respectively :

$$f(\vec{p}, T) = \frac{1}{e^{(E-\mu)/T} \pm 1} , \tag{2.81}$$

where plus (minus) in the denominator is for fermion (boson), and $\vec{p}$, E, and μ are the spatial momentum, energy, and chemical potential of the particle, respectively. The thermodynamical intensive variables are calculated by integrating the distribution function over the particle momentum with some weight. The number density, energy density, and pressure of a given particle are given by

$$n(T) = g \int \frac{d^3p}{(2\pi)^3} f(\vec{p}, T) , \tag{2.82}$$

$$\rho(T) = g \int \frac{d^3p}{(2\pi)^3} E(\vec{p}) f(\vec{p}, T) , \tag{2.83}$$

$$p(T) = g \int \frac{d^3p}{(2\pi)^3} \frac{|\vec{p}|^2}{3E(\vec{p})} f(\vec{p}, T) , \tag{2.84}$$

where g is the internal degrees of freedom for the particle. The temperature dependence of these values varies according to whether the particles are fermion or boson, and relativistic or non-relativistic.

When particles are relativistic, the relation, $m \ll T$, is satisfied. If the chemical potential is negligible compared to the temperature, the number density, energy density, and pressure of a

given particle are given by

$$n(T) = \begin{cases} \frac{3}{4}\frac{\zeta(3)}{\pi^2} g T^3 & \text{[fermion]} \\ \frac{\zeta(3)}{\pi^2} g T^3 & \text{[boson]} \end{cases} , \tag{2.85}$$

$$\rho(T) = \begin{cases} \frac{7}{8}\frac{\pi^2}{30} g T^4 & \text{[fermion]} \\ \frac{\pi^2}{30} g T^4 & \text{[boson]} \end{cases} , \tag{2.86}$$

$$p(T) = \frac{1}{3}\rho(T) , \tag{2.87}$$

where $\zeta(z)$ is the Riemann zeta function.

When particles are non-relativistic, the relation, $T \ll m$, is satisfied. Regardless of whether the particles are fermion or boson, the above variables are given by

$$n(T) = g\left(\frac{mT}{2\pi}\right)^{\frac{3}{2}} e^{-\frac{m-\mu}{T}} , \tag{2.88}$$

$$\rho(T) = \left(m + \frac{3}{2}T\right) n(T) , \tag{2.89}$$

$$p(T) = n(T)T \ll \rho(T) . \tag{2.90}$$

As shown in Eqs. (2.85) $\sim$ (2.90), the thermodynamical variables of non-relativistic partcles are much suppressed by exponential factors. Thus, relativistic ones dominate most of these variables, and the non-relativistic ones do not give a significant contribution to them. Neglecting the non-relativistic component, the total energy density of the Universe is given by the sum of contributions from all kinds of relativistic particles :

$$\rho(T) \approx \rho_r(T) = \frac{\pi^2}{30} g_*(T) T^4 , \tag{2.91}$$

where g_* is the effective relativistic degrees of freedom given by

$$g_*(T) = \sum_{i_b \in \text{boson}} g_{i_b} + \frac{7}{8} \sum_{i_f \in \text{fermion}} g_{i_f} , \tag{2.92}$$

with $g_{i_{b(f)}}$ being the internal degrees of freedom for the particle $i_{b(f)}$. In Eq. (2.92), the thermal equilibrium between photon and particle $i_{b(f)}$ is assumed, and the temperature of $i_{b(f)}$ is taken to be the same value as that of photon. However, even though particles are relativistic, if they are decoupled from the thermal bath, generally their temperature is different from that of the photon. In that case, the effective relativistic degrees of freedom is given by

$$g_*(T) = \sum_{i_b \in \text{boson}} g_{i_b} \left(\frac{T_{i_b}}{T}\right)^4 + \frac{7}{8} \sum_{i_f \in \text{fermion}} g_{i_f} \left(\frac{T_{i_f}}{T}\right)^4 , \tag{2.93}$$

Next, we discuss the time dependence of temperature. In the previous subsection, we derived Eq. (2.68) corresponding to the energy conservation law. This equation leads to the following

equation :

$$0 = \frac{1}{T}\left(d(\rho a^3) + pd(a^3)\right) = \frac{1}{T}\left(dU + pdV\right) \\ = dS + \frac{1}{T}\sum_i \mu_i dN_i \ , \tag{2.94}$$

with the internal energy of the Universe, U, comoving volume, $V = a^3$, entropy, S, number of particle i, N_i, and chemical potential of i, μ_i. Therefore, if the numbers of particles are preserved or the chemical potentials are negligible, the entropy in the comoving volume is also preserved. Even if it is not the case, if particle reactions are in chemical equilibrium, the sum of $\mu_i dN_i$ vanishes, and the entropy is also preserved. By substituting Eq. (2.94) for Eq. (2.93), the entropy density is calculated as

$$s(T) \equiv \frac{S(T)}{a(T)^3} = \frac{4}{3}\frac{\rho(T)}{T} = \frac{2\pi^2}{45} g_{*s}(T) T^3 \ , \tag{2.95}$$

where g_{*s} is the entropic effective degrees of freedom defined by

$$g_{*s}(T) = \sum_{i_b \in \text{boson}} g_{i_b} \left(\frac{T_{i_b}}{T}\right)^3 + \frac{7}{8} \sum_{i_f \in \text{fermion}} g_{i_f} \left(\frac{T_{i_f}}{T}\right)^3 \ . \tag{2.96}$$

During the expansion of the Universe, if the entropic effective degrees of freedom does not change, the entropy is preserved because of the above discussion, and then the evolution of the scale factor is described as

$$S(T) = \frac{2\pi^2}{45} g_{*s}(T) T^3 a(T)^3 = \text{const} \Longrightarrow a(t) \propto T^{-1} \propto t^{\frac{1}{2}} \ . \tag{2.97}$$

At the end of this subsection, we see the temperature dependence of the Hubble parameter in the radiation dominant era for the discussion in the next subsection. By substituting Eq. (2.91) for Eq. (2.66), we obtain

$$H(T) = \left(\frac{\pi^2 g_*(T)}{90}\right)^{\frac{1}{2}} \frac{T^2}{M_{\rm P}} \propto t^{-1} \ , \tag{2.98}$$

with $M_{\rm P} \equiv 1/\sqrt{8\pi G} \simeq 2.4 \times 10^{18}$ GeV being the reduced Planck mass. Therefore, the Hubble parameter decreases with the expansion in the radiation dominant era.

2.3.4 Decoupling of Neutrino and Photon

In the early Universe, particles frequently interact with each other, and they are in thermal equilibrium. With the cooling of the Universe, the interaction rate drops, and the particles are decoupled from the thermal bath. In this subsection, we review the decoupling of neutrino and photon in the thermal history of the Universe.

Neutrino is one of the SM particles and interacts with other ones through weak interaction. The rate of the weak interaction is roughly given by

$$\Gamma_\nu \sim G_F^2 T^5 \ , \tag{2.99}$$

with $G_F \simeq 10^{-5}$ GeV^{-2} being the Fermi coupling constant, which gives the typical strength of weak interaction. Comparing Eq. (2.98) and (2.99), the decoupling temperature of neutrino is calculated as $T_{\nu,\mathrm{dec}} \sim 1.5$ MeV. After decoupling, a neutrino with energy, E, and momentum, $\vec{p}$, propagates as a free particle in the Universe, and, by redshift, its momentum decreases as

$$\vec{p}(t) = \frac{a(t_{\mathrm{dec}})}{a(t)} \vec{p}(t_{\mathrm{dec}}) \ , \tag{2.100}$$

where t_{dec} is the time at the neutrino decoupling. Because neutrinos do not interact with other particles, the number of them is preserved, and the number density of neutrinos decreases as $n(t) \propto a(t)^3$ with the expansion of the Universe. Therefore, for $t > t_{\mathrm{dec}}$, the distribution function of neutrinos is described by

$$f(\vec{p}(t), T(t)) = f\left(\frac{a(t_{\mathrm{dec}})}{a(t)} \vec{p}(t_{\mathrm{dec}}), T_{\mathrm{dec}} \right) = \frac{1}{\exp\left(\frac{|\vec{p}|}{T_\nu}\right) + 1} \ , \tag{2.101}$$

where $T_\nu(t) \equiv (a(t_{\mathrm{dec}})/a(t))\, T_{\mathrm{dec}}$ is the neutrino temperature after decoupling. When the temperature falls below the electron mass, electrons and positron annihilate through the following process : $e^+ + e^- \to 2\gamma$. At that time, they inject entropy into the photon and change the temperature of the photon. Before the annihilation of the electron, the temperatures of photon and neutrino are the same : $T_{\nu,b} = T_b$, where the subscript, $b(a)$ denotes before (after) the disappearance of the electron, respectively. After the disappearance, the temperatures of neutrino satisfies $T_{\nu,a} a_a = T_{\mathrm{dec}} a(t_{\mathrm{dec}}) = T_b a_b$. Moreover, from the entropy conservation, we obtain

$$g_{*s,b} T_b^3 a_b^3 = g_{*s,a} T_a^3 a_a^3 \ , \tag{2.102}$$

with

$$g_{*s,b} = g_\gamma + \frac{8}{7} \left\{ g_e \left(\frac{T_e}{T_b} \right)^3 + g_\nu \left(\frac{T_{\nu,b}}{T_b} \right)^3 \right\} = 2 + \frac{8}{7} \left\{ 4 + 2 \times 3 \right\} = \frac{43}{4} \ , \tag{2.103}$$

$$g_{*s,a} = g_\gamma + \frac{8}{7} g_\nu \left(\frac{T_{\nu,b}}{T_a} \right)^3 = 2 + \frac{8}{7} \times 2 \times 3 \times \left(\frac{T_{\nu,a}}{T_a} \right)^3 = 2 + \frac{21}{4} \left(\frac{T_{\nu,a}}{T_a} \right)^3 \ , \tag{2.104}$$

and three in the neutrino term of the above equations comes from the number of neutrino flavors. Combining these relations, we lastly see the relation between the temperatures of photon and neutrino after the annihilation of the electron as follows :

$$T_{\nu,a} = \left(\frac{4}{11} \right)^{\frac{1}{3}} T_a \ . \tag{2.105}$$

Using Eq. (2.105), the energy density of neutrinos is written in terms of that of the photon as

$$\rho_\nu(T) = \frac{7}{8} \times N_{\rm eff} \times \left(\frac{4}{11}\right)^{\frac{4}{3}} \rho_\gamma(T) \ , \tag{2.106}$$

with $N_{\rm eff}$ is the effective number of neutrino species and equal to be three when neutrinos were decoupled instantaneously in the early Universe. Some previous works [111–115] give the precise calculations without assuming instantaneous neutrino decoupling and with considering neutrino oscillation, and they predict the different evolution of momentum spectra of neutrinos from that in the naive calculation. Therefore, the effective number of neutrino species deviates from three and is given as $N_{\rm eff,SM} = 3.046$ [112]. The relativistic energy density of the Universe is parametrized in terms of $N_{\rm eff,SM}$ as follows

$$\rho_r(T) = \left[1 + \frac{7}{8} \times N_{\rm eff,SM} \times \left(\frac{4}{11}\right)^{\frac{4}{3}}\right] \rho_\gamma(T) \ . \tag{2.107}$$

However, if there are extra radiation components beyond the SM, extra factors are added into Eq. (2.107), and it is useful to parametrize the extra contributions by $\Delta N_{\rm eff}$ being deviation of $N_{\rm eff,SM}$ from the SM value as follows :

$$\rho_r(T) = \left[1 + \frac{7}{8} \times (N_{\rm eff,SM} + \Delta N_{\rm eff}) \times \left(\frac{4}{11}\right)^{\frac{4}{3}}\right] \rho_\gamma(T) \ . \tag{2.108}$$

If there are extra particles beyond the SM that couple to neutrinos, and they decouple from the thermal bath after the neutrino decoupling, extra particles inject entropy into neutrinos and heat the neutrino temperature. Therefore, $\Delta N_{\rm eff}$ deviates from $\Delta N_{\rm eff,SM}$. The recent Planck result of the CMB observation gives $N_{\rm eff} = 3.11^{+0.44}_{-0.43}$ (95% C.L., TT+lowE+lensing+BAO), and extra particles are constrained by comparing the Planck result and theoretical prediction.

After neutrino decoupling and BBN, photon eventually decouples from the other particles. In the early Universe, electrons exist as plasma and interact with photons through a coupling process between the electron and proton : $p + e \leftrightarrow {}^1{\rm H} + \gamma$, called recombination of hydrogen. The number densities of electron, proton, and hydrogen atom in thermal equilibrium are given by

$$n_i = g_i \left(\frac{m_i T}{2\pi}\right)^{\frac{3}{2}} e^{-\frac{m_i - \mu_i}{T}} \qquad (i = e, p, H) \ , \tag{2.109}$$

where g_i, m_i and μ_i denote the internal degrees of freedom, mass, and chemical potential for particle i. The condition for chemical equilibrium is written by

$$\mu_e + \mu_p = \mu_H \ . \tag{2.110}$$

From Eq. (2.109) and (2.110), we obtain

$$n_H = \frac{g_H}{g_e g_p} n_e n_p \left(\frac{m_e T}{2\pi}\right)^{-\frac{3}{2}} e^{\frac{B}{T}} \ , \tag{2.111}$$

$$B = m_e + m_p - m_H = 13.6 \text{ eV} \ . \tag{2.112}$$

Moreover, from the conservation laws of electromagnetic charge and baryon number, $n_e = n_p$ and $n_p + n_H = n_b$, with n_b being the baryon number density. With the cooling of the Universe, electrons couple to protons in the plasma and form hydrogen atoms. The ionization fraction $X_e \equiv n_p/n_b$ is calculated by the following Saha formura [116, 117] :

$$\frac{1 - X_e}{X_e^2} = \frac{4\sqrt{2}\zeta(3)}{\sqrt{\pi}} \eta_b \left(\frac{T}{m_e}\right)^{\frac{3}{2}} e^{\frac{B}{T}} \ , \tag{2.113}$$

with $\eta_b \equiv n_b/n_\gamma$. From Eq. (2.113), the ionization fraction fall much below one around $T \sim 4000$ K $= 0.4$ eV. In the derivation of Eq. (2.113), the thermal equilibrium is assumed, however with proceeding recombination of hydrogen, $p + e \leftrightarrow {}^1\mathrm{H} + \gamma$ process is driven out of equilibrium, and Eq. (2.113) is improper in such a condition. According to the precise analyses, the ionization fraction near recombination time ($800 < z < 1200$) is given in terms of the redshift, $z(t) \equiv (a(t_0)/a(t)) - 1$ with the present time t_0, as following fitting formula [118] :

$$X(z) \simeq 2.4 \times 10^{-3} \frac{1}{\Omega_b h} \left(\frac{z}{1000}\right)^{12.75} \qquad (800 < z < 1200) \ , \tag{2.114}$$

where $\Omega_b = \rho_b/\rho_c$ is the baryon density parameter.

For $T \lesssim 3000$ K, photons interact with electrons through the Thomson scattering, and electrons do with baryons through electromagnetic interaction.[9] Therefore, photons indirectly couple to baryons, and they behave as a mixed fluid. Because of gravitational gradient originated from inflation, this fluid accumulates in a dense region, and the density gradient consequently increases. On the other hand, the denser number fluid density is, the stronger pressure of the fluid is, and then such a pressure propagates in the fluid as oscillation, which is called the baryon acoustic oscillation. With the decreasing of free electrons, the Thomson scatterings between photons and electrons become rare, and around for $T \sim 3000$ K, the optical depth of Thomson scattering becomes one. Then photons stream without scattering with electrons, and such photons are observed now as CMB. The baryon acoustic oscillation is recorded as density fluctuations of baryon and photon and has been observed in CMB.

[9] See also Ref. [119].

Chapter 3

WIMP Dark Matter and Thermal Freeze-out Scenario

Dark matter (DM) has only quite weak interaction with the SM particles and affects visible matters through gravitational potential. The existence of dark matter firstly has been proposed by F. Zwicky in 1933 [120, 121]. He applied the virial theorem to the Coma Cluster and the estimated value of the total mass. By comparing it to the value estimated from the brightness and number of galaxies, he concluded the existence of missing mass. Moreover, starting with V. C. Rubin's work [19], distributions of rotation velocities of various galaxies have been observed, and they indicate the existence of missing mass. After these pioneer works, various observations indicate the existence of DM up to the present time. So far, CMB observations by the Planck satellite give the most precise value of the DM energy density in the Universe, and DM makes up 32% of the total energy density.

There is no candidate in the SM, and various types of DM are proposed from the perspective of the other BSM physics. For successful DM scenarios, it is important how DM is produced, and the observed relic density is realized. Weakly Interacting Massive Particles (WIMPs) are one of the attractive candidates and give a simple solution to the DM production, so-called thermal freeze-out mechanism. In the last several decades, many kinds of WIMP models are discussed, and great efforts have been underway to detect WIMPs.

In this chapter, we give a short review of WIMP dark matter and thermal freeze-out scenario. First, in Section 3.1, we show how thermal relic abundance of WIMP is calculated in the thermal freeze-out scenario. In Section 3.2, we introduce one of the DM models, called secluded DM, and discuss differences from other DM models. In Section 3.3, we give a review about DM search and current bounds from direct and indirect detection experiments.

3.1 Thermal Freeze-out Mechanism

In this section, we give a short review of the thermal freeze-out mechanism and an analytic formula of thermal relic abundance of DM, which appears in Chapter 7.

First, we show a rough story of the thermal freeze-out scenario. In the early Universe, DM is relativistic and in thermal equilibrium with the SM particles, and, from Eq. (2.85), the behavior of its number density is proportional to $T^3 \propto a^{-3}$. At a temperature where DM becomes non-relativistic, the behavior of DM number density changes and obeys Eq. (2.88). DM, however, interacts with the SM particles in the thermal bath and decreases with the expansion of the Universe. When the interaction rate with the SM particles, $\Gamma_{\rm int}$ is equal to be the Hubble parameter, H, the time interval of interactions reaches the age of the Universe, and the reactions is driven out of equilibrium. Then, the interactions freeze out, and the DM number density decreases by the expansion of the Universe and is proportional to a^{-3}.

To obtain a quantitative value of DM number density, we introduce the Boltzmann equation which describes the statistical behavior of a thermodynamic system. As shown in Appendix B.1, the Boltzmann equation for DM number density is given as follows :

$$\frac{dn_{\rm DM}}{dt} + 3Hn_{\rm DM} = -\left\langle \sigma_{\rm ann} v_{\rm rel} \right\rangle \left(n_{\rm DM}^2 - (n_{\rm DM}^{\rm eq})^2 \right) \ , \tag{3.1}$$

where $n_{\rm DM}$ ($n_{\rm DM}^{\rm eq}$) is the (equilibrium) number density of DM and $\langle \sigma_{\rm ann} v_{\rm rel} \rangle$ is the DM annihilation cross section. The DM relic density can be obtained by solving Eq. (3.1) numerically. In general, a solution of Eq. (3.1) can not be obtained analytically. However, by assuming $\langle \sigma_{\rm ann} v_{\rm rel} \rangle$ to be constant, and applying sudden freeze-out approximation [122], we can estimate the DM relic density.

Firstly we use an useful expression of DM number density, $Y_{\rm DM} \equiv n_{\rm DM}/s$, instead of n. In the expanding Universe, DM number density, $n_{\rm DM}$, is not invariant even if the DM number does not change. This is because $n_{\rm DM}$ is proportional to cubic scale parameter, a^{-3}. On the other hand, the ratio of DM number density to entropy density, $Y_{\rm DM}$, is invariant as far as the change of DM number and entropy production does not occur because the entropy density is also proportional to cubic scale parameter, a^{-3}. Using $Y_{\rm DM}$, the Boltzmann equation for DM number density in Eq. (3.1) is rearranged as follows :

$$\frac{x}{Y_{\rm DM}} \frac{dY_{\rm DM}}{dx} = -\frac{\Gamma_{\rm ann}}{H} \left\{ \left(\frac{Y_{\rm DM}}{Y_{\rm DM}^{\rm eq}} \right)^2 - 1 \right\} \ , \tag{3.2}$$

where $x \equiv m_{\rm DM}/T$ is a new parapeter, instead of time, and $\Gamma_{\rm ann} \equiv n_{\rm DM}^{\rm eq} \langle \sigma_{\rm ann} v_{\rm rel} \rangle$ is the rate of DM annihilation process. During $\Gamma_{\rm ann}(x) > H(x)$, DM is in thermal equilibrium and $Y_{\rm DM}$ is almost equal to be $Y_{\rm DM}^{\rm eq}$. When the annihilation rate decreases with the decreasing of DM number density and reaches the Hubble parameter as follows : $\Gamma_{\rm ann}(x) = H(x)$ at $x = x_f$, DM is

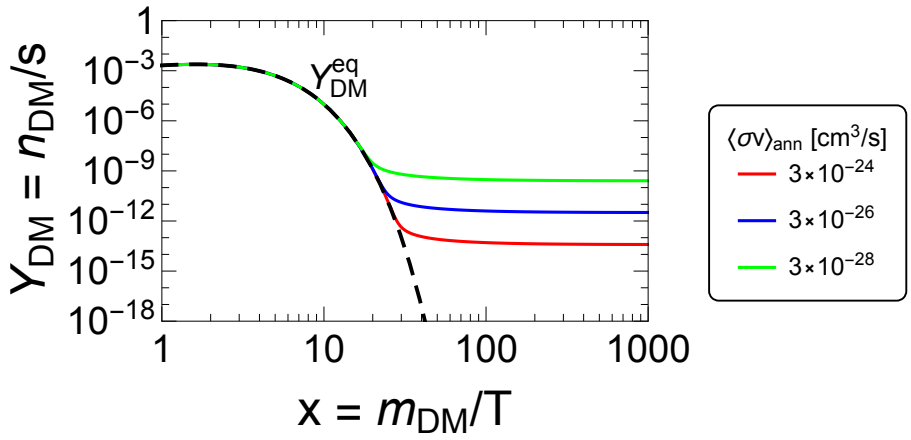

Figure 3.1: Time evolution of the ratio of the DM number density to the entropy density for $m_{\rm DM} = 100$ GeV. The DM annihilation cross section is varied to be 3×10^{-24} (red), 3×10^{-26} (blue, canonical value), and 3×10^{-28} cm^3/s (green). Black dashed line corresponds to $Y_{\rm DM}$ when the annihilation process is in thermal equilibrium.

suddenly driven out of thermal equilibrium. And then the ratio, $Y_{\rm DM}$ is frozen at the value when the annihilation process is driven out of thermal equilibrium. The parameter at the freeze-out, x_f, is approximately calculated as

$$x_f = \ln(y) + \ln(\ln(y)) \ , \tag{3.3}$$

$$y \approx \sqrt{\frac{45}{4\pi^5}} \frac{g_{\rm DM}}{g_*^{\frac{1}{2}}} M_{\rm pl} m_{\rm DM} \langle\sigma_{\rm ann} v_{\rm rel}\rangle \ , \tag{3.4}$$

and typically $x_f \sim$ 20-30. The DM relic density is eventually obtained by

$$Y_{\rm DM}\Big|_{x=\infty} = \sqrt{\frac{45 g_*}{8\pi^2}} \frac{x_f}{g_{*s} \langle\sigma_{\rm ann} v_{\rm rel}\rangle M_{\rm P} m_{\rm DM}} \ . \tag{3.5}$$

Instead of the ratio, $Y_{\rm DM}$, the DM number density and density parameter are obtained by

$$n_{\rm DM,0} = 2.2 \times 10^3 \ \frac{g_*^{\frac{1}{2}} x_f}{g_{*s} M_{\rm P} m_{\rm DM} \langle\sigma_{\rm ann} v_{\rm rel}\rangle} \ , \tag{3.6}$$

$$\begin{aligned} \Omega_{\rm DM,0} h^2 &= 1.07 \times 10^9 \frac{x_f}{(g_{*s}/g_*^{1/2}) M_{\rm P} m_{\rm DM} \langle\sigma_{\rm ann} v_{\rm rel}\rangle} \\ &= 0.1 \left(\frac{3 \times 10^{-26} \ {\rm cm}^3/{\rm s}}{\langle\sigma_{\rm ann} v_{\rm rel}\rangle} \right) x_f \ . \end{aligned} \tag{3.7}$$

Typical value of annihilation cross section which realizes the observed DM relic abundance is $\langle\sigma_{\rm ann} v_{\rm rel}\rangle \sim 3 \times 10^{-26}$ cm^3/s, and called canonical value. In Fig. 3.1, we show time evolution of the ratio of the DM number density to the entropy density, $Y_{\rm DM}$, for $m_{\rm DM} = 100$ GeV. The red, blue, and green solid lines correspond to the results for $\langle\sigma_{\rm ann} v_{\rm rel}\rangle = 3 \times 10^{-24}$, 3×10^{-26}

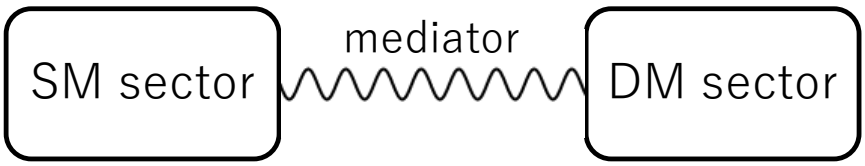

Figure 3.2: The SM and DM sectors connect each other via a mediator.

(canonical value), and 3×10^{-28} cm^3/s, respectively. The black dashed line corresponds to $Y_{\rm DM}$ when the annihilation process is in thermal equilibrium. Fig. 3.1 shows us that $Y_{\rm DM}$ follows the equilibrium value during annihilation process is in equilibrium, and then is frozen when annihilation is driven out of equilibrium, namely, $x = x_f \approx$ 20-30. Moreover, as shown in Eq. (3.5), the ratio decreases as the DM annihilation cross section increases.

3.2 Secluded Dark Matter

There is various pieces of evidence of DM existence, and a lot of experiments have been performed to search WIMP DM with electroweak scale mass. However, although great efforts have been devoted to DM detection, DM has not been observed directly yet, and only strong bounds on the interaction between DM an SM particles are obtained as discussed in the following Section 3.3 If DM is WIMP and produced through the thermal freeze-out mechanism, DM generally needs a sizable connection to the SM sector via a mediator to be generated thermally and annihilate to realize the observed DM relic abundance, see Fig. 3.2. On the other hand, such a connection leads to sizable scattering cross section with nucleons and threatens WIMP DM models with the severe constraints from direct detection experiments. Therefore, simple WIMP DM models are facing severe difficulties, and there have to be some tricks to avoid a strong connection to the SM sector.

Secluded DM [123–125] is one of attractive possibilities to avoid the experimental difficulties. One of the differences between standard WIMP DM and secluded DM is a way to annihilate into the SM particles. For the usual WIMP case ($m_{\rm DM} < m_{\rm med}$ with $m_{\rm med}$ being mediator mass), DM annihilates into SM particles via virtual mediator like the left panel of Fig. 3.3. In this case, annihilation cross section is proportional to $g^2_{\rm DM} g^2_{\rm SM}$ with $g_{\rm DM(SM)}$ being coupling between DM (SM) and mediator, and scattering cross section with SM particles also has the same dependence. Therefore, couplings, $g_{\rm DM(SM)}$, to realize the DM relic abundance leads to large scattering cross section. On the other hand, for the secluded DM case ($m_{\rm DM} > m_{\rm med}$), another annihilation channel like the right panel of Fig. 3.3 opens. In this case, DM annihilates into on-shell mediators, and then those mediators decay into the SM particles. The annihilation cross section of this process is proportional to $g^4_{\rm DM}$, and thus this process is dominant if $g_{\rm DM}$ is

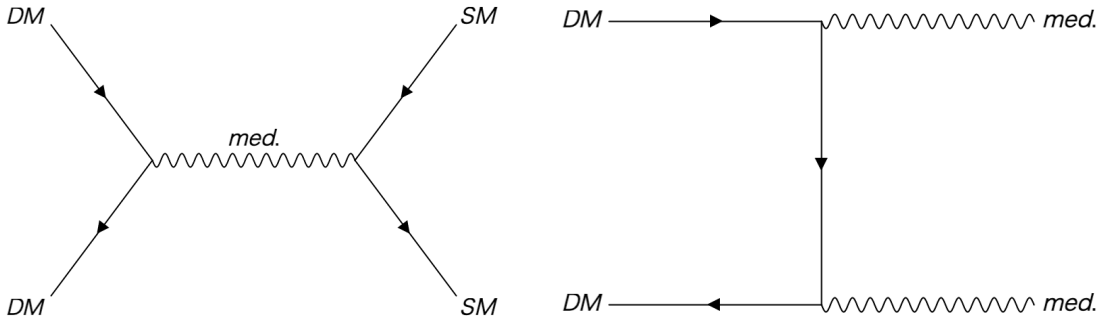

Figure 3.3: WIMP annihilation processes for $m_{\rm DM} < m_{\rm med}$ (left) and $m_{\rm DM} > m_{\rm med}$ (right, secluded DM).

much larger than $g_{\rm SM}$. On the other hand, scattering cross section with the SM particles also is proportional to $g_{\rm DM}^2 g_{\rm SM}^2$ as the standard WIMP models. Therefore, even if the annihilation cross section is large, the scattering cross section can be small to avoid the severe constraints from the recent direct detection experiments.

3.3 Dark Matter Searches

A lot of experiments are performed to detect signals from DM in various ways. These experiments are classified roughly into the following three types, as shown in Fig. 3.4. The first is called direct detection. A lot of DM passes through the earth and some of them scatter with target particles elastically. Direct detection experiments are trying to detect recoils of target particles. The second is called indirect detection. In the Universe, especially in the center of the galaxy, huge amount of DM are crowding, and some of them annihilate into SM particles. Indirect detection experiments are trying to detect cosmic rays from DM annihilation. The third is collider searches of DM. By collision of SM particles, DM is produced through the inverse process of DM annihilation. Produced DM goes away without any signal, and missing energy is a clue of DM.

In this section, we give a brief review of DM searches and show the present constraints on DM. Although there are many kinds of DM models, we discuss fermion DM and vector mediator in this section because they have something to do with the following Chapter 7.

3.3.1 Direct Searches

Dark matters have no electromagnetic charge, and then it is quite difficult to detect them. However, if they scatter with target particles in the detector and recoil targets are detected,

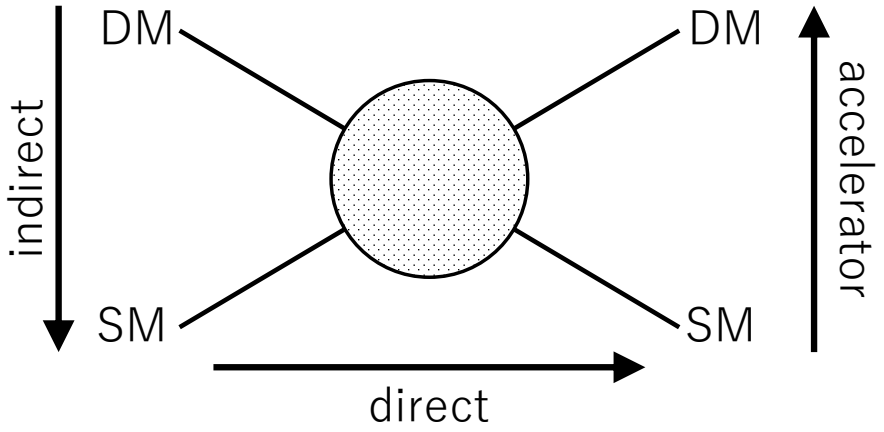

Figure 3.4: Rough classification of WIMP DM searches. Direct detection experiments detect recoils of target particles by elastic scatterings between DM and target particles. Indirect detection experiments detect cosmic rays produced by DM annihilation. Collider experiments produce DM directly and detect missing energy taken away by DM.

we can detect DM. This idea firstly has been proposed in 1985 by M. W. Goodman and E. Witten [126]. After this proposal, various experiments have been trying to detect recoils by scattering with DM for several decades. There are many kinds of detectors, and according to the mass range of DM, suitable matters are chosen as targets in detectors.

For detection of DM with electroweak scale mass, nuclear recoils are mainly used. This is because spin-independent (SI) scattering cross section between DM and nuclei is proportional to squared mass number, not the mass number, as shown in the following discussion. We consider the following interaction between DM and nuclei via vector mediator :

$$\mathcal{L}_{\rm int} = \bar{\psi}\gamma^\mu \left(g_{\psi_v,X} + g_{\psi_a,X}\gamma_5\right)\psi X_\mu + \sum_{f\in {\rm SM}} \bar{f}\gamma^\mu \left(g_{f_v,X} + g_{f_a,X}\gamma_5\right) f X_\mu \ , \tag{3.8}$$

where ψ and X are fermion DM and vector mediator, respectively, and $g_{i_{v(a),X}}$ is vector (axial) coupling between mediator and particle i. We notice that the coefficients, $g_{i_{v(a)},X}$ are model dependent, and $g_{\psi_{a(v)},X} = 0$ for Dirac (Majorana) fermion DM. The above interactions lead to X mediated elastic scattering between DM and nucleon, and there are two types of elastic scattering cross sections. One is the spin-independent (SI) cross section. SI scattering cross section of DM and nucleon is given by [127–129]

$$\sigma_{\rm SI}^{(\text{per nucleon})} = \frac{\mu_{\psi n}^2}{\pi}\left[\frac{Z f_p + (A-Z) f_n}{A}\right]^2 \ , \tag{3.9}$$

where A and Z are the mass and atomic numbers, respectively. $\mu_{\psi n}$ is the reduced mass of DM and nucleon, and defined by $\mu_{\psi n} \equiv m_\psi m_n/(m_\psi + m_n)$. For much heavier DM than nucleon, the reduced mass is approximated as $\mu_{\psi n} \approx m_n$, on the other hand, for much lighter DM, $\mu_{\psi n} \approx m_\psi$.

Table 3.1: Spin fraction of proton and neutron carried by quark [131, 132].

	proton	neutron
Δ_u	0.78 ± 0.02	-0.48 ± 0.02
Δ_d	-0.48 ± 0.02	0.78 ± 0.02
Δ_s	-0.15 ± 0.02	-0.15 ± 0.02

f_p and f_n are the effective coupling constants of $\bar{\psi}\psi\bar{p}p$ and $\bar{\psi}\psi\bar{n}n$, respectively, and calculated by

$$f_p = \frac{g_{\psi_v,X}}{m_X^2}\left(2g_{u_v,X} + g_{d_v,X}\right) \ , \qquad f_n = \frac{g_{\psi_v,X}}{m_X^2}\left(g_{u_v,X} + 2g_{d_v,X}\right) \ , \tag{3.10}$$

with m_X being the vector mediator mass. Because of the condition that DM avoids falling into the center of the galaxy, the averaged velocity of DM is about 230 km/s $\sim 10^{-3}c$ with c being the speed of light. The de Broglie wavelength of DM is $\mathcal{O}(1)$ fm for $m_{\rm DM} \sim 100$ GeV, which is the same scale as nuclei. Therefore, the SI scattering cross section of DM and nucleus is enhanced by the coherence of all nucleons in the nucleus and given by

$$\sigma_{\rm SI}^A \simeq A^2 \left(\frac{\mu_{\psi A}}{\mu_{\psi n}^2}\right)^2 \sigma_{\rm SI}^{(\text{per nucleon})} \ , \tag{3.11}$$

with $\mu_{\psi A}$ being the reduced mass of DM and nucleus with the mass number A. In particular, in the limit of $f_p = f_n$, the SI scattering cross section is proportional to the squared mass number, A^2, and moreover, for $m_n \ll Am_n \approx m_\psi$, A^4.

The other type of elastic scattering cross section is spin-dependent (SD) one. SD scattering cross section of DM and nucleon is given by [126–128, 130]

$$\sigma_{\rm SD}^{(i)} \approx \frac{4\mu_{\psi n}^2}{\pi}\left[\sum_{q=u,d,s} h_q \lambda_q\right]^2 J_N(J_N+1) \quad (i = p, n) \ , \tag{3.12}$$

where J_N is the angular momentum of the nucleus, and it is equal to be $1/2$ for free proton or neutron. h_q is the effective coupling constant of $\bar{\psi}\gamma^\mu\gamma_5\psi\bar{q}\gamma_\mu\gamma_5 q$ and given by

$$h_q = \frac{g_{\psi a} g_{qa}}{m_{Z'}^2} \ . \tag{3.13}$$

λ_q is the fractional quark-spin coefficient, and for free proton and neutron, equal to be the spin fraction of the nucleon carried by quark, Δ_q. These values are shown in Tab. 3.1. For nucleus with mass number, A, the fractional quark-spin coefficients, λ_q, are more complicated and given by

$$\lambda_q \simeq \frac{1}{J_N}\left[\Delta_q^{(p)}\langle S_p\rangle + \Delta_q^{(n)}\langle S_n\rangle\right] \ , \tag{3.14}$$

where $\langle S_p \rangle$ and $\langle S_n \rangle$ are the respective expectation values for the proton and neutron group spin contents in the nucleus, and the detail is shown in Ref. [30]. The values of $\langle S_p \rangle$ and $\langle S_n \rangle$ depend on models[1] , and we do not discuss the detail here.

Next, we show the current bounds and prospects from the direct detection experiments. In Fig. 3.5, we show the recent and projected bounds on the SI elastic scattering cross section of DM and nucleon. The regions above the solid, dashed, dotted, and dot-dashed lines, and red shaded

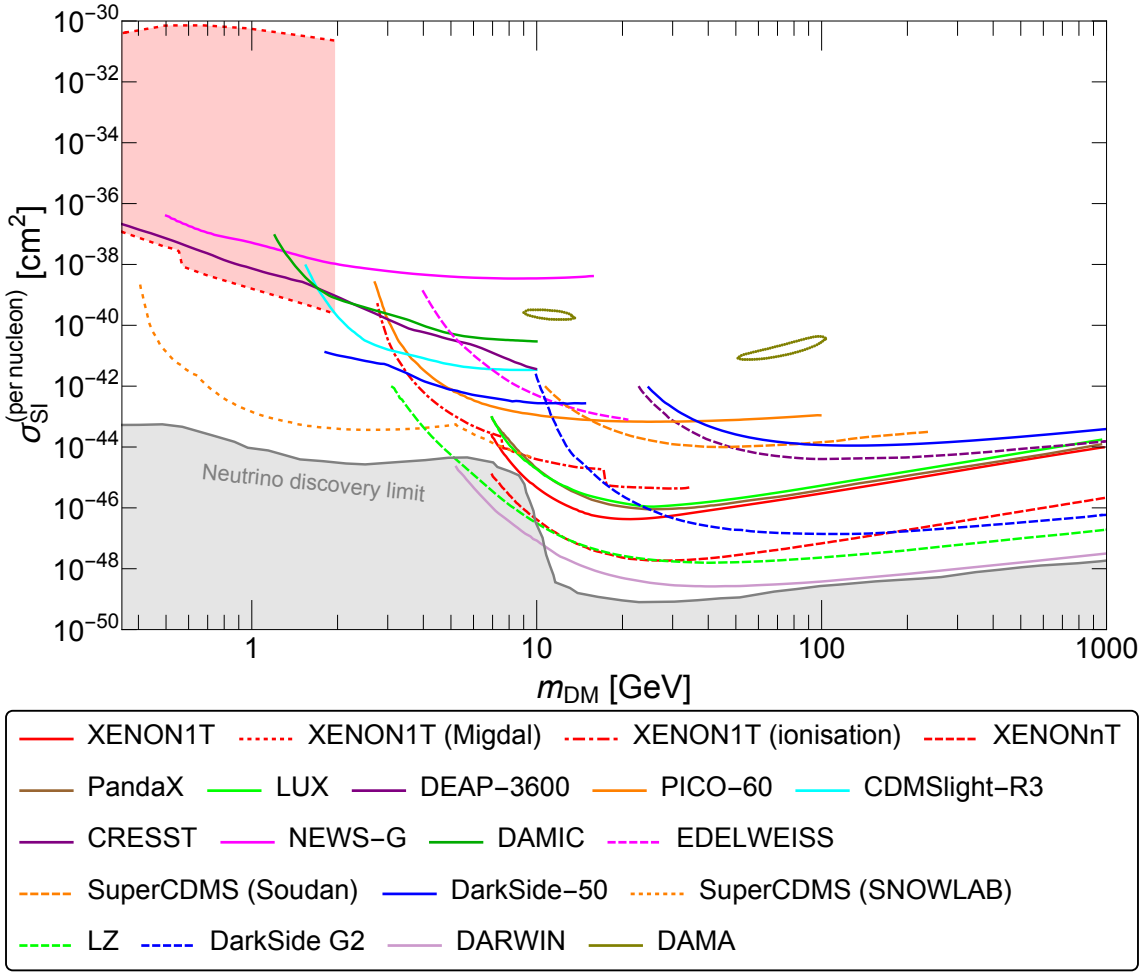

Figure 3.5: Recent constraints on the spin-independent elastic scattering cross section of DM with nucleon by XENON1T [32], XENON1T (Migdal) [34], XENON1T (ionisation only) [33], XENONnT [135], PandaX-II [136], LUX [137], DEAP-3600 [138], PICO-60 [139], CDMSlight-R3 [140], CRESST-III [141], NEWS-G [142], DAMIC [143], EDELWEISS [144], SuperCDMS (@Soudan) [145], DarkSide-50 [146], SuperCDMS (@SNOWLAB) [147], LUX-ZEPLIN (LZ) [148], DarkSide G2 [149], DARWIN [150], and DAMA [151, 152]. The gray shaded region shows the neutrino floor [153].

[1]For example, concrete values of $\langle S_p \rangle$ and $\langle S_n \rangle$ are given in Ref. [133, 134].

one are excluded or will be proved by XENON1T [32], XENON1T (Migdal) [34], XENON1T (ionisation only) [33], XENONnT [135], PandaX-II [136], LUX [137], DEAP-3600 [138], PICO-60 [139], CDMSlight-R3 [140], CRESST-III [141], NEWS-G [142], DAMIC [143], EDELWEISS [144], SuperCDMS (@Soudan) [145], DarkSide-50 [146], SuperCDMS (@SNOWLAB) [147], LUX-ZEPLIN (LZ) [148], DarkSide G2 [149], and DARWIN [150]. In Fig. 3.5, the DM local density is assumed to be $\rho_{\rm DM} = 0.3$ GeV/cm^3. The regions inside the olive-colored rings are allowed at at 90% confidence level by DAMA/NaI [151] and DAMA/LIBRA [152] collaborations. These collaborations claimed that they had detected annual modulated events and discovered DM by more than 100 kg highly radiopure NaI(Tl) scintillators, and finally at a significance of 9.3σ [154]. However, although their high statistics data, such regions are excluded by other non-NaI(Tl)-based direct detection experiments, as shown in Fig. 3.5. So far, several direct detection experiments, for example, COSINE-100 [155], SABRE [156], ANAIS [157], PICO-LON [158], and so on, are trying to verify the results of DAMA/RIBRA by NaI(Tl) scintillators, which are the same way as DAMA/RIBRA. Searching regions of lower scattering cross section of DM is quite difficult. The gray shaded region shows the neutrino floor [153]. In the sun, a lot of high energy neutrinos ($E_\nu < 15$ MeV) are produced by decays of ^{8}B originated by the proton-proton chain. These solar neutrinos induce coherent elastic scattering of neutrino and nucleus, and this kind of events with nuclear recoil energies below ∼few keV becomes background which is difficult to remove. This difficulty in searching DM is firstly mentioned in Ref. [159], and some kinds of direct detection experiments, such as NaI-based experiments mentioned above, NEWAGE [160], NEWSdm [161], and so on, are trying to avoid this difficulty by detections of annual modulated events or directional sensitivity.

In Fig. 3.6 and 3.7, we show the recent and projected bounds on the SD elastic scattering cross section of DM with proton and neutron, respectively. The regions above the solid, dashed, dotted, and dot-dashed lines, and shaded ones are excluded or will be proved by PICO-60 [139], PICASSO [162], SIMPLE [163], COUPP [164], PandaX-II [165], XENON1T [166], LUX [167], SuperKamiokande [168], IceCube [169], and DARWIN [150].

Next, we give a review of direct detection experiments based on DM-electron scattering. Electrons are much lighter than nucleons, and thus lighter DM can give enough recoil energy to electrons in target nuclei. Assuming the above Lagrangian in Eq. (3.8), scattering cross section of DM with the electron is given by [170]

$$\sigma^{(e)} = \frac{\mu_{\psi e}^2}{\pi} \frac{g_{\psi v}^2 g_{ev}^2}{\left(q_{\rm ref}^2 + m_{Z'}^2\right)^2} \ , \tag{3.15}$$

where $\mu_{\psi e} = m_\psi m_e/(m_\psi + m_e)$ is the reduced mass of DM and electron. $p_{\rm ref} = \alpha m_e$ is the reference momentum transfer with α being the fine structure constant, and is conventionally used as a reference value.

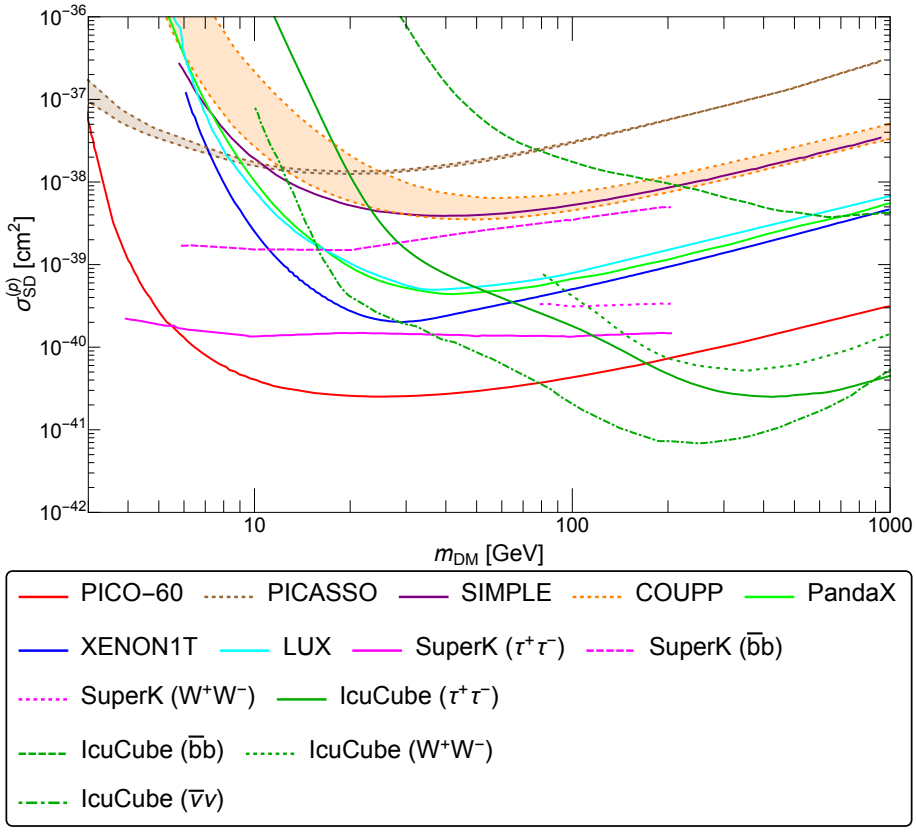

Figure 3.6: Recent constraints on the spin-dependent elastic scattering cross section of DM with proton by PICO-60 [139], PICASSO [162], SIMPLE [163], COUPP [164], PandaX-II [165], XENON1T [166], LUX [167], SuperKamiokande [168], and IceCube [169].

The recent bounds on the elastic scattering cross section of DM with the electron are shown in Fig. 3.8. The regions above the solid, dashed lines are excluded by XENON10 [171], XENON100 [172], XENON1T [33], analyses of XENON10 and XENON100 results by R. Essig *et. al.* [173], SENSEI [174], protoSENSEI (@Surface) [175], protoSENSEI (@MINOS) [176], DarkSide-50 [177], CDMS-HVeV [178], and DAMIC-SNOWLAB [179].

3.3.2 Indirect Searches

In the thermal freeze-out mechanism, WIMP dark matter is produced thermally in the early Universe. The produced DM annihilates into the SM particles, and its number density decreases following $Y^{\rm eq}_{\rm DM}$. This decreasing stops at the point when the annihilation process is driven out of equilibrium. DM exists all over the present Universe, and its density is not uniform because of the structure of the Universe and gravitational potential. Generally, DM rich regions are in matter rich ones, and, for example, the center of the galaxy, Milky Way galactic halo, dwarf

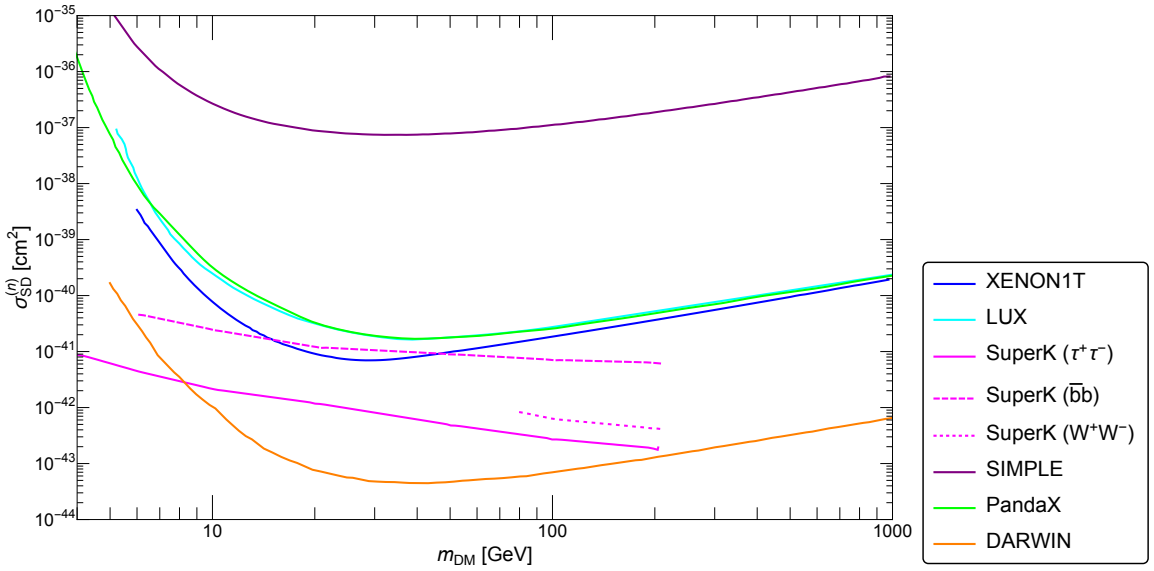

Figure 3.7: Recent constraints on the spin-dependent elastic scattering cross section of DM with proton by XENON1T [166], LUX [167], SuperKamiokande [168], SIMPLE [163], PandaX-II [165], and DARWIN [150].

spheroidal galaxies, galaxy clusters, and so on. In such regions, DM frequently annihilates into SM stable particles or unstable ones which subsequently decay into SM ones, and then fly to the earth as cosmic rays. The larger the DM annihilation cross section is, the more cosmic rays are produced, and therefore the DM annihilation cross section can be constrained by observation of cosmic rays. In this subsection, first, we give a short review of the calculation of cosmic ray flux originated from DM annihilation, and then show the recent observational bounds on DM annihilation cross section.

In the galactic halo, a huge amount of DM is trapped by gravitational potential, and various models have been proposed as DM density distribution in the galactic halo. Well-known DM halo profiles are shown in Tab. 3.2. In the table, $r_s = 20$ kpc is the scale radius, and ρ_s is the normalization factor of DM density profile such as to satisfy $\rho(r = 8.5\text{ kpc}) = 0.4\text{ GeV/cm}^3$. For Einasto profile, α is the fitting parameter and taken to be $\alpha = 1 \sim 2$. All DM density profiles in Fig. 3.2 are based on sphericity of galaxies, and however, the possibility of non-sphericity is also explored, for example, [188]. However, in this thesis, we assume isotropic distribution of DM number density, and therefore $\rho(\vec{\mathbf{x}})$ depends only on the distance from the galactic center (GC).

The production rate of final state particles, f, by DM annihilation at a point $\vec{\mathbf{x}}$ is given

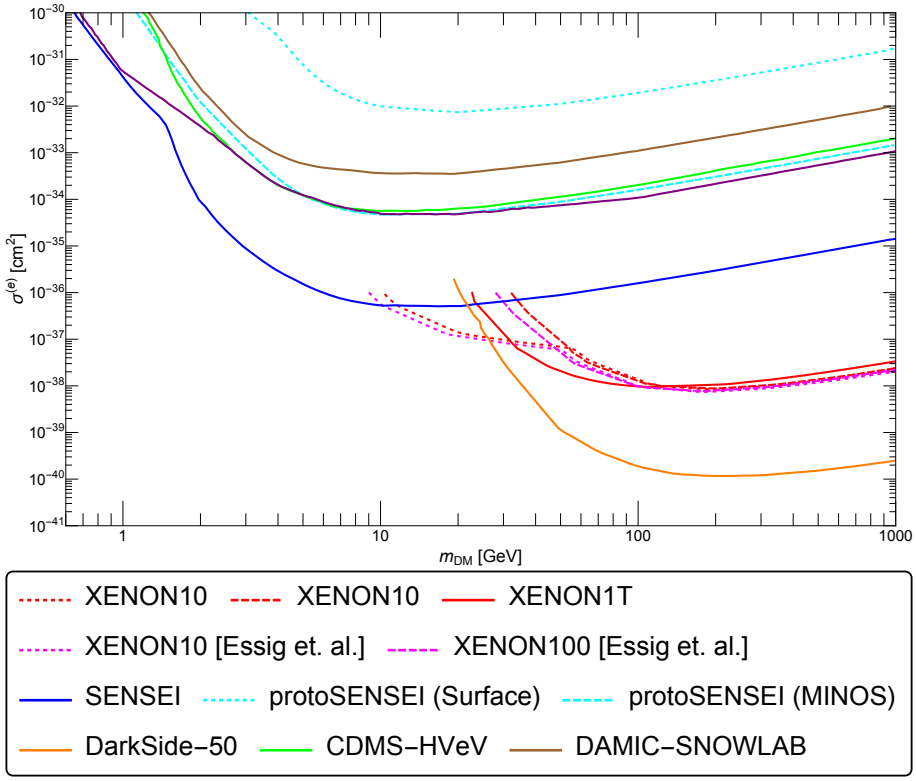

Figure 3.8: Recent constraints on the elastic scattering cross section of DM with electron by XENON10 [171], XENON100 [172], XENON1T [33], analyses of XENON10 and XENON100 results by Essig, Volansky, and Yu [173], SENSEI [174], protoSENSEI (@Surface) [175], protoSENSEI (@MINOS) [176], DarkSide-50 [177], CDMS-HVeV [178], and DAMIC-SNOWLAB [179]. The bounds are obtained by assuming $f_p = f_n$.

by [50]

$$\frac{d\Gamma_f^{\rm ann}}{dE_f} = c\frac{\rho_\psi(\vec{\mathbf{x}})^2}{m_\psi^2}\langle\sigma_{\rm ann}v_{\rm rel}\rangle\frac{dN_f^{\rm ann}}{dE_f} \ , \tag{3.16}$$

where $dN_f^{\rm ann}/dE$ denotes the energy spectrum of the final state particle per one annihilation, and c is equal to 1/4 (1/2) for Dirac (Majorana) DM. The total flux of the final state particles, for example, photons, electrons, and neutrinos, from the DM halo in the galaxy is calculated by integrating $d\Gamma_f^{\rm ann}/dE$ over the galactic region as follows [50]:

$$\frac{d\Phi_f^{\rm ann}}{dE_f} = \frac{c}{4\pi}\frac{\langle\sigma_{\rm ann}v_{\rm rel}\rangle}{m_\psi^2}\frac{dN_f^{\rm ann}}{dE_f}J_{\Delta\Omega} \ , \tag{3.17}$$

where $J_{\Delta\Omega}$ is the so-called J-factor with units of GeV^2 cm^{-5}, and in the polar coordinate (s, b, l), calculated by integrating over the target solid angles in the sky and line of sight as follows [50] :

$$J_{\Delta\Omega} \equiv \int_{b_{\rm min}}^{b_{\rm max}} db\cos b\int_{l_{\rm min}}^{l_{\rm max}} dl\int_0^{s_{\rm max}} ds\ \rho_\psi(r(s,b,l))^2 \ , \tag{3.18}$$

Table 3.2: DM density distributions in the garactic halo based on astrophysical obsrvations, numerical simulations, and theoretical models.

profile	$\rho(r)$	Ref.
NFW	$\rho_s \left(\frac{r_s}{r}\right) \frac{1}{(1+r/r_s)^2}$	[180]
Isothermal	$\rho_s \frac{1}{1+(r/r_s)^2}$	[21, 181]
Burkert	$\rho_s \frac{1}{(1+r/r_s)(1+(r/r_s)^2)}$	[182]
Moore	$\rho_s \left(\frac{r_s}{r}\right)^{1.16} \left(1+\frac{r}{r_s}\right)^{-1.84}$	[183, 184]
generalized NFW (gNFW)	$\rho_s \left(\frac{r_s}{r}\right)^{\gamma} \frac{1}{(1+r/r_s)^{3-\gamma}}$	[185]
Einasto	$\rho_s \exp\left[-\frac{2}{\alpha}\left\{\left(\frac{r}{r_s}\right)^{\alpha}-1\right\}\right]$	[186, 187]

where r is the distance from the solar system to the point (s, b, l) on the line of sight given by

$$r(s,b,l) = \sqrt{s^2 + r_\odot^2 - 2sr_\odot \cos b \cos l} \ , \tag{3.19}$$

with the distance from the GC to the solar system, $r_\odot$. Here, we define the direction of the GC as $b = l = 0°$, and the solar system is placed at the origin. The upper limit of the integration over the line of sight, $s_{\max}$, is given by

$$s_{\max}(b,l) = \sqrt{R_{\rm halo}^2 - r_\odot^2 + r_\odot^2 \cos^2 b \cos^2 l} + r_\odot \cos b \cos l \ , \tag{3.20}$$

with the size of the galaxy halo, $R_{\rm halo}$. For charged particles, such as electron and proton, the propagation of the produced particles are affected by interstellar radiation and magnetic field in the galaxy, and the energy spectrum of the flux of the final state particles are practically not simple as Eq. (3.17). For cosmic neutrino, which is discussed in Chapter. 7, and gamma rays produced by the annihilation of DM freely propagate in the space because of the weakness of interaction with other particles. Therefore, Eq. (3.17) gives a better estimation of the total flux. However, even for the neutrino and photon cases, we have to note that bounds on the DM annihilation cross section from indirect detection experiments have several astrophysical uncertainties, for example, J-factor.

Next, we show the current bounds and prospects from the indirect detection experiments. In Fig. 3.9, and 3.10, we show the recent bounds and future prospects for DM annihilation cross section from Fermi Large Area Telescope (Fermi-LAT) [189, 190], Cherenkov Telescope Array (CTA) [191], and High Energy Stereoscopic System (HESS) [192]. We also show the favored regions based on the assumption, that the observed gamma-ray excess in the inner galaxy and the GC is derived from DM annihilation, in Ref. [193–195]. However, there are the claims that this excess can be explained by young pulsars and millisecond pulsars (MSPs) [197, 198]. Moreover, such regions are excluded by Fermi-LAT observations of nearby satellite dwarf

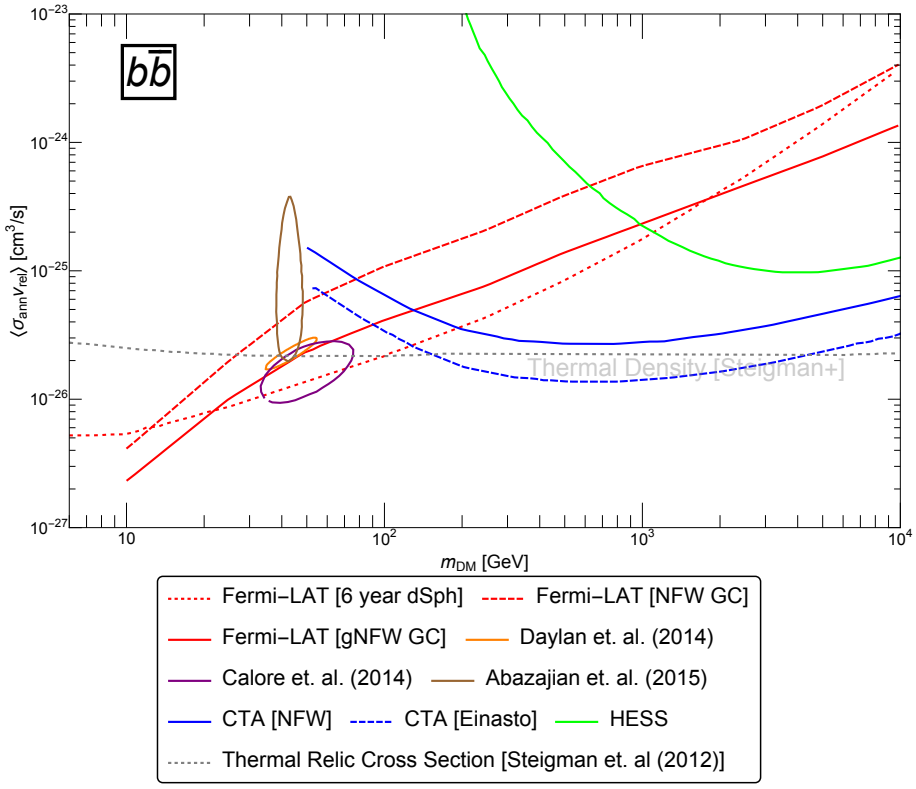

Figure 3.9: Recent constraints and future prospects for the DM annihilation cross section, $\overline{\mathrm{DM}}\mathrm{DM} \to \bar{b}b$, by Fermi-LAT [189, 190], CTA [191], and HESS [192]. Regions inside solid orange, purple, and brown rings are favored by gamma-ray excess in the inner galaxy and the GC in Ref. [193–195]. Gray dotted line corresponds to the thermal cross section [196].

spheroidal galaxies, but we show these results for references. The gray dotted lines in Fig. 3.9, and 3.10 represent the thermal relic annihilation cross section of DM [196].

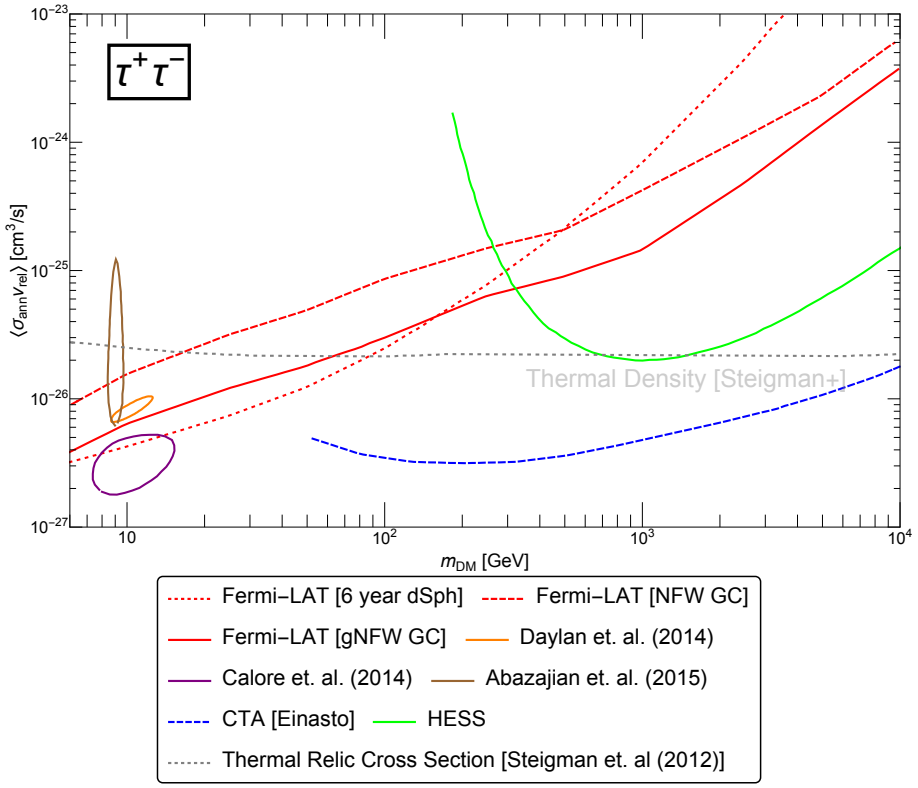

Figure 3.10: Same as Fig. 3.9, except that the colored lines show bounds or favored regions for DM annihilation process as $\overline{\text{DM}}\text{DM} \to \tau^+\tau^-$.

Chapter 4

Baryon Asymmetry of the Universe and Leptogenesis

The matter contents of the Standard Model include both matter and antimatter. Because of the existence of antimatter, the SM satisfies CPT invariance, and antimatter have already been discovered by various experiments and observations, for example, the observations of cosmic rays. However, such detected antimatter are secondary cosmic rays, and no detection of antimatter that exist since the early Universe [199–201]. If there is no asymmetry between baryon and antibaryon, the same amount of baryon and antibaryon exist in the early Universe. Hence, they annihilate each other, and the observed baryon density can not be explained. Moreover, if there are regions where stars and galaxies are formed by antimatter in the observable Universe, the annihilation of electrons and positrons happens on the boundary between antimatter space and our matter one, and characteristic 511 keV gamma rays are produced. However, such cosmic rays have not been detected as of now. Therefore, there is no possibility of existence of the above antimatter space in the observable Universe [199, 200, 202, 203]. On the other hand, even if there is matter-antimatter asymmetry before inflation, expansion of the Universe during the inflation negligibly dilutes it, and the observed baryon-antibaryon asymmetry can not be explained. Therefore, matter-antimatter asymmetry has to be generated after inflation.

In this section, we first give a brief review of baryon asymmetry and then summarize the production of baryon asymmetry. Especially, we mention one of the production scenarios of baryon asymmetry, so-called *leptogenesis*, and this scenario is important for the discussion in chapter 6.

4.1 Baryon Asymmetry in the Universe

As mentioned briefly in subsection 2.3.2, non-relativistic matter occupies about 32% of the energy density in the present Universe, and baryon does only a few percents of them. However, such a

small amount of baryon, compared to total energy density, gives considerable contributions to the evolution of the Universe.

4.1.1 Observational Estimation of Baryon Asymmetry

Baryon-antibaryon asymmetry in the Universe is expressed in the following three different ways :

$$\Omega_b h^2 \equiv \frac{\rho_b}{\rho_c} \ , \tag{4.1}$$

$$\eta_B \equiv \frac{n_B - n_{\bar{B}}}{n_\gamma} \ , \tag{4.2}$$

$$Y_{\Delta B} \equiv \frac{n_B - n_{\bar{B}}}{s} \ , \tag{4.3}$$

where $n_B(n_{\bar{B}})$ and ρ_b are the number and energy densities of (anti)baryon, respectively. Among the above three, η_B and $Y_{\Delta B}$ are invariant during the expansion of the Universe because all n_B, $n_{\bar{B}}$, n_γ and s are proportional to $a(t)^{-3} \propto T^3$ from Eq. (2.85) and (2.95). However, η_B change in the early Universe by particle decays and annihilation, while $Y_{\Delta B}$ is invariant as long as entropy production does not occur.

From Eq. (2.85) and (2.95), the ratio of entropy density to photon number density is given by

$$\left.\frac{s}{n_\gamma}\right|_0 = \frac{g_{*s}}{g_\gamma}\frac{2\pi^4}{45\zeta(3)} = 7.04 \ , \tag{4.4}$$

and thus the relation between η_B and $Y_{\Delta B}$ is obtained by

$$\eta_B = 7.04 Y_{\Delta B} \ . \tag{4.5}$$

Moreover, $\Omega_b h^2$ and η_B have the following relation :

$$\Omega_B h^2 = \frac{\rho_b}{\rho_c} h^2 = \frac{n_B m_B h^2}{\rho_c} = \frac{m_B n_\gamma h^2}{\rho_c}\eta_B = 3.65 \times 10^7 \eta_B \ , \tag{4.6}$$

where m_B is the averaged baryon mass, and in Eq. (4.6), we use the proton mass $m_p = 938$ MeV as m_B.

The baryon asymmetry in the Universe is estimated or measured by two independent methods. One is the BBN, and the baryon asymmetry can be obtained by using the fact that the abundances of light elements, such as deuterium (D), ^{3}He, ^{4}He, ^{7}Li, and so on, depend only on the baryon asymmetry, η_B, except for the uncertainty of neutron lifetime [1]. The abundances

[1]Neutrons contribute to the BBN process through, for example, $p + n \to \mathrm{D} + \gamma$ and $\mathrm{D} + n \to {}^3\mathrm{H} + \gamma$, and therefore, the neutron lifetime affects its abundance, consequently the abundace of light elements. Neutron lifetime is measured by two independent approaches, such as bottle and beam methods. In the bottle method [204–211], ultracold neutrons (UCN) are storing in bottle, and remaining UCNs are counted after some time. In the beam method [212, 213], neutron beam is pass through charged particle detectors, and beta decays of neutrons are detected. The former gives $\tau_n = 879.4 \pm 0.6$ s (PDG average [50]), and the latter gives $\tau_n = 887.7 \pm 2.3$ s [213].

of light elements are calculated by solving the nuclear reaction network, which is a system of ordinary differential equations including the effect of the expansion of the Universe. The baryon asymmetry can be estimated by comparing the prediction from the nuclear reaction network and the observed value of abundances of light elements, and the recent analysis gives [50]

$$5.8 \leq \eta_B \times 10^{10} \leq 6.5 \quad (95\%\ \mathrm{CL})\ . \tag{4.7}$$

We notice that the lithium constraint is not taken into account because there is a considerable discrepancy between the favored value of η_B from ^{7}Li and the other light elements, and this is called the lithium problem.

The other way is measurements of the CMB. As discussed in subsection 2.3.4, the fluctuation of the CMB is produced by that of baryon-photon mixed fluid, and thus the baryon asymmetry can be obtained by observation of the temperature fluctuation of the CMB. The recent value estimated by the Planck observation [25] is given by

$$\eta_B = (6.14 \pm 0.03) \times 10^{-10}\ . \tag{4.8}$$

4.1.2 Conditions of baryon number production

To produce baryon asymmetry during the evolution of the Universe, it is well-known that the following Sakharov's three conditions are satisfied [214] :

(i) Baryon number violation
After inflation, the baryon number (B) density is zero or negligibly small, and thus B-number violating processes are needed to produce B-number.

(ii) C and CP violation
If C and CP are conserved, probabilities of baryon and antibaryon production are equal. Therefore, C and CP should be violated, and the frequency of baryon and antibaryon production should be different.

(iii) Departure from thermal equilibrium
In a thermal equilibrium system, process and inverse process of baryon production occur with the same frequency, and thus the system should depart from thermal equilibrium.

For the scenarios of departure from thermal equilibrium, some are proposed, and the well-known examples are as follows :

- Departure from the equilibrium of decay process of heavy particles
  $\longrightarrow$ Leptogenesis, GUT baryogenesis

- Electroweak phase transition
  $\longrightarrow$ Electroweak baryogenesis

Among them, the leptogenesis scenario is important for this thesis, especially in Chapter 6, and therefore we give only a short review of leptogenesis.

4.1.3 Sphaleron process

In the SM, baryon (B) and lepton (L) numbers are conserved at tree level, and currents of B and L numbers, j_B^μ and j_L^μ, satisfy

$$\partial_\mu j_B^\mu = \partial_\mu j_L^\mu = 0 \ . \tag{4.9}$$

However, the B and L numbers are violated at the quantum level, and the divergences of their currents are given by

$$\partial_\mu j_B^\mu = \partial_\mu j_L^\mu = \frac{N_f}{32\pi^2}\left(g^2 W_{\mu\nu}^a \tilde{W}^{a\mu\nu} - g'^2 B_\mu \tilde{B}^{\mu\nu}\right) \ , \tag{4.10}$$

where $g(g')$ is the gauge coupling constant of $\mathrm{SU}(2)_L$ ($\mathrm{U}(1)_Y$), and N_f is the number of fermion generation. The field strengths of the gauge fields with a tilde are the self-dual fields of gauge fields and defined by

$$\tilde{W}^{a\mu\nu} = \frac{1}{2}\epsilon^{\mu\nu\rho\sigma} W_{\rho\sigma}^a, \quad \tilde{B}^{\mu\nu} = \frac{1}{2}\epsilon^{\mu\nu\rho\sigma} W_{\rho\sigma} \ . \tag{4.11}$$

From Eq. (4.10), the B and L numbers are not conserved. However, both have the same divergence, and thus their difference $(B-L)$ is conserved because of $\partial_\mu(j_B^\mu - j_L^\mu) = 0$. On the other hand, their sum $(B+L)$ is not conserved, and the divergence of $(B+L)$ current $j_{B+L}^\mu = j_B^\mu + j_L^\mu$ is given by

$$\begin{aligned} \partial_\mu j_{B+L}^\mu &= \frac{N_f}{16\pi^2}\left(g^2 W_{\mu\nu}^a \tilde{W}^{a\mu\nu} - g'^2 B_\mu \tilde{B}^{\mu\nu}\right) \\ &= 2N_f\left(\partial_\mu K^\mu - \partial_\mu k^\mu\right) \ , \end{aligned} \tag{4.12}$$

where

$$K^\mu = \frac{g^2}{32\pi^2}\epsilon^{\mu\nu\rho\sigma}\left(W_{\nu\rho}^a W_\sigma^a - \frac{g}{3}\epsilon^{abc} W_\nu^a W_\rho^b W_\sigma^c\right) \ , \tag{4.13}$$

$$k^\mu = \frac{g'^2}{32\pi^2}\epsilon^{\mu\nu\rho\sigma} B_{\nu\rho} B_\sigma \ . \tag{4.14}$$

Integrating Eq. (4.12) with respective to the coordinate, the left-hand side (LHS) is transformed as follows :

$$\begin{aligned} (LHS) &= \int_{t_i}^{t_f} dt \int d^3x \partial_\mu j_{B+L}^\mu \\ &= \int d^3x \left(j_{B+L}^0(t_f) - j_{B+L}^0(t_i)\right) \\ &= (B+L)(t_f) - (B+L)(t_i) \equiv \Delta(B+L) \ . \end{aligned} \tag{4.15}$$

On the other hand, the right-hand side (RHS) is

$$\begin{aligned}(RHS) &= \int_{t_i}^{t_f} dt \int d^3x \; 2N_f \left(\partial_\mu K^\mu - \partial_\mu k^\mu\right) \\ &= N_f \left(N_{\rm CS}(t_f) - N_{\rm CS}(t_i)\right) \ , \end{aligned} \tag{4.16}$$

where $N_{\rm CS}(t)$ is the Chern-Simons number of gauge field, which is topological invariant value, given by

$$N_{\rm CS}(t) = \frac{g^2}{32\pi^2} \int d^3x \epsilon_{ijk} \left(W^a_{ij} W^a_k - \frac{1}{3} W^{ai} W^{bj} W^{ck} \right) \ . \tag{4.17}$$

From Eqs. (4.16) and (4.16),

$$\Delta(B+L) = N_f \left(N_{\rm CS}(t_f) - N_{\rm CS}(t_i)\right) \ , \tag{4.18}$$

and therefore, $(B+L)$ number is not conserved. This kind of phenomenon appears only when the gauge symmetry corresponding to the gauge boson is non-Abelian. In non-Abelian gauge theory, there are infinite degenerate vacuums distinguished by the Chern-Simons number. As mentioned above, the Chern-Simons number is topological invariant and does not change under gauge transformation. However, there are, in fact, two processes that change the Chern-Simons number of vacuums, namely, baryon number. One is the tunneling process, and its transition probability calculated by semiclassical approximation is given by

$$\Gamma_{\rm tunnel} \sim e^{-\frac{16\pi}{g^2}} = \mathcal{O}(10^{-162}) \ , \tag{4.19}$$

for $N_{\rm CS}(t_f) - N_{\rm CS}(t_i) = 1$. The probability is suppressed exponentially, and thus this process can be neglected.

The other is sphaleron process [37, 215, 216]. Sphaleron is a classical saddle point solution which connects two vacuums with different Chern-Simons numbers, and state transitions which change baryon number occur in the early Universe. Accoroding to Ref. [217] (more accurate calculation in Ref. [218]), the transition rate par volume after the electroweak phase transition ($T < T_{\rm EW}$) is calculated by

$$\frac{\Gamma_{\rm sph}}{V} \sim \left(\frac{E_{\rm sph}}{T}\right)^3 \left(\frac{m_W(T)}{T}\right)^4 T^4 e^{-\frac{E_{\rm sph}(T)}{T}} \sim e^{-\frac{m_W}{\alpha T}} \ , \tag{4.20}$$

Where $E_{\rm sph}$ is the sphaleron energy given by

$$E_{\rm sph}(T) \simeq \frac{8\pi}{g} v(T) \ , \tag{4.21}$$

with $v(T)$ being the vacuum expectation value (VEV) of the Higgs field. In Eq. (4.20), the transition rate of the sphaleron process after the electroweak phase transition is also suppressed

exponentially and very small. On the other hand, according to Ref. [219, 220], the rate before electroweak phase transition ($T \geq T_{\rm EW}$) is given by

$$\frac{\Gamma_{\rm sph}}{V} \sim 25\alpha_W^5 T^4 \ , \tag{4.22}$$

with $\alpha_W = g^2/4\pi$. In this case, the rate has no exponential suppression factor, and thus, baryon and lepton number violations often occur. From Gamov's criterion, the sphaleron process is in thermal equilibrium when

$$T_{\rm EW} \sim 100 \text{ GeV} < T \lesssim 10^{12} \text{ GeV} \ . \tag{4.23}$$

4.1.4 Relation between produced baryon and lepton numbers

In subsection 4.1.2, we give a short review of the condition for the production of baryon number, and we show the relation between baryon and lepton numbers produced through some mechanism in this subsection. In the leptogenesis scenario, lepton number is first generated by decays of heavy right-handed neutrinos, and then some of them are converted into baryon number through the sphaleron process.

The difference between the number density of particle i and antiparticle $\bar{i}$ is given by

$$\begin{aligned} n_i - n_{\bar{i}} &= g_i \int \frac{d^3k}{(2\pi)^3} \left[\frac{1}{e^{(E-\mu_i)/T} \pm 1} - \frac{1}{e^{(E+\mu_i)/T} \pm 1} \right] \\ &\simeq \frac{1}{6} \xi g_i T^3 \frac{\mu_i}{T} \qquad (\text{for } m, |\mu_i| \ll T), \end{aligned} \tag{4.24}$$

with $\xi = 1(2)$ for fermion (boson), and μ_i being chemical potential of particle i.

In thermal plasma with high temperature, the SM quarks, leptons, and Higgs boson are in equilibrium through gauge and Yukawa interaction and sphaleron process. Hereafter, we show relations between chemical potentials of particles in equilibrium (see also Ref. [221]). For generality, we set numbers of fermion generation and Higgs doublets to be N_f and N_H, respectively ($N_f = 3$ and $N_H = 1$ for the SM).

Sphaleron process

$$\sum_\alpha \left(\mu_{u_{L,\alpha}} + 2\mu_{d_{L,\alpha}} + \mu_{\nu_{L,\alpha}} \right) = 0 \ , \tag{4.25}$$

with α being the index of fermion generation.

Yukawa interaction

$$\begin{aligned}
\mu_{d_{L,\alpha}} - \mu_{d_{R,\beta}} - \mu_{\phi^0} &= 0 \ , \\
\mu_{u_{L,\alpha}} - \mu_{u_{R,\beta}} + \mu_{\phi^0} &= 0 \ , \\
\mu_{e_{L,\alpha}} - \mu_{e_{R,\beta}} - \mu_{\phi^0} &= 0 \ .
\end{aligned} \tag{4.26}$$

Gauge interaction

$$\begin{aligned}
\mu_{u_{L,\alpha}} - \mu_{d_{R,\alpha}} + \mu_W &= 0 \ , \\
\mu_{\nu_{L,\alpha}} - \mu_{e_{L,\alpha}} + \mu_W &= 0 \ , \\
\mu_{\phi^-} + \mu_{\phi^0} - \mu_W &= 0 \ .
\end{aligned} \tag{4.27}$$

Using these relations, the densities of baryon B and lepton L numbers, electroweak charge Q, and the third component of $\mathrm{SU}(2)_L$, Q_3 are given by

$$B \equiv \frac{n_B}{s} = \frac{15 g_f}{4\pi^2 g_{s*} T} \sum_\alpha \left(\mu_{u_{L,\alpha}} + \mu_{u_{R,\beta}} + \mu_{d_{L,\alpha}} + \mu_{d_{R,\alpha}} \right) = \frac{15 g_f}{4\pi^2 g_{s*} T} \sum_\alpha \left(4\mu_{u_{L,\alpha}} + 2\mu_W \right) \ , \tag{4.28}$$

$$L \equiv \frac{n_L}{s} = \frac{15 g_f}{4\pi^2 g_{s*} T} \sum_\alpha \left(\mu_{\nu_{L,\alpha}} + \mu_{e_{L,\alpha}} + \mu_{e_{R,\alpha}} \right) = \frac{15 g_f}{4\pi^2 g_{s*} T} \sum_\alpha \left(3\mu_{\nu_{L,\alpha}} + 2\mu_W - \mu_{\phi^0} \right) \ , \tag{4.29}$$

$$\begin{aligned}
Q &\equiv \frac{n_Q}{s} \\
&= \frac{15 g_f}{4\pi^2 g_{s*} T} \sum_\alpha \left\{ 3 \times \frac{2}{3} (\mu_{u_{L,\alpha}} + \mu_{u_{R,\beta}}) - 3 \times \frac{1}{3} (\mu_{d_{L,\alpha}} + \mu_{d_{R,\beta}}) \right. \\
&\qquad \left. - (\mu_{e_{L,\alpha}} + \mu_{e_{R,\alpha}}) - \frac{4}{N_f} \mu_W - \frac{2N_H}{N_f} \mu_{\phi^-} \right\} \\
&= \frac{15 g_f}{4\pi^2 g_{s*} T} \sum_\alpha \left\{ 2\mu_{u_{L,\alpha}} - 2\mu_{\nu_{L,\alpha}} - \frac{4N_f + 2N_H + 4}{N_f} \mu_W + \frac{4N_f + 2N_H}{N_f} \mu_{\phi^0} \right\} \ ,
\end{aligned} \tag{4.30}$$

$$\begin{aligned}
Q_3 &\equiv \frac{n_{Q_3}}{s} \\
&= \frac{15 g_f}{4\pi^2 g_{s*} T} \sum_\alpha \left\{ 3 \times \frac{1}{2} (\mu_{u_{L,\alpha}} - \mu_{d_{L,\beta}}) + \frac{1}{2} (\mu_{\nu_{L,\alpha}} - \mu_{e_{L,\alpha}}) - \frac{4}{N_f} \mu_W - \frac{N_H}{N_f} (\mu_{\phi^0} + \mu_{\phi^-}) \right\} \\
&= -\frac{15 g_f}{4\pi^2 g_{s*} T} (2N_f + N_H + 4) \mu_W \ ,
\end{aligned} \tag{4.31}$$

with g_f being the degree of freedom of left and right-handed fermion. Before the electroweak phase transition ($T \geq T_{\mathrm{EW}}$), both Q and Q_3 must be zero. The latter condition implies $\mu_W = 0$, and using the former one, the baryon and lepton number densities are given by

$$B = \frac{8N_f + 4N_H}{22N_f + 13N_H} (B - L) \ , \quad L = -\frac{14N_f + 9N_H}{22N_f + 13N_H} (B - L) \ . \tag{4.32}$$

For the SM case,

$$B = \frac{28}{79}(B-L)\ , \quad L = -\frac{51}{79}(B-L)\ . \tag{4.33}$$

Immediately after inflation, the total $(B-L)=0$, and thus, Eq. (4.32) implies a need for $(B-L)$-violating process in order to generate baryon asymmetry.

4.2 Leptogenesis

In subsection 4.1.4, we show that not only $(B+L)$-violating sphaleron process but also $(B-L)$-violating one are necessary for generation of baryon asymmetry. In leptogenesis scenario [36], decays of heavy right-handed neutrinos (RHNs) violate lepton number, and then it is converted into baryon number. The produced baryon asymmetry is evaluated by asymmetry parameter ϵ_1, defined below. In this section, we give a brief review of leptogenesis, which is important for the discussion in chapter 6.

First, we show how lepton asymmetry is generated by decays of heavy RHNs and formula of asymmetry parameter in subsection 4.2.1. In subsection 4.2.2, we give a brief review of the thermal leptogenesis scenario, in which heavy RHNs are produced in the SM thermal plasma. We, finally, show non-thermal leptogenesis scenario [222–229], in which heavy neutrinos are produced by decays of scalars, and this scenario appears in chapter 6.

4.2.1 Asymmetry Parameter

In the leptogenesis scenario, baryon number is generated through the sphaleron process that is in thermal equilibrium before the electroweak phase transition, and thus, we discuss only much higher temperature than the electroweak scale ($T \gg T_{\rm EW} \sim \mathcal{O}(10^2)$ GeV). In this case, the electroweak symmetry is not violated, and the SM neutral and charged Higgs bosons $\phi = (\phi^+, \phi^0)^T$ have the same masses, and the SM gauge bosons have no mass. The light active neutrinos have no mass, while the heavy RHNs have non-zero masses because of the Majorana masses.

In the basis where the Majorana mass matrix is diagonal, the Lagrangian relative to neutrinos are given by

$$\Delta\mathcal{L} = -\hat{\lambda}_{i\alpha}\hat{N}_i^c(L_\alpha \cdot H) - \frac{1}{2}M_i\hat{N}_i^c\hat{N}_i^c + \text{h.c.}\ , \tag{4.34}$$

where $\hat{N}_i$ is i-th mass eigenstate of heavy neutrinos with mass eigenvalue M_i, and $\hat{\lambda}_{i\alpha}$ is neutrino Dirac Yukawa coupling. $\hat{N}_i$ decays into $\mathrm{SU}(2)_L$ doublet Higgs boson and lepton like $\hat{N}_i \to \phi + L_\alpha$,

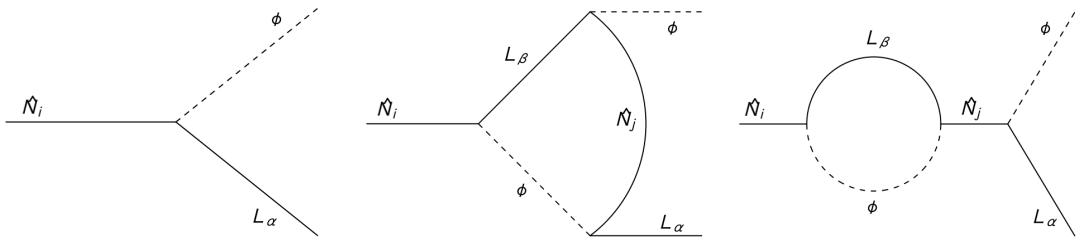

(a) tree diagram (b) vertex collection (c) self-energy

Figure 4.1: Diagrams of decays of the SM singlet RHNs contributing to lepton asymmetry. Lepton asymmetry is generated by interference between (a) tree and (b,c)one-loop level diagrams.

and decay rate of this process is given by

$$\begin{aligned}\Gamma_{D_i} &= \sum_\alpha \left[\Gamma(N_i \to L_\alpha + \phi) + \Gamma(N_i \to \bar{L}_\alpha + \bar{\phi})\right] \\ &= \frac{1}{8\pi}(\hat{\lambda}\hat{\lambda}^\dagger)_{ii} M_i \ . \end{aligned} \tag{4.35}$$

Because of $\mathrm{SU}(2)_L$ gauge symmetry, the following conditions are satisfied :

$$\Gamma(\hat{N}_i \to \nu_\alpha + \phi^0) = \Gamma(\hat{N}_i \to e_\alpha^- + \phi^+) \equiv \frac{1}{2}\Gamma(\hat{N}_i \to L_\alpha + \phi) \ , \tag{4.36}$$

$$\Gamma(\hat{N}_i \to \bar{\nu}_\alpha + \phi^{0*}) = \Gamma(\hat{N}_i \to e_\alpha^+ + \phi^-) \equiv \frac{1}{2}\Gamma(\hat{N}_i \to \bar{L}_\alpha + \bar{\phi}) \ . \tag{4.37}$$

From the Sakharov condition, it is necessary for the generation of lepton number that decay processes of heavy RHNs are driven out of equilibrium :

$$\Gamma_{D_i} < H|_{T=M_i} \ . \tag{4.38}$$

When the lightest mass eigenstate of heavy neutrinos $\hat{N}_i$ is much lighter than the others $\hat{N}_{2,3}$, only the time evolution of $\hat{N}_1$ is important for the generation of lepton asymmetry. This is because lepton asymmetry generated by decays of $\hat{N}_{2,3}$ for $T \gg M_1$ is washed out by the processes involving $\hat{N}_1$. For $M_1 \simeq M_{2,3}$, the contribution of $\hat{N}_{2,3}$ decay to lepton asymmetry has to be taken into account. The leptogenesis scenario under such a situation is called resonant leptogenesis, and the details are not discussed in this thesis. This scenario is discribed in, for example, Refs. [230–236].

When the temperature goes below M_1 ($T < M_1$), $\hat{N}_1$ is driven out of thermal equilibrium, and the lepton asymmetry is generated by interference terms between tree and one-loop level diagrams of the decay process, shown in Fig. 4.1. The generated lepton asymmetry is expressed

in terms of the asymmetry parameter ϵ_1, which is calculated by [232, 237, 238]

$$\epsilon_1 = \frac{\sum_\alpha \left[\Gamma(\hat{N}_1 \to L_\alpha \phi) - \Gamma(\hat{N}_1 \to \bar{L}_\alpha \phi^*)\right]}{\sum_\alpha \left[\Gamma(\hat{N}_1 \to L_\alpha \phi) + \Gamma(\hat{N}_1 \to \bar{L}_\alpha \phi^*)\right]}$$
$$\simeq \frac{1}{8\pi} \frac{1}{(\hat{\lambda}\hat{\lambda}^\dagger)_{11}} \sum_{j=2,3} \mathrm{Im}\left[\left\{(\hat{\lambda}\hat{\lambda}^\dagger)_{1j}\right\}^2\right] f\left(\frac{M_j^2}{M_1^2}\right) , \tag{4.39}$$

$$f(x) = \sqrt{x}\left[1 - (x+1)\ln\left(1 + \frac{1}{x}\right) - \frac{1}{x-1}\right] . \tag{4.40}$$

Among the terms in the definition of $f(x)$, the first and second terms are originated from interference between tree and vertex correction diagrams, and the third term is from that between tree and self-energy ones. For the hierarchical masses $M_1 \ll M_{2,3}$, $f(x)$ is approximately $-2/3\sqrt{2}$, and the asymmetry parameter is given by

$$\epsilon_1 \simeq -\frac{3}{8\pi} \frac{1}{(\hat{\lambda}\hat{\lambda}^\dagger)_{11}} \sum_{i=2,3} \mathrm{Im}\left\{(\hat{\lambda}\hat{\lambda}^\dagger)^2_{1j}\right\} \frac{M_1}{M_i} . \tag{4.41}$$

4.2.2 Thermal Leptogenesis

In this subsection, we show a rough story of thermal leptogenesis. However, the leptogenesis scenario discussed in chapter 6 is the non-thermal case, and therefore, we here do not go into the detail of the thermal leptogenesis scenario.

In the early Universe, heavy RHNs are produced thermally in the SM thermal plasma. Produced RHNs decay into the SM particles and generate lepton asymmetry. This is the first step of the thermal leptogenesis proposed in Ref. [36]. However, when the decay process of heavy RHNs is in thermal equilibrium, the lepton asymmetry L generated by N_1 decays are washed out by the asymmetry with the inverse sign $-L$ generated by inverse decay and scattering. Therefore, the decay process should be driven out of equilibrium to avoid wash-out of the produced lepton asymmetry. From Gamov's criterion, such a condition is given by

$$K \equiv \frac{\Gamma_{D_1}}{H|_{T=M_1}} \simeq \frac{(\hat{\lambda}\hat{\lambda}^\dagger)_{11} M_1/(8\pi)}{1.66\sqrt{g_*} M_1^2/M_{\rm pl}} \simeq \frac{M_{\rm pl}}{41.7\sqrt{g_*}} \frac{(\hat{\lambda}\hat{\lambda}^\dagger)_{11}}{M_1} < 1 , \tag{4.42}$$

with $g_* = 106.75$ being the degree of freedom of relativistic particles. This condition leads to the following constraint on the effective mass of the lightest neutrino $\tilde{m}_1$ [239, 240] :

$$\tilde{m}_1 \equiv (\hat{\lambda}\hat{\lambda}^\dagger)_{11} \frac{v^2}{M_1} \simeq 41.7\sqrt{g_*} \frac{v^2}{M_{\rm pl}} \left.\frac{\Gamma_{D_1}}{H}\right|_{T=M_1} < 10^{-3}\ \text{eV} . \tag{4.43}$$

The remained lepton asymmetry after wash-out is given by [119]

$$Y_L = \frac{n_L - n_{\bar{L}}}{s} = \kappa_f \frac{\epsilon_1}{g_*} , \tag{4.44}$$

where κ_f is the efficiency factor of lepton asymmetry production and depends on the decay parameter K in Eq. (4.42). The final baryon asymmetry generated through thermal leptogenesis is obtained by multiplying Y_L by the sphaleron conversion factor in Eq. (4.33) as follows :

$$Y_B = \frac{28}{79} Y_{B-L} = -\frac{28}{79} Y_L = -\frac{28}{79} \kappa_f \frac{\epsilon_1}{g_*} \ . \tag{4.45}$$

For $K \gg 1$, such a situation is called the "strong wash-out" regime. In this case, both decay and inverse decay processes frequently occur, and thus, many RHNs are produced through the inverse decay process. During $T > M_1$, decay and inverse decay processes get in thermal equilibrium, and the number density of lightest RHN N_{N_1} is equal to be its equilibrium value $N_{N_1}^{\rm eq}$. When the temperature goes below M_1, the processes are driven out of equilibrium, and $(B-L)$-number is produced as RHNs decay. The efficiency factor, in this case, is given by [241]

$$\kappa_f \simeq 0.02 \left(\frac{0.01 {\rm eV}}{\tilde{m}_1} \right)^{1.1} = 0.02 \left(\frac{10}{K} \right)^{1.1} \ . \tag{4.46}$$

On the other hand, for $K < 1$, such a situation is called the "weak wash-out" regime. In this case, both decay and inverse decay processes are suppressed. Thus, the temperature of the Universe goes below M_1 before N_{N_1} reaches its equilibrium value $N_{N_1}^{\rm eq}$, and then decay process is driven out of equilibrium. Therefore, the amount of produced RHNs is less than the strong wash-out case, and the $(B-L)$-number generated by their decays is also less. The efficiency factor, in this case, is given by [241]

$$\kappa_f \simeq \left(\frac{3\pi}{8} K \right)^2 \ . \tag{4.47}$$

4.2.3 Non-Thermal Leptogenesis

In this subsection, we give a brief review of non-thermal leptogenesis [222–229], which plays an important role in chapter 6. In the thermal leptogenesis scenario described in the previous subsection, heavy RHNs are produced thermally in the SM plasma. On the other hand, in the non-thermal leptogenesis scenario, RHNs are produced by decays of a scalar field coupled to RHNs. Produced RHNs are supposed to be out of equilibrium, and thus wash-out effect is not effective. Therefore, the lepton asymmetry is produced by decays of all RHNs, and it becomes the final value of generated $(B-L)$-number without wash-out.

Lepton asymmetry generated in non-thermal leptogenesis scenario is evaluated by the following formula [222–229]

$$Y_L = \frac{n_L}{s} = \sum_i \frac{n_\sigma}{s} \frac{n_{N_i}}{n_\sigma} \frac{n_L}{n_{N_i}} = \sum_{i,j} \frac{n_\sigma}{s} \times {\rm Br}(\sigma \to \hat{N}_i \hat{N}_j) \times (\epsilon_i + \epsilon_j) \ , \tag{4.48}$$

where σ is a scalar which has coupling to RHNs, and $\mathrm{Br}(\sigma \to \hat{N}_i \hat{N}_j)$ is the branching ratio of $\sigma \to \hat{N}_i \hat{N}_j$ process. The final baryon asymmetry generated through non-thermal leptogenesis is obtained by multiplying the above Y_L by the sphaleron conversion factor in Eq. (4.33) as follows :

$$Y_B = \frac{28}{79} Y_{B-L} = -\frac{28}{79} Y_L = -\frac{28}{79} \sum_{i,j} \frac{n_\sigma}{s} \times \mathrm{Br}(\sigma \to \hat{N}_i \hat{N}_j) \times (\epsilon_i + \epsilon_j) \ . \tag{4.49}$$

The number density of the scalar σ is dependent on the dynamics of σ in the early Universe, and generally, this value is calculated by solving the Boltzmann equation, mentioned in section 3.1. In chapter 6, we assume the above scalar is inflaton, and in this case, the number density of inflaton is calculated in terms of the inflaton mass and reheating temperature. The detail is shown in chapter 6.

Part II

Original Works

Chapter 5

Predictions for the neutrino parameters in the minimal gauged $U(1)_{L_\mu - L_\tau}$ model

The neutrino sector is one of the most mysterious parts in the SM, we know that this sector should be extended because of the observations of neutrino oscillation and the existence of non-zero neutrino masses. One possibility of extensions of the neutrino sector is introducing right-handed neutrinos (RHNs), and it simply explains the neutrino masses. Moreover, if the neutrinos are Majorana particles, their Majorana nature gives the neutrino sector rich phenomenology, such as neutrinoless double beta decay (subsection 2.2.1), the seesaw mechanism (subsection 2.2.2), and leptogenesis (section 4.2).

The $U(1)_{L_\mu - L_\tau}$ gauge symmetry also gives interesting phenomenology to the neutrino sector. Gauge symmetries control interactions between fields in gauge theories, and in the $U(1)_{L_\mu - L_\tau}$ case, only the leptons are transformed non-trivially. In the gauged $U(1)_{L_\mu - L_\tau}$ model, some mass terms in the neutrino sector are forbidden by the gauge symmetry, and the degree of freedom of parameters in the neutrino mass matrices is less than the case without $U(1)_{L_\mu - L_\tau}$. So far, many previous studies have explored the relations between the mass structures of the neutrinos in the $U(1)_{L_\mu - L_\tau}$ models and the observed values relative to neutrinos, for example, Refs. [42–44, 242–250]. As mentioned above, the $U(1)_{L_\mu - L_\tau}$ gauge symmetry constrains the neutrino sector and force the neutrino Dirac and Majorana mass matrices to be diagonal and block-diagonal, respectively. Because of the type-I seesaw mechanism (see Eq. (2.37) of subsection 2.2.2), the active neutrino mass matrix is also block-diagonal and cannot explain the neutrino oscillation data. Therefore, the $U(1)_{L_\mu - L_\tau}$ gauge symmetry should be broken, and one scalar with $U(1)_{L_\mu - L_\tau}$ charge is introduced for the spontaneous symmetry breaking. There are several possibilities as $U(1)_{L_\mu - L_\tau}$-breaking scalar, but only $SU(2)_L$ singlet with $U(1)_{L_\mu - L_\tau}$ charge ± 1 realizes the observed neutrino oscillation and avoids the cosmological constraint on

the neutrino masses [42, 43]. Introduction of one $SU(2)_L$ singlet scalar is the minimal extension which is consistent with the existing experimental and cosmological results, and such a model is called the minimal gauged $U(1)_{L_\mu - L_\tau}$ model.

The minimal gauged $U(1)_{L_\mu - L_\tau}$ model naturally realizes the so-called *two-zero minor structure*, namely, two components in the inverse of the active neutrino mass matrix vanish. Relations between lepton flavor-dependent U(1) gauge symmetries and two-zero minor structure have been discussed, for example, in [244, 245]. And, focusing on less degree of freedom, those between two-zero minor structure and neutrino parameters have been discussed, for example, [42–44, 243, 246–252]. Among them, the author's works [42–44] have exactly analyzed the constraints on the neutrino parameters from the two-zero minor structure and obtained the neutrino CP phases, sum of the neutrino masses, effective Majorana neutrino mass for the neutrinoless double beta decay, and so on. And we have obtained these parameters as functions of the neutrino oscillation parameters. In this model, all the neutrino parameters are determined by the neutrino oscillation parameters. Therefore, this model has predictive power for the effective Majorana neutrino mass for neutrinoless double beta decay and lepton asymmetry generated by decays of heavy RHNs.

In this chapter, we discuss the relations between the two-zero minor structure and neutrino parameters, following Refs. [42–44]. This chapter is organized as follows. In section 5.1, we introduce the minimal gauged $U(1)_{L_\mu - L_\tau}$ model and derive the relations between the two-zero minor structure and neutrino parameters. In section 5.2, using the results in the previous section, we show the predictions for the neutrino parameters, including the effective Majorana neutrino mass for neutrinoless double beta decay. Lastly, in section 5.3, we summarize this chapter.

5.1 Minimal Gauged $U(1)_{L_\mu - L_\tau}$ Model and Neutrino Mass Structure

In the minimal gauged $U(1)_{L_\mu - L_\tau}$ model, three RHNs are introduced for non-zero neutrino masses. Moreover, neutrinos are assumed to be Majorana particles to realize the seesaw mechanism and leptogenesis scenario. In the $U(1)_{L_\mu - L_\tau}$ gauge theory, muon $\mu_{L,R}$, mu-type neutrino ν_μ, and mu-type RHN N_τ have the $U(1)_{L_\mu - L_\tau}$ charge $+1$, tau particle $\tau_{L,R}$, tau-type neutrino ν_τ, and tau-type RHN N_τ have the $U(1)_{L_\mu - L_\tau}$ charge -1, and the other SM fields have the zero $U(1)_{L_\mu - L_\tau}$ charge. We summarize the charge assignment of the field content in the minimal gauged $U(1)_{L_\mu - L_\tau}$ model in Tab. 5.1. Under this charge assignment, the neutrino Dirac and Majorana Yukawa mass terms which are invariant under the $U(1)_{L_\mu - L_\tau}$ gauge transformation

field	$L_\mu = \begin{pmatrix} \nu_\mu \\ \mu_L \end{pmatrix}, \mu_R, N_\mu$	$L_\tau = \begin{pmatrix} \nu_\tau \\ \tau_L \end{pmatrix}, \tau_R, N_\tau$	σ	others
$\mathrm{U}(1)_{L_\mu - L_\tau}$ charge	+1	-1	+1	0

Table 5.1: $\mathrm{U}(1)_{L_\mu - L_\tau}$ charges of the field content in the minimal gauged $\mathrm{U}(1)_{L_\mu - L_\tau}$ model.

are obtained as follows :

$$\text{Dirac} \ : \ \mathcal{M}_D = \begin{pmatrix} * & 0 & 0 \\ 0 & * & 0 \\ 0 & 0 & * \end{pmatrix}, \qquad \text{Majorana} \ : \ \mathcal{M}_R = \begin{pmatrix} * & 0 & 0 \\ 0 & 0 & * \\ 0 & * & 0 \end{pmatrix}, \tag{5.1}$$

where $*$ denotes no-zero mass component. From Eq. (2.37), the mass matrix for the active neutrinos is given by

$$\mathcal{M}_{\nu_L} \simeq -\mathcal{M}_D \mathcal{M}_R^{-1} \mathcal{M}_D^T = \begin{pmatrix} * & 0 & 0 \\ 0 & 0 & * \\ 0 & * & 0 \end{pmatrix}, \tag{5.2}$$

This result is interpreted as $\theta_{12} = \theta_{13} = 0$ and $\theta_{23} = \pi/2$, and these mixing angles are clearly different from the observed values. Therefore, the $\mathrm{U}(1)_{L_\mu - L_\tau}$ gauge symmetry should be violated.

Here, we introduce one SM singlet scalar σ with the $\mathrm{U}(1)_{L_\mu - L_\tau}$ charge +1. This scalar develops a vacuum expectation value (VEV), and then breaks the $\mathrm{U}(1)_{L_\mu - L_\tau}$ gauge symmetry spontaneously. Under these charge assignments, the most general renormalizable interaction terms in the neutrino sector are given by

$$\begin{aligned} \mathcal{L}_N = & -\lambda_e N_e^c (L_e \cdot H) - \lambda_\mu N_\mu^c (L_\mu \cdot H) - \lambda_\tau N_\tau^c (L_\tau \cdot H) \\ & - \frac{1}{2} M_{ee} N_e^c N_e^c - M_{\mu\tau} N_\mu^c N_\tau^c - \frac{1}{2} \sum_{\alpha,\beta=e,\mu} h_{\alpha\beta} \sigma N_\alpha^c N_\beta^c - \frac{1}{2} \sum_{\alpha,\beta=e,\tau} h_{\alpha\beta} \sigma^* N_\alpha^c N_\beta^c + \text{h.c.} , \end{aligned} \tag{5.3}$$

where the dots between L_α and H denotes the contraction of the $\mathrm{SU}(2)_L$ indices. $h_{\alpha\beta}$ is a symmetric matrix with $h_{e\mu} = h_{\mu e}$, $h_{e\tau} = h_{\tau e}$, and all other elements being zero. After the Higgs field H and the $\mathrm{U}(1)_{L_\mu - L_\tau}$-breaking scalar σ acquire VEVs $\langle H \rangle = v/\sqrt{2}$, and $\langle \sigma \rangle$,[1] the neutrino mass terms are written in the flavor basis as follows :

$$\mathcal{M}_D = \begin{pmatrix} \lambda_e & 0 & 0 \\ 0 & \lambda_\mu & 0 \\ 0 & 0 & \lambda_\tau \end{pmatrix} \langle H \rangle \ , \quad \mathcal{M}_R = \begin{pmatrix} M_{ee} & h_{e\mu} \langle \sigma \rangle & h_{e\tau} \langle \sigma \rangle \\ h_{e\mu} \langle \sigma \rangle & 0 & M_{\mu\tau} \\ h_{e\tau} \langle \sigma \rangle & M_{\mu\tau} & 0 \end{pmatrix} . \tag{5.4}$$

As shown in Eq. (5.4), the Dirac mass matrix $\mathcal{M}_D$ is diagonal, and then the active neutrino mass matrix $\mathcal{M}_{\nu_L}$ is diagonalized by the PMNS matrix, which appears in subsection 2.2.3, as

[1] We can always take the VEV of σ to be real by using $\mathrm{U}(1)_{L_\mu - L_\tau}$ transformations.

follows :

$$U_{\rm PMNS}^T\ \mathcal{M}_{\nu_L}\ U_{\rm PMNS} = {\rm diag}(m_1, m_2, m_3)\ , \tag{5.5}$$

with m_i the mass eigenvalues of the active neutrinos. [2] From Eqs. (2.37) and (5.5), the following relation is obtained :

$$\mathcal{M}_{\nu_L}^{-1} = U_{\rm PMNS}\ {\rm diag}(m_1^{-1}, m_2^{-1}, m_3^{-1})\ U_{\rm PMNS}^T \simeq -(\mathcal{M}_D^{-1})^T \mathcal{M}_R \mathcal{M}_D^{-1}\ . \tag{5.6}$$

We then notice that the (μ,μ) and (τ,τ) components of these terms vanish because $\mathcal{M}_D$ is diagonal, and those of $\mathcal{M}_R$ also vanishes, as shown in Eq. (5.4). Therefore, we obtain the following two complex conditions :

$$\frac{1}{m_1}V_{\mu1}^2 + \frac{1}{m_2}V_{\mu2}^2 e^{i\alpha_2} + \frac{1}{m_3}V_{\mu3}^2 e^{i\alpha_3} = 0\ , \tag{5.7}$$

$$\frac{1}{m_1}V_{\tau1}^2 + \frac{1}{m_2}V_{\tau2}^2 e^{i\alpha_2} + \frac{1}{m_3}V_{\tau3}^2 e^{i\alpha_3} = 0\ , \tag{5.8}$$

where the unitary matrix $V_{\alpha i}$ and the Majorana CP phases $\alpha_{2,3}$ are defined in Eqs. (2.52) and (2.53), respectively. We note that the above conditions are independent of the VEV of the $\mathrm{U}(1)_{L_\mu - L_\tau}$-breaking scalar $\langle\sigma\rangle$ and the Majorana mass $M_{ee}, M_{\mu\tau}$. This point is much important and indicates that the following analyses and results shown in section 5.2 are independent of the scales of the $\mathrm{U}(1)_{L_\mu - L_\tau}$-breaking and Majorana mass.

Regarding the neutrino oscillation parameters as the inputs and solving Eqs. (5.7) and (5.8) for $e^{i\alpha_2}, e^{i\alpha_3}$, we obtain

$$e^{i\alpha_2} = \frac{m_2}{m_1}R_2(\delta), \quad e^{i\alpha_3} = \frac{m_3}{m_1}R_3(\delta)\ , \tag{5.9}$$

with

$$R_2(\delta) \equiv \frac{(V_{\mu1}V_{\tau3} + V_{\mu3}V_{\tau1})V_{e2}^*}{(V_{\mu2}V_{\tau3} + V_{\mu3}V_{\tau2})V_{e1}^*}, \quad R_3(\delta) \equiv \frac{(V_{\mu1}V_{\tau2} + V_{\mu2}V_{\tau1})V_{e3}^*}{(V_{\mu2}V_{\tau3} + V_{\mu3}V_{\tau2})V_{e1}^*}\ . \tag{5.10}$$

In Appendix C.2, we give explicit expressions for R_2 and R_3 in terms of neutrino oscillation parameters. Taking the absolute values of both sides of two equations in Eqs. (5.9), the ratios of the mass eigenvalues of the active neutrinos are obtained as follows :

$$\frac{m_2}{m_1} = \frac{1}{|R_2(\delta)|}, \quad \frac{m_3}{m_1} = \frac{1}{|R_3(\delta)|}\ . \tag{5.11}$$

Here, R_2 and R_3 depend only on the Dirac CP phase δ, except for the neutrino mixing angles, and satisfy $R_{2,3}^*(-\delta) = R_{2,3}(\delta)$. Therefore, the mass ratios $m_{2,3}/m_1$ is symmetric under sign flip of $\delta : \delta \to -\delta$ $(\pi + \delta \to \pi - \delta)$. In Fig. 5.1, we plot the mass ratios m_2/m_1 and m_3/m_1

[2] For $m_1 = 0$ (NO) or $m_3 = 0$ (IO), the determinant of $\mathcal{M}_{\nu_L}$ is equal to be zero. Because of the discussion in Appendix C.1, this case leads to a block-diagonal $\mathcal{M}_{\nu_L}$ and then conflicts with the observed neutrino oscillation. Therefore, we assume $m_i \neq 0$ in this chapter.

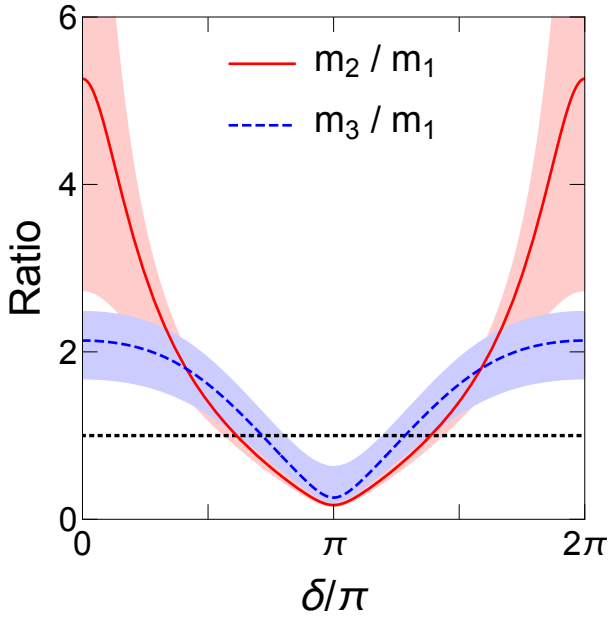

Figure 5.1: The mass ratios m_2/m_1 and m_3/m_1 as functions of the Dirac CP phase δ, from Eq. (5.11). The bands show uncertainty coming from the 1σ error in the neutrino mixing parameters. The thin dotted line corresponds to $m_{2,3}/m_1 = 1$.

against the Dirac CP phase δ using Eq. (5.11). The bands show uncertainty coming from the 1σ error in the neutrino mixing parameters. For input parameters of the neutrino mixing angles, we use $\sin^2\theta_{12} = 3.10^{+0.13}_{-0.12} \times 10^{-1}$, $\sin^2\theta_{13} = 2.237^{+0.0066}_{-0.0065} \times 10^{-2}$, and $\sin^2\theta_{23} = 5.63^{+0.18}_{-0.24} \times 10^{-1}$ [109, 110] (see Tab. 2.2). It is found that the resultant uncertainty mainly comes from the error in θ_{23}. From this figure, we find that when $\delta \simeq \pi$ the observed neutrino mixing angles are incompatible with the condition $m_1 < m_2$, and thus these regions are excluded. Moreover, around $\delta \simeq 0,\ 2\pi$ we have $m_1 < m_3 < m_2$, which disagrees with the possible neutrino mass ordering: either $m_1 < m_2 < m_3$ or $m_3 < m_1 < m_2$ [50]. As a consequence, in the region where a consistent neutrino mass ordering is obtained, the neutrino mass ordering is always Quasi-Degenerate Normal Ordering with $m_1 \lesssim m_2 \lesssim m_3$, which is realized around $\delta \sim \pi/2$ and $3\pi/2$.

According to the recent global-fit analysis in Ref. [110], the NO is somewhat favored over IO at $\sim 2.5\sigma$ level. There are quite a few proposed experiments that may determine the neutrino mass ordering at more than 3σ level within a decade [253, 254], such as PINGU [255], ORCA [256], and JUNO [257, 258]. To confirm NO in these future experiments would be the first consistency check of our model.

Now that the mass ordering has been fixed, we determine m_1 and δ by using the above

results. From the neutrino oscillation experiments, we can measure [3]

$$\delta m^2 \equiv m_2^2 - m_1^2 \ , \tag{5.13}$$

$$\Delta m^2 \equiv m_3^2 - (m_2^2 + m_1^2)/2 \ . \tag{5.14}$$

These quantities are related to the neutrino mass ratios as

$$\delta m^2 = m_1^2 \left(\frac{m_2^2}{m_1^2} - 1 \right) = m_1^2 \left(\frac{1}{|R_2(\delta)|^2} - 1 \right) \ , \tag{5.15}$$

$$\Delta m^2 + \frac{\delta m^2}{2} = m_1^2 \left(\frac{m_3^2}{m_1^2} - 1 \right) = m_1^2 \left(\frac{1}{|R_3(\delta)|^2} - 1 \right) \ . \tag{5.16}$$

By solving these equations, we can determine m_1 and δ. The observed values of δm^2 and Δm^2 are given by $\delta m^2 \simeq 7.39 \times 10^{-5}$ eV^2 and $\Delta m^2 \simeq 2.528 \times 10^{-3}$ eV^2, respectively [109, 110]. This means that the right-hand side of Eq. (5.15) is much smaller than that in Eq. (5.16). From Fig. 5.1, we see that such a hierarchy can be realized only when $m_2^2/m_1^2 \simeq 1$, *i.e.*, $|R_2(\delta)| \simeq 1$. With the explicit formula of $R_2(\delta)$ in Eq. (c.3), this leads to

$$\cos\delta \simeq \frac{\cot 2\theta_{12} \cot 2\theta_{23}}{\sin\theta_{13}} \ . \tag{5.17}$$

When the best-fit values of the mixing angles θ_{ij} are used, this leads to $\cos\delta \simeq -0.34$, which corresponds to $\delta \simeq 0.61\pi$ or 1.39π. In Eq. (c.5) in Appendix C.3, we give a cubic equation whose solution gives an exact value of $\cos\delta$ as a function of the mixing angles θ_{ij} and the squared mass differences δm^2 and Δm^2. As discussed there, the solution (5.17) approximates the real solution of the cubic equation (c.5) at $\mathcal{O}(\delta m^2/\Delta m^2)$ level. By solving Eq. (c.5) numerically, we find $\cos\delta = -0.349$ for the best-fit values of θ_{ij}, δm^2, and Δm^2, which means $\delta = 0.613\pi$ or 1.387π, and justifies the expected accuracy of the approximated formula (5.17).

Before closing this section, let us give a general remark about quantum corrections to the neutrino mass matrix. If the $\mathrm{U}(1)_{L_\mu - L_\tau}$ symmetry breaking scale is much higher than the electroweak scale, we expect sizable quantum corrections to the neutrino mass matrix. Such quantum corrections can be taken into account by using renormalization group equations. Remarkably, it is found that the two-zero minor structure of $\mathcal{M}_{\nu_L}$ is preserved throughout the renormalization group flow [259, 260]. To see this, we first note that below the right-handed neutrino mass scale, which is around the $\mathrm{U}(1)_{L_\mu - L_\tau}$ symmetry breaking scale in this model, right-handed neutrinos are integrated out to give the following dimension-five effective operator:

$$\mathcal{L}_{\rm eff} = \frac{1}{2} C_{\alpha\beta} (L_\alpha \cdot H)(L_\beta \cdot H) + \text{h.c.} \ , \tag{5.18}$$

[3] In terms of the squared mass differences $\Delta m_{21}^2 \equiv m_2^2 - m_1^2$ and $\Delta m_{31}^2 \equiv m_3^2 - m_1^2$, δm^2 and Δm^2 are expressed as

$$\delta m^2 = \Delta m_{21}^2 \ , \qquad \Delta m^2 = \Delta m_{31}^2 - \frac{1}{2} \Delta m_{21}^2 \ . \tag{5.12}$$

where $C_{\alpha\beta}$ has the two-zero minor structure at the right-handed neutrino mass scale. The renormalization group equation of the Wilson coefficient $C_{\alpha\beta}$ at one-loop level is [261]

$$\mu\frac{dC}{d\mu} = -\frac{3}{32\pi^2}\left[\left(Y_e^\dagger Y_e\right)^T C + C\left(Y_e^\dagger Y_e\right)\right] + \frac{K}{16\pi^2}C \ , \tag{5.19}$$

with

$$K = -3g_2^2 + 2\mathrm{Tr}\left(3Y_u^\dagger Y_u + 3Y_d^\dagger Y_d + Y_e^\dagger Y_e\right) + 2\lambda \ , \tag{5.20}$$

where Y_u, Y_d, and Y_e denote the up-type, down-type, and charged-lepton Yukawa matrices, respectively, g_2 is the $\mathrm{SU}(2)_L$ gauge coupling, and λ is the Higgs quartic coupling: $\mathcal{L}_{\mathrm{quart}} = -\frac{1}{2}\lambda(H^\dagger H)^2$. Now recall that the charged lepton Yukawa matrix is diagonal in our model. In this case, the above equation can readily be solved as follows [262]:

$$C(t) = I_K(t)\,\mathcal{I}(t)\,C(0)\,\mathcal{I}(t) \ , \tag{5.21}$$

where $t \equiv \ln(\mu/\mu_0)$ with μ_0 being the initial scale, and

$$I_K(t) = \exp\left[\frac{1}{16\pi^2}\int_0^t K(t')\,dt'\right] \ , \qquad \mathcal{I}(t) = \exp\left[-\frac{3}{32\pi^2}\int_0^t Y_e^\dagger Y_e(t')\,dt'\right] \ . \tag{5.22}$$

Note that $\mathcal{I}(t)$ is a diagonal matrix. Therefore, if $C_{\mu\mu}^{-1}(0) = C_{\tau\tau}^{-1}(0) = 0$, then $C_{\mu\mu}^{-1}(t) = C_{\tau\tau}^{-1}(t) = 0$, which proves that the two-zero minor structure of the Wilson coefficient C remains at low energies. As a result, the two-zero minor neutrino-mass structure in our model is robust against quantum corrections, even if the $\mathrm{U}(1)_{L_\mu - L_\tau}$ symmetry breaking scale is much higher than the electroweak scale.

5.2 Predictions for the Neutrino Parameters

Using the results obtained above, we now compute quantities relevant to neutrino experiments with the errors in the neutrino oscillation parameters taken into account. For input values, we use the values given in Ref. [109, 110], which are summarized in Table 2.2. In particular, we take the three mixing angles and the two mass squared differences,

$$\theta_{12},\ \theta_{23},\ \theta_{13},\ \delta m^2,\ \Delta m^2 \ , \tag{5.23}$$

as input parameters, and evaluate the predicted values of the other parameters, including Dirac CP phase δ, the absolute masses m_i, their sum $\sum_i m_i$, and the effective Majorana neutrino mass $\langle m_{\beta\beta}\rangle$. The prediction for the Majorana phases α_2 and α_3 is also presented in Appendix C.2.

In Fig. 5.2, we plot the Dirac CP phase δ as functions of θ_{23} in the red lines. We vary θ_{23} in the 3σ renege, where the 1σ range is in between the vertical thin dotted lines. The dark (light)

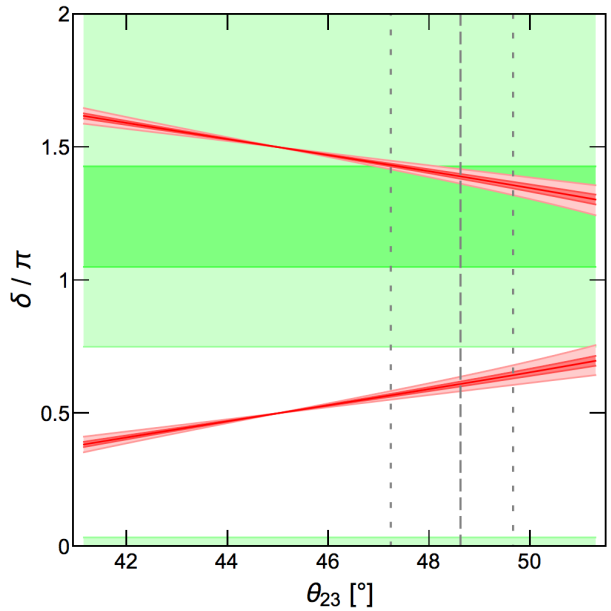

Figure 5.2: The prediction for the Dirac CP phase δ in the minimal gauged U(1)$_{L_\mu - L_\tau}$ model. The red lines show the CP phase δ against θ_{23}. θ_{23} is varied in the 3σ range, and the 1σ range is in between the vertical thin dotted lines. The dark (light) red bands show the uncertainty coming from the 1σ (3σ) errors in the parameters θ_{12}, θ_{13}, δm^2, and Δm^2. We also show the 1σ (3σ) favored region of δ in the dark (light) horizontal green bands.

red bands show the uncertainty coming from the 1σ (3σ) errors in the other parameters θ_{12}, θ_{13}, δm^2, and Δm^2. We find that this uncertainty is dominated by the error in θ_{12}. We also show the 1σ (3σ) favored region of δ in the dark (light) horizontal green bands.[4] As we discussed in the previous section, there are two solutions for δ for each value of θ_{23}. Intriguingly, the upper line is right in the middle of the favored range of δ; in particular, $\theta_{23} \simeq 48.6^\circ$ gives $\delta \simeq 1.4\pi$, both of which are within the 1σ allowed region. Consequently, this model predicts $\delta \simeq 1.36\pi$–1.43π (1.30π–1.62π) within 1σ (3σ). Future neutrino experiments can test this prediction through precision measurements of θ_{23} and δ [264].

Next, we evaluate the neutrino masses m_i, which are shown in Fig. 5.3a as functions of θ_{23}. Here, the other parameters are fixed to be their best-fit values. We see that all of these masses are predicted to be $\gtrsim \sqrt{\Delta m^2} \simeq 5 \times 10^{-2}$ eV. We also plot the sum of these neutrino masses as a function of θ_{23} in Fig. 5.3b, where the dark (light) red band shows the uncertainty coming from the 1σ (3σ) errors in the parameters other than θ_{23}. In this case, it turns out that the dominant contribution to the uncertainty (except for that from the error in θ_{23}) comes from the error in θ_{13}, though the error in Δm^2 also gives a sizable contribution. We also show in the black dashed line the present limit given by Ref. [107] : $\sum_i m_i < 0.146$ eV (normal ordering, 95% C.L.). From this figure, we find that a wide range of the parameter region predicts a value

[4]The recent result by NOvA experiment reports that $\delta < \pi$ is favored in the NO case [263].

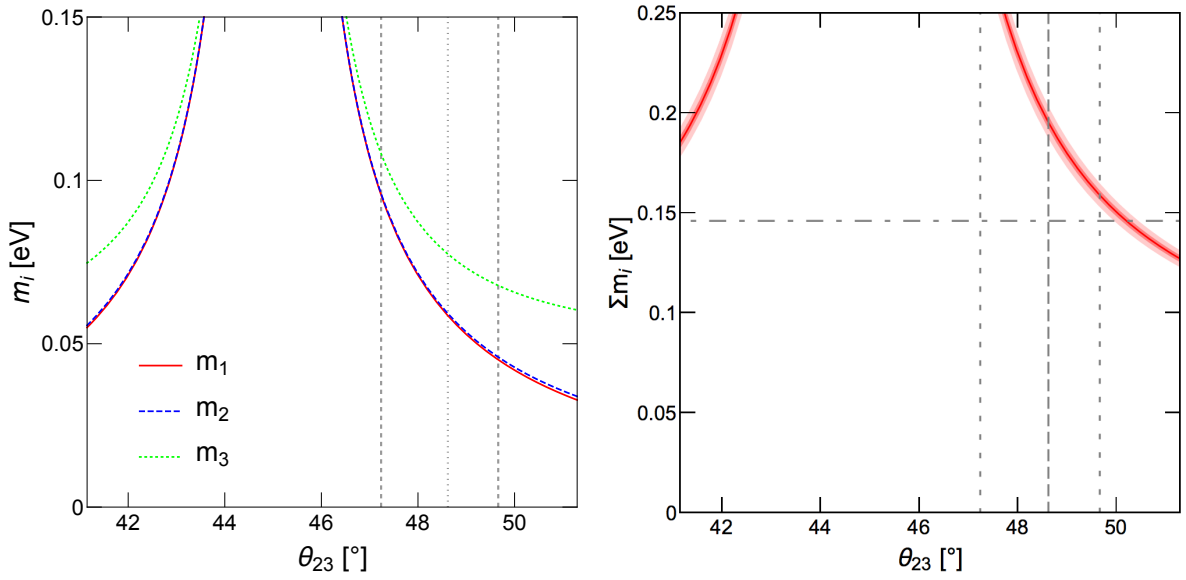

(a) Mass spectrum (b) $\sum_i m_i$

Figure 5.3: (a) The prediction for the neutrino masses in the minimal gauged $U(1)_{L_\mu - L_\tau}$ model. The neutrino masses m_i are shown as functions of θ_{23}. The other four parameters (θ_{12}, θ_{13}, δm^2, and Δm^2) are fixed to their best-fit values. (b) The sum of the neutrino masses as a function of θ_{23}. The dark (light) red band shows the uncertainty coming from the 1σ (3σ) errors in the parameters θ_{12}, θ_{13}, δm^2, and Δm^2. The entire region is within the 3σ range of θ_{23}, while its 1σ range is between the thin vertical dotted lines. We also show in the black dashed line the present limit given by Ref. [107] : $\sum_i m_i < 0.146$ eV (normal ordering, 95% C.L.).

of $\sum_i m_i$ which is above the present limit, but the region around $\theta_{23} \sim 50°$ is still marginally viable.

These relatively large values of m_i open up a possibility of testing this model in neutrinoless double beta decay experiments. The rate of neutrinoless double beta decay is proportional to the square of the effective Majorana neutrino mass $\langle m_{\beta\beta} \rangle$, which is given by Eq. (2.31) in subsection 2.2.1. It should be emphasized that, in the minimal gauged $U(1)_{L_\mu - L_\tau}$ model, not only the neutrino masses m_i but also the Majorana phases $\alpha_{2,3}$ are uniquely determined as functions of the other neutrino oscillation parameters. Thus, the value of the effective mass $\langle m_{\beta\beta} \rangle$ is also predicted unambiguously. Note also that this quantity has reflection symmetry with respect to $\delta \to -\delta$ and thus depends only on $\cos\delta$. In Fig. 5.4, we show $\langle m_{\beta\beta} \rangle$ as a function of θ_{23}, where the dark (light) red band shows the uncertainty coming from the 1σ (3σ) errors in the parameters other than θ_{23}. We also show in the light blue band the current bound on $\langle m_{\beta\beta} \rangle$ given by the KamLAND-Zen experiment, $\langle m_{\beta\beta} \rangle < 0.061$-$0.165$ eV [106], where the uncertainty stems from the estimation of the nuclear matrix element for ^{136}Xe. As we see in Fig. 5.4, $\langle m_{\beta\beta} \rangle$ is predicted to be $\simeq 0.021$ eV for $\theta_{23} \simeq 51°$, which is well below the present KamLAND-Zen limit, and this value can be within the reach of future neutrinoless double beta

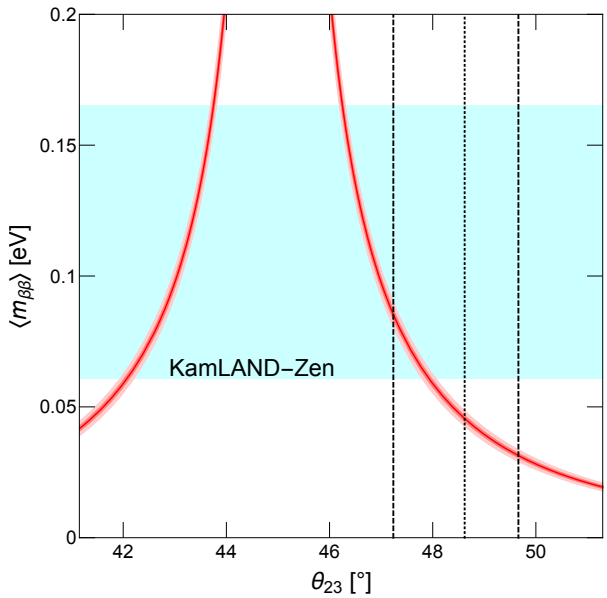

Figure 5.4: The prediction for the effective Majorana neutrino mass $\langle m_{\beta\beta} \rangle$ as a function of θ_{23} in the minimal gauged $U(1)_{L_\mu - L_\tau}$ model. The dark (light) red band shows the uncertainty coming from the 1σ (3σ) errors in the parameters other than θ_{23}. The entire region is within the 3σ range of θ_{23}, while its 1σ range is between the thin vertical dotted lines. The light blue band shows the current upper limit on $\langle m_{\beta\beta} \rangle$ given by the KamLAND- Zen experiment, $\langle m_{\beta\beta} \rangle < 0.061$-$0.165$ eV [106].

decay experiments, such as CUPID [101] and nEXO [105].

5.3 Summary and Discussions of Chapter 5

In this chapter, we have discussed the minimal gauged $U(1)_{L_\mu - L_\tau}$ model and the restrictions on the structure of the neutrino mass matrices, following Refs. [42–44]. In the minimal gauged $U(1)_{L_\mu - L_\tau}$ model, because of the gauge symmetries, the structures of the Dirac and Majorana mass matrices are tightly restricted, and the mass matrix for the active neutrinos has two-zero minor structure. These restrictions connect the low-energy neutrino parameters, and four of them are given as functions of the rest of the parameters, namely the neutrino mixing angles and squared mass differences. Using these relations, we obtained the prediction for the Dirac and Majorana CP phases, sum of the neutrino masses, and effective Majorana neutrino mass. We emphasize that these predictions are independent of the scales of the $U(1)_{L_\mu - L_\tau}$-breaking and Majorana masses. This is because the two-zero minor structure of the neutrino mass matrix and the relations derived from the structure also do not depend on these scales. In the following chapters, we assume that the $U(1)_{L_\mu - L_\tau}$ is broken at the much higher scale (Chap. 6) and electroweak one (Chap. 7). Although the breaking scales in chapter 6 and 7 are different from

each other, the results in this chapter are valid as long as the neutrino sector has the same structure as the minimal gauged $\mathrm{U}(1)_{L_\mu - L_\tau}$ model.

Chapter 6

Non-thermal Leptogenesis in the $U(1)_{L_\mu - L_\tau}$ Model and Sign of Baryon Asymmetry

In the previous chapter, we have shown that the $U(1)_{L_\mu - L_\tau}$ gauge symmetry restricts the neutrino mass matrices and connects the neutrino parameters with the neutrino oscillation parameters. This result brings us to an interesting fact that the sign of the baryon asymmetry generated by leptogenesis is determined by the neutrino oscillation parameters. This is because the neutrino CP phases, which are the origin of lepton asymmetry, are also determined by the oscillation parameters. The relations between the sign of baryon asymmetry and neutrino oscillation parameters have been analyzed in the author's works [42, 44], and [45] has discussed the non-thermal leptogenesis case, as a concrete example, and founded that the minimal gauged $U(1)_{L_\mu - L_\tau}$ model can realize successful baryogenesis and inflation simultaneously.

In this chapter, we discuss non-thermal leptogenesis in the minimal gauged $U(1)_{L_\mu - L_\tau}$ model, following Ref. [45]. This chapter is organized as follows. In section 6.1, we show the sign of the asymmetry parameter in the minimal gauged $U(1)_{L_\mu - L_\tau}$ model, using the results in the previous chapter. In section 6.2, we discuss the leptogenesis model which we assume in this chapter. In section 6.3, we assume the concrete inflation model and discuss the baryon asymmetry generated by non-thermal leptogenesis. Lastly, in section 6.4, we summarize this chapter.

6.1 Asymmetry Parameter of the Right-handed Neutrino Decay

We consider the non-thermal leptogenesis scenario in the minimal gauged $U(1)_{L_\mu - L_\tau}$ model, described in Chap. 5. First, we discuss the CP-violating decay of heavy RHNs in our model. As seen in the previous chapter, the effective light neutrino mass matrix is subject to the two-zero minor conditions, *i.e.*, the inverse of the matrix, $\mathcal{M}_\nu^{-1}$, contains two zeros among its nine

components. These two conditional equations force four free parameters to be dependent on the others, whose values are fixed in the following analysis as the best-fit values, except for θ_{23}. θ_{23} is fixed to be $\theta_{23} = 51^\circ$ to avoid the present constraint on the sum of the neutrino masses. Still, there are several coupling constants undetermined in the Lagrangian in Eq. (5.3). It is then convenient to take λ_α as input parameters; with this choice, all the entries in $\mathcal{M}_D$ and $\mathcal{M}_R$ are uniquely determined in terms of λ_α and the neutrino oscillation parameters. By diagonalizing the mass matrix of the RHNs, the Lagrangian (5.3) can be rewritten as

$$\Delta\mathcal{L} = -\hat{\lambda}_{i\alpha}\hat{N}_i^c(L_\alpha \cdot H) - \frac{1}{2}M_i\hat{N}_i^c\hat{N}_i^c + \text{h.c.} \ , \tag{6.1}$$

where

$$\mathcal{M}_R = \Omega^* \text{diag}(M_1, M_2, M_3)\Omega^\dagger \ , \tag{6.2}$$

$$\hat{N}_i^c = \sum_\alpha \Omega_{\alpha i}^* N_\alpha^c \ , \tag{6.3}$$

$$\hat{\lambda}_{i\alpha} = \Omega_{\alpha i}\lambda_\alpha \ \text{(not summed)} \ , \tag{6.4}$$

where Ω is a unitary matrix and M_i $(i = 1, 2, 3)$ are the mass eigenvalues of $\mathcal{M}_R$. These quantities are, again, uniquely determined in terms of λ_α, for a given set of the neutrino oscillation parameters.

In leptogenesis, the final baryon asymmetry depends on the asymmetry parameters of the decay of RHNs, as shown in Eq. (4.39):[1]

$$\epsilon_i = \frac{\Gamma(\hat{N}_i \to LH) - \Gamma(\hat{N}_i \to \bar{L}H^*)}{\Gamma(\hat{N}_i \to LH) + \Gamma(\hat{N}_i \to \bar{L}H^*)} \ . \tag{6.5}$$

At the leading order, it is computed as

$$\epsilon_i = \frac{1}{8\pi}\frac{1}{\left(\hat{\lambda}\hat{\lambda}^\dagger\right)_{ii}}\sum_{j\neq i}\text{Im}\left\{\left(\hat{\lambda}\hat{\lambda}^\dagger\right)_{ij}^2\right\} f\left(\frac{M_j^2}{M_i^2}\right) \ , \tag{6.6}$$

$$f(x) = \sqrt{x}\left[1 - (1+x)\ln\left(\frac{1+x}{x}\right) + \frac{1}{1-x}\right] \ . \tag{6.7}$$

The significance of the effect of each asymmetry parameter on the resultant lepton asymmetry highly depends on the leptogenesis scenarios. As mentioned in subsection 4.2.2, in the thermal leptogenesis, for instance, the decay of the lightest right-handed neutrino tends to give the dominant contribution to the lepton asymmetry, since the asymmetry generated by the heavier RHNs are washed out—in this case, the final baryon asymmetry, n_B, is essentially proportional to ϵ_1. In the case discussed in the next section, we will consider the decay of all three RHNs.

[1] In the following analysis, we assume that the mass of the $\text{U}(1)_{L_\mu - L_\tau}$ gauge boson, X, is sufficiently large so that the decay modes that contain X in the final state, such as $\hat{N}_i \to \hat{N}_j X$ and $\hat{N}_i \to \nu_j X$, are kinematically forbidden.

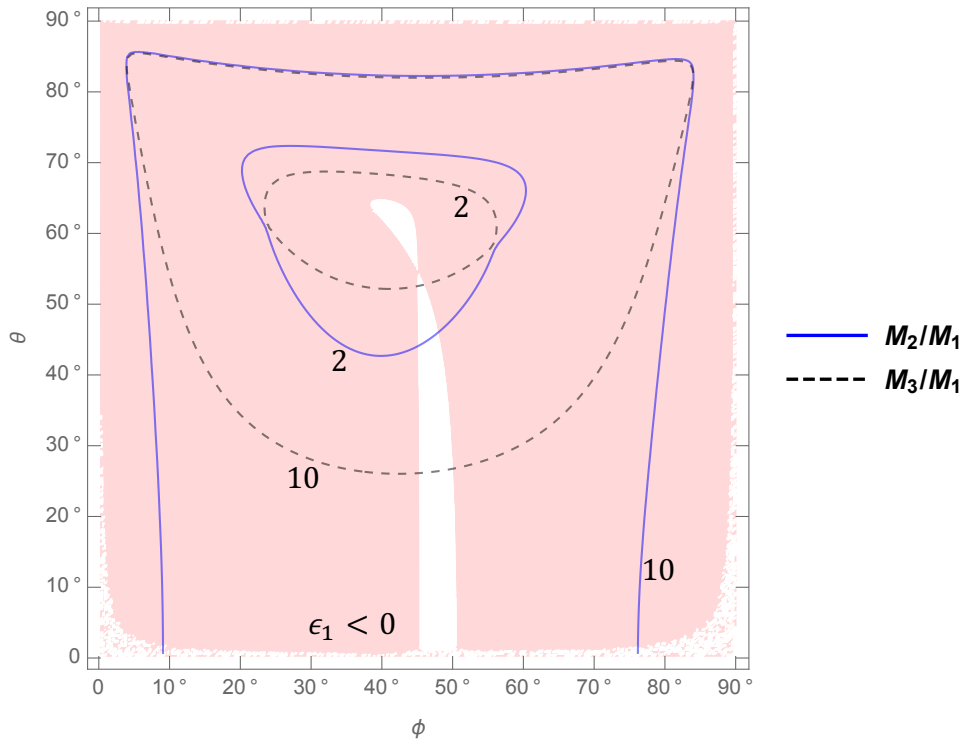

Figure 6.1: The sign of the asymmetry parameter for the lightest right-handed neutrino, ϵ_1, in the ϕ-θ plane for $\delta > \pi$. The shaded region corresponds to a negative value of ϵ_1. For $\delta < \pi$, the sign of ϵ_1 is flipped. The blue solid and gray dashed contour lines show the ratios of the right-handed neutrino masses, M_2/M_1 and M_3/M_1, respectively.

In the present scenario, the sign of ϵ_i, and thus that of the resultant baryon asymmetry as well, for the case of $\delta > \pi$ turns out to be opposite to that for $\delta < \pi$. As can easily be seen from the analytical expressions for the Majorana CP phases $\alpha_{2,3}$ given by Eqs. (5.9), the transformation $\delta \to 2\pi - \delta$ flips the signs of $\alpha_{2,3}$ and leads to $U_{\rm PMNS} \to U^*_{\rm PMNS}$, which then results in $\mathcal{M}_\nu \to \mathcal{M}^*_{\nu_L}$, $\mathcal{M}_R \to \mathcal{M}^*_R$, $\Omega \to \Omega^*$, $\hat{\lambda} \to \hat{\lambda}^*$, and thus $\epsilon_i \to -\epsilon_i$. To obtain the correct sign (positive) for baryon asymmetry in leptogenesis, the generated lepton asymmetry n_L must be negative, because the sphaleron processes predict $n_B/n_L < 0$, shown in Eq. (4.33). This, in particular, indicates that ϵ_1 should be negative when the decay of the lightest RHN predominantly generates lepton asymmetry.

To see the predicted sign of ϵ_1 in our scenario, in Fig. 6.1, we show the sign of the asymmetry parameter for the lightest RHN, ϵ_1. In visualizing this, we parametrize the coupling constants λ_α as

$$(\lambda_e, \lambda_\mu, \lambda_\tau) = \lambda\ (\cos\theta, \sin\theta\cos\phi, \sin\theta\sin\phi)\ , \tag{6.8}$$

with $0 \le \theta, \phi \le \pi/2$ and $\lambda > 0$, and show $\mathrm{sgn}(\epsilon_1)$ in the ϕ-θ plane. Here, we take $\delta > \pi$, as

favored by the neutrino oscillation data [109, 110]. We see that the desirable sign, $\epsilon_1 < 0$, is obtained in almost all the parameter region, except in the small crack around $\phi = 45^\circ$. Notice that, as discussed above, the sign of ϵ_i is flipped under the transformation $\delta \to -\delta + 2\pi$. This has interesting implications for our model; the experimentally favored Dirac CP phase, $\delta > \pi$, generically leads to the correct sign of baryon asymmetry, whilst the experimentally disfavored one, $\delta < \pi$, yields the wrong sign.[2]

We also show in Fig. 6.1 the ratios of the RHN masses, M_2/M_1 and M_3/M_1, in the blue solid and gray dashed contour lines, respectively. It is found that this model predicts a moderately degenerate mass spectrum for RHNs, except near the edge of the plane.

As can be seen from Eq. (4.40), the asymmetry parameters ϵ_i are proportional to λ^2. We have also checked that the magnitude of the asymmetry parameter ϵ_1 is predicted to be $|\epsilon_1|/\lambda^2 \lesssim \mathcal{O}(10^{-4})$ in the typical parameter region in Fig. 6.1, and thus the observed baryon asymmetry can be reproduced for a sufficiently large λ. A more detailed analysis of the thermal leptogenesis in the present scenario is beyond the scope of this letter and will be given elsewhere. In the next section, instead, we study the non-thermal leptogenesis for a minimal inflation scenario in our model.

6.2 Inflation Model

Now we investigate the non-thermal leptogenesis that proceeds through the inflaton decay into RHNs [222–229] in the minimal gauged $\mathrm{U}(1)_{L_\mu - L_\tau}$ model. We identify the $\mathrm{U}(1)_{L_\mu - L_\tau}$ breaking field σ as the inflaton field and assume the following form of the Lagrangian terms for this field [266] (see also Refs. [267–270]):

$$\mathcal{L}_\sigma = \frac{|D_\mu \sigma|^2}{(1 - |\sigma|^2/\Lambda^2)^2} - \kappa(|\sigma|^2 - \langle\sigma\rangle^2)^2 \ , \tag{6.9}$$

where Λ is a parameter with mass dimension one, taken such that $\Lambda > \langle\sigma\rangle$. By using a $\mathrm{U}(1)_{L_\mu - L_\tau}$ gauge transformation, we can always take the direction of the field excursion to be real; in this basis, $\varphi \equiv \sqrt{2}\mathrm{Re}(\sigma)$ plays the role of the inflaton. The pole of the kinetic term guarantees that the effective potential becomes very flat at large field values [271, 272]. The inflaton field is canonically normalized with a change of variable,

$$\frac{\varphi}{\sqrt{2}\Lambda} \equiv \tanh\left(\frac{\widetilde{\varphi}}{\sqrt{2}\Lambda}\right) \ , \tag{6.10}$$

which leads to

$$\mathcal{L}_\sigma = \frac{1}{2}(\partial_\mu \widetilde{\varphi})^2 - V(\widetilde{\varphi}) \ , \tag{6.11}$$

[2]Note that the sign of ϵ_1 obtained here is opposite to that found in Ref. [42]. This difference is attributed to the different choices of the input parameters, especially θ_{23}; in Ref. [42], the value of θ_{23} was taken from the global fit performed in Ref. [265], which was in the first octant—the preferred value of θ_{23} has moved to the second octant since then, as found in Refs. [109, 110], and this change results in a sign flip in ϵ_1.

with

$$V(\widetilde{\varphi}) = \kappa\Lambda^4 \left[\tanh^2\left(\frac{\widetilde{\varphi}}{\sqrt{2}\Lambda}\right) - \left(\frac{\langle\sigma\rangle}{\Lambda}\right)^2 \right]^2 . \tag{6.12}$$

This potential becomes flat for a large field value of $\widetilde{\varphi}$, allowing $\widetilde{\varphi}$ to behave as an inflaton field. As we see below, in the parameter region of interest, $\langle\sigma\rangle \ll \Lambda$; in this case, the VEV of the canonically-normalized field $\widetilde{\varphi}$ is simply given by $\langle\widetilde{\varphi}\rangle \simeq \sqrt{2}\,\langle\sigma\rangle$. Near this minimum, φ differs from $\widetilde{\varphi}$ by a factor of $1 - |\,\langle\sigma\rangle\,|^2/\Lambda^2$, which is very close to unity when $\langle\sigma\rangle \ll \Lambda$—we, thus, ignore this factor in the following expressions.

The scalar potential receives quantum corrections via the couplings of the σ field with the RHNs and the $\mathrm{U}(1)_{L_\mu - L_\tau}$ gauge field.[3] These corrections turn out to be negligible if

$$|h_{e\mu}|^2 + |h_{e\tau}|^2 \ll 4\pi\sqrt{\kappa} , \tag{6.13}$$

$$g_X^2 \ll 4\pi\sqrt{\kappa} , \tag{6.14}$$

where g_X is the $\mathrm{U}(1)_{L_\mu - L_\tau}$ gauge coupling constant. We assume these conditions to be satisfied in the following analysis.

The number of e-folds after the CMB modes left the horizon is defined by

$$N_e \equiv \ln\left(\frac{a_f}{a_k}\right) , \tag{6.15}$$

where a_f is the scale factor at the end of inflation, $a_k \equiv k/H_{\rm inf}$ with $H_{\rm inf}$ the Hubble parameter during inflation, and k is a wave-number which corresponds to the CMB scale. We set k equal to the default pivot scale adopted by the Planck collaboration [25], $k = 0.05\ \mathrm{Mpc}^{-1}$, and evaluate N_e as [273]

$$\begin{aligned} N_e &\simeq 62 + \frac{1}{3}\ln\left(\frac{H_{\rm inf} T_R}{M_P^2}\right) \\ &\simeq 49 + \frac{1}{3}\ln\left(\frac{H_{\rm inf}}{10^{11}\ \mathrm{GeV}}\right) + \frac{1}{3}\ln\left(\frac{T_R}{10^9\ \mathrm{GeV}}\right) , \end{aligned} \tag{6.16}$$

where T_R is the reheating temperature. On the other hand, given the inflaton potential (6.12), we can express N_e in terms of the inflaton field $\widetilde{\varphi}$ as

$$\begin{aligned} N_e &\simeq \int_{\widetilde{\varphi}_f}^{\widetilde{\varphi}_N} \left(\frac{V}{M_P^2 V'}\right) d\widetilde{\varphi} \\ &= \frac{1}{8M_P^2}\left\{ \left(\Lambda^2 - \langle\sigma\rangle^2\right)\ \cosh\left(\frac{2\widetilde{\varphi}}{\sqrt{2}\Lambda}\right) - 4\,\langle\sigma\rangle^2\ \ln\left[\sinh\left(\frac{\widetilde{\varphi}}{\sqrt{2}\Lambda}\right)\right]\right\}\Bigg|_{\widetilde{\varphi}_f}^{\widetilde{\varphi}_N} , \end{aligned} \tag{6.17}$$

where $\widetilde{\varphi}_N$ and $\widetilde{\varphi}_f$ are the field values when the fluctuations observed in the CMB are created and inflation ends, respectively. In the present model, inflation ends when $|V'' M_P^2/V| \sim 1$ and

[3] The radiative corrections by the self-coupling κ are insignificant as long as κ is perturbative.

it turns out that the corresponding field value $\widetilde{\varphi}_f$ is in general much smaller than $\widetilde{\varphi}_N$. In this case, we can obtain an approximate solution of Eq. (6.17) with respect to $\widetilde{\varphi}_N$, by noting that $\langle\sigma\rangle \ll \Lambda$ and that the first term dominates the second term in Eq. (6.17) for $\widetilde{\varphi}_N > \Lambda$:

$$\widetilde{\varphi}_N \simeq \frac{\Lambda}{\sqrt{2}} \ln\left(\frac{16 N_e M_P^2}{\Lambda^2}\right) . \tag{6.18}$$

We then evaluate the slow-roll parameters as

$$\epsilon \equiv \frac{M_P}{2}\left(\frac{V'}{V}\right)^2 \simeq \left(\frac{\Lambda}{2N_e M_P}\right)^2 , \tag{6.19}$$

$$\eta \equiv \frac{V''}{V} M_P^2 \simeq -\frac{1}{N_e} , \tag{6.20}$$

as well as the scalar spectral index n_s and the tensor-to-scalar ratio r as

$$n_s = 1 - 6\epsilon + 2\eta \simeq 1 - \frac{2}{N_e} , \tag{6.21}$$

$$r = 16\epsilon \simeq \left(\frac{2\Lambda}{M_P N_e}\right)^2 \simeq 3 \times 10^{-8} \times \left(\frac{\Lambda}{10^{16}\ \mathrm{GeV}}\right)^2 \left(\frac{N_e}{50}\right)^{-2} . \tag{6.22}$$

From Eq. (6.21), we see that $n_s \simeq 0.96$ for $N_e \simeq 50$; this is compatible with the Planck best-fit value $n_s = 0.9649 \pm 0.0042$ [25]. On the other hand, the predicted value of the tensor-to-scalar ratio is much smaller than the Planck limit [25], $r_{0.002} < 0.10$ (95%, TT,TE,EE+lowE+lensing) at pivot scale 0.002 Mpc^{-1}, and unable to be probed in the next-generation CMB experiments.

The power spectrum of the curvature perturbation P_ζ is

$$P_\zeta = \frac{V^3}{12\pi^2 M_P^6 V'^2} \simeq \frac{\kappa N_e^2 \Lambda^2}{6\pi^2 M_P^2} .$$

With the measured value of the power spectrum, $P_\zeta \simeq (2.10 \pm 0.03) \times 10^{-9}$ [25], we determine the coupling κ:

$$\kappa \simeq 3 \times 10^{-6} \times \left(\frac{N_e}{50}\right)^{-2} \left(\frac{\Lambda}{10^{16}\ \mathrm{GeV}}\right)^{-2} . \tag{6.23}$$

We then obtain the Hubble parameter during inflation and the inflaton mass as

$$H_{\mathrm{inf}} \simeq \frac{\Lambda^2}{M_P}\sqrt{\frac{\kappa}{3}} \simeq 4 \times 10^{10}\ \mathrm{GeV} \times \left(\frac{\Lambda}{10^{16}\ \mathrm{GeV}}\right)\left(\frac{N_e}{50}\right)^{-1} , \tag{6.24}$$

$$m_\varphi \simeq 2\sqrt{\kappa}\,\langle\sigma\rangle \simeq 3 \times 10^{10}\ \mathrm{GeV} \times \left(\frac{\langle\sigma\rangle}{10^{13}\ \mathrm{GeV}}\right)\left(\frac{\Lambda}{10^{16}\ \mathrm{GeV}}\right)^{-1}\left(\frac{N_e}{50}\right)^{-1} . \tag{6.25}$$

Also, the mass of the $\mathrm{U}(1)_{L_\mu - L_\tau}$ gauge boson is given by

$$m_X \simeq \sqrt{2} g_X \langle\sigma\rangle . \tag{6.26}$$

For $\Lambda \gg \langle\sigma\rangle$, the potential height at the origin is much lower than the potential energy during inflation. In this case, the $\mathrm{U}(1)_{L_\mu - L_\tau}$ gauge symmetry would be restored during the (p)reheating process [274]. The subsequent symmetry breaking then leads to the formation of a cosmic-string network. Throughout cosmic history, oscillating string loops in the network emit gravitational waves, yielding a stochastic background of gravitational waves. The most stringent limits on this signature are imposed by pulsar timing arrays (PTAs), such as the Parkes PTA [275, 276], the European PTA [277], and the North American Nanohertz Observatory for Gravitational Waves (NANOGrav) [278, 279]. With these data, as well as the theoretical predictions given in Refs. [280, 281], one obtains $G\mu \lesssim \mathcal{O}(10^{-11})$, where μ is the mass per unit length of the cosmic string. For the Bogomol'nyi-Prasad-Sommerfield strings, which correspond to the case with $m_\varphi = m_X$, we have $\mu = 2\pi \langle\sigma\rangle^2$, for which the above limit leads to $\langle\sigma\rangle \lesssim 2 \times 10^{13}$ GeV. This bound slightly depends on the choice of parameters, κ and g_X, through the change in μ. For example, in the limit $m_X \gg m_\varphi$, we have $\mu \to 2\pi \langle\sigma\rangle^2 / \ln(m_X/m_\varphi)$ [282], with which we obtain a weaker bound on $\langle\sigma\rangle$ than the aforementioned one. Future interferometric gravitational-wave detectors are expected to be sensitive to a much smaller value of $G\mu$; for example, the Laser Interferometer Space Antenna (LISA) can probe the gravitational waves emitted by cosmic strings with $G\mu \gtrsim 10^{-17}$ [283], which corresponds to $\langle\sigma\rangle \gtrsim 2 \times 10^{10}$ GeV. Moreover, the NANOGrav collaboration analyzed 12.5 years pulsar timing data and reported strong evidence for a stochastic common-spectrum process which can be interpreted as a gravitational wave (GW) with frequency $f \sim 1/\mathrm{yr}$ [284]. Various works (for example, Refs. [285–288]) explore the possibility that the above GW is originated from cosmic strings formed by breaking of U(1) gauge symmetry, and the relation between the NANOGrav results and lentogenesis in the minimal gauged $\mathrm{U}(1)_{L_\mu - L_\tau}$ model will be study in future work [289].

6.3 Non-thermal Leptogenesis in the Minimal Gauged $\mathrm{U}(1)_{L_\mu - L_\tau}$ Model

After inflation ends, the Universe is reheated through the inflaton decay. In the following discussions, we consider the case where the inflaton decays dominantly into RHNs; more specifically, we assume that the quartic coupling $\lambda_{H\sigma}|H|^2|\sigma|^2$ is negligibly small and that $m_\varphi < 2m_{Z'}$.[4] The total decay rate of inflaton in this case is given by

$$\Gamma_\varphi = \sum_{i,j} \frac{m_\varphi}{32\pi} \left[1 - \frac{2(M_i^2 + M_j^2)}{m_\varphi^2} + \frac{(M_i^2 - M_j^2)^2}{m_\varphi^4}\right]^{\frac{1}{2}} \times \left[\mathrm{Re}\left(\hat{h}_{ij}\right)^2 \left\{1 - \frac{(M_i + M_j)^2}{m_\varphi^2}\right\} + \mathrm{Im}\left(\hat{h}_{ij}\right)^2 \left\{1 - \frac{(M_i - M_j)^2}{m_\varphi^2}\right\}\right] , \quad (6.27)$$

[4] We can instead assume that g'_Z is negligibly small. In either case, we can always find a value of g'_Z that satisfies the condition (6.14).

where $\hat{h}_{ij} \equiv \sum_{\alpha,\beta} h_{\alpha\beta}\Omega_{\alpha i}\Omega_{\beta j}$. As it turns out later, the couplings $\hat{h}_{ij}$ are perturbative and $\Gamma_\varphi \ll H_{\rm inf}$ in the parameter region of our interest. We then estimate the reheating temperature as

$$T_R \simeq \left(\frac{90}{\pi^2 g_*}\right)^{\frac{1}{4}} \sqrt{\Gamma_\varphi M_P} \ , \tag{6.28}$$

where $g_* = 106.75$ is the relativistic degrees of freedom at the end of reheating.

If $T_R \lesssim 0.1 M_1$, the produced RHNs are out of thermal equilibrium,[5] and their subsequent non-thermal decay generates a lepton asymmetry. In this work, we focus on such a parameter region where this condition is satisfied and leptogenesis takes place non-thermally. For a higher reheating temperature, we need to take account of the inverse decay and scattering processes with the thermal plasma; a detailed analysis for this case will be given in the author's future work.

As shown in Eq. (4.49), the baryon asymmetry generated in the non-thermal leptogenesis is computed

$$Y_B \equiv \frac{n_B}{s} = -\frac{28}{79} \cdot \frac{3T_R}{4m_\varphi} \cdot (2\epsilon_{\rm eff}) \ , \tag{6.29}$$

where $\epsilon_{\rm eff}$ is the effective asymmetry parameter defined by the averaged asymmetry parameter over the RHN decays:

$$\epsilon_{\rm eff} \equiv \frac{1}{2} \sum_{i \le j} (\epsilon_i + \epsilon_j) {\rm Br}(\varphi \to N_i N_j) \ . \tag{6.30}$$

As seen in Eq. (6.29), to obtain $Y_B > 0$, we need $\epsilon_{\rm eff} < 0$.

Now we show the predictions of our model. Let us begin with briefly summarizing the input parameters in this model. As discussed in Sec. 5.1, there are nine parameters in the light neutrino sector, among which four parameters are determined as functions of the other five parameters through the two-zero minor conditions $[\mathcal{M}_\nu^{-1}]_{\mu\mu} = [\mathcal{M}_\nu^{-1}]_{\tau\tau} = 0$ as in Eqs. (5.7) and (5.8). We then fix four of the remaining five parameters using the neutrino oscillation data as in Tab. 2.2 and θ_{23} to be 51° for the avoidance of the present constraint on the sum of the neutrino masses. As a result, there is no free parameter in the light neutrino sector. For the input parameters in the RHN and inflation sectors, we take:

- λ, θ and ϕ in Eq. (6.8) for the Dirac Yukawa couplings
- VEV of the ${\rm U}(1)_{L_\mu - L_\tau}$-breaking Higgs field, $\langle\sigma\rangle$

[5] We, however, note that the temperature of the Universe during reheating is in general larger than T_R [290, 291] and thus RHNs may be produced from the thermal bath even if $T_R \lesssim 0.1 M_1$. In the following analysis, we neglect their contribution just for simplicity.

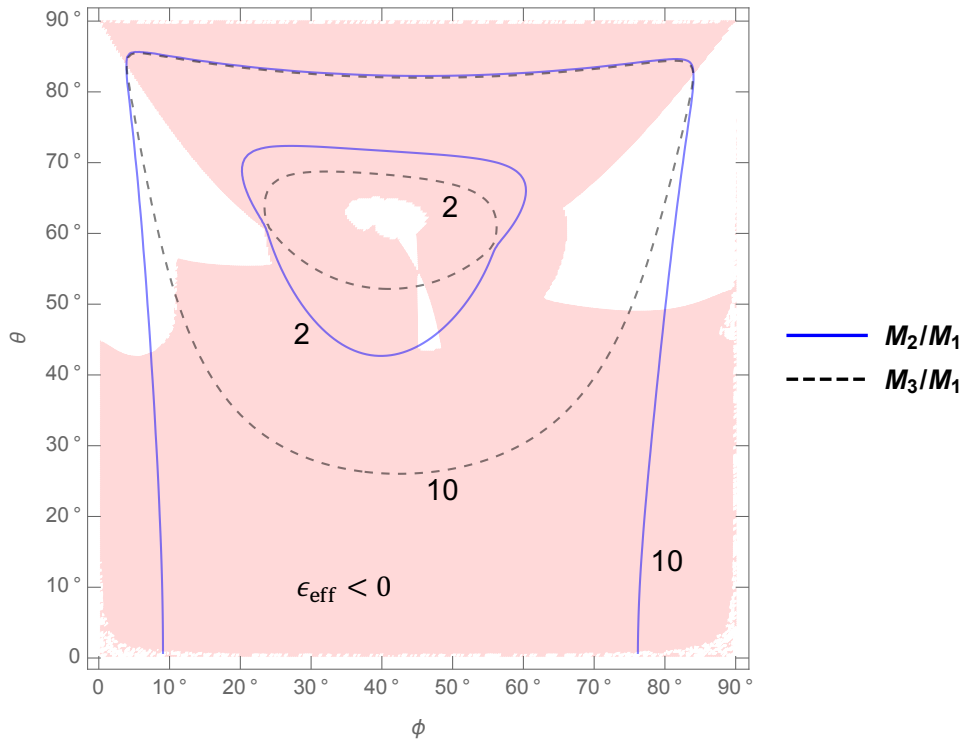

Figure 6.2: The ϕ-θ plane for $\lambda = 0.01$, $\langle\sigma\rangle = 10^{13}$ GeV, and $\Lambda = 10^{16}$ GeV, exhibiting the area where $\epsilon_{\rm eff} < 0$ in the pink shaded region. The blue solid (gray dashed) contours show the ratio M_2/M_1 (M_3/M_1).

- Λ in Eq. (6.9)

Once the values of λ, θ and ϕ are chosen, together with the neutrino oscillation parameters, we can uniquely determine the heavy RHN mass matrix as discussed in Sec. 6.1, as well as the couplings $h_{\alpha\beta}$ for a given value of $\langle\sigma\rangle$.[6] The parameter κ in Eq. (6.23) and the e-folding number N_e are determined by solving Eq. (6.16), Eq. (6.24), Eq. (6.25), and Eq. (6.28) for a given set of the above input parameters. Here, we require $N_e \geq 46$ in order to satisfy the constraint on the spectral index n_s within 2σ. We do not specify the value of the $\mathrm{U}(1)_{L_\mu - L_\tau}$ gauge coupling, g_X, as it does not affect the following analysis—we just assume that g_X is taken to be in the range $\sqrt{\kappa/2} < g_X \ll (16\pi^2\kappa)^{1/4}$ to satisfy $m_\varphi < 2m_X$ and the condition (6.14). We can always find such a g_X for a perturbative value of κ.

The pink shaded region on the ϕ-θ plane in Fig. 6.2 shows the area in which $\epsilon_{\rm eff}$ is predicted to be negative, corresponding to $Y_B > 0$, for $\lambda = 0.01$, $\langle\sigma\rangle = 10^{13}$ GeV, and $\Lambda = 10^{16}$ GeV. We also show the ratios of the RHN masses, M_2/M_1 and M_3/M_1, by the blue solid and gray dashed contours, respectively, which are identical to the ones shown in Fig. 6.1. Comparing Figs. 6.1

[6] We note that in this case $h_{\alpha\beta} \propto \langle\sigma\rangle^{-1}$.

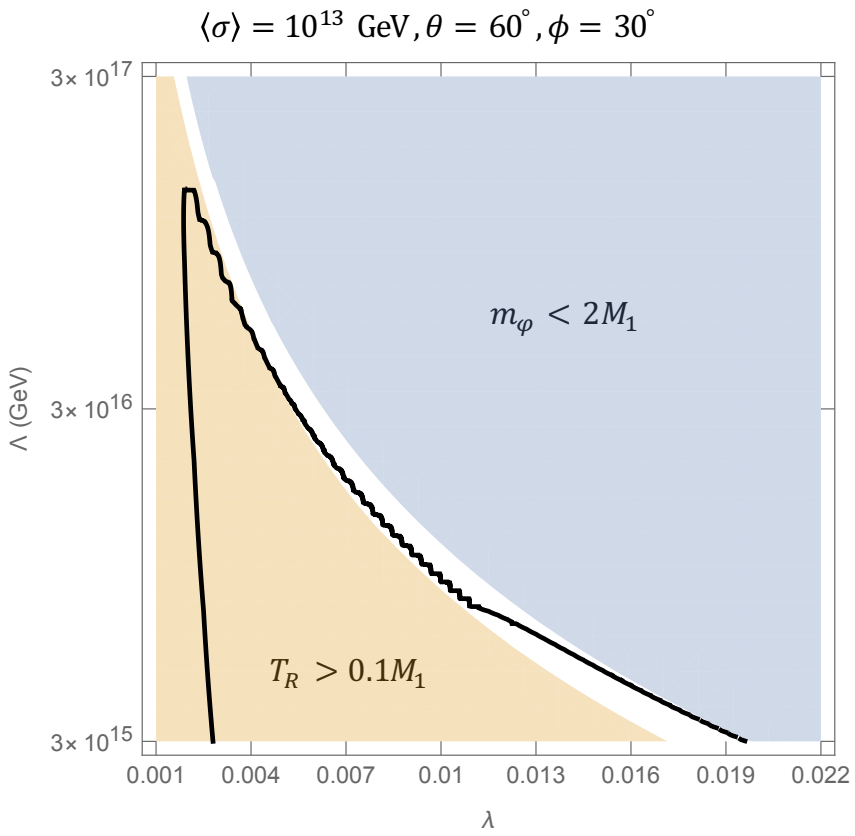

Figure 6.3: The λ-Λ plane for $\theta = 60°$, $\phi = 30°$, and $\langle\sigma\rangle = 10^{13}$ GeV. In the blue shaded region, $m_\varphi < 2M_1$ and thus the decay of inflaton into right-handed neutrinos is kinematically forbidden. In the orange shaded region, $T_R > 0.1M_1$, for which our analysis for the non-thermal leptogenesis is inappropriate. The black solid curve corresponds to $Y_B \simeq 8.7 \times 10^{-11}$ [25].

and 6.2, we see that the contribution of the heavier RHNs to the effective asymmetry parameter is sizable—in a part of the region on the ϕ-θ plane, $\epsilon_1 < 0$ but $\epsilon_{\rm eff} > 0$, and vice versa. It is also found that $\epsilon_{\rm eff} < 0$ is realized in a fairly large fraction of the parameter space.

Now we show in Fig. 6.3 the allowed parameter region of this model on the λ-Λ plane for $\theta = 60°$, $\phi = 30°$, and $\langle\sigma\rangle = 10^{13}$ GeV. This value of $\langle\sigma\rangle$ is chosen such that the cosmic-string bound discussed in Sec. 6.2 is evaded. In the blue shaded region, $m_\varphi < 2M_1$ and thus the decay of inflaton into RHNs is kinematically forbidden. In the orange shaded region, $T_R > 0.1M_1$, for which our analysis for the non-thermal leptogenesis is inappropriate. The black solid curve corresponds to the observed baryon asymmetry $Y_B \simeq 8.7 \times 10^{-11}$ [25]. We find that the latter can be reproduced within the allowed parameter region indicated by the white strip between the blue and orange areas. The mass scale of the inflaton and RHNs in this case is found to be $\mathcal{O}(10^{10})$ GeV, and the reheating temperature is $\mathcal{O}(10^8)$ GeV. Over the parameter space shown in this figure, the couplings $h_{\alpha\beta}$ are $\mathcal{O}(10^{-3})$ and thus perturbative and compatible with the condition (6.13). The value of the spectral index, n_s, is predicted to be $n_s \simeq 0.96$. This

prediction can be tested in future CMB experiments such as CMB-S4 [292, 293].

The shape of the black solid curve in Fig. 6.3 can be understood as follows. In the bulk region below this curve, Y_B is predicted to be larger than the observed value. To see the change of Y_B in this region, we first fix λ and examine the dependence of Y_B on Λ. In this case, the right-handed neutrino masses are fixed and thus the couplings $h_{\alpha\beta}$ are also fixed. This means that the inflaton decay width, Γ_φ, is determined solely by the inflaton mass, and approximately goes as $\propto m_\varphi \propto \Lambda^{-1}$ in the bulk region. It then follows that T_R/m_φ, and thus Y_B as well, gets larger for a larger Λ, roughly scales as $\propto \Lambda^{1/2}$. Just below the blue shaded region, however, the inflaton decay width is highly suppressed by the kinematic factor, resulting in a suppression in the reheating temperature and therefore in Y_B. As a result, we can find a correct value of Y_B below the blue shaded area. Next, we fix Λ and consider the dependence of Y_B on λ. In this case, as λ decreases, the right-handed neutrino masses, and thus $h_{\alpha\beta}$ as well, get smaller. This leads to a lower reheating temperature. The asymmetric parameters ϵ_i in Eq. (6.6) are also suppressed for a smaller λ. Hence, Y_B decreases as λ gets smaller ($Y_B \sim \lambda^4$) and at a certain point ($\lambda \simeq 0.002$) it coincides with the observed value, $Y_B \simeq 8.7 \times 10^{-11}$ [25].

A large value of Y_B in the bulk region below the black curve would be depleted once we include the thermalization of the RHNs and the wash-out of the lepton asymmetry by the thermal bath. This implies that we may find other parameter regions that are compatible with the observed baryon asymmetry, with the thermal effect taken into account. This possibility will be explored in the author's future work.

If we take a smaller value of $\langle\sigma\rangle$ than that in Fig. 6.3, we need a smaller Λ in order to keep m_φ larger than $2M_1$ (see Eq. (6.25)). On the other hand, the reheating temperature is larger for a smaller $\langle\sigma\rangle$ since $h_{\alpha\beta}$ increase as $\propto \langle\sigma\rangle^{-1}$, as noted in footnote 6, and therefore the boundary of the $T_R > 0.1M_1$ region gets closer to the $m_\varphi < 2M_1$ region; namely, we need $m_\varphi \simeq 2M_1$ to suppress the inflaton decay width kinematically so that the non-thermal condition is satisfied. As a result, the allowed parameter region is considerably narrowed down, though the observed value of the baryon asymmetry is still reproduced along the border of the kinematic bound.

All in all, we conclude that the non-thermal leptogenesis can be realized successfully in the framework of the minimal gauged $\mathrm{U}(1)_{L_\mu - L_\tau}$ model, though the allowed parameter space is rather restricted. Our inflation model can be tested in the future with a precise measurement of n_s in CMB experiments, as well as through the search for the cosmic string signatures in gravitational-wave experiments such as LISA.

6.4 Summary and Discussions of Chapter 6

In this chapter, we have discussed the non-thermal leptogenesis in the minimal gauged $\mathrm{U}(1)_{L_\mu - L_\tau}$ model as an example of interesting phenomenology in the case where the $\mathrm{U}(1)_{L_\mu - L_\tau}$ are broken at high energy scale. We regard the $\mathrm{U}(1)_{L_\mu - L_\tau}$-breaking scalar as inflaton and consider the Lagrangian in Eq. (6.9) for this field and then found that this potential can offer successful inflation that is consistent with the CMB observation. By requiring that the measured value of the power spectrum be reproduced, we determine the value of the inflaton self-coupling κ as a function of other input parameters, for which we take Λ and $\langle\sigma\rangle$ in Eq. (6.9).

As discussed in the previous chapter, the minimal gauged $\mathrm{U}(1)_{L_\mu - L_\tau}$ model has nine parameters in the light neutrino sector, and among them, four ones are determined by the other five ones because of the two-zero minor structure of the neutrino mass matrix. Also, the structure of the RHN mass matrix is determined by fixing three parameters for the Dirac Yukawa couplings, λ_α ($\alpha = e, \mu, \tau$) [42]. Our model, therefore, has five free parameters, Λ, $\langle\sigma\rangle$, and λ_α ($\alpha = e, \mu, \tau$).

We then study the non-thermal leptogenesis in our model, focusing on the case where the inflaton decays only into RHNs, and these RHNs are never thermalized after the Universe is reheated. The successive decay of RHNs then generates a lepton asymmetry, which is converted to a baryon asymmetry through sphaleron processes. We find that the observed value of baryon asymmetry can be explained in this scenario. In particular, the correct sign of baryon asymmetry can be obtained in a wide range of parameter space. We recall that our choice of $\delta > \pi$, which is favored by the present neutrino oscillation data [109, 110, 294], was crucial in obtaining this result; if we instead chose $\delta < \pi$, we would obtain a wrong sign for the baryon asymmetry in most parameter regions.

Our analysis shows that baryon asymmetry tends to be overproduced in the non-thermal leptogenesis scenario. This observation gives a strong motivation for a more detailed study on leptogenesis in this model with the effect of the thermal plasma taken into account—we shall return to this issue in future work [289].

Chapter 7

Secluded dark matter in the $U(1)_{L_\mu - L_\tau}$ model and indirect detection by neutrino telescope

In the previous chapters, we have focused on the $U(1)_{L_\mu - L_\tau}$ gauge symmetry itself and discussed the neutrino mass structure in chapter 5 and implication for leptogenesis in chapter 6. In the previous chapter, we have assumed that the scale of the $U(1)_{L_\mu - L_\tau}$-breaking is much higher than the electroweak scale. On the other hand, we focus on the $U(1)_{L_\mu - L_\tau}$-breaking at the electroweak scale in this chapter.

We have seen that the WIMP dark matter, which is one of the strongest candidates, has two kinds of regimes, namely, the usual WIMP regime and secluded one, in chapter 3. WIMP DM can be produced naturally through the thermal freeze-out mechanism and has been discussed in various previous works. For several decades, lots of experiments and observations have tried to discover WIMP DM. However, no one detects it so far, and scattering and annihilation cross sections between DM and SM particles are severely constrained, as shown in section 3.3. The secluded DM, which is reviewed in section 3.2, is one possibility to relax the severe direct detection constraints on the DM-nucleon scattering cross section because the DM annihilation cross section depends only on the coupling between DM and mediator. Therefore, scattering cross section can be small while keeping large annihilation cross section.

$U(1)_{L_\mu - L_\tau}$ gauge symmetry and corresponding gauge boson play important roles in the secluded WIMP DM scenario. First, if DM has $U(1)_{L_\mu - L_\tau}$ charge, an accidental symmetry guarantees the DM stability even after spontaneous symmetry breaking of $U(1)_{L_\mu - L_\tau}$ gauge symmetry. Therefore, we do not have to introduce Z_2 discrete symmetry by hand for DM stability. Second, the $U(1)_{L_\mu - L_\tau}$ gauge boson has no coupling to electron and quarks at tree level, and thus, not only the gauge boson can avoid experimental searches, but also the $U(1)_{L_\mu - L_\tau}$ charged DM can do severe constraints from direct detection experiments.

This chapter is dedicate to the $U(1)_{L_\mu - L_\tau}$-charged DM and indirect detection by neutrino observation experiments, and this discussion is based on Ref. [35]. In Sec. 7.1, we summarize a history of DM in the $U(1)_{L_\mu - L_\tau}$ models. In previous works, many attempts have been made to explain the relic abundance of $U(1)_{L_\mu - L_\tau}$-charged DM and muon anomalous magnetic moment simultaneously. We explain the previous works and the difference between them and this thesis. In Sec. 7.2, we show the $U(1)_{L_\mu - L_\tau}$-charged DM model. In Sec. 7.3, we discuss DM physics in the $U(1)_{L_\mu - L_\tau}$ model. First, fixing the $U(1)_{L_\mu - L_\tau}$ gauge boson mass and gauge coupling constant to explain the muon $g-2$ discrepancy, we explore whether the observed abundance of DM can be produced in the thermal freeze-out scenario. Then we also investigate experimental and astrophysical constraints. As revealed later, although the mediator has no coupling to the electrons and quarks, the direct detection experiments give strong constraints on the $U(1)_{L_\mu - L_\tau}$-charged DM, and this DM is required to have sub-GeV mass. In Sec. 7.4, we discuss the possibility of DM indirect detection by neutrino observation experiments, such as Super-Kamiokande (SK) and Hyper-Kamiokande (HK).

7.1 History of $U(1)_{L_\mu - L_\tau}$ Charged Dark Matter

Before discussing $U(1)_{L_\mu - L_\tau}$ charged DM and indirect detection by neutrino observation experiments, in this section, we briefly summarize DM in $U(1)_{L_\mu - L_\tau}$ models which have discussed in the previous researches.

First discussion of $U(1)_{L_\mu - L_\tau}$ charged DM has appeared in the context of the muon $g-2$ in Ref. [295], and the DM relic abundance and contribution of $U(1)_{L_\mu - L_\tau}$ gauge boson to the muon $g-2$ have been mentioned briefly. After that, in Ref. [296], the $U(1)_{L_\mu - L_\tau}$ charged DM model which explains the muon $g-2$ discrepancy simultaneously has been discussed in detail. Refs. [296, 297] have explored the possibility of direct, indirect, and collider experiments, and the excess of positron flux in cosmic rays reported by HEAT, PAMELA, and Fermi-LAT collaborations have been explained. These works assume that DM and $U(1)_{L_\mu - L_\tau}$ gauge boson has GeV$\sim$TeV scale masses. After these works, Ref. [55] has focused on contributions of the $U(1)_{L_\mu - L_\tau}$ gauge boson to neutrino trident production process ($\nu_\mu N \to \nu_\mu N \mu^+ \mu^-$) and obtained the constraints on the $U(1)_{L_\mu - L_\tau}$ gauge boson by analyzing the results of CHARM-II [53] and CCFR [54]. Then the $U(1)_{L_\mu - L_\tau}$ gauge boson with more than GeV scale mass has been excluded as a new particle which explains the muon $g-2$ discrepancy.

After the above analysis of the constraint from neutrino trident production, the works related to the $U(1)_{L_\mu - L_\tau}$ charged DM are roughly classified into three types :

- The $U(1)_{L_\mu - L_\tau}$ gauge coupling constant which explains the muon $g-2$ discrepancy is too small to realize the observed relic abundance of DM. When DM mass is close to a half of

fields	$SU(2)_L$	$U(1)_Y$	$U(1)_{L_\mu - L_\tau}$
(L_e, L_μ, L_τ)	**2**	$-1/2$	$(0, +1, -1)$
(e_R, μ_R, τ_R)	**1**	$-1/2$	$(0, +1, -1)$
ψ	**1**	0	q_ψ

Table 7.1: Charge assignment

the $U(1)_{L_\mu - L_\tau}$ gauge boson mass, the annihilation cross section of DM is enhanced by the Breit-Wigner enhancement, and the $U(1)_{L_\mu - L_\tau}$ gauge boson can be a mediator [298].

- To obtain enough annihilation cross section, other mediators are introduced, and the $U(1)_{L_\mu - L_\tau}$ gauge boson is devoted to explaining the muon $g-2$ anomaly [62, 299–301].
- Abandoning the explanation of the muon $g-2$ discrepancy, contributions of the $U(1)_{L_\mu - L_\tau}$ gauge boson to other BSM physics are studied. For example, relations with B meson anomaly [302–307], excess in gamma-ray signal near the Galactic center [308], and positron excess observed by AMS-02 [307] are explored.

In this chapter, both the relic abundance of $U(1)_{L_\mu - L_\tau}$ charged DM and explanation of the muon $g-2$ discrepancy are realized without other mediators and Breit-Wigner enhancement, and this point is one of the novelties of this thesis.

7.2 Model

In this section, we show the $U(1)_{L_\mu - L_\tau}$ charged Dirac fermion DM model, based on Ref. [35]. This model is based on an $SU(3)_c \times SU(2)_L \times U(1)_Y \times U(1)_{L_\mu - L_\tau}$ gauge theory. We introduce a SM singlet Dirac fermion DM ψ that carries an $L_\mu - L_\tau$ charge q_ψ in the unit of the muon (tau) charge being $+1(-1)$. As mentioned in subsection 2.1.1, the above Dirac fermion DM produces no gauge anomaly because it transforms vector-like under $U(1)_{L_\mu - L_\tau}$ gauge transformation. The charge assignment for DM and leptons is summarized in Table 7.1. In this model, DM has much larger $U(1)_{L_\mu - L_\tau}$ charge than the SM fields, and then, ψ must appear with $\bar{\psi}$ in the Lagrangian to preserve the invariance of the $U(1)_{L_\mu - L_\tau}$ gauge symmetry. Therefore, even after the spontaneous symmetry breaking of the $U(1)_{L_\mu - L_\tau}$, an accidental global U(1) symmetry of which only DM has non-zero charge remains. [1] Moreover, because of the observations of neutrino oscillation by various experiments, at least two mass eigenstates of the neutrinos are undoubtedly massive, and thus the neutrino sector should be extended. There are many previous works in

[1] If there are scalar fields with $U(1)_{L_\mu - L_\tau}$ charge q_ψ or $q_\psi \pm 1$ in this model, Yukawa interaction terms between DM and SM leptons can be formed. In this case, there is no symmetry which guarantees the DM stability. Therefore, we assume that such scalar fields do not exist in this model.

which the relation between $\mathrm{U}(1)_{L_\mu - L_\tau}$ gauge symmetry and neutrino masses is discussed, for example, Refs. [42–44, 243–245, 247]. However, neutrino masses is much lighter than the other particles in the model, and they are negligible and irrelevant in the following discussion about DM physics. Therefore, we assume that the neutrino masses can be approximated massless.

The model Lagrangian is given by

$$\begin{aligned}\mathcal{L} = \mathcal{L}_{\mathrm{SM}} &- g_X X_\lambda \left(\bar{\mu}\gamma^\lambda \mu - \bar{\tau}\gamma^\lambda \tau + \bar{\nu}_{\mu L}\gamma^\lambda \nu_{\mu L} - \bar{\nu}_{\tau L}\gamma^\lambda \nu_{\tau L} \right) \\ &- \frac{1}{4} X_{\rho\lambda} X^{\rho\lambda} + \frac{1}{2} m_X^2 X_\lambda X^\lambda - \frac{\epsilon}{2} X_{\rho\lambda} B^{\rho\lambda} \\ &+ \bar{\psi}\left(i\partial\!\!\!/ - m_\psi \right)\psi - q_\psi g_X X_\lambda \bar{\psi}\gamma^\lambda \psi \ , \end{aligned} \tag{7.1}$$

Here, we assume that the mass of X is generated by the Higgs mechanism. However, since the origin of the mass and scalar sector are irrelevant to our discussion about DM physics, we do not specify them. Now, we have five free parameters, m_X, g_X, m_ψ, q_ψ and ϵ in the model. In this paper, we will consider q_ψ as a free parameter that takes an arbitrary value unless it violates unitarity. As will see in section 7.3, a large q_ψ is indeed required to explain the observed DM abundance. Such a large q_ψ is allowed phenomenologically, but it may be unnatural from the theoretical perspective. We do not discuss in this paper any UV origin of the large charge hierarchy between DM and muon, but one of possible UV extensions includes the addition of another dark U(1) gauge symmetry that is coupled only to DM. If DM is not charged under the $\mathrm{U}(1)_{L_\mu - L_\tau}$ symmetry and there is a small mixing between two U(1)'s, we will be able to apparently realize the large charge hierarchy.

We further assume the kinetic mixing ϵ of X and the hypercharge gauge field B is vanishing at some high scale. Nonetheless, as shown in subsection 2.1.2, the gauge kinetic mixing between X and the SM photon appears in this model, and then X couples to the electromagnetic current as follows :

$$\mathcal{L}_{X,\mathrm{EM}} = \epsilon_A e X_\mu J^\mu_{\mathrm{EM}} \ . \tag{7.2}$$

This interaction contributes to the elastic scattering process of the DM with the nucleon and electron, and the constraints from the direct detection experiments are given, as discussed in subsection 7.3.2.

This model has four free parameters, the mass of the $\mathrm{U}(1)_{L_\mu - L_\tau}$ gauge boson m_X, gauge coupling constant g_X, DM mass m_ψ, and $\mathrm{U}(1)_{L_\mu - L_\tau}$ charge of DM q_ψ. Among them, we set m_X and g_X so that the $\mathrm{U}(1)_{L_\mu - L_\tau}$ gauge boson explain the discrepancy of the muon $g-2$ [50] :

$$\Delta a_\mu = a_\mu^{\mathrm{exp}} - a_\mu^{\mathrm{SM}} = (261 \pm 79) \times 10^{-11} \ . \tag{7.3}$$

From Eq. (2.16), the parameter region in $m_X - g_X$ plane where the above discrepancy can be explain is given by Fig. 7.1. As explained in subsection 2.1.3, the favored region by the muon

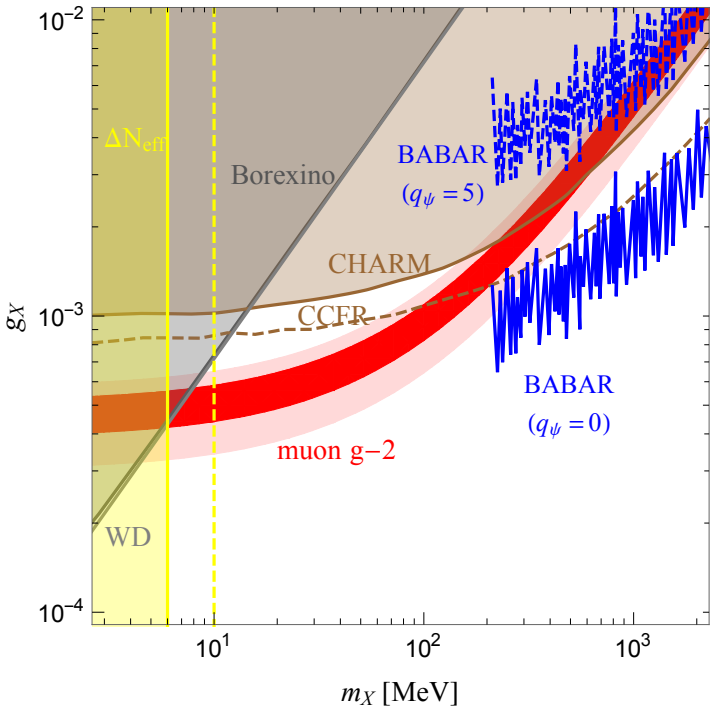

Figure 7.1: Constraints on the $U(1)_{L_\mu - L_\tau}$ boson and muon $g-2$ favored region. Dark (light) red area corresponds to the $1\sigma(2\sigma)$ favored region of the muon $g-2$, respectively.

$g-2$ at $1\sigma(2\sigma)$ level is shown in dark (light) red area, and the experimental, cosmological, and astrophysical constraints correspond to the various colored lines and areas. In the model with $U(1)_{L_\mu - L_\tau}$ charged DM, the bound from the BABAR experiment is different from the tha case without DM. The dashed blue line corresponds to the constraint when the Dirac fermion DM has five times larger $U(1)_{L_\mu - L_\tau}$ charge. As mentioned in subsection 2.1.3, BABAR experiment constraints on X by the search for $e^+e^- \to \mu^+\mu^- X$ process with a subsequent decay $X \to \mu^+\mu^-$. Therefore, as q_ψ is much larger than the charge of the muon, the branching fraction of $X \to \mu^+\mu^-$ decay is much smaller than the case for $q_\psi = 0$, and then the limit by BABAR experiment is weaker. We show in the figure the BABAR limit for $q_\psi = 5$ with the dashed blue line, assuming DM is much lighter than X. Hereafter, we focus on the parameter space where the muon $g-2$ is explained within 2σ while avoiding the other constraints from the BABAR, CHARM, Borexino experiments, WD cooling, and $\Delta N_{\rm eff}$.

7.3 Dark Matter Physics

In this section, we study the DM thermal production and constraints from direct detection and CMB observations.

7.3.1 Dark Matter Relic Density

As shown in Eq. (3.1) in section 3.1, the DM thermal relic abundance is calculated by the Boltzmann equation and given by

$$\frac{dn_{\rm d}}{dt} + 3Hn_{\rm d} = -\frac{\langle\sigma_{\rm ann}v_{\rm rel}\rangle}{2}\left(n_{\rm d}^2 - (n_{\rm d}^{\rm eq})^2\right) \ , \tag{7.4}$$

where H denotes the Hubble parameter, and n_d does the DM number density. The right-hand side of Eq. (7.4) is different by 1/2 from that of Eq. (3.1). This is because the DM ψ in this model is Dirac fermion, and the total (equilibrium) DM number density is given by $n_{\rm d}^{\rm (eq)} = n_{\psi}^{\rm (eq)} + n_{\bar{\psi}}^{\rm (eq)}$. Therefore, the annihilation cross section of ψ averaged over the thermal distributions of the initial state $\langle\sigma_{\rm ann}v_{\rm rel}\rangle$ should be twice that of total DM ($\psi + \bar{\psi}$). Study on precise calculation of the thermal relic density [196, 309] indicates the canonical value of the cross section to explain the observed DM abundance,

$$\langle\sigma_{\rm ann}v_{\rm rel}\rangle\,/2 \simeq 3\times10^{-26}\ {\rm cm}^3/{\rm s} \ , \tag{7.5}$$

for DM mass ranging from MeV to 100 TeV.[2] In this chapter, we employ `micromegas_4_3_5` [310] to calculate the DM thermal abundance numerically.

In the $\mathrm{U}(1)_{l_\mu - L_\tau}$ charged DM model, there are two kinds of DM annihilation processes, $\psi\bar{\psi} \to f\bar{f}$ ($f = \mu, \tau, \nu_\mu, \nu_\tau$) and $\psi\bar{\psi} \to XX$. If the DM is lighter than the $\mathrm{U}(1)_{L_\mu - L_\tau}$ gauge boson, the only possible annihilation process is $\psi\bar{\psi} \to f\bar{f}$ through the s-channel X boson exchanging. The annihilation cross section is given by

$$(\sigma v)_{f\bar{f}} = \begin{cases} \dfrac{q_\psi^2 g_X^4}{2\pi}\dfrac{(2m_\psi^2 + m_f^2)(1 - m_f^2/m_\psi^2)^{1/2}}{(4m_\psi^2 - m_X^2)^2 + m_X^2\Gamma_X^2} & (f = \mu, \tau) \ , \\ \dfrac{q_\psi^2 g_X^4}{2\pi}\dfrac{m_\psi^2}{(4m_\psi^2 - m_X^2)^2 + m_X^2\Gamma_X^2} & (f = \nu_\mu, \nu_\tau) \ , \end{cases} \tag{7.6}$$

where Γ_X denotes the total decay width of X and we only keep the partial s-wave. Since the gauge coupling constant g_X is as small as $\mathcal{O}(10^{-4})$ for the successful explanation of the muon $g-2$, the resulting annihilation cross section is too small to achieve the correct relic abundance for $q_\psi = \mathcal{O}(1)$. Therefore, for enough annihilation cross section, the DM mass have to be fine tuned to satisfy $m_\psi \simeq m_X/2$ or the $\mathrm{U}(1)_{l_\mu - L_\tau}$ charge of DM satisfies $q_\psi \gg 1$. A comprehensive study of the resonant production has been made on a benchmark point $m_\psi = 0.45 m_X$ [298], including various experimental constraints. We study another option of exploiting the large DM charge as well as the resonant case.

[2] Ref. [309] precisely calculates the annihilation cross section of WIMP DM that requires for a successful production of WIMP DM through the thermal freeze-out mechanism and indicates that DM with MeV mass requires $\langle\sigma_{\rm ann}v_{\rm rel}\rangle \sim 4\times10^{-26}$ [cm^3/s].

If DM is heavier than the $U(1)_{l_\mu - L_\tau}$ gauge boson, the other annihilation channel $\psi\bar{\psi} \to XX$ opens, and the annihilation cross section of that process is given by

$$(\sigma v)_{XX} = \frac{(q_\psi g_X)^4}{4\pi m_\psi} \frac{(m_\psi^2 - m_X^2)^{3/2}}{(2m_\psi^2 - m_X^2)^2} \ . \tag{7.7}$$

The annihilation cross section of $\psi\bar{\psi} \to XX$ process in Eq. (7.7) is proportional to q_ψ^4, while that of $\psi\bar{\psi} \to f\bar{f}$ in Eq. (7.6) to q_ψ^2. Therefore, even if there is no enhancement by tuning between the DM and $U(1)_{L_\mu - L_\tau}$ gauge boson masses, the DM annihilation cross section can be large enough to realize the successful thermal production only for $q_\psi \gg 1$, and $\psi\bar{\psi} \to XX$ process gives dominant contribution.

7.3.2 Direct Detection Constraints

As shown in Eq. (7.2), the $U(1)_{L_\mu - L_\tau}$ gauge boson couples to the electromagnetic current $J_{\rm EM}$ through the small gauge kinetic mixing ϵ_A, and then the scattering of DM with a nucleus and an electron can occur, although the cross section is suppressed by ϵ_A^2. The mixing with the Z boson ϵ_Z also causes the scattering. However, ϵ_Z is suppressed by a factor of m_X^2/m_Z^2, compared with the leading contribution, and thus we neglect it.

In this model, the effective coupling constants of $\bar{\psi}\psi\bar{p}p$ and $\bar{\psi}\psi\bar{n}n$ are given by

$$f_p = \frac{\epsilon_A e q_\psi g_X}{m_X^2} \ , \quad f_n = 0 \ , \tag{7.8}$$

and from Eqs. (3.9) and (3.11), the SI scattering cross section of DM with a nucleus is given by

$$\sigma_N^{\rm SI} = \frac{\mu_N^2}{\pi} \frac{Z^2 \epsilon_A^2 e^2 q_\psi^2 g_X^2}{m_X^4} \ , \tag{7.9}$$

here $\mu_N = m_N m_\psi/(m_\psi + m_N)$ is the reduced mass of DM and a nucleus with m_N being the nucleus mass, Z the atomic number of the nucleus. This scattering is very similar to the one via the photon exchanging induced by the DM charge radius, $b_\psi = \epsilon_A q_\psi g_X/m_X^2$. Thus, the cross section is proportional to Z^2 rather than A^2 with A being the atomic mass. As shown in Fig. 3.5, the most stringent current limit on the cross section is set by XENON1T ($5\,{\rm GeV} \lesssim m_\psi$) [32], XENON1T with ionization signals ($3\,{\rm GeV} \lesssim m_\psi \lesssim 5\,{\rm GeV}$) [33], DarkSide-50 ($2\,{\rm GeV} \lesssim m_\psi \lesssim 3\,{\rm GeV}$) [311], XENON1T with migdal effects ($0.1\,{\rm GeV} \lesssim m_\psi \lesssim 2\,{\rm GeV}$) [34], and a `TEA-LAB` simulated experiment inspired by the DarkSide50 result ($0.05\,{\rm GeV} \lesssim m_\psi \lesssim 0.1\,{\rm GeV}$) [312].

Similarly, from Eq. (3.15), the cross section of the DM-electron scattering is given by

$$\bar{\sigma}_e = \frac{\mu_e^2}{\pi} \frac{\epsilon_A^2 e^2 q_\psi^2 g_X^2}{(m_X^2 + \alpha^2 m_e^2)^2} \ , \tag{7.10}$$

where μ_e denotes the DM-electron reduced mass. The constraints strongly depend on the scenario if the scattering depends on momentum-transfer q or not. If the X boson mass is much lighter than keV, the scattering is enhanced at a small momentum transfer. Then, we have to take into account a DM form factor, $F_{\rm DM} = (\alpha m_e/q)^2$. Since we are interested in $m_X \gtrsim 6$ MeV, however, the scattering is momentum-transfer independent, so that we can use the limit with a DM form factor, $F_{\rm DM} = 1$, in the literature. As shown in Fig. 3.8, the most stringent current limit on the cross section is set by XENON1T (30 MeV $\lesssim m_\psi$) [33], DarkSide50 (20 MeV $\lesssim m_\psi \lesssim$ 30 MeV) [311], XENON10 (10 MeV $\lesssim m_\psi \lesssim$ 20 MeV) [171], and SENSEI ($m_\psi \lesssim$ 10 MeV) [174].

7.3.3 Cosmological Bounds

DM pair-annihilates into charged leptons and neutrinos. These annihilations during the cosmic dark ages and the BBN era have impacts on the ionization history and $N_{\rm eff}$, bringing us cosmological bounds. We will give brief comments on these bounds in the following.

A. CMB

Annihilation of DM into charged particles and photons increases the ionization fraction in the post-recombination era, modifying the CMB anisotropies and in turn providing the strong limit on the cross section. According to Refs. [313, 314], we adopt a conservative limit on the thermal averaged cross section into charged final states, $(\sigma v)_{\rm charged}/(2m_\psi) \leq 5.1\times10^{-27}\,{\rm cm}^3\,{\rm s}^{-1}\,{\rm GeV}^{-1}$[3]. It suggests that there is a lower mass bound $m_\psi \gtrsim 5$ GeV if the annihilation into charged particles is only responsible for the thermal production.

Let us see the impact of the CMB limit on the model. For $m_\psi \leq m_X$, DM can only annihilate into the muon, tau particle, and neutrinos. Since the cross section for these three processes is almost same, $(\sigma v)_{\mu^+\mu^-,\tau^+\tau^-} \simeq 10^{-26}\,{\rm cm}^3/{\rm s}$ is suggested if kinematically possible, excluding the DM mass up to several GeV. Thus, the CMB observation excludes the region where $m_\mu < m_\psi$.

For $m_\psi > m_X$, the annihilation is dominated by $\psi\bar{\psi} \to XX$ followed by $X \to \nu\bar{\nu}$. The cross section for the annihilation into charged states is smaller by a factor of $(1/q_\psi^2)$ than $\psi\bar{\psi} \to XX$. In this case, there is less significant energy release from DM annihilation into electron and photon. The CMB bound is much weaker than that for $m_\psi \leq m_X$. Nonetheless, the CMB observations partly limit the parameter space. We shall estimate it by considering $m_X \ll m_\psi$ for simplicity. The cross section of $\psi\bar{\psi} \to \mu^+\mu^-$ is related to that of $\psi\bar{\psi} \to XX$ as

$$(\sigma v)_{\mu^+\mu^-} = \frac{\left[1 + m_\mu^2/(2m_\psi^2)\right]\left(1 - m_\mu^2/m_\psi^2\right)^{1/2}}{q_\psi^2} \times (\sigma v)_{XX}. \tag{7.11}$$

[3]Since we consider Dirac DM with the symmetric relic, the left-hand side is divided by 2.

The canonical cross section is $(\sigma v)_{XX}/2 \simeq 5 \times 10^{-26}\,\mathrm{cm}^3/\mathrm{s}$ for Dirac DM [196, 309] in the sub-GeV region where the direct detection bound will be avoided. Plugging the canonical value in Eq. (7.11), the CMB bound reads

$$q_\psi^2 \gtrsim 9.8 \left(\frac{\mathrm{GeV}}{m_\psi}\right) \left(1 + \frac{m_\mu^2}{2m_\psi^2}\right) \left(1 - \frac{m_\mu^2}{m_\psi^2}\right)^{1/2} . \tag{7.12}$$

It follows from this equation that $q_\psi \lesssim 6.9$ is excluded for $m_\psi = 200$ MeV. We illustrate the CMB bound expressed by Eq. (7.12) in Fig. 3.1 (right).

B. Effective neutrino number N_{eff}

The annihilation into neutrinos reheats the SM plasma when DM becomes non-relativistic. If it occurs after the neutrino decoupling, only the neutrino is reheated and the neutrino-to-photon temperature ratio increases, resulting in a higher expansion rate at the BBN than the standard scenario. The expansion rate at the BBN, together with the baryon-to-photon ratio, affects the primordial abundances of helium and deuteron.

The change of the expansion rate is rendered in the effective neutrino number N_{eff}. A significant deviation of N_{eff} from the standard value $N_{\mathrm{eff,SM}} = 3.046$ [112] is faced with the precise Planck observations. In [315–318], the authors calculate the increase of N_{eff} by a relic particle coupled to neutrinos, assuming that the particle is only in equilibrium with the neutrinos during the BBN. They obtain the lower mass bound of Dirac DM $m_\psi \gtrsim 10\,\mathrm{MeV}$, which is drawn in Fig. 7.2 with light blue.

7.3.4 Allowed Region

Fig. 7.2 shows the allowed region in the (m_ψ, q_ψ) plane. The left panel corresponds to the usual WIMP case ($m_\psi < m_X$), while the right panel to the secluded case ($m_\psi > m_X$). In both panels, we scan two parameters, m_X and g_X, such that the experimental and cosmological limits given in subsection 7.2 are avoided. The DM observed abundance, $\Omega_{\mathrm{CDM}}h^2 = 0.12$, can be explained in all the regions in the plots, except for the dark gray region where $\Omega_\psi h^2 > 0.12$ is predicted. We also highlight the 1σ (2σ) muon $g-2$ favored region with the (light) red band.

In Fig. 7.2 (left) with $m_\psi < m_X$, the muon $g-2$ explanation and DM production are simultaneously achieved in a wide DM mass range. In particular, we find that the non-resonant DM production is realized for $q_\psi \gtrsim \mathcal{O}(10)$, otherwise, a large resonant enhancement is needed. We also show the excluded regions from the CMB (green) and N_{eff} (light blue). These restrict the DM mass to be 10 MeV $\lesssim m_\psi \lesssim$ 100 MeV. Note that the BABAR limit (blue) depends on q_ψ for $m_\psi < m_X/2$. We estimate this limit by rescaling the announced BABAR limit [59] with the branching ratio: $g_X \to g_X \cdot \{\mathrm{Br}_{X\to\mu^+\mu^-}|_{q_\psi}/\mathrm{Br}_{X\to\mu^+\mu^-}|_{q_\psi=0}\}^{1/2}$. Naively speaking, the limit

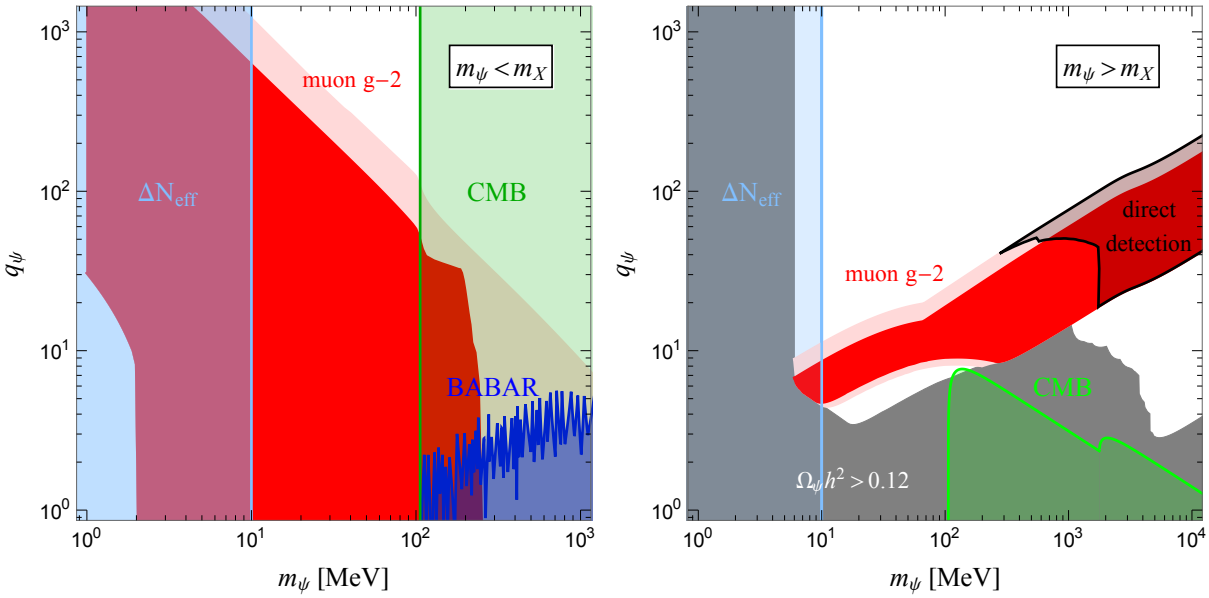

Figure 7.2: The allowed parameter region in the plane of the DM parameters. Dark (light) red region is favored the muon $g-2$ at 1σ (2σ) level. Shaded regions are excluded by the CMB (green), $\Delta N_{\rm eff}$ (light blue) and direct detection (black) and the BABAR (blue) experiments. The dark gray region is disfavored by the DM overabundance ($\Omega_\psi h^2 > 0.12$).

is weakened by a factor of q_ψ, compared to the announced one. The BABAR limit excludes the region of $q_\psi \lesssim 5$, although it is overlapped with the CMB limit.

It is obvious from Fig. 7.2 (right) that allowing the large q_ψ opens a new mass regime, $m_\psi > m_X$, that has not been pointed out in the previous study. The heavy DM mass, even $\mathcal{O}(100$ GeV), is allowed in this regime. The leading constraints in the heavy mass region are set by the direct detection experiments. Given the current results, the DM mass should be lighter than 2 GeV to resolve the muon $g-2$ anomaly. In contrast, if we do not require the muon $g-2$ explanation, the direct detection limit can be very weak, since we can consider the heavy X boson outside the light red band in Fig. 7.2. The gain of the X boson mass does not affect the DM production much, while it considerably reduces the elastic scattering with nuclei and electrons, thereby weakening the direct detection bound[4]. As far as the indirect bounds are concerned, the $N_{\rm eff}$ bound disfavors $m_\psi \lesssim 10$ MeV, while the CMB gives a complementary constraint in the $\mathcal{O}(100$ MeV) region, but only a small part is covered yet. Altogether, it is $10\,\text{MeV} \lesssim m_\psi \lesssim 2\,\text{GeV}$ where the muon $g-2$ anomaly and DM are both addressed. One may wonder if the large DM charge will generate a sizable Sommerfeld enhancement at the freeze-out or in indirect searches. We have confirmed, however, that there is no sizable Sommerfeld effect in the parameters space we consider.

[4]The leading constraint on the heavy X boson is *e.g.* from a CMS search [319], but it is weaker than the constraints on the light X boson. Thus, we have no difficulty in making the X boson heavy enough to avoid the direct detection limit.

It has turned out so far that allowing the large DM charge opens two new DM production regimes; (i) the non-resonant production for $m_\psi < m_X$ and (ii) the secluded production for $m_\psi > m_X$. These are overlooked possibilities in the previous study. Given the new phenomenological possibilities, it is natural to explore the signals of DM in this new parameter space. In the next section, we will study the indirect signals of this DM candidate at neutrino telescope experiments.

7.4 Indirect Detection by Neutrino Telescope

In subsection 7.3.4, we have shown that the DM annihilation cross section is large enough to realize the successful thermal production of the $\mathrm{U}(1)_{L_\mu - L_\tau}$ charged DM without the resonance enhancement by the fine tuning of the X and ψ masses when the DM $\mathrm{U}(1)_{L_\mu - L_\tau}$ charge is large enough. This large annihilation cross section leads to an excess of the neutrino flux from the galactic space. In this section, we discuss the sensitivity of the SK to the neutrino flux excess and the prospect at the HK.

There are some dedicated works which discuss signature of neutrinos originated from DM annihilation in the framework of simplified models [320–327]. In these works, the DM annihilation is considered in the usual WIMP regime, namely, it produces a pair of neutrinos. The resulting monochromatic neutrino fluxes are compared with the results of searches for unknown extraterrestrial neutrino sources [328, 329], supernova relic neutrino (SRN) searches [330–332] and atmospheric neutrino measurements [333], to derive upper limits on the annihilation cross sections. In the following, we perform an independent analyses for the DM signals measured at the SK, assuming that the extra neutrino flux originates from the direct annihilation $\psi\bar{\psi} \to \nu\bar{\nu}$ or the secluded annihilation $\psi\bar{\psi} \to XX \to 2\nu 2\bar{\nu}$ in the Milky Way. We also note that the analysis in this section is applicable as far as the event topologies are the same only by changing the model-dependent flux normalization.

7.4.1 Neutrino flux from DM annihilation

We here assume that neutrinos are Dirac particles for definiteness, but the result will be unchanged even if these are Majorana particles. From Eq. (3.16), the expected electron (anti-)neutrino flux at the detector from DM pair annihilation in the galactic halo is expressed by

$$\frac{d\Phi^{\mathrm{ann}}_{\nu_e(\bar{\nu}_e)}}{dE_\nu} = \frac{1}{4\pi} \sum_i \frac{\langle \sigma v \rangle_i}{4m_\psi^2} \ \kappa \ \frac{dN_i}{dE_\nu} J_{\Delta\Omega} \ , \tag{7.13}$$

where $\langle \sigma v \rangle_i$ denotes the annihilation cross section into a final state i, κ is a model dependent constant which characterizes electron-neutrino flavor fraction, dN_i/dE_ν the neutrino spectral function for the final state i, $J_{\Delta\Omega}$ the astrophysical J-factor shown in Eq. (3.18). Here, we assume

the NFW profile as DM density distributions in the galactic halo, and we set the parameters in the NFW profile and J-factor as the following conventional values :

$$\begin{aligned} \text{scale radius} &: r_s = 20 \text{ kpc} , \\ \text{normalized density profile} &: \rho(r = r_\odot) = 0.4 \text{ GeV/cm}^3 , \\ \text{angular range} &: 0^\circ \leq b \leq 90^\circ,\ 0^\circ \leq l \leq 180^\circ . \end{aligned} \tag{7.14}$$

The resulting all-sky J-factor is $J_{\Delta\Omega} \simeq 1.5 \times 10^{23}$ GeV^2/cm^5. As an example for calculating the model dependent constant κ in Eq. (7.13), if the neutrino flavor ratio at source is $\nu_e : \nu_\mu : \nu_\tau = 0 : 1 : 1$, then the flavor ratio at the detector is $1 : 2 : 2$. Thus, $\kappa = 1/5$ is obtained for U(1)$_{L_\mu - L_\tau}$ DM model. If we consider other gauged U(1) models, the neutrino flux is obtained by changing the value of κ. For example, in the U(1)$_{B-L}$ model, the neutrino flavor ratio at source is $\nu_e : \nu_\mu : \nu_\tau = 1 : 1 : 1$, then the flavor ratio at the detector is also $1 : 1 : 1$, and then $\kappa = 1/3$ is obtained.

The neutrino flux exhibits a distinctive feature. There are two important annihilation modes, which are $\psi\bar{\psi} \to \nu\bar{\nu}, XX$. The former is dominant for $m_\psi \leq m_X$, while the latter for $m_\psi > m_X$. In the former annihilation, the neutrino spectrum is monochromatic at $E_\nu = m_\psi$ in the center-of-mass frame of the annihilation. Since DM is almost at rest in the galactic halo, the monochromatic feature is maintained in the lab frame that is the rest frame of the DM halo. When the annihilation occurs in the Milky Way, the redshift is negligible. Therefore, the neutrino spectrum at the detector keeps the monochromatic form, $dN/dE_\nu \propto \delta(E_\nu - m_\psi)$. This spiky spectrum is easy to be disentangled from the smooth background spectrum, providing a good sensitivity.

In the secluded annihilation $\psi\bar{\psi} \to XX \to 2\nu 2\bar{\nu}$, the neutrino spectrum takes another characteristic form. The spectral feature from such a cascade annihilation has been studied in [334] for an intermediate state with an arbitrary spin, and the authors have shown that the spectral shape in general depends on the polarization of the intermediate state. In what follows, we restrict ourselves to an annihilation process $\psi\bar{\psi} \to VV \to 2\nu 2\bar{\nu}$ with a vector boson V (not necessarily be the X boson), and briefly review the spectral form. In the rest frame of the decaying V, each of emitted neutrinos has a monochromatic spectrum at $E'_\nu = m_V$. In the lab frame, the neutrino energy is boosted and reads

$$E_\nu = \frac{m_\psi}{2} \frac{r_V^2}{1 - \cos\theta\sqrt{1 - r_V^2}}, \tag{7.15}$$

where $r_V = m_V/m_\psi$ and θ is the angle between momenta of the parent V boson and the emitted neutrino in the lab frame. There is a sharp kinematical cut of the neutrino energy. The maximum (minimum) neutrino energy corresponds to $\theta = 0^\circ$ (180°). Since the emission angle θ determines the neutrino energy in the lab frame, we can obtain the neutrino energy spectrum

once we know the angular distribution of the neutrino emitted by the V boson decay. If the V boson produced in $\psi\bar{\psi} \to VV$ is unpolarized, the neutrino emission is isotropic and has no angular distribution. In this case, the neutrino spectrum has no energy dependence between the kinematical endpoints, *i.e.* it takes the so-called box shape [335, 336],

$$\frac{dN}{dE_\nu} = \frac{2}{m_\psi(1-r_V^2)^{1/2}}\Theta(y-y_-)\Theta(y_+-y), \tag{7.16}$$

where $y = E_\nu/m_\psi$ and $y_\pm = \left(1 \pm \sqrt{1-r_V^2}\right)/2$ and $\Theta(y)$ is the Heaviside theta function. On the other hand, if the produced V boson is polarized, the neutrino emission has an angular distribution and hence the resulting neutrino spectrum has an energy dependence.

In general, the neutrino spectrum in the $\psi\bar{\psi} \to VV \to 2\nu 2\bar{\nu}$ process is expressed by

$$\frac{dN}{dE_\nu} = \frac{1}{m_\psi}\sum_{m,n} \mathrm{Br}_{m,n}\left[f_m(y) + f_n(y)\right], \tag{7.17}$$

where the summation runs over V boson helicity $m, n = +1, 0, -1$ and $\mathrm{Br}_{m,n}$ denotes the production branching fraction for each helicity state,

$$\mathrm{Br}_{m,n} = \frac{\sigma v(\psi\bar{\psi} \to V_m V_n)}{\sum_{m,n}\sigma v(\psi\bar{\psi} \to V_m V_n)}. \tag{7.18}$$

The spectral functions $f_m(y)$ are in the form of

$$f_0(y) = \frac{3}{2}\frac{4y - 4y^2 - r_X^2}{(1-r_X^2)^{3/2}}\Theta(y-y_-)\Theta(y_+-y), \tag{7.19}$$

$$f_{\pm1}(y) = \frac{3}{4}\frac{\Theta(y-y_-)\Theta(y_+-y)}{(1-r_X^2)^{3/2}} \times \left[2 - 4y + 4y^2 - r_X^2 \pm 2(C_{+1}-C_{-1})(2y-1)\sqrt{1-r_X^2}\right], \tag{7.20}$$

where C_m are model-dependent coefficients that characterize how the intermediate state with the different polarizations couples to the decay products. For example, when the vector boson couples to the final state fermions as $\bar{f}\left(g_{f_R,V}\gamma^\mu P_R + g_{f_L,V}\gamma^\mu P_L\right) f' V_\mu$, we find

$$C_0 \simeq \frac{m_f^2 + m_{f'}^2}{2m_V^2} + \frac{2g_{f_L,V}g_{f_R,V}}{g_{f_L,V}^2 + g_{f_R,V}^2}\frac{m_f m_{f'}}{m_V^2}, \tag{7.21}$$

$$C_{+1} \simeq \frac{g_{f_R,V}^2(1-C_0)}{g_{f_L,V}^2 + g_{f_R,V}^2} + \frac{2g_{f_L,V}g_{f_R,V}(g_{f_L,V}^2 - g_{f_R,V}^2)}{(g_{f_L,V}^2 + g_{f_R,V}^2)^2}\frac{m_f m_{f'}}{m_V^2}, \tag{7.22}$$

$$C_{-1} \simeq \frac{g_{f_L,V}^2(1-C_0)}{g_{f_L,V}^2 + g_{f_R,V}^2} - \frac{2g_{f_L,V}g_{f_R,V}(g_{f_L,V}^2 - g_{f_R,V}^2)}{(g_{f_L,V}^2 + g_{f_R,V}^2)^2}\frac{m_f m_{f'}}{m_V^2}, \tag{7.23}$$

in the leading order in m_f/m_V or $m_{f'}/m_V$ [334]. Here, we would like to mention the relation,

$$\frac{1}{3}\sum_m f_m(y) = \frac{\Theta(y-y_-)\Theta(y_+-y)}{(1-r_V^2)^{1/2}}. \tag{7.24}$$

It follows from this relation that if the branching fraction is helicity-independent, *i.e.* the V boson is unpolarized, then we exactly obtain the box-shape spectrum Eq.(7.16).

Now let us return to our model. The X boson mostly couples to the left-handed neutrinos which can be regarded as massless, so that $C_0 \simeq C_{+1} \simeq 0$ and $C_{-1} \simeq 1$. Further, the polarization of the X boson produced in the annihilation $\psi\bar{\psi} \to X_m X_n$ is purely transverse,

$$\mathrm{Br} = \mathrm{diag}(1/2, 0, 1/2). \tag{7.25}$$

As a result, the neutrino spectrum is in the form of a bowl-shape,

$$\frac{dN}{dE_\nu} = \frac{2}{m_\psi} \frac{3(2 - 4y + 4y^2 - r_X^2)}{4(1 - r_X^2)^{3/2}} \Theta(y - y_-)\Theta(y_+ - y). \tag{7.26}$$

In Fig. 7.3, we show the neutrino spectrum Eq.(7.26), which is symmetric with respect to $E_\nu = m_\psi/2$. The width of the spectrum is determined solely by kinematics and is given by $\sqrt{1 - r_V^2}$. As ψ and X are more degenerate, the width is narrower and the height is taller.

We would like to remark on the DM model dependence of the neutrino spectrum from the secluded annihilation. For example, if DM is a complex scalar charged under the $\mathrm{U}(1)_{L_\mu - L_\tau}$ gauge group as considered in [337], the annihilation into the longitudinally polarized X boson is nonvanishing and the branching fraction depends on the mass degeneracy of DM and X,

$$\mathrm{Br} \propto \mathrm{diag}\left(1, \frac{r_X^4}{(2 - r_X^2)^2}, 1\right). \tag{7.27}$$

With a small r_X, the annihilation into the longitudinal polarization is sub-leading and the spectral form is similar to the bowl-shape, while all polarizations contribute equally with $r_X \simeq 1$ and the spectrum gets close to the box-shape. Moreover, the annihilation into the longitudinal polarization can be even dominant if DM is sizably coupled to the Nambu-Goldstone mode of the $\mathrm{U}(1)_{L_\mu - L_\tau}$ Higgs field. In this case, the spectrum is like an upside-down bowl. With the current and even future-planned precision, however, it will be difficult to distinguish the difference and these spectra will look practically the same shape in experiments. It might be interesting if any effort in future would realize good enough capability to discern the difference of the spectra.

7.4.2 Analysis

In this subsection, we explain our analytical method. We try to reinterpret the result of the 2,853 days SK search for SRN [331], to derive the limits on the DM annihilation cross section. The signal in this experiment is an electron and a positron produced in the reaction of the inverse beta decay (IBD) ($\bar{\nu}_e + p \to e^+ + n$) the neutrino absorption by Oxygen in the charged current (CC) interactions ($\nu_e(\bar{\nu}_e) + {}^{16}\mathrm{O} \to e^-(e^+) + X_A$). The energy of the produced electron/positron

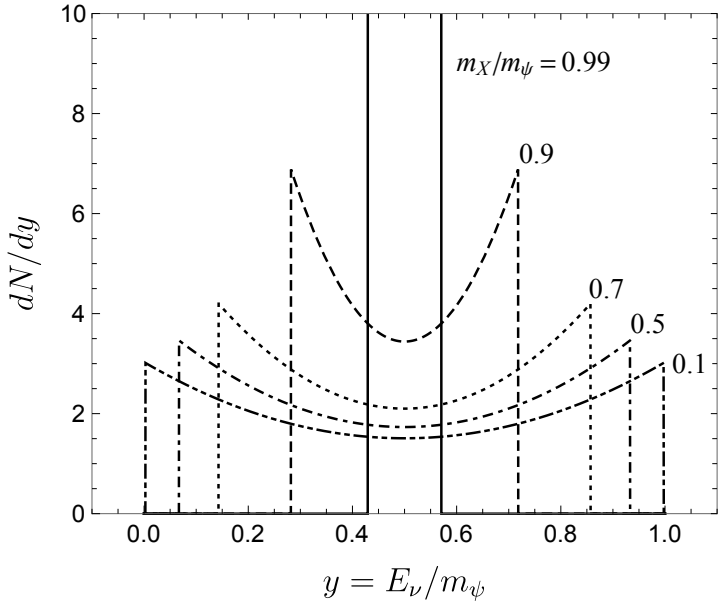

Figure 7.3: The shape of the neutrino spectrum for the $\psi\bar{\psi} \to XX \to 2\nu 2\bar{\nu}$ annihilation.

is related to the initial neutrino energy as follows :

$$\begin{aligned} E_e &\simeq E_\nu - 1.3 \text{ MeV} \quad (\bar{\nu}_e p) \ , \\ E_e &\simeq E_\nu - 15.4 \text{ MeV} \quad (\nu_e \mathrm{O}) \ , \\ E_e &\simeq E_\nu - 11.4 \text{ MeV} \quad (\bar{\nu}_e \mathrm{O}) \ . \end{aligned} \tag{7.28}$$

If no excess of the recoil events is found, one can derive the limit on the neutrino flux, which is in turn translated into the bound on the annihilation cross section.

The signal region is set to $E_e = 16$–$88\,\mathrm{MeV}$ which is divided into 18 bins with a $4\,\mathrm{MeV}$ width. The number of the signal events measured in the i-th bin is expressed by

$$\begin{aligned} N_{i,\mathrm{sig}} = N_{\mathrm{SK}}\, T_{\mathrm{SK}} \int dE_\nu \frac{d\Phi_{\nu_e}}{dE_\nu} \int_{E_i}^{E_{i+1}} dE_{\mathrm{vis}} \int dE_e\, R(E_e, E_{\mathrm{vis}})\, \epsilon(E_{\mathrm{vis}}) \\ \times \left\{ \frac{d\sigma_{\bar{\nu}_e p}}{dE_e}(E_\nu, E_e) + \frac{1}{2} \left(\frac{d\sigma_{\nu_e \mathrm{O}}}{dE_e}(E_\nu, E_e) + \frac{d\sigma_{\bar{\nu}_e \mathrm{O}}}{dE_e}(E_\nu, E_e) \right) \right\} , \end{aligned} \tag{7.29}$$

where $N_{\mathrm{SK}} = 1.5 \times 10^{33}$ denotes the number of free protons in the SK detector, T_{SK} the exposure time of SK.

We combine SK-I (1,497 days), SK-II (794 days), and SK-III (562 days) data. To take into account the detector efficiency and the finite energy resolution, we introduce the efficiency function, $\epsilon(E_{\mathrm{vis}})$ (Fig. 10 of [331]), and the Gaussian-like resolution function,

$$R(E_e, E_{\mathrm{vis}}) = \frac{1}{\sqrt{2\pi}\sigma} \exp\left\{ -\frac{(E_e - E_{\mathrm{vis}})^2}{2\sigma^2} \right\} , \tag{7.30}$$

with the width $\sigma(E_e) = 0.4\ \mathrm{MeV}\sqrt{E_e/\mathrm{MeV}} + 0.03E_e$ [321]. Here, E_e is the actual electron/positron energy, $E_{\rm vis}$ the measured energy at detector and $d\Phi_{\nu_e}/dE_\nu$ the neutrino flux originated from the galactic DM annihilation in Eq.(7.13). We use the NLO analytical expression for the IBD cross section, $d\sigma_{\bar{\nu}_e p}/dE_e$, in [338] and extract $d\sigma_{\nu_e \mathrm{O}}/dE_e$ and $d\sigma_{\overline{\nu_e}\mathrm{O}}/dE_e$ from [339, 340]. For the latter, we assume the electron energy is mono-energetic, e.g. $d\sigma_{\nu_e\mathrm{O}}/dE_\nu(E_\nu, E_e) = \sigma_{\nu_e\mathrm{O}}(E_\nu)\,\delta(E_e - E_\nu - 15.4\,\mathrm{MeV})$, and determine $\sigma_{\nu_e\mathrm{O}}(E_\nu)$ from Fig.2 of [340].

There are four main backgrounds in the signal region $E_e = [16, 88]\,\mathrm{MeV}$. The first one is an electron from the Michel decay of a muon that is produced by the CC interaction of the atmospheric muon neutrino in the water of the detector. If the momentum of the produced muon is lower than the Cherenkov threshold, this muon is invisible and its decay electron cannot be removed. This is called the invisible muon background. This has a kinematical edge at $E_e \simeq 60\,\mathrm{MeV}$. The second one comes from the CC interaction of the atmospheric electron neutrino, producing the monotonically increasing events with the increasing E_e. This dominates the background above the kinematical endpoint of the invisible muon. The third one is an electron produced via the neutral current (NC) interaction of the atmospheric neutrinos. This is increased at the low energy bins. The last grouping of the background is due to heavy charged particles, pions and muons, created in the NC reactions. Some of them survive the pion and Cherenkov angle cut, and enter in the signal region. These backgrounds are shown in Fig. 7.4.

To derive the 90% confidence level (C.L.) limit, we first introduce a likelihood function,

$$\mathcal{L}_i(N_{i,\mathrm{sig}}) = \frac{(N_{i,\mathrm{bkg}} + N_{i,\mathrm{sig}})^{N_{i,\mathrm{obs}}}}{N_{i,\mathrm{obs}}!} e^{-(N_{i,\mathrm{bkg}}+N_{i,\mathrm{sig}})}, \tag{7.31}$$

for each bin and each SK phase. With this likelihood, we define the test statistic (TS) as

$$\mathrm{TS} = -2\sum_i \ln\left(\frac{\mathcal{L}_i(N_{i,\mathrm{sig}})}{\mathcal{L}_i(0)}\right). \tag{7.32}$$

where the summation runs over 18 energy bins and from SK-I to SK-III. The 90% C.L. limit is obtained by solving $\mathrm{TS} \leq 2.71$. Since TS is a function of the DM mass and annihilation cross section $\mathrm{TS}(m_\psi, \sigma v)$, we obtain an exclusion curve in the $(m_\psi, \sigma v)$ plane. To estimate the HK sensitivity, we consider the 374 kton fiducial volume and 10 yrs livetime with the same efficiency and energy resolution as the SK. The HK detector has an option of doping Gd to reduce the backgrounds. In our analysis, it is assumed that the doped Gd reduces the invisible muon background by 50% or 80%. The sensitivity curves are obtained by solving $\mathrm{TS} = 2.71$ with $N_{\mathrm{obs}} = N_{\mathrm{bkg}}$.

7.4.3 SK bounds and HK sensitivity

We compare the DM signal events with the observed events at the SK-I (1,497 days) in Fig. 7.4. The left panel corresponds to $\psi\bar{\psi} \to \nu\bar{\nu}$ and the right panel to $\psi\bar{\psi} \to XX$ with $m_X/m_\psi = 0.5$.

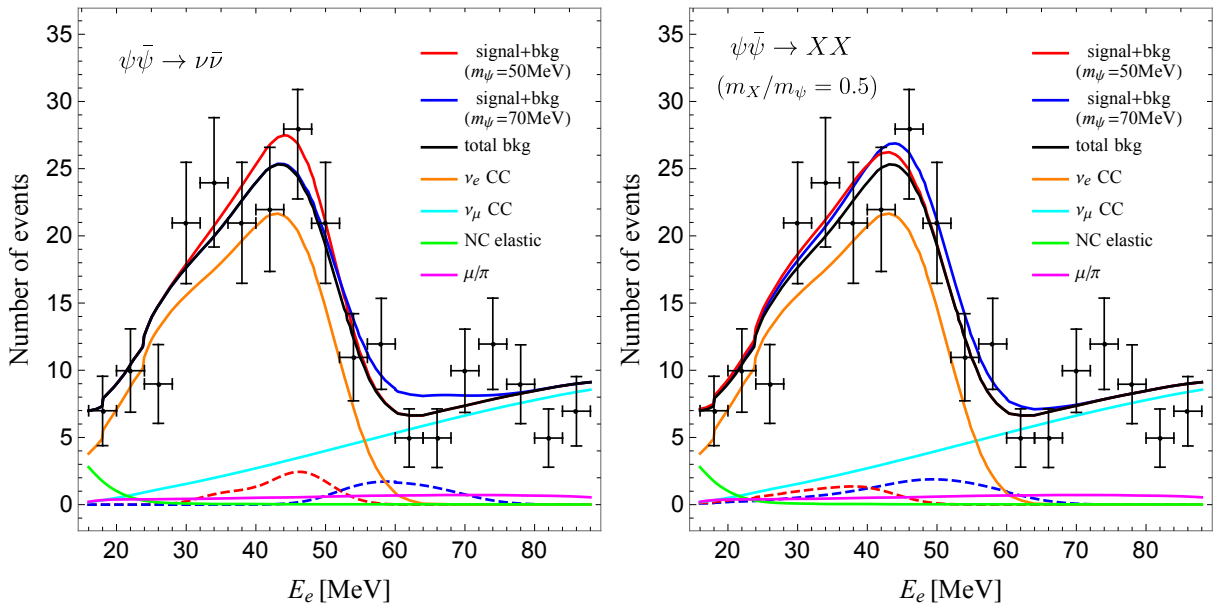

Figure 7.4: The DM signal events measured in the SK-I (1,497 days) for $\psi\bar{\psi} \to \nu\bar{\nu}$ (left) and for $\psi\bar{\psi} \to XX$ (right). The cross section is fixed such that TS = 2.71. Solid (dashed) red and blue curves correspond to the expected signal events with (without) backgrounds. Black points correspond to the observed number of events in the bins with the error bars. The other colored lines correspond to various kinds of background events that are taken from figure 14 of [331].

We assume 100 % branching fraction for the corresponding annihilation and fix the cross section such that TS = 2.71. The red and blue curves represent the number of events in presence of the DM annihilation. The dashed one is the signal and the solid one is the sum of the signal and backgrounds.

The monochromatic flux predicts the distinct event shape, which is peaked at $E_e \simeq m_\psi$ for 50 MeV DM. The shape is broader for 70 MeV DM, on the other hand. This is because there are three reactions that produce the electron/positron with different energy: the IBD with $E_e \simeq E_\nu - 1.3\,\mathrm{MeV}$ and $\nu_e(\bar{\nu}_e) + {}^{16}\mathrm{O}$ scattering with $E_e \simeq E_\nu - 15.4\,(11.4)$ MeV. The cross sections for the latter two scatterings are still smaller at 50 MeV than the former, while these become comparable at 70 MeV. Thus, another peak appears at an energy 10 MeV below the DM mass. The resulting event shape takes a flatter form. The bowl-shape flux induced by the secluded annihilation produces the broader event shape. The event excess in each bin is not sizable, but it equally contributes to multiple bins, not losing sensitivity. The center of the neutrino spectrum is at half of DM mass. On the other hand, the peak appears at slightly higher energy because the cross section grows as the energy.

We show the 90% C.L. upper limits on the annihilation cross section and the future HK sensitivity in Fig. 7.5. For the $\psi\bar{\psi} \to \nu\bar{\nu}$ annihilation, we illustrate the similar limits derived in the previous works [324, 325] for comparison. Our SK limit is consistent with their results

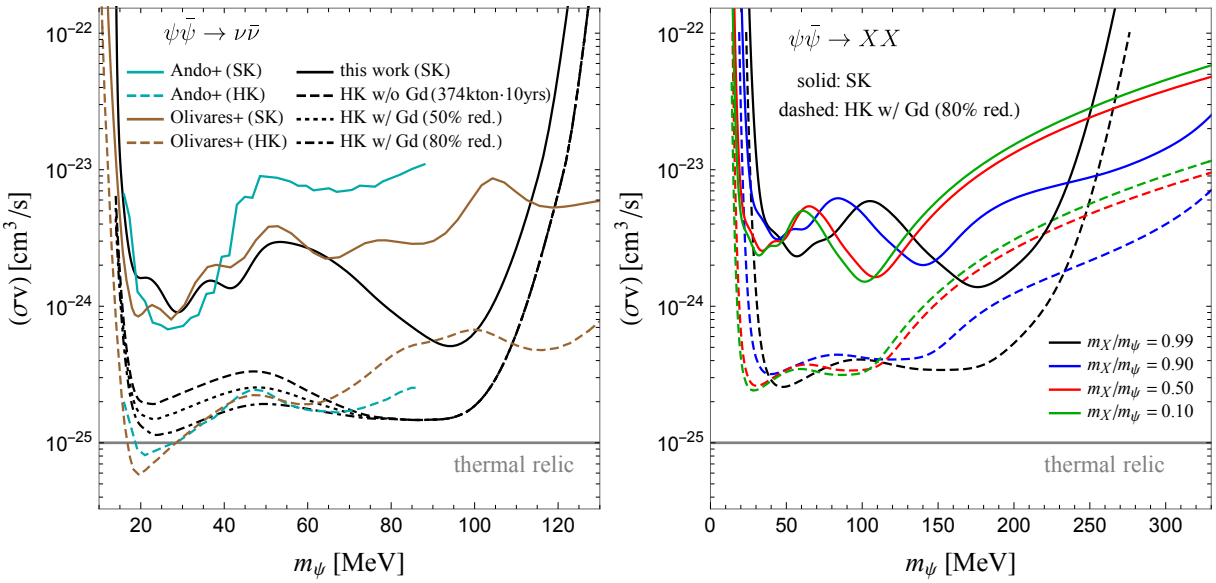

Figure 7.5: The 90% C.L. upper limits on and the future HK sensitivity to the annihilation cross section for $\psi\bar{\psi} \to \nu\bar{\nu}$ (left) and $\psi\bar{\psi} \to XX$ (right) cases. The black solid (dashed) line corresponds to the limit on the annihilation cross section from SK (HK). The results given in [324, 325] are shown for reference and are shown in turquoise and brown lines.

below $m_\psi = 50$ MeV, while it is a little aggressive for higher mass. We guess the disagreement originates from the difference in modeling the $\nu_e{}^{16}$O cross section. We just assume the mono-energetic electron in the reaction, but in general, the electron has a broad energy distribution. This will weaken the signal strength and decrease sensitivity. For the secluded annihilation, the limits depend on the mass degeneracy. When ψ and X are highly degenerate ($m_X/m_\psi = 0.99$), the spectrum has a very narrow width and looks the line shape within the detector resolution, so that the structure of the exclusion curve resembles the monochromatic one. On the other hand, the curve is stretched, which reflects the spectral shape that has the center at $E_\nu = m_\psi/2$. As ψ and X are less degenerate, the curve is shifting to the lighter mass. Interestingly, the exclusion curves extend to the high mass region above 300 MeV due to the wide spectrum. The sensitivity in this mass region is rapidly decreasing as the lower energy cut of the neutrino flux, $E_- = y_- m_\psi$, exceeds about 100 MeV. For instance, $E_- \simeq 0.28\, m_\psi$ with $m_X/m_\psi = 0.9$, so that $m_\psi \sim 350$ MeV is the boundary. In the high mass region, the sensitivity may be increased by combining other observations, such as measurements of the atmospheric neutrino flux by the SK [333]. In both annihilation modes, the current SK limits are much above the canonical thermal relic cross section, but the future HK sensitivity may reach down to it. We would like to add that Ref. [325] also studies the reach of DUNE [341] and JUNO [257] experiments, that is more sensitive than the HK in the same mass range. These sensitivity plots are shown in Fig. 7.6 (left). Also, the gray solid line shows in the left and right panels of Fig. 7.6 the canonical value

of the DM annihilation cross section, $\langle\sigma v\rangle \sim 10^{-25}$ cm^3/s [5] as a reference. We should note that, for $\psi\bar{\psi} \to \nu\bar{\nu}$ case, if the U(1)$_{L_\mu - L_\tau}$ charge of DM is not large, the resonant enhancement of DM annihilation cross section is required at the early Universe. Therefore, the annihilation cross section at the present time can be smaller than that at the typical freeze-out time. We also note that the difference in modeling the ν_eO cross section will affect the exclusion limits in the secluded annihilation as well. Nevertheless, we expect that the modeling error is not so large compared with the monochromatic case unless DM and X are highly degenerate. This is mainly because the neutrino flux is basically broad in the secluded annihilation, in contrast to the monochromatic one, and hence the electron event shape is also broad without the electron energy distribution in the ν_eO reaction. Thus, the exclusion limits will not largely be changed even if another modeling generates a broad electron distribution in the reaction. The detailed study of modeling the ν_eO cross section and its potential error is beyond the scope of this paper and will be followed in a future work.

It may be useful to comment on how large impact the polarizations of the intermediate state have on the cross section limits in Fig. 7.5 (right). If the intermediate state in the secluded annihilation is an unpolarized vector or a scalar, the neutrino flux is box-shape. We have analyzed the neutrino signature and calculated the upper limit on the cross section for such a neutrino spectrum. Comparing the results with those of the bowl-shape spectrum, we have found the difference is at most 10–20%. Since in general the neutrino spectrum is a medium of the box and bowl-shape, we expect the cross section limit to be comparable with the ones in Fig. 7.5 (right), independently of the annihilation fraction into each polarization state.

7.4.4 Implication for U(1)$_{L_\mu - L_\tau}$ DM

In the above subsections, we have formulated the analysis of neutrino signature and evaluated the experimental reach to the extra neutrino flux from the DM annihilation with neutrino telescopes. In this subsection, we discuss the impact on the U(1)$_{L_\mu - L_\tau}$ DM.

In Fig. 7.6, we plot the predictions of the annihilation cross section for the parameter points that can explain the observed DM abundance and the muon $g-2$ as well as being consistent with the experimental constraints in Fig. 7.2. The magenta and orange points give the cross sections for $m_\psi < m_X$ and $m_\psi > m_X$, respectively. The velocity of DM is assumed to be a typical virial velocity in the galaxy, $v_{\rm rel} \sim 10^{-3}$. We also summarize various limits on the cross section derived in the literature, in addition to our results (black lines with the $\diamondsuit$ mark). To avoid the messy figure, however, we omit the similar limits that are already shown in Fig. 7.5. The lines with the same mark ($\clubsuit$, $\heartsuit$) are extracted from the same paper: $\clubsuit$ Ando et al. [325],

[5] According to Ref. [309], the canonical value depends on the DM mass and $\langle\sigma v\rangle \sim$ 8-9 $\times 10^{-26}$ cm^3/s is more precise for 10 MeV $\lesssim m_\psi \lesssim$ 1 GeV.

♡ Arguelles et al. [326] and SK20 [342]. In referring to these limits, we appropriately adjust the neutrino flavor fraction to $\kappa = 1/5$.

We see in Fig. 7.6 (left) that for $m_\psi < m_X$, the model predicts so large cross section that the future experiments can reach. For some parameter points, the cross section is significantly boosted to have even $\langle\sigma v\rangle = 10^{-22}\,\mathrm{cm}^3/\mathrm{s}$. Such parameter points correspond to the resonant mass region $m_\psi \simeq m_X/2$. If the DM mass is fine-tuned to such values at or below % level, the thermal history of the DM production is modified to delay the freeze-out. Such a delay requires a larger cross section than the standard case to deplete the number density down to the observed value. The mechanism for boosting the cross section in this way is discussed in [343, 344]. We review the detail of this mechanism in the Appendix B.2. Interestingly, some of such resonant parameter sets have already been excluded by the SK data. When the mass tuning to $m_\psi \simeq m_X/2$ is moderate, on the other hand, suppressed cross sections can also be obtained. These are distributed over $\langle\sigma v\rangle \lesssim \mathcal{O}(10^{-26})$ cm^3/s in the figure (magenta points). The suppression is caused if the cross section is highly enhanced at the typical freeze-out time due to the physical X boson resonance. In this case, the small DM charge is enough to thermally produce the DM abundance. As a result, the late-time annihilation, e.g. in the galaxy, is suppressed because the DM velocity in the galaxy is too small to produce the X boson resonance. This region corresponds mainly to $q_\psi = \mathcal{O}(1)$. In the non-resonant region, the DM thermal production works in the standard way, so that we have an almost constant canonical cross section, $\langle\sigma v\rangle \simeq 10^{-25}$ cm^3/s. None of the current experiments can reach the canonical value, but future experiments including DUNE and JUNO will be able to cover the DM mass of 20–100 MeV.

In the secluded region ($m_\psi > m_X$), the direct annihilation into a neutrino pair is suppressed and the size of the cross section is at most $\sim 10^{-26}$ cm^3/s. This tendency is more pronounced as DM is heavier. In this case, however, the secluded annihilation can be large (see Fig. 7.6 (right)). We see the model predictions distributed slightly below the canonical value, $\langle\sigma v\rangle = 10^{-25}$ cm^3/s. There is no enhancement in this mass region. The cross section can be kinematically suppressed in the mass degenerate case, because the phase-space of the produced X boson becomes small for the low DM velocity. Thus, a moderate mass splitting is favored to observe the signal, although the high degeneracy produces the sharp neutrino spectrum and leads the strong limits. Indeed, we see some parameter points lying much below the canonical value, where DM and the X boson have close mass. The current SK limit is over one order of magnitude larger than the predicted cross section. The estimate of the future reach is above the prediction by a factor of 3 or more. We hope that some future updates or improvements of the analysis will grow the experimental sensitivity and reach the thermal relic cross section. Compared the HK sensitivity with the DUNE and JUNO ones in Fig. 7.6 (left), the latter ones have better sensitivity. If this is the case for the secluded annihilation, it will be important to analyze the similar signals at

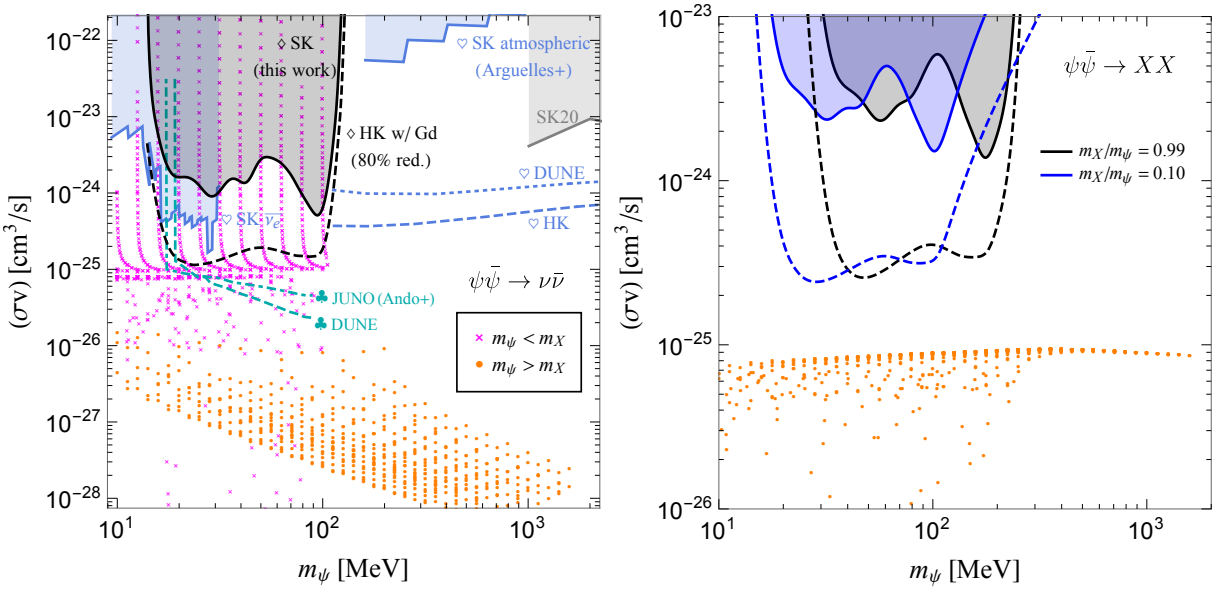

Figure 7.6: The predicted annihilation cross section in the allowed region of the $\mathrm{U}(1)_{L_\mu - L_\tau}$ DM mass and $\mathrm{U}(1)_{L_\mu - L_\tau}$ gauge coupling constant for $\psi\bar{\psi} \to \nu\bar{\nu}$ (left) and $\psi\bar{\psi} \to XX$ (right) cases. The magenta and orange points correspond to $m_\psi < m_X$ and $m_\psi > m_X$, respectively. The various sensitivity curves presented in the literature are shown, in addition to our results (black lines with the ♢ mark). The lines with the same mark (♣, ♡) are extracted from the same paper: ♣ Ando et al. [325], ♡ Arguelles et al. [326] and SK20 [342]. To avoid being messy, we omit the similar lines shown in Fig. 7.5.

these neutrino observatories, that will be pursued in the future.

It is worth mentioning other possibilities that predict significant neutrino flux from sub-GeV DM. Indeed, a great deal of effort has been devoted to non-renormalizable DM-neutrino interactions. The prime difficulty in embedding them in a renormalizable model is that the model includes interactions with charged leptons, which are isospin partners of neutrinos. Such interactions make DM or a mediator particle visible in terrestrial experiments and cosmological observations and, hence, will strongly limit the categories that achieve the sizable DM-neutrino interactions in a renormalizable manner. The model considered here is one of the simplest renormalizable models, that evades the experimental constraints and does not suffer from theoretical requirements, such as gauge anomalies. The other type of possibility is realized by employing a t-channel mediator. Examples of feasible renormalizable models incorporating a t-channel mediator include [345–348].

7.5 Summary and Discussions of Chapter 7

In this chapter, we have discussed a simple Dirac fermion DM ψ with the $\mathrm{U}(1)_{L_\mu - L_\tau}$ charge as an example of low energy physics in the gauged $\mathrm{U}(1)_{L_\mu - L_\tau}$ model. The gauged $\mathrm{U}(1)_{L_\mu - L_\tau}$ model

has the corresponding gauge boson X, and X boson has an attractive feature that X couples to the muon, while not to electron and quarks. Therefore, X boson gives a contribution to the muon magnetic moment through a one-loop diagram and can explain its discrepancy without conflict with X boson search experiments. Moreover, the gauge $\mathrm{U}(1)_{L_\mu - L_\tau}$ model plays several important roles for the DM model. One is the contribution to the DM stability guaranteed by an accidental U(1) symmetry. The other is a role as a mediator of DM and SM interactions. Because of no coupling to electron and quark at tree level, elastic scattering cross section of DM with them is suppressed, and the $\mathrm{U}(1)_{L_\mu - L_\tau}$ charged DM and X are expected to avoid severe constraints from the current direct detection experiments. However, the $\mathrm{U}(1)_{L_\mu - L_\tau}$ gauge coupling constant which explains the muon $g-2$ discrepancy leads too small DM annihilation cross section to realize the observed thermal relic DM abundance.

DM annihilation occurs through two kinds of processes. One is the s-channel $\psi\bar{\psi} \to f\bar{f}$ which is important for $m_X > m_\psi$. The other is the t-channel $\psi\bar{\psi} \to XX$. The latter is allowed for $m_X < m_\psi$ and is more significant, in comparison with the former, as the DM $\mathrm{U}(1)_{L_\mu - L_\tau}$ charge q_ψ increases. We have found that, in both cases, large q_ψ allows DM thermal production and explanation for the muon $g-2$ simultaneously without the resonance of X boson mass pole and conflict with the current bounds. This is pointed out for the first time by the author's work [35].

The DM annihilation leads to neutrino flux from the DM halo, and its energy spectrum depends on which annihilation process is dominant. In the latter half of this chapter, we have formulated the analysis of the indirect neutrino signal of DM in a model-independent way and applied it to $\mathrm{U}(1)_{L_\mu - L_\tau}$ DM model. From the $\psi\bar{\psi} \to \nu\bar{\nu}$ process, neutrinos with monochromatic energy are predicted, while from the $\psi\bar{\psi} \to XX$ process followed by $X \to \nu\bar{\nu}$, the energy spectrum of neutrinos is bowl-shape. Neutrinos produced in the DM halo can be detected by neutrino telescopes. We have calculated the number of the signal events expected at SK and HK detectors and estimated the upper limits from the future HK sensitivity to the DM annihilation cross section. As we have shown in Fig. 7.6, the future sensitivity to the annihilation cross section at HK almost reaches the canonical thermal relic cross section in the $\psi\bar{\psi} \to \nu\bar{\nu}$ case. On the other hand, in the $\psi\bar{\psi} \to XX \to 2\nu 2\bar{\nu}$ case, the obtained future sensitivity is several times larger than the canonical one. Further improvement of the experimental sensitivity is necessary to cover the wide range of the model predictions. We hope that the analysis of, for example, the scattering process between anti-electron neutrinos originated from DM annihilation and electrons in detectors with directional information may help the background subtraction, and it will be shown in the author's future works.

Chapter 8

Summary and Conclusion

$U(1)_{L_\mu - L_\tau}$ gauge symmetry is one of the extensions of the SM and can be introduced to the SM without gauge anomaly. $U(1)_{L_\mu - L_\tau}$ gauge boson has couplings to μ and τ-type leptons and does not interact with electron and quarks at tree level. Therefore, this gauge boson avoids severe experimental and cosmological constraints and has been discussed in the context of phenomenology relative to the muon, tau particle, and neutrinos. Muon $g-2$ discrepancy is one of the clues for exploring the BSM physics, and the $U(1)_{L_\mu - L_\tau}$ gauge boson can explain this problem without conflicting with the current experimental bounds. Besides the muon $g-2$, the $U(1)_{L_\mu - L_\tau}$ gauge boson can play important roles because of its avoidance of interactions with electrons and quarks.

Mediator which connects the DM to the SM sector is one possibility, and as an example, the Dirac fermion DM model has been discussed in the author's work [35]. This model is attractive because not only the DM avoids the severe bounds from the current direct detection experiments, but also the DM stability is guaranteed by an accidental symmetry. DM in $U(1)_{L_\mu - L_\tau}$ models has been discussed so far in many previous works. However, it is difficult to obtain enough DM annihilation cross section because of the smallness of the $U(1)_{L_\mu - L_\tau}$ gauge coupling constant to explain the muon $g-2$. Therefore, in many cases, mass tuning between DM and $U(1)_{L_\mu - L_\tau}$ gauge boson is needed to realize the DM relic abundance and explanation of muon $g-2$ simultaneously.

In chapter 7 of this thesis, the DM has a much larger $U(1)_{L_\mu - L_\tau}$ charge than the SM particles, and then the above difficulty is avoided, and sub or several GeV DM mass is predicted. Moreover, neutrinos are important for the indirect detection of such a DM. When the DM is heavier than the $U(1)_{L_\mu - L_\tau}$ gauge boson, t-channel DM annihilation process $\psi\bar{\psi} \to XX$ gives dominant contribution, and in this case, the predicted neutrino flux originated from DM annihilation is different from that in the usual s-channel annihilation case. We study the energy spectrum of neutrinos in the usual WIMP and secluded regimes and we calculate the number of the signal events expected at SK and HK detectors and estimated the upper limits from the future HK

sensitivity to the DM annihilation cross section. The future sensitivity to the annihilation cross section at HK almost reaches the canonical thermal relic cross section in $\psi\bar{\psi} \to \nu\bar{\nu}$ case. On the other hand, in the $\psi\bar{\psi} \to XX \to 2\nu 2\bar{\nu}$ case, the obtained future sensitivity is several times larger than the canonical one. Further improvement of the experimental sensitivity is necessary to cover the wide range of the model predictions. We hope that the analysis with directional information may help the background subtraction.

Besides the $\mathrm{U}(1)_{L_\mu - L_\tau}$ gauge boson, the $\mathrm{U}(1)_{L_\mu - L_\tau}$ gauge symmetry itself performs an important function for the neutrino sector. The active neutrino mass matrix is restricted by the $\mathrm{U}(1)_{L_\mu - L_\tau}$ gauge symmetry and has the two-zero minor structure in the minimal gauged $\mathrm{U}(1)_{L_\mu - L_\tau}$ model. The nine parameters of the light neutrinos, such as one Dirac and two Majorana CP phases, a sum of the neutrino masses, three mixing angles, and two squared mass differences, are related to each other by the two-zero minor conditions. In chapter 5, we analyze these conditions and obtain the former four parameters as functions of the latter five neutrino oscillation parameters. Moreover, using these predictions, we obtained the prediction of the effective Majorana neutrino mass for the neutrinoless double beta decay, which value can be within the reach of future neutrinoless double beta decay experiments. These predictions are independent of the scales of the $\mathrm{U}(1)_{L_\mu - L_\tau}$-breaking and Majorana masses because two-zero minor conditions are also independent of these scales.

In chapter 6, we study the non-thermal leptogenesis in the minimal gauged $\mathrm{U}(1)_{L_\mu - L_\tau}$ model. In this model, the neutrino CP phases are determined by the neutrino oscillation parameter. Moreover, the heavy neutrino masses are also determined by them and three neutrino Dirac Yukawa couplings. Therefore, this model can predict the baryon asymmetry generated by leptogenesis with less uncertainty. In this thesis, the $\mathrm{U}(1)_{L_\mu - L_\tau}$-breaking scalar is regarded as inflaton, and we assume that the RHNs are produced by the decays of the inflaton. We find that the observed value of baryon asymmetry can be explained in this scenario. In particular, the correct sign of baryon asymmetry can be obtained in a wide range of parameter space. We recall that our choice of $\delta > \pi$, which is favored by the present neutrino oscillation data [109, 110, 294], was crucial in obtaining this result; if we instead chose $\delta < \pi$, we would obtain a wrong sign for the baryon asymmetry in most parameter regions.

In this thesis, we explore novel possibilities of the $\mathrm{U}(1)_{L_\mu - L_\tau}$ models, as written above. As discussed in many previous works, the muon $g-2$ discrepancy is one of the motivations for introducing the $\mathrm{U}(1)_{L_\mu - L_\tau}$ gauge symmetry. The theoretical calculations including the lattice QCD have recently been developed. Moreover, the novel experiments to measure the muon $g-2$ discrepancy are being carried out and expected to release new results in the near future. These results remain to be seen, however, regardless of whether the muon $g-2$ discrepancy exists, the $\mathrm{U}(1)_{L_\mu - L_\tau}$ models offer rich phenomenology as studied in this thesis and have considerable motivations. We look forward to further progress in the $\mathrm{U}(1)_{L_\mu - L_\tau}$ models and experimentally

testing them in the future.

Appendix A

Gauge Kinetic Mixing

The field strengths of the gauge fields are invariant under the gauge transformation. Therefore, their mixing terms are also gauge invariant, and such terms are called gauge kinetic mixing [1]. Because of the existence of the gauge kinetic mixing, there are deviations of the physical gauge bosons from ones without the mixing. In this appendix, we give a short review of these deviations and their effects on the phenomenology.

A.1 Gauge Kinetic Mixing in the $U(1)_{L_\mu - L_\tau}$ model

Here, we consider the following Lagrangian relative to the kinetic terms of the gauge fields :

$$\mathcal{L}^{\rm kin}_{\rm gauge} = -\frac{1}{4}\hat{B}_{\lambda\rho}\hat{B}^{\lambda\rho} - \frac{1}{4}\hat{X}_{\lambda\rho}\hat{X}^{\lambda\rho} - \frac{\sin\epsilon}{2}\hat{B}_{\lambda\rho}\hat{X}^{\lambda\rho} \ , \tag{a.1}$$

where $\hat{B}^{\lambda\rho}$ and $\hat{X}^{\lambda\rho}$ are the field strengths of the $U(1)_Y$ and $U(1)_{L_\mu - L_\tau}$ gauge bosons, respectively. By a linear transformation of the gauge fields, the above kinetic mixing can be diagonalized

$$\mathcal{L}^{\rm kin}_{\rm gauge} = -\frac{1}{4}\tilde{B}_{\lambda\rho}\tilde{B}^{\lambda\rho} - \frac{1}{4}\tilde{X}_{\lambda\rho}\tilde{X}^{\lambda\rho} \ , \tag{a.2}$$

$$\begin{pmatrix}\hat{B}^\lambda \\ \hat{X}^\lambda\end{pmatrix} = \begin{pmatrix}1 & -\tan\epsilon \\ 0 & \frac{1}{\cos\epsilon}\end{pmatrix}\begin{pmatrix}\tilde{B}^\lambda \\ \tilde{X}^\lambda\end{pmatrix} = \begin{pmatrix}1 & -\epsilon \\ 0 & 1\end{pmatrix}\begin{pmatrix}\tilde{B}^\lambda \\ \tilde{X}^\lambda\end{pmatrix} + \mathcal{O}(\epsilon^2) \ . \tag{a.3}$$

[1] For further detail about gauge kinetic mixing in the $U(1)_{L_\mu - L_\tau}$ model, please see Ref. [304], for example.

The physical states of the gauge fields $(A_\lambda, Z_\lambda, X_\lambda)$ are obtained by the following field redefinition :

$$\begin{aligned}
\mathcal{L}^{\rm mass}_{\rm gauge} &= +\frac{1}{2}\begin{pmatrix}\hat{B}_\lambda & \hat{W}_{3\lambda} & \hat{X}_\lambda\end{pmatrix}\begin{pmatrix}\hat{s}_W^2\hat{m}_Z^2 & -\hat{s}_W\hat{c}_W\hat{m}_Z^2 & 0\\ -\hat{s}_W\hat{c}_W\hat{m}_Z^2 & \hat{c}_W^2\hat{m}_Z^2 & 0\\ 0 & 0 & \hat{m}_X^2\end{pmatrix}\begin{pmatrix}\hat{B}^\lambda\\ \hat{W}_3^\lambda\\ \hat{X}^\lambda\end{pmatrix}\\
&= +\frac{1}{2}\begin{pmatrix}\tilde{B}_\lambda & \tilde{W}_{3\lambda} & \tilde{X}_\lambda\end{pmatrix}\begin{pmatrix}\hat{s}_W^2\hat{m}_Z^2 & -\hat{s}_W\hat{c}_W\hat{m}_Z^2 & -\hat{s}_W^2 t_\epsilon\hat{m}_Z^2\\ -\hat{s}_W\hat{c}_W\hat{m}_Z^2 & \hat{c}_W^2\hat{m}_Z^2 & \hat{s}_W\hat{c}_W t_\epsilon\hat{m}_Z^2\\ -\hat{s}_W^2 t_\epsilon\hat{m}_Z^2 & \hat{s}_W\hat{c}_W t_\epsilon\hat{m}_Z^2 & \hat{s}_W^2 t_\epsilon\hat{m}_Z^2+\frac{\hat{m}_X^2}{c_\epsilon^2}\end{pmatrix}\begin{pmatrix}\tilde{B}^\lambda\\ \tilde{W}_3^\lambda\\ \tilde{X}^\lambda\end{pmatrix}\\
&= +\frac{1}{2}\begin{pmatrix}\tilde{A}_\lambda & \tilde{Z}_\lambda & \tilde{X}_\lambda\end{pmatrix}\begin{pmatrix}0 & 0 & 0\\ 0 & \hat{m}_Z^2 & \hat{s}_W t_\epsilon\hat{m}_Z^2\\ 0 & \hat{s}_W t_\epsilon\hat{m}_Z^2 & \hat{s}_W^2 t_\epsilon^2\hat{m}_Z^2+\frac{\hat{m}_X^2}{c_\epsilon^2}\end{pmatrix}\begin{pmatrix}\tilde{A}^\lambda\\ \tilde{Z}^\lambda\\ \tilde{X}^\lambda\end{pmatrix}\\
&= +\frac{1}{2}\begin{pmatrix}A_\lambda & Z_\lambda & X_\lambda\end{pmatrix}\begin{pmatrix}0 & 0 & 0\\ 0 & m_Z^2 & 0\\ 0 & 0 & m_X^2\end{pmatrix}\begin{pmatrix}A^\lambda\\ Z^\lambda\\ X^\lambda\end{pmatrix}\,, \qquad \text{(a.4)}
\end{aligned}$$

$$\begin{pmatrix}\hat{B}^\lambda\\ \hat{W}_3^\lambda\\ \hat{X}^\lambda\end{pmatrix} = \begin{pmatrix}1 & 0 & -t_\epsilon\\ 0 & 1 & 0\\ 0 & 0 & \frac{1}{c_\epsilon}\end{pmatrix}\begin{pmatrix}\hat{c}_W & -\hat{s}_W & 0\\ \hat{s}_W & \hat{c}_W & 0\\ 0 & 0 & 1\end{pmatrix}\begin{pmatrix}1 & 0 & 0\\ 0 & \hat{c}_\zeta & -\hat{s}_\zeta\\ 0 & \hat{s}_\zeta & \hat{c}_\zeta\end{pmatrix}\begin{pmatrix}A^\lambda\\ Z^\lambda\\ X^\lambda\end{pmatrix}\,, \qquad \text{(a.5)}$$

where $\hat{m}_Z = (g'^2+g^2)v^2/4$ and $\hat{m}_X = g_X^2 v_{\mu\tau}^2$ are the mass parameters, respectively, and $v_{\mu\tau}$ is the VEV of the $\mathrm{U}(1)_{L_\mu - L_\tau}$-breaking scalar. Here, we refer to $\sin\xi$, $\cos\xi$, and $\tan\xi$ as s_ξ, c_ξ, and t_ξ, respectively, and assume $\hat{m}_X < \hat{m}_Z$. The physical mass of the Z and X bosons are given by

$$m_{Z/X}^2 = \frac{1}{2}\left\{\hat{m}^2 \pm \sqrt{\hat{m}^4 - \frac{4\hat{m}_Z^2\hat{m}_X^2}{c_\epsilon^2}}\right\}\,, \qquad \text{(a.6)}$$

with

$$\hat{m}^2 = \hat{m}_Z^2\left(1+\hat{s}_W^2 t_\epsilon^2\right) + \frac{\hat{m}_X^2}{c_\epsilon^2} = \hat{m}_Z^2 + \hat{m}_X^2 + \mathcal{O}(\epsilon^2)\,. \qquad \text{(a.7)}$$

ζ is the mixing angle that determines the rotation from the $\tilde{Z}^\lambda$ and $\tilde{X}^\lambda$ to the Z^λ and X^λ fields and defined by

$$\begin{aligned}
\tan\zeta &= \frac{1-r^2-\sqrt{(1-r)^2 - 4\hat{s}_W^2 t_\epsilon^2 r^2}}{2\hat{s}_W t_\epsilon r^2}\\
&= \frac{\hat{s}_W\epsilon}{1-r^2} + \mathcal{O}(\epsilon^3)\,, \qquad \text{(a.8)}
\end{aligned}$$

with $r = m_X/m_Z$.

A.2 Interactions between Gauge Bosons and Fermions

Interactions between the neutral gauge bosons and SM fermions are given by

$$\begin{aligned}\mathcal{L}_{\text{int}} &= -\sum_f \bar{f}\gamma^\lambda \left\{ g' \left(Y_L P_L + Y_R P_R \right) \hat{B}_\lambda + g T_3 P_L \hat{W}_{3\lambda} + g_X Y_{L_\mu - L_\tau} \hat{X}_\lambda \right\} f \\ &= -\sum_f \bar{f}\gamma^\lambda \left\{ eQA_\lambda + \left(g_{f_L,Z} P_L + g_{f_R,Z} P_R \right) Z_\lambda + \left(g_{f_L,X} P_L + g_{f_R,X} P_R \right) X_\lambda \right\} \ , \end{aligned} \tag{a.9}$$

where

$$g_{f_L,Z} = \frac{e c_\zeta}{\hat{s}_W \hat{c}_W} \left\{ \left(1 + \hat{s}_W t_\epsilon t_\zeta \right) T_3 - \left(\hat{s}_W^2 + \hat{s}_W t_\epsilon t_\zeta \right) Q \right\} + g_X \frac{s_\zeta}{c_\epsilon} Y_{L_\mu - L_\tau} \ , \tag{a.10}$$

$$g_{f_R,Z} = -\frac{e c_\zeta}{\hat{s}_W \hat{c}_W} \left(\hat{s}_W^2 + \hat{s}_W t_\epsilon t_\zeta \right) Q + g_X \frac{s_\zeta}{c_\epsilon} Y_{L_\mu - L_\tau} \ , \tag{a.11}$$

$$g_{f_L,X} = \frac{e c_\zeta}{\hat{s}_W \hat{c}_W} \left\{ \left(\hat{s}_W t_\epsilon - t_\zeta \right) T_3 + \left(\hat{s}_W^2 t_\zeta - \hat{s}_W t_\epsilon \right) Q \right\} + g_X \frac{c_\zeta}{c_\epsilon} Y_{L_\mu - L_\tau} \ , \tag{a.12}$$

$$g_{f_R,X} = \frac{e c_\zeta}{\hat{s}_W \hat{c}_W} \left(\hat{s}_W^2 t_\zeta - \hat{s}_W t_\epsilon \right) Q + g_X \frac{c_\zeta}{c_\epsilon} Y_x \ , \tag{a.13}$$

and Q, T_3, and $Y_{L_\mu - L_\tau}$ are the electroweak charge, weak isospin, and $\mathrm{U}(1)_{L_\mu - L_\tau}$ charge of the SM fermion f, respectively, and $Y_{L(R)}$ is the weak hypercharge of the left (right)-handed SM fermion $f_{L(R)}$. For $\epsilon, r \ll 1$, the above interaction terms are simplified as follows :

$$\begin{aligned}\mathcal{L}_{\text{int}} \simeq -\sum_f \bar{f}\gamma^\lambda \Bigg[eQA_\lambda + \left\{ \frac{e}{\hat{s}_W \hat{c}_W} \left(T_3 P_L - \hat{s}_W^2 Q \right) + \epsilon g_X \hat{s}_W Y_{L_\mu - L_\tau} \right\} Z_\lambda \\ + \left\{ -\epsilon \frac{e}{\hat{c}_W} \left(4r^2 T_3 P_L + Q \right) + \epsilon g_X Y_{L_\mu - L_\tau} \right\} X_\lambda \Bigg] \ . \end{aligned} \tag{a.14}$$

A.3 Effect on the ρ-parameter

Lastly, we comment on the relation between the mixing parameter $\hat{\theta}_W$ and the physical weak mixing angle θ_W. The physical θ_W is obtain by [304, 349]

$$s_W^2 c_W^2 = \frac{\pi \alpha(m_Z)}{\sqrt{2} G_F m_Z^2} \ , \tag{a.15}$$

with $\alpha(m_Z)$ being the fine structure constant at the Z-pole. The mixing parameter $\hat{\theta}_W$ satisfies the Eq. (a.15)-like relation with $s_W \to \hat{s}_W$, $c_W \to \hat{c}_W$, and $m_Z \to \hat{m}_Z$, and then, assuming $\alpha(m_Z) = \alpha(\hat{m}_Z)$, θ_W and $\hat{\theta}_W$ satisfy the following relation :

$$s_W^2 c_W^2 m_Z^2 = \hat{s}_W^2 \hat{c}_W^2 \hat{m}_Z^2 \ . \tag{a.16}$$

From Eqs. (a.16) and (a.6), we obtain

$$\sin^2 \theta_W = \sin^2 \hat{\theta}_W \left(1 - \frac{\sin^2 2\hat{\theta}_W \epsilon^2}{4 \cos 2\hat{\theta}_W (1 - r^2)} \right) + \mathcal{O}(\epsilon^4) \ . \tag{a.17}$$

Therefore, the ρ-parameter is corrected as follows :

$$\rho \equiv \frac{m_W^2}{m_Z^2 c_W^2} = \frac{\hat{m}_W^2}{\hat{m}_Z^2 \hat{c}_W^2} \frac{s_W^2}{\hat{s}_W^2} = \frac{s_W^2}{\hat{s}_W^2} \ . \tag{a.18}$$

From Eq. (a.17), ρ-parameter is approximated for $\epsilon \ll 1$ as follows :

$$\rho = 1 - \frac{\sin^2 2\hat{\theta}_W \epsilon^2}{4 \cos 2\hat{\theta}_W (1 - r^2)} + \mathcal{O}(\epsilon^4) \ . \tag{a.19}$$

Appendix B

DM Relic Density and Indirect Detection

In section 3.1, we discuss the thermal freeze-out mechanism and the Boltzmann equation that gives the quantitative value of the DM relic density. In section 7.5, we mention the mechanism for boosting the annihilation cross section of DM, so-called Breit-Wigner enhancement. In this appendix, we explain these topics.

B.1 Boltzmann equation

Here, we show a brief review of the Boltzmann equation discussed in section 3.1. This is important to evaluate DM relic density quantitatively, and here, we derive Eq. (3.1) in section 3.1.

The Boltzmann equation gives a solution of the time evolution of phase-space distribution function and is written as follows :

$$\hat{\mathbf{L}} f_{\rm DM}(\vec{p}, T) = \mathbf{C}[f_{\rm DM}] \ , \tag{b.1}$$

where the left-hand side is the drift term corresponding to change of the distribution function by motions of particles and depends on the expansion of the Universe. The right-hand one is called the collision term coming from interactions with the SM particles in the thermal bath, and depends on the detail of particles. For non-relativistic particles, the operator $\hat{\mathbf{L}}$ in Eq. (b.1) is the Liouville operator given by

$$\hat{\mathbf{L}} = E\frac{\partial}{\partial t} - H|\vec{\mathbf{p}}|^2\frac{\partial}{\partial E} \ , \tag{b.2}$$

with E and $\vec{\mathbf{p}}$ being energy and momentum of the particle, respectively. From Eq. (b.2), DM number density

$$n_{\rm DM}(t) = g_{\rm DM}\int \frac{d^3p}{(2\pi)^3} f(\vec{\mathbf{p}}, t) \ , \tag{b.3}$$

with $g_{\rm DM}$ being the internal degrees of freedom for the DM, satisfies

$$\frac{dn_{\rm DM}}{dt} + 3Hn_{\rm DM} = g_{\rm DM}\int \frac{d^3p}{(2\pi)^3}\frac{1}{E(\vec{\mathbf{p}})}\mathbf{C}[f_{\rm DM}] \ . \tag{b.4}$$

When the thermal relic abundance of DM is realized by DM annihilation into SM particles, like ${\rm DM} + \overline{\rm DM} \to {\rm SM} + \overline{\rm SM}$, the collision term is written in terms of the distribution function of particle i, f_i, as follows :

$$\begin{aligned} & g_{\rm DM}\int \frac{d^3p}{(2\pi)^3}\frac{1}{E(\vec{\mathbf{p}})}\mathbf{C}[f_{\rm DM}] \\ & = -\int d\Pi_{\rm DM}\, d\Pi_{\overline{\rm DM}}\, d\Pi_{\rm SM}\, d\Pi_{\overline{\rm SM}}\, (2\pi)^4\delta^4(p_{\rm DM} + p_{\overline{\rm DM}} - p_{\rm SM} - p_{\overline{\rm SM}}) \\ & \quad \times \left\{ |\mathcal{M}_{\rm ann}|^2 f_{\rm DM} f_{\overline{\rm DM}}(1 \pm f_{\rm SM})(1 \pm f_{\overline{\rm SM}}) - |\mathcal{M}_{\rm pro}|^2 f_{\rm SM} f_{\overline{\rm SM}}(1 \pm f_{\rm DM})(1 \pm f_{\overline{\rm DM}}) \right\} \ , \end{aligned} \tag{b.5}$$

where $\Pi_i \equiv d^3p_i\,/(2\pi)^3(2E_i)$, and minus (plus) in parentheses is for boson (fermion). The Dirac delta function comes from the conservation law for energy and momentum. $\mathcal{M}_{\rm ann}$ and $\mathcal{M}_{\rm pro}$ are amplitudes of annihilation and production process of DM pair. Here, we assume the CP-invariance of annihilation and production processes. From the CP-invariance, $|\mathcal{M}_{\rm ann}|^2 = |\mathcal{M}_{\rm pro}|^2$ is derived because of the CPT-invariance. When Fermi degeneracy and Bose-Einstein condensation do not occur, and the SM particles are in thermal equilibrium, Eq. (b.5) can be rearranged as

$$\begin{aligned} g_{\rm DM}\int \frac{d^3p}{(2\pi)^3}\frac{1}{E(\vec{\mathbf{p}})}\mathbf{C}[f_{\rm DM}] = & -\int d\Pi_{\rm DM}\, d\Pi_{\overline{\rm DM}}\, d\Pi_{\rm SM}\, d\Pi_{\overline{\rm SM}}\, (2\pi)^4\delta^4(p_{\rm DM} + p_{\overline{\rm DM}} - p_{\rm SM} - p_{\overline{\rm SM}}) \\ & \times |\mathcal{M}|^2 \left(f_{\rm DM} f_{\overline{\rm DM}} - f^{\rm eq}_{\rm SM} f^{\rm eq}_{\overline{\rm SM}} \right) \\ & -\int d\Pi_{\rm DM}\, d\Pi_{\overline{\rm DM}}\, d\Pi_{\rm SM}\, d\Pi_{\overline{\rm SM}}\, (2\pi)^4\delta^4(p_{\rm DM} + p_{\overline{\rm DM}} - p_{\rm SM} - p_{\overline{\rm SM}}) \\ & \times |\mathcal{M}|^2 \left(f_{\rm DM} f_{\overline{\rm DM}} - f^{\rm eq}_{\rm DM} f^{\rm eq}_{\overline{\rm DM}} \right) \ . \end{aligned} \tag{b.6}$$

In the rearrange of Eq. (b.6), we used the relation, $f^{\rm eq}_{\rm DM} = f^{\rm eq}_{\rm SM}$, and this relation is guaranteed by the conservation law of energy. The annihilation cross section averaged over the thermal distribution is defined by

$$\begin{aligned} \langle \sigma_{\rm ann} v_{\rm rel} \rangle = \frac{1}{(n^{\rm eq}_{\rm DM})^2}\int & d\Pi_{\rm DM}\, d\Pi_{\overline{\rm DM}}\, d\Pi_{\rm SM}\, d\Pi_{\overline{\rm SM}}\, (2\pi)^4\delta^4(p_{\rm DM} + p_{\overline{\rm DM}} - p_{\rm SM} - p_{\overline{\rm SM}}) \\ & \times |\mathcal{M}|^2 f_{\rm DM} f_{\overline{\rm DM}} \ , \end{aligned} \tag{b.7}$$

and, by assuming the relation, $f_{\rm DM} = f^{\rm eq}_{\rm DM} n_{\rm DM}/n^{\rm eq}_{\rm DM}$, we eventually obtain Boltzmann equation for DM number densty as follows :

$$\frac{dn_{\rm DM}}{dt} + 3Hn_{\rm DM} = -\langle \sigma_{\rm ann} v_{\rm rel} \rangle \left(n^2_{\rm DM} - (n^{\rm eq}_{\rm DM})^2 \right) \ . \tag{b.8}$$

B.2 Breit-Wigner Enhancement

As shown in Fig. 7.6, there is a significant enhancement in indirect detection via the unphysical X boson pole. In this appendix, we briefly review the effect. We consider the $\psi\bar{\psi} \to \nu\bar{\nu}$ process. Assuming the initial state DM is non-relativistic, we express the center of mass energy and DM mass as

$$s \simeq 4m_\psi^2 + m_\psi^2 v_{\rm rel}^2, \quad 4m_\psi^2 = m_X^2(1+\delta), \tag{b.9}$$

where $v_{\rm rel}$ denotes the relative velocity of DM. Then, the annihilation cross section is written by

$$(\sigma v)_{\nu\bar{\nu}} \simeq \frac{q_\psi^2 g_X^4}{\pi} \frac{1}{m_X^4} \frac{m_\psi^2}{(\delta + v_{\rm rel}^2/4)^2 + \gamma_X^2}, \tag{b.10}$$

where $\gamma_X = \Gamma_X/m_X$.

Let us consider how the DM freeze-out process is changed for $\delta \ll 1$. First of all, we approximate the cross section

$$(\sigma v)_{\nu\nu} \approx \frac{q_\psi^2 g_X^4}{\pi} \frac{m_\psi^2}{m_X^4} \times \begin{cases} (\mathrm{Max}[v_{\rm rel}^2/4, \gamma_X])^{-2} & (v_{\rm rel}^2 > \delta) \\ (\mathrm{Max}[\delta, \gamma_X])^{-2} & (v_{\rm rel}^2 < \delta) \end{cases} \tag{b.11}$$

It follows from this equation that as DM velocity decreases with the expanding universe, the cross section becomes large as $(\sigma v)_{\nu\bar{\nu}} \propto v_{\rm rel}^{-4}$. The increase of the cross section continues until $v_{\rm rel}^2 \lesssim \mathrm{Max}[\delta, \gamma_X]$ is satisfied. In this case, the DM number density does not freeze out at the typical freeze-out temperature $x_f = m_\psi/T_f \sim 20$ ($v_{\rm rel}^2 \sim 0.1$), and continues to decrease via the annihilation even at lower temperature. As a result, the actual freeze-out time is delayed and the produced thermal abundance is modified to be

$$\Omega h^2 \sim 0.1 \times \left(\frac{10^{-26}\,\mathrm{cm}^3/\mathrm{s}}{\langle \sigma v \rangle_{T=0}} \right) \frac{x_b}{x_f}, \tag{b.12}$$

where $x_f \simeq 20$ is the typical freeze-out temperature and x_b is the actual one. The actual freeze-out temperature is given by [343, 344]

$$\frac{1}{x_b} \simeq \frac{1}{\langle \sigma v \rangle_{T=0}} \int_{x_f}^{\infty} \frac{\langle \sigma v \rangle}{x^2} dx \simeq \mathrm{Max}[\delta, \gamma_X]. \tag{b.13}$$

It suggests that the cross section is boosted by a factor of x_b/x_f. $\mathrm{BF} = x_b/x_f$ is called the boost factor. We have $\gamma_X \propto g_X^2 \lesssim 10^{-6}$ in the model, the boost factor can be as large as 10^6 in a case.

Indirect detection experiments observe the neutrinos from DM annihilation in our Galaxy. Since the DM velocity is $v_{\rm rel} \sim 10^{-3}$ at most, we can approximate $(\sigma v)_{\nu\nu} \simeq \langle \sigma v \rangle_{T=0}$ for e.g. $\delta = 10^{-3}$. In this case, the boost factor is expected to have

$$\mathrm{BF} \simeq \frac{1}{10\,\mathrm{Max}[\delta, \gamma_X]} \sim 100 \tag{b.14}$$

leading to the enhanced cross section,

$$(\sigma v)_{\nu\bar{\nu}} \sim \mathrm{BF} \times 10^{-26}\,\mathrm{cm}^3/\mathrm{s}. \tag{b.15}$$

Before closing, we derive Eq.(b.12). In the standard way, the approximate solution of the Boltzmann equation is obtained by integrating the equation,

$$\frac{dY_{\mathrm{DM}}}{dx} \simeq -\frac{\lambda}{x^2} Y_{\mathrm{DM}}^2, \tag{b.16}$$

over $[x_f, \infty]$, where x_f is determined by appropriately matching the approximate solution with the actual one. Above, we assumed the s-wave DM annihilation and introduced $Y_{\mathrm{DM}} = n_{\mathrm{DM}}/s$ with s being the entropy density and

$$\lambda = \sqrt{\frac{8\pi^2}{45} g_*} M_{\mathrm{P}} m_{DM} \langle \sigma v \rangle_{T=0}\,. \tag{b.17}$$

Taking into account the resonant behavior of the cross section, the equation is modified as

$$\frac{dY_{\mathrm{DM}}}{dx} \simeq -\frac{\lambda}{x^2} \frac{\langle \sigma v \rangle_T}{\langle \sigma v \rangle_{T=0}} Y_{\mathrm{DM}}^2. \tag{b.18}$$

One can readily get Eq.(b.12) by solving this equation.

Appendix C

Miscellaneous formulae in Chapter 5

In this appendix, we give formulae that are useful for the study of the neutrino mass structure in the minimal gauged $\mathrm{U}(1)_{L_\mu - L_\tau}$ model discussed in chapter 5.

C.1 Mass Matrix for Active Neutrinos

From Eq. (2.37), the mass matrix for the active neutrinos are written in terms of the parameters of the Lagrangian in Eq (5.3) as follows :

$$\begin{aligned}\mathcal{M}_{\nu_L} =& \frac{v^2}{2(M_{ee}M_{\mu\tau} - 2h_{e\mu}h_{e\tau}\langle\sigma\rangle^2)} \\ &\times \begin{pmatrix} -\lambda_e^2 M_{\mu\tau} & \lambda_e\lambda_\mu h_{e\tau}\langle\sigma\rangle & \lambda_e\lambda_\tau h_{e\mu}\langle\sigma\rangle \\ \lambda_e\lambda_\mu h_{e\tau}\langle\sigma\rangle & -\frac{\lambda_\mu^2 h_{e\tau}^2\langle\sigma\rangle^2}{M_{\mu\tau}} & \frac{\lambda_\mu\lambda_\tau(-M_{ee}M_{\mu\tau}+h_{e\mu}h_{e\tau}\langle\sigma\rangle^2)}{M_{\mu\tau}} \\ \lambda_e\lambda_\tau h_{e\mu}\langle\sigma\rangle & \frac{\lambda_\mu\lambda_\tau(-M_{ee}M_{\mu\tau}+h_{e\mu}h_{e\tau}\langle\sigma\rangle^2)}{M_{\mu\tau}} & -\frac{\lambda_\tau^2 h_{e\mu}^2\langle\sigma\rangle^2}{M_{\mu\tau}} \end{pmatrix}. \end{aligned} \tag{c.1}$$

The determinant of $\mathcal{M}_{\nu_L}$ is given by

$$\det(\mathcal{M}_{\nu_L}) = \frac{\lambda_e^2\lambda_\mu^2\lambda_\tau^2 v^6}{8M_{\mu\tau}(M_{ee}M_{\mu\tau} - 2h_{e\mu}h_{e\tau}\langle\sigma\rangle^2)} \,. \tag{c.2}$$

From Eq. (c.2), the determinant is equal to be zero for $\lambda_\alpha = 0 (\alpha = e, \mu, \tau)$, and then $\mathcal{M}_{\nu_L}$ is block-diagonal. Therefore, the PMNS matrix is also block-diagonal, and this result conflicts with the observed neutrino mixing. From the above discussion, the determinant of $\mathcal{M}_{\nu_L}$ should not be zero, and this statement is the same as the lightest mass eigenvalue of the active neutrinos should not be zero.

C.2 R_2 and R_3

The explicit expression for R_2 and R_3 defined in Eqs. (5.10) are written in terms of the neutrino oscillation parameters as

$$R_2(\delta) = -\frac{2\sin^2\theta_{12}\cos 2\theta_{23} + \sin 2\theta_{12}\sin 2\theta_{23}\sin\theta_{13}e^{i\delta}}{2\cos^2\theta_{12}\cos 2\theta_{23} - \sin 2\theta_{12}\sin 2\theta_{23}\sin\theta_{13}e^{i\delta}} \ , \tag{c.3}$$

$$R_3(\delta) = -\frac{\sin\theta_{13}e^{2i\delta}[2\cos 2\theta_{12}\cos 2\theta_{23}\sin\theta_{13} - \sin 2\theta_{12}\sin 2\theta_{23}(e^{-i\delta} + \sin^2\theta_{13}e^{i\delta})]}{\cos^2\theta_{13}[2\cos^2\theta_{12}\cos 2\theta_{23} - \sin 2\theta_{12}\sin 2\theta_{23}\sin\theta_{13}e^{i\delta}]} \ . \tag{c.4}$$

C.3 Cubic Equation for $\cos\delta$

Here, we show a cubic equation whose real solution in terms of x gives $\cos\delta$:

$$\begin{aligned}
&s_{13}^2\big[4s_{13}^2\cos^2 2\theta_{12}\cos^2 2\theta_{23} - s_{13}\sin 4\theta_{12}\sin 4\theta_{23}(1+s_{13}^2)\,x \\
&+ \sin^2 2\theta_{12}\sin^2 2\theta_{23}\left(c_{13}^4 + 4s_{13}^2\,x^2\right)\big]\left[2\left(2\cos 2\theta_{12}\cos^2 2\theta_{23} - s_{13}\sin 2\theta_{12}\sin 4\theta_{23}\,x\right)\right] \\
&- \epsilon\left[4s_{12}^4\cos^2 2\theta_{23} + s_{13}^2\sin^2 2\theta_{12}\sin^2 2\theta_{23} + 4s_{12}^3 c_{12}s_{13}\sin 4\theta_{23}\,x\right] \\
&\times\left[4\cos^2 2\theta_{23}(c_{12}^4c_{13}^4 - s_{13}^4\cos^2 2\theta_{12}) - s_{13}\sin 4\theta_{23}\{4c_{13}^4c_{12}^3s_{12} - s_{13}^2\sin 4\theta_{12}(1+s_{13}^2)\}\,x\right. \\
&\left.- 4s_{13}^4\sin^2 2\theta_{12}\sin^2 2\theta_{23}\,x^2\right] = 0 \ ,
\end{aligned} \tag{c.5}$$

where

$$\epsilon \equiv \frac{\delta m^2}{\Delta m^2 + \delta m^2/2} \ . \tag{c.6}$$

In the limit of $\epsilon \to 0$, the above equation leads to

$$4s_{13}^2\cos^2 2\theta_{12}\cos^2 2\theta_{23} - s_{13}\sin 4\theta_{12}\sin 4\theta_{23}(1+s_{13}^2)\,x + \sin^2 2\theta_{12}\sin^2 2\theta_{23}\left(c_{13}^4 + 4s_{13}^2\,x^2\right) = 0 \ , \tag{c.7}$$

or

$$2\cos 2\theta_{12}\cos^2 2\theta_{23} - s_{13}\sin 2\theta_{12}\sin 4\theta_{23}\,x = 0 \ . \tag{c.8}$$

The discriminant of the quadratic equation (c.7) is given by

$$8c_{13}^4s_{13}^2\sin^2 2\theta_{12}\sin^2 2\theta_{23}(\cos 4\theta_{12} + \cos 4\theta_{23}) \ , \tag{c.9}$$

which is negative as $\cos 4\theta_{12} + \cos 4\theta_{23} \simeq -1.68 < 0$. Thus, Eq. (c.7) does not give a real solution. On the other hand, Eq. (c.8) gives

$$x = \frac{\cot 2\theta_{12}\cot 2\theta_{23}}{\sin\theta_{13}} \ , \tag{c.10}$$

which agrees to Eq. (5.17). From the above derivation, we see that the solution (c.10) approximates the real solution of the cubic equation (c.5) with an accuracy of $\mathcal{O}(\epsilon) = \mathcal{O}(\delta m^2/\Delta m^2)$.

Bibliography

[1] Muon g-2 collaboration, G. Bennett et al., *Measurement of the positive muon anomalous magnetic moment to 0.7 ppm*, *Phys. Rev. Lett.* **89** (2002) 101804, [hep-ex/0208001].

[2] Muon g-2 collaboration, G. Bennett et al., *Measurement of the negative muon anomalous magnetic moment to 0.7 ppm*, *Phys. Rev. Lett.* **92** (2004) 161802, [hep-ex/0401008].

[3] Muon g-2 collaboration, G. Bennett et al., *Final Report of the Muon E821 Anomalous Magnetic Moment Measurement at BNL*, *Phys. Rev. D* **73** (2006) 072003, [hep-ex/0602035].

[4] T. Aoyama, M. Hayakawa, T. Kinoshita and M. Nio, *Complete Tenth-Order QED Contribution to the Muon g-2*, *Phys. Rev. Lett.* **109** (2012) 111808, [1205.5370].

[5] T. Aoyama, T. Kinoshita and M. Nio, *Revised and Improved Value of the QED Tenth-Order Electron Anomalous Magnetic Moment*, *Phys. Rev. D* **97** (2018) 036001, [1712.06060].

[6] S. Volkov, *Calculating the five-loop QED contribution to the electron anomalous magnetic moment: Graphs without lepton loops*, *Phys. Rev. D* **100** (2019) 096004, [1909.08015].

[7] M. Knecht, S. Peris, M. Perrottet and E. De Rafael, *Electroweak hadronic contributions to the muon (g-2)*, *JHEP* **11** (2002) 003, [hep-ph/0205102].

[8] A. Czarnecki, W. J. Marciano and A. Vainshtein, *Refinements in electroweak contributions to the muon anomalous magnetic moment*, *Phys. Rev. D* **67** (2003) 073006, [hep-ph/0212229].

[9] C. Gnendiger, D. Stöckinger and H. Stöckinger-Kim, *The electroweak contributions to* $(g-2)_\mu$ *after the Higgs boson mass measurement*, *Phys. Rev. D* **88** (2013) 053005, [1306.5546].

[10] T. Ishikawa, N. Nakazawa and Y. Yasui, *Numerical calculation of the full two-loop electroweak corrections to muon (g-2)*, *Phys. Rev. D* **99** (2019) 073004, [1810.13445].

[11] M. Davier, A. Hoecker, B. Malaescu and Z. Zhang, *A new evaluation of the hadronic vacuum polarisation contributions to the muon anomalous magnetic moment and to* $\boldsymbol{\alpha(m_Z^2)}$, *Eur. Phys. J. C* **80** (2020) 241, [1908.00921].

[12] A. Keshavarzi, D. Nomura and T. Teubner, $g-2$ *of charged leptons,* $\alpha(M_Z^2)$ *, and the hyperfine splitting of muonium*, *Phys. Rev. D* **101** (2020) 014029, [1911.00367].

[13] M. Benayoun, L. Delbuono and F. Jegerlehner, *BHLS*$_2$*, a New Breaking of the HLS Model and its Phenomenology*, *Eur. Phys. J. C* **80** (2020) 81, [1903.11034].

[14] M. Hoferichter, B.-L. Hoid and B. Kubis, *Three-pion contribution to hadronic vacuum polarization*, *JHEP* **08** (2019) 137, [1907.01556].

[15] T. Blum, N. Christ, M. Hayakawa, T. Izubuchi, L. Jin, C. Jung et al., *Hadronic Light-by-Light Scattering Contribution to the Muon Anomalous Magnetic Moment from Lattice QCD*, *Phys. Rev. Lett.* **124** (2020) 132002, [1911.08123].

[16] T. Aoyama et al., *The anomalous magnetic moment of the muon in the Standard Model*, 2006.04822.

[17] V. C. Rubin and J. Ford, W.Kent, *Rotation of the Andromeda Nebula from a Spectroscopic Survey of Emission Regions*, *Astrophys. J.* **159** (1970) 379–403.

[18] V. C. Rubin, J. Ford, W. Kent and N. Thonnard, *Extended rotation curves of high-luminosity spiral galaxies. IV. Systematic dynamical properties, Sa through Sc*, *Astrophys. J. Lett.* **225** (1978) L107–L111.

[19] V. Rubin, N. Thonnard and J. Ford, W.K., *Rotational properties of 21 SC galaxies with a large range of luminosities and radii, from NGC 4605 /R = 4kpc/ to UGC 2885 /R = 122 kpc/*, *Astrophys. J.* **238** (1980) 471.

[20] V. Rubin, D. Burstein, J. Ford, W.K. and N. Thonnard, *Rotation velocities of 16 SA galaxies and a comparison of Sa, Sb, and SC rotation properties*, *Astrophys. J.* **289** (1985) 81.

[21] K. Begeman, A. Broeils and R. Sanders, *Extended rotation curves of spiral galaxies: Dark haloes and modified dynamics*, *Mon. Not. Roy. Astron. Soc.* **249** (1991) 523.

[22] WMAP collaboration, D. Spergel et al., *First year Wilkinson Microwave Anisotropy Probe (WMAP) observations: Determination of cosmological parameters*, *Astrophys. J. Suppl.* **148** (2003) 175–194, [astro-ph/0302209].

[23] Planck collaboration, P. Ade et al., *Planck 2013 results. XVI. Cosmological parameters*, *Astron. Astrophys.* **571** (2014) A16, [1303.5076].

[24] Planck collaboration, P. Ade et al., *Planck 2015 results. XIII. Cosmological parameters*, *Astron. Astrophys.* **594** (2016) A13, [1502.01589].

[25] Planck collaboration, N. Aghanim et al., *Planck 2018 results. VI. Cosmological parameters*, *Astron. Astrophys.* **641** (2020) A6, [1807.06209].

[26] ACT collaboration, S. Aiola et al., *The Atacama Cosmology Telescope: DR4 Maps and Cosmological Parameters*, 2007.07288.

[27] Super-Kamiokande collaboration, Y. Fukuda et al., *Evidence for oscillation of atmospheric neutrinos*, *Phys. Rev. Lett.* **81** (1998) 1562–1567, [hep-ex/9807003].

[28] S. D. White, C. Frenk and M. Davis, *Clustering in a Neutrino Dominated Universe*, *Astrophys. J. Lett.* **274** (1983) L1–L5.

[29] S. D. M. White, M. Davis and C. S. Frenk, *The size of clusters in a neutrino-dominated universe*, *M.N.R.A.S.* **209** (1984) 27–31.

[30] G. Jungman, M. Kamionkowski and K. Griest, *Supersymmetric dark matter*, *Phys. Rept.* **267** (1996) 195–373, [hep-ph/9506380].

[31] G. Servant and T. M. Tait, *Is the lightest Kaluza-Klein particle a viable dark matter candidate?*, *Nucl. Phys. B* **650** (2003) 391–419, [hep-ph/0206071].

[32] XENON collaboration, E. Aprile et al., *Dark Matter Search Results from a One Ton-Year Exposure of XENON1T*, *Phys. Rev. Lett.* **121** (2018) 111302, [1805.12562].

[33] XENON collaboration, E. Aprile et al., *Light Dark Matter Search with Ionization Signals in XENON1T*, *Phys. Rev. Lett.* **123** (2019) 251801, [1907.11485].

[34] XENON collaboration, E. Aprile et al., *Search for Light Dark Matter Interactions Enhanced by the Migdal Effect or Bremsstrahlung in XENON1T*, *Phys. Rev. Lett.* **123** (2019) 241803, [1907.12771].

[35] K. Asai, S. Okawa and K. Tsumura, *Search for $U(1)_{L_\mu - L_\tau}$ charged Dark Matter with neutrino telescope*, 2011.03165.

[36] M. Fukugita and T. Yanagida, *Baryogenesis Without Grand Unification*, *Phys. Lett. B* **174** (1986) 45–47.

[37] V. Kuzmin, V. Rubakov and M. Shaposhnikov, *On the Anomalous Electroweak Baryon Number Nonconservation in the Early Universe*, *Phys. Lett. B* **155** (1985) 36.

[38] P. Minkowski, *$\mu \to e\gamma$ at a Rate of One Out of 10^9 Muon Decays?*, *Phys. Lett. B* **67** (1977) 421–428.

[39] T. Yanagida, *Horizontal gauge symmetry and masses of neutrinos*, *Conf. Proc. C* **7902131** (1979) 95–99.

[40] M. Gell-Mann, P. Ramond and R. Slansky, *Complex Spinors and Unified Theories*, *Conf. Proc. C* **790927** (1979) 315–321, [1306.4669].

[41] R. N. Mohapatra and G. Senjanovic, *Neutrino Mass and Spontaneous Parity Nonconservation*, *Phys. Rev. Lett.* **44** (1980) 912.

[42] K. Asai, K. Hamaguchi and N. Nagata, *Predictions for the neutrino parameters in the minimal gauged $U(1)_{L_\mu - L_\tau}$ model*, *Eur. Phys. J. C* **77** (2017) 763, [1705.00419].

[43] K. Asai, K. Hamaguchi, N. Nagata, S.-Y. Tseng and K. Tsumura, *Minimal Gauged $U(1)_{L_\alpha - L_\beta}$ Models Driven into a Corner*, *Phys. Rev. D* **99** (2019) 055029, [1811.07571].

[44] K. Asai, *Predictions for the neutrino parameters in the minimal model extended by linear combination of $U(1)_{L_e - L_\mu}$, $U(1)_{L_\mu - L_\tau}$ and $U(1)_{B-L}$ gauge symmetries*, *Eur. Phys. J. C* **80** (2020) 76, [1907.04042].

[45] K. Asai, K. Hamaguchi, N. Nagata and S.-Y. Tseng, *Leptogenesis in the minimal gauged $U(1)_{L_\mu - L_\tau}$ model and the sign of the cosmological baryon asymmetry*, 2005.01039.

[46] R. Foot, *New Physics From Electric Charge Quantization?*, *Mod. Phys. Lett. A* **6** (1991) 527–530.

[47] X. He, G. C. Joshi, H. Lew and R. Volkas, *NEW Z-prime PHENOMENOLOGY*, *Phys. Rev. D* **43** (1991) 22–24.

[48] X.-G. He, G. C. Joshi, H. Lew and R. Volkas, *Simplest Z-prime model*, *Phys. Rev. D* **44** (1991) 2118–2132.

[49] R. Foot, X. He, H. Lew and R. Volkas, *Model for a light Z-prime boson*, *Phys. Rev. D* **50** (1994) 4571–4580, [hep-ph/9401250].

[50] Particle Data Group collaboration, P. Zyla et al., *Review of Particle Physics*, *PTEP* **2020** (2020) 083C01.

[51] S. Borsanyi et al., *Leading-order hadronic vacuum polarization contribution to the muon magnetic momentfrom lattice QCD*, 2002.12347.

[52] M. Bauer, P. Foldenauer and J. Jaeckel, *Hunting All the Hidden Photons*, *JHEP* **18** (2020) 094, [1803.05466].

[53] CHARM-II collaboration, D. Geiregat et al., *First observation of neutrino trident production*, *Phys. Lett. B* **245** (1990) 271–275.

[54] CCFR collaboration, S. Mishra et al., *Neutrino tridents and W Z interference*, *Phys. Rev. Lett.* **66** (1991) 3117–3120.

[55] W. Altmannshofer, S. Gori, M. Pospelov and I. Yavin, *Neutrino Trident Production: A Powerful Probe of New Physics with Neutrino Beams*, *Phys. Rev. Lett.* **113** (2014) 091801, [1406.2332].

[56] G. Bellini et al., *Precision measurement of the 7Be solar neutrino interaction rate in Borexino*, *Phys. Rev. Lett.* **107** (2011) 141302, [1104.1816].

[57] R. Harnik, J. Kopp and P. A. Machado, *Exploring nu Signals in Dark Matter Detectors*, *JCAP* **07** (2012) 026, [1202.6073].

[58] Y. Kaneta and T. Shimomura, *On the possibility of a search for the $L_\mu - L_\tau$ gauge boson at Belle-II and neutrino beam experiments*, *PTEP* **2017** (2017) 053B04, [1701.00156].

[59] BaBar collaboration, J. Lees et al., *Search for a muonic dark force at BABAR*, *Phys. Rev. D* **94** (2016) 011102, [1606.03501].

[60] H. K. Dreiner, J.-F. Fortin, J. Isern and L. Ubaldi, *White Dwarfs constrain Dark Forces*, *Phys. Rev. D* **88** (2013) 043517, [1303.7232].

[61] P. Foldenauer, *Dark Sectors from the Hidden Photon Perspective*, *PoS* **LHCP2019** (2019) 179, [1907.10630].

[62] A. Kamada, K. Kaneta, K. Yanagi and H.-B. Yu, *Self-interacting dark matter and muon $g-2$ in a gauged $U(1)_{L_\mu - L_\tau}$ model*, *JHEP* **06** (2018) 117, [1805.00651].

[63] M. Escudero, D. Hooper, G. Krnjaic and M. Pierre, *Cosmology with A Very Light $L_\mu - L_\tau$ Gauge Boson*, *JHEP* **03** (2019) 071, [1901.02010].

[64] BNL-E949 collaboration, A. Artamonov et al., *Study of the decay $K^+ \to \pi^+ \nu\bar{\nu}$ in the momentum region $140 < P_\pi < 199$ MeV/c*, *Phys. Rev. D* **79** (2009) 092004, [0903.0030].

[65] E949 collaboration, A. Artamonov et al., *Search for heavy neutrinos in $K^+ \to \mu^+ \nu_H$ decays*, *Phys. Rev. D* **91** (2015) 052001, [1411.3963].

[66] M. Ibe, W. Nakano and M. Suzuki, *Constraints on $L_\mu - L_\tau$ gauge interactions from rare kaon decay*, *Phys. Rev. D* **95** (2017) 055022, [1611.08460].

[67] S. Gninenko, N. Krasnikov and V. Matveev, *Muon g-2 and searches for a new leptophobic sub-GeV dark boson in a missing-energy experiment at CERN*, *Phys. Rev. D* **91** (2015) 095015, [1412.1400].

[68] S. Gninenko and N. Krasnikov, *Probing the muon g_μ - 2 anomaly, $L_\mu - L_\tau$ gauge boson and Dark Matter in dark photon experiments*, *Phys. Lett. B* **783** (2018) 24–28, [1801.10448].

[69] Belle-II collaboration, T. Abe et al., *Belle II Technical Design Report*, 1011.0352.

[70] T. Araki, S. Hoshino, T. Ota, J. Sato and T. Shimomura, *Detecting the $L_\mu - L_\tau$ gauge boson at Belle II*, *Phys. Rev. D* **95** (2017) 055006, [1702.01497].

[71] Y. Jho, Y. Kwon, S. C. Park and P.-Y. Tseng, *Search for muon-philic new light gauge boson at Belle II*, *JHEP* **10** (2019) 168, [1904.13053].

[72] Muon g-2 collaboration, J. Grange et al., *Muon (g-2) Technical Design Report*, 1501.06858.

[73] Muon g-2 collaboration, A. Keshavarzi, *The Muon $g-2$ Experiment at Fermilab*, *EPJ Web Conf.* **212** (2019) 05003, [1905.00497].

[74] J-PARC g-2 collaboration, T. Mibe, *Measurement of muon g-2 and EDM with an ultra-cold muon beam at J-PARC*, *Nucl. Phys. B Proc. Suppl.* **218** (2011) 242–246.

[75] M. Abe et al., *A New Approach for Measuring the Muon Anomalous Magnetic Moment and Electric Dipole Moment*, *PTEP* **2019** (2019) 053C02, [1901.03047].

[76] SHiP collaboration, M. Anelli et al., *A facility to Search for Hidden Particles (SHiP) at the CERN SPS*, 1504.04956.

[77] S. Alekhin et al., *A facility to Search for Hidden Particles at the CERN SPS: the SHiP physics case*, *Rept. Prog. Phys.* **79** (2016) 124201, [1504.04855].

[78] W. Altmannshofer, S. Gori, M. Pospelov and I. Yavin, *Quark flavor transitions in $L_\mu - L_\tau$ models*, *Phys. Rev. D* **89** (2014) 095033, [1403.1269].

[79] A. Crivellin, G. D'Ambrosio and J. Heeck, *Explaining $h \to \mu^\pm\tau^\mp$, $B \to K^*\mu^+\mu^-$ and $B \to K\mu^+\mu^-/B \to Ke^+e^-$ in a two-Higgs-doublet model with gauged $L_\mu - L_\tau$*, *Phys. Rev. Lett.* **114** (2015) 151801, [1501.00993].

[80] LHCb collaboration, R. Aaij et al., *Measurement of Form-Factor-Independent Observables in the Decay $B^0 \to K^{*0}\mu^+\mu^-$*, *Phys. Rev. Lett.* **111** (2013) 191801, [1308.1707].

[81] F. Reines and C. Cowan, *Detection of the free neutrino*, *Phys. Rev.* **92** (1953) 830–831.

[82] C. Cowan, F. Reines, F. Harrison, H. Kruse and A. McGuire, *Detection of the free neutrino: A Confirmation*, *Science* **124** (1956) 103–104.

[83] E. Majorana, *Teoria simmetrica dell'elettrone e del positrone*, *Nuovo Cim.* **14** (1937) 171–184.

[84] H. Bethe and R. Bacher, *Nuclear Physics A. Stationary States of Nuclei*, *Rev. Mod. Phys.* **8** (1936) 82–229.

[85] NEMO-3 collaboration, R. Arnold et al., *Measurement of the double-beta decay half-life and search for the neutrinoless double-beta decay of ^{48}Ca with the NEMO-3 detector*, *Phys. Rev. D* **93** (2016) 112008, [1604.01710].

[86] J. Schechter and J. Valle, *Neutrinoless Double beta Decay in SU(2) x U(1) Theories*, *Phys. Rev. D* **25** (1982) 2951.

[87] B. Pontecorvo, *Inverse beta processes and nonconservation of lepton charge*, *Sov. Phys. JETP* **7** (1958) 172–173.

[88] Z. Maki, M. Nakagawa and S. Sakata, *Remarks on the unified model of elementary particles*, *Prog. Theor. Phys.* **28** (1962) 870–880.

[89] H. Klapdor-Kleingrothaus, A. Dietz, H. Harney and I. Krivosheina, *Evidence for neutrinoless double beta decay*, *Mod. Phys. Lett. A* **16** (2001) 2409–2420, [hep-ph/0201231].

[90] H. Klapdor-Kleingrothaus, I. Krivosheina, A. Dietz and O. Chkvorets, *Search for neutrinoless double beta decay with enriched Ge-76 in Gran Sasso 1990-2003*, *Phys. Lett. B* **586** (2004) 198–212, [hep-ph/0404088].

[91] H. Klapdor-Kleingrothaus and I. Krivosheina, *The evidence for the observation of 0nu beta beta decay: The identification of 0nu beta beta events from the full spectra*, *Mod. Phys. Lett. A* **21** (2006) 1547–1566.

[92] C. Aalseth et al., *Comment on 'Evidence for neutrinoless double beta decay'*, *Mod. Phys. Lett. A* **17** (2002) 1475–1478, [hep-ex/0202018].

[93] Y. Zdesenko, F. A. Danevich and V. Tretyak, *Has neutrinoless double beta decay of Ge-76 been really observed?*, *Phys. Lett. B* **546** (2002) 206–215.

[94] F. Feruglio, A. Strumia and F. Vissani, *Neutrino oscillations and signals in beta and 0nu2beta experiments*, *Nucl. Phys. B* **637** (2002) 345–377, [hep-ph/0201291].

[95] B. Schwingenheuer, *Status and prospects of searches for neutrinoless double beta decay*, *Annalen Phys.* **525** (2013) 269–280, [1210.7432].

[96] M. Koga, *Kamland-zen 800 status and future prospects*, in *6th International Conference on New Frontiers in Physics (ICNFP 2017) Kolymbari, Crete, Greece, August 17-26,2017*, 2017.

[97] KamLAND-Zen collaboration, J. Shirai, *Results and future plans for the KamLAND-Zen experiment*, *J. Phys. Conf. Ser.* **888** (2017) 012031.

[98] SNO+ collaboration, S. Andringa et al., *Current Status and Future Prospects of the SNO+ Experiment*, *Adv. High Energy Phys.* **2016** (2016) 6194250, [1508.05759].

[99] LEGEND collaboration, N. Abgrall et al., *The Large Enriched Germanium Experiment for Neutrinoless Double Beta Decay (LEGEND)*, *AIP Conf. Proc.* **1894** (2017) 020027, [1709.01980].

[100] CUORE collaboration, J. Ouellet, *The Search for Neutrinoless Double Beta Decay with CUORE*, *PoS* **HQL2016** (2017) 015.

[101] CUPID collaboration, G. Wang et al., *CUPID: CUORE (Cryogenic Underground Observatory for Rare Events) Upgrade with Particle IDentification*, 1504.03599.

[102] NEXT collaboration, V. Alvarez et al., *NEXT-100 Technical Design Report (TDR): Executive Summary*, *JINST* **7** (2012) T06001, [1202.0721].

[103] NEXT collaboration, J. Martín-Albo et al., *Sensitivity of NEXT-100 to Neutrinoless Double Beta Decay*, *JHEP* **05** (2016) 159, [1511.09246].

[104] C. Patrick and F. Xie, *Status of the SuperNEMO $0\nu\beta\beta$ experiment*, in *Prospects in Neutrino Physics*, 4, 2017, 1704.06670.

[105] nEXO collaboration, J. Albert et al., *Sensitivity and Discovery Potential of nEXO to Neutrinoless Double Beta Decay*, *Phys. Rev. C* **97** (2018) 065503, [1710.05075].

[106] KamLAND-Zen collaboration, A. Gando et al., *Search for Majorana Neutrinos near the Inverted Mass Hierarchy Region with KamLAND-Zen*, *Phys. Rev. Lett.* **117** (2016) 082503, [1605.02889].

[107] S. Roy Choudhury and S. Hannestad, *Updated results on neutrino mass and mass hierarchy from cosmology with Planck 2018 likelihoods*, *JCAP* **07** (2020) 037, [1907.12598].

[108] G. Bellini, L. Ludhova, G. Ranucci and F. Villante, *Neutrino oscillations*, *Adv. High Energy Phys.* **2014** (2014) 191960, [1310.7858].

[109] "**NuFIT** Collaboration, "Nufit v4.1"." http://www.nu-fit.org.

[110] I. Esteban, M. Gonzalez-Garcia, A. Hernandez-Cabezudo, M. Maltoni and T. Schwetz, *Global analysis of three-flavour neutrino oscillations: synergies and tensions in the determination of θ_{23}, δ_{CP}, and the mass ordering*, *JHEP* **01** (2019) 106, [1811.05487].

[111] N. Y. Gnedin and O. Y. Gnedin, *Cosmological neutrino background revisited*, *Astrophys. J.* **509** (1998) 11–15, [astro-ph/9712199].

[112] G. Mangano, G. Miele, S. Pastor, T. Pinto, O. Pisanti and P. D. Serpico, *Relic neutrino decoupling including flavor oscillations*, *Nucl. Phys. B* **729** (2005) 221–234, [hep-ph/0506164].

[113] J. Birrell, C.-T. Yang and J. Rafelski, *Relic Neutrino Freeze-out: Dependence on Natural Constants*, *Nucl. Phys. B* **890** (2014) 481–517, [1406.1759].

[114] E. Grohs, G. M. Fuller, C. T. Kishimoto, M. W. Paris and A. Vlasenko, *Neutrino energy transport in weak decoupling and big bang nucleosynthesis*, *Phys. Rev. D* **93** (2016) 083522, [1512.02205].

[115] P. F. de Salas and S. Pastor, *Relic neutrino decoupling with flavour oscillations revisited*, *JCAP* **07** (2016) 051, [1606.06986].

[116] M. Saha, *LIII. Ionization in the solar chromosphere*, *The London, Edinburgh, and Dublin Philosophical Magazine and Journal of Science* **40** (1920) 472–488.

[117] M. Saha, *On a physical theory of stellar spectra*, *Proc. R. Soc. Lond. A* **99** (1921) 135–153.

[118] J. A. Peacock, *Cosmological Physics*. Cambridge University Press, 1998.

[119] E. W. Kolb and M. S. Turner, *The Early Universe*, vol. 69. 1990.

[120] F. Zwicky, *Die Rotverschiebung von extragalaktischen Nebeln*, *Helv. Phys. Acta* **6** (1933) 110–127.

[121] F. Zwicky, *On the Masses of Nebulae and of Clusters of Nebulae*, *Astrophys. J.* **86** (1937) 217–246.

[122] B. W. Lee and S. Weinberg, *Cosmological Lower Bound on Heavy Neutrino Masses*, *Phys. Rev. Lett.* **39** (1977) 165–168.

[123] M. Pospelov, A. Ritz and M. B. Voloshin, *Secluded WIMP Dark Matter*, *Phys. Lett. B* **662** (2008) 53–61, [0711.4866].

[124] M. Pospelov and A. Ritz, *Astrophysical Signatures of Secluded Dark Matter*, *Phys. Lett. B* **671** (2009) 391–397, [0810.1502].

[125] N. Arkani-Hamed, D. P. Finkbeiner, T. R. Slatyer and N. Weiner, *A Theory of Dark Matter*, *Phys. Rev. D* **79** (2009) 015014, [0810.0713].

[126] M. W. Goodman and E. Witten, *Detectability of Certain Dark Matter Candidates*, *Phys. Rev. D* **31** (1985) 3059.

[127] A. Alves, A. Berlin, S. Profumo and F. S. Queiroz, *Dark Matter Complementarity and the Z' Portal*, *Phys. Rev. D* **92** (2015) 083004, [1501.03490].

[128] A. Alves, A. Berlin, S. Profumo and F. S. Queiroz, *Dirac-fermionic dark matter in $U(1)_X$ models*, *JHEP* **10** (2015) 076, [1506.06767].

[129] R. Essig, *Direct Detection of Non-Chiral Dark Matter*, *Phys. Rev. D* **78** (2008) 015004, [0710.1668].

[130] P. Agrawal, Z. Chacko, C. Kilic and R. K. Mishra, *A Classification of Dark Matter Candidates with Primarily Spin-Dependent Interactions with Matter*, 1003.1912.

[131] J. R. Ellis, A. Ferstl and K. A. Olive, *Reevaluation of the elastic scattering of supersymmetric dark matter*, *Phys. Lett. B* **481** (2000) 304–314, [hep-ph/0001005].

[132] G. Mallot, *The Spin structure of the nucleon*, *eConf* **C990809** (2000) 521–537, [hep-ex/9912040].

[133] M. Ressell, M. B. Aufderheide, S. D. Bloom, K. Griest, G. J. Mathews and D. A. Resler, *Nuclear shell model calculations of neutralino - nucleus cross-sections for Si-29 and Ge-73*, *Phys. Rev. D* **48** (1993) 5519–5535, [hep-ph/9307228].

[134] V. Dimitrov, J. Engel and S. Pittel, *Scattering of weakly interacting massive particles from Ge-73*, *Phys. Rev. D* **51** (1995) 291–295, [hep-ph/9408246].

[135] XENON collaboration, E. Aprile et al., *Projected WIMP Sensitivity of the XENONnT Dark Matter Experiment*, 2007.08796.

[136] PandaX-II collaboration, X. Cui et al., *Dark Matter Results From 54-Ton-Day Exposure of PandaX-II Experiment*, *Phys. Rev. Lett.* **119** (2017) 181302, [1708.06917].

[137] LUX collaboration, D. Akerib et al., *Results from a search for dark matter in the complete LUX exposure*, *Phys. Rev. Lett.* **118** (2017) 021303, [1608.07648].

[138] DEAP collaboration, R. Ajaj et al., *Search for dark matter with a 231-day exposure of liquid argon using DEAP-3600 at SNOLAB*, *Phys. Rev. D* **100** (2019) 022004, [1902.04048].

[139] PICO collaboration, C. Amole et al., *Dark Matter Search Results from the Complete Exposure of the PICO-60 C_3F_8 Bubble Chamber*, *Phys. Rev. D* **100** (2019) 022001, [1902.04031].

[140] SuperCDMS collaboration, R. Agnese et al., *Search for Low-Mass Dark Matter with CDMSlite Using a Profile Likelihood Fit*, *Phys. Rev. D* **99** (2019) 062001, [1808.09098].

[141] CRESST collaboration, A. Abdelhameed et al., *First results from the CRESST-III low-mass dark matter program*, *Phys. Rev. D* **100** (2019) 102002, [1904.00498].

[142] NEWS-G collaboration, Q. Arnaud et al., *First results from the NEWS-G direct dark matter search experiment at the LSM*, *Astropart. Phys.* **97** (2018) 54–62, [1706.04934].

[143] DAMIC collaboration, A. Aguilar-Arevalo et al., *Results on low-mass weakly interacting massive particles from a 11 kg-day target exposure of DAMIC at SNOLAB*, 2007.15622.

[144] EDELWEISS collaboration, Q. Arnaud et al., *Optimizing EDELWEISS detectors for low-mass WIMP searches*, *Phys. Rev. D* **97** (2018) 022003, [1707.04308].

[145] SuperCDMS collaboration, R. Agnese et al., *Results from the Super Cryogenic Dark Matter Search Experiment at Soudan*, *Phys. Rev. Lett.* **120** (2018) 061802, [1708.08869].

[146] DarkSide collaboration, P. Agnes et al., *Low-Mass Dark Matter Search with the DarkSide-50 Experiment*, *Phys. Rev. Lett.* **121** (2018) 081307, [1802.06994].

[147] SuperCDMS collaboration, R. Agnese et al., *Projected Sensitivity of the SuperCDMS SNOLAB experiment*, *Phys. Rev. D* **95** (2017) 082002, [1610.00006].

[148] LZ collaboration, D. Akerib et al., *LUX-ZEPLIN (LZ) Conceptual Design Report*, 1509.02910.

[149] C. Aalseth et al., *The DarkSide Multiton Detector for the Direct Dark Matter Search*, *Adv. High Energy Phys.* **2015** (2015) 541362.

[150] DARWIN collaboration, J. Aalbers et al., *DARWIN: towards the ultimate dark matter detector*, *JCAP* **11** (2016) 017, [1606.07001].

[151] R. Bernabei et al., *Dark matter search*, *Riv. Nuovo Cim.* **26N1** (2003) 1–73, [astro-ph/0307403].

[152] DAMA collaboration, R. Bernabei et al., *First results from DAMA/LIBRA and the combined results with DAMA/NaI*, *Eur. Phys. J. C* **56** (2008) 333–355, [0804.2741].

[153] J. Billard, L. Strigari and E. Figueroa-Feliciano, *Implication of neutrino backgrounds on the reach of next generation dark matter direct detection experiments*, *Phys. Rev. D* **89** (2014) 023524, [1307.5458].

[154] R. Bernabei et al., *Final model independent result of DAMA/LIBRA-phase1*, *Eur. Phys. J. C* **73** (2013) 2648, [1308.5109].

[155] COSINE-100 collaboration, G. Adhikari et al., *Search for a Dark Matter-Induced Annual Modulation Signal in NaI(Tl) with the COSINE-100 Experiment*, *Phys. Rev. Lett.* **123** (2019) 031302, [1903.10098].

[156] SABRE collaboration, M. Antonello et al., *The SABRE project and the SABRE Proof-of-Principle*, *Eur. Phys. J. C* **79** (2019) 363, [1806.09340].

[157] J. Amaré et al., *First Results on Dark Matter Annual Modulation from the ANAIS-112 Experiment*, *Phys. Rev. Lett.* **123** (2019) 031301, [1903.03973].

[158] PICO-LON collaboration, K. Fushimi et al., *Dark matter search project PICO-LON*, *J. Phys. Conf. Ser.* **718** (2016) 042022, [1512.04645].

[159] J. Vergados and H. Ejiri, *Can Solar Neutrinos be a Serious Background in Direct Dark Matter Searches?*, *Nucl. Phys. B* **804** (2008) 144–159, [0805.2583].

[160] R. Yakabe et al., *First limits from a 3d-vector directional dark matter search with the NEWAGE-0.3b' detector*, 2005.05157.

[161] NEWSdm collaboration, N. Agafonova et al., *Discovery potential for directional Dark Matter detection with nuclear emulsions*, *Eur. Phys. J. C* **78** (2018) 578, [1705.00613].

[162] E. Behnke et al., *Final Results of the PICASSO Dark Matter Search Experiment*, *Astropart. Phys.* **90** (2017) 85–92, [1611.01499].

[163] SIMPLE collaboration, M. Felizardo et al., *The SIMPLE Phase II Dark Matter Search*, *Phys. Rev. D* **89** (2014) 072013, [1404.4309].

[164] COUPP collaboration, E. Behnke et al., *First Dark Matter Search Results from a 4-kg CF_3I Bubble Chamber Operated in a Deep Underground Site*, *Phys. Rev. D* **86** (2012) 052001, [1204.3094].

[165] PandaX-II collaboration, J. Xia et al., *PandaX-II Constraints on Spin-Dependent WIMP-Nucleon Effective Interactions*, *Phys. Lett. B* **792** (2019) 193–198, [1807.01936].

[166] XENON collaboration, E. Aprile et al., *Constraining the spin-dependent WIMP-nucleon cross sections with XENON1T*, *Phys. Rev. Lett.* **122** (2019) 141301, [1902.03234].

[167] LUX collaboration, D. Akerib et al., *Limits on spin-dependent WIMP-nucleon cross section obtained from the complete LUX exposure*, *Phys. Rev. Lett.* **118** (2017) 251302, [1705.03380].

[168] Super-Kamiokande collaboration, K. Choi et al., *Search for neutrinos from annihilation of captured low-mass dark matter particles in the Sun by Super-Kamiokande*, *Phys. Rev. Lett.* **114** (2015) 141301, [1503.04858].

[169] IceCube collaboration, M. Aartsen et al., *Improved limits on dark matter annihilation in the Sun with the 79-string IceCube detector and implications for supersymmetry*, *JCAP* **04** (2016) 022, [1601.00653].

[170] R. Essig, M. Fernandez-Serra, J. Mardon, A. Soto, T. Volansky and T.-T. Yu, *Direct Detection of sub-GeV Dark Matter with Semiconductor Targets*, *JHEP* **05** (2016) 046, [1509.01598].

[171] XENON10 collaboration, J. Angle et al., *A search for light dark matter in XENON10 data*, *Phys. Rev. Lett.* **107** (2011) 051301, [1104.3088].

[172] XENON100 collaboration, E. Aprile et al., *Observation and applications of single-electron charge signals in the XENON100 experiment*, *J. Phys. G* **41** (2014) 035201, [1311.1088].

[173] R. Essig, T. Volansky and T.-T. Yu, *New Constraints and Prospects for sub-GeV Dark Matter Scattering off Electrons in Xenon*, *Phys. Rev. D* **96** (2017) 043017, [1703.00910].

[174] SENSEI collaboration, L. Barak et al., *SENSEI: Direct-Detection Results on sub-GeV Dark Matter from a New Skipper-CCD*, *Phys. Rev. Lett.* **125** (2020) 171802, [2004.11378].

[175] SENSEI collaboration, M. Crisler, R. Essig, J. Estrada, G. Fernandez, J. Tiffenberg, M. Sofo haro et al., *SENSEI: First Direct-Detection Constraints on sub-GeV Dark Matter from a Surface Run*, *Phys. Rev. Lett.* **121** (2018) 061803, [1804.00088].

[176] SENSEI collaboration, O. Abramoff et al., *SENSEI: Direct-Detection Constraints on Sub-GeV Dark Matter from a Shallow Underground Run Using a Prototype Skipper-CCD*, *Phys. Rev. Lett.* **122** (2019) 161801, [1901.10478].

[177] DarkSide collaboration, P. Agnes et al., *Constraints on Sub-GeV Dark-Matter–Electron Scattering from the DarkSide-50 Experiment*, *Phys. Rev. Lett.* **121** (2018) 111303, [1802.06998].

[178] SuperCDMS collaboration, R. Agnese et al., *First Dark Matter Constraints from a SuperCDMS Single-Charge Sensitive Detector*, *Phys. Rev. Lett.* **121** (2018) 051301, [1804.10697].

[179] DAMIC collaboration, A. Aguilar-Arevalo et al., *Constraints on Light Dark Matter Particles Interacting with Electrons from DAMIC at SNOLAB*, *Phys. Rev. Lett.* **123** (2019) 181802, [1907.12628].

[180] J. F. Navarro, C. S. Frenk and S. D. White, *A Universal density profile from hierarchical clustering*, *Astrophys. J.* **490** (1997) 493–508, [astro-ph/9611107].

[181] J. N. Bahcall and R. Soneira, *The Universe at faint magnetidues. 2. Models for the predicted star counts*, *Astrophys. J. Suppl.* **44** (1980) 73–110.

[182] A. Burkert, *The Structure of dark matter halos in dwarf galaxies*, *IAU Symp.* **171** (1996) 175, [astro-ph/9504041].

[183] B. Moore, S. Ghigna, F. Governato, G. Lake, T. R. Quinn, J. Stadel et al., *Dark matter substructure within galactic halos*, *Astrophys. J. Lett.* **524** (1999) L19–L22, [astro-ph/9907411].

[184] J. Diemand, B. Moore and J. Stadel, *Convergence and scatter of cluster density profiles*, *Mon. Not. Roy. Astron. Soc.* **353** (2004) 624, [astro-ph/0402267].

[185] Y. Jing and Y. Suto, *Density profiles of dark matter halo are not universal*, *Astrophys. J. Lett.* **529** (2000) L69–72, [astro-ph/9909478].

[186] J. F. Navarro, E. Hayashi, C. Power, A. Jenkins, C. S. Frenk, S. D. White et al., *The Inner structure of Lambda-CDM halos 3: Universality and asymptotic slopes*, *Mon. Not. Roy. Astron. Soc.* **349** (2004) 1039, [astro-ph/0311231].

[187] J. Einasto, *О ПОСТРОЕНИИ СОСТАВНОЙ МОДЕЛИ ГАЛАКТИКИ И ОПРЕДЕЛЕНИИ СИСТЕМЫ ГАЛАКТИЧЕСКИХ ПАРАМЕТРОВ*, *Trudy Astrofizicheskogo Instituta Alma-Ata* **5** (1965) 87–100.

[188] K. Hayashi and M. Chiba, *Probing non-spherical dark halos in the Galactic dwarf galaxies*, *Astrophys. J.* **755** (2012) 145, [1206.3888].

[189] Fermi-LAT collaboration, M. Ackermann et al., *Searching for Dark Matter Annihilation from Milky Way Dwarf Spheroidal Galaxies with Six Years of Fermi Large Area Telescope Data*, *Phys. Rev. Lett.* **115** (2015) 231301, [1503.02641].

[190] Fermi-LAT collaboration, M. Ackermann et al., *The Fermi Galactic Center GeV Excess and Implications for Dark Matter*, *Astrophys. J.* **840** (2017) 43, [1704.03910].

[191] CTA Consortium collaboration, B. Acharya et al., *Science with the Cherenkov Telescope Array*. WSP, 11, 2018, 10.1142/10986.

[192] H.E.S.S. collaboration, H. Abdallah et al., *Search for dark matter annihilations towards the inner Galactic halo from 10 years of observations with H.E.S.S*, *Phys. Rev. Lett.* **117** (2016) 111301, [1607.08142].

[193] T. Daylan, D. P. Finkbeiner, D. Hooper, T. Linden, S. K. N. Portillo, N. L. Rodd et al., *The characterization of the gamma-ray signal from the central Milky Way: A case for annihilating dark matter*, *Phys. Dark Univ.* **12** (2016) 1–23, [1402.6703].

[194] F. Calore, I. Cholis and C. Weniger, *Background Model Systematics for the Fermi GeV Excess*, *JCAP* **03** (2015) 038, [1409.0042].

[195] K. N. Abazajian and R. E. Keeley, *Bright gamma-ray Galactic Center excess and dark dwarfs: Strong tension for dark matter annihilation despite Milky Way halo profile and diffuse emission uncertainties*, *Phys. Rev. D* **93** (2016) 083514, [1510.06424].

[196] G. Steigman, B. Dasgupta and J. F. Beacom, *Precise Relic WIMP Abundance and its Impact on Searches for Dark Matter Annihilation*, *Phys. Rev. D* **86** (2012) 023506, [1204.3622].

[197] O. Macias, C. Gordon, R. M. Crocker, B. Coleman, D. Paterson, S. Horiuchi et al., *Galactic bulge preferred over dark matter for the Galactic centre gamma-ray excess*, *Nature Astron.* **2** (2018) 387–392, [1611.06644].

[198] R. Bartels, E. Storm, C. Weniger and F. Calore, *The Fermi-LAT GeV excess as a tracer of stellar mass in the Galactic bulge*, *Nature Astron.* **2** (2018) 819–828, [1711.04778].

[199] G. Steigman, *Observational tests of antimatter cosmologies*, *Ann. Rev. Astron. Astrophys.* **14** (1976) 339–372.

[200] G. Steigman, *When Clusters Collide: Constraints On Antimatter On The Largest Scales*, *JCAP* **10** (2008) 001, [0808.1122].

[201] AMS collaboration, J. Alcaraz et al., *Search for anti-helium in cosmic rays*, *Phys. Lett. B* **461** (1999) 387–396, [hep-ex/0002048].

[202] A. G. Cohen, A. De Rujula and S. Glashow, *A Matter - antimatter universe?*, *Astrophys. J.* **495** (1998) 539–549, [astro-ph/9707087].

[203] A. G. Cohen and A. De Rujula, *Scars on the CBR?*, astro-ph/9709132.

[204] W. Mampe, L. Bondarenko, V. Morozov, Y. Panin and A. Fomin, *Measuring neutron lifetime by storing ultracold neutrons and detecting inelastically scattered neutrons*, *JETP Lett.* **57** (1993) 82–87.

[205] A. Serebrov et al., *Measurement of the neutron lifetime using a gravitational trap and a low-temperature Fomblin coating*, *Phys. Lett. B* **605** (2005) 72–78, [nucl-ex/0408009].

[206] A. Pichlmaier, V. Varlamov, K. Schreckenbach and P. Geltenbort, *Neutron lifetime measurement with the UCN trap-in-trap MAMBO II*, *Phys. Lett. B* **693** (2010) 221–226.

[207] A. Steyerl, J. Pendlebury, C. Kaufman, S. Malik and A. Desai, *Quasielastic scattering in the interaction of ultracold neutrons with a liquid wall and application in a reanalysis of the Mambo I neutron-lifetime experiment*, *Phys. Rev. C* **85** (2012) 065503.

[208] S. Arzumanov, L. Bondarenko, S. Chernyavsky, P. Geltenbort, V. Morozov, V. Nesvizhevsky et al., *A measurement of the neutron lifetime using the method of storage of ultracold neutrons and detection of inelastically up-scattered neutrons*, *Phys. Lett. B* **745** (2015) 79–89.

[209] A. Serebrov et al., *New measurement of the neutron lifetime with a large gravitational trap*, *JETP Lett.* **106** (2017) 623–629.

[210] J. Pattie, R.W. et al., *Measurement of the neutron lifetime using a magneto-gravitational trap and in situ detection*, *Science* **360** (2018) 627–632, [1707.01817].

[211] V. Ezhov et al., *Measurement of the neutron lifetime with ultra-cold neutrons stored in a magneto-gravitational trap*, *JETP Lett.* **107** (2018) 671–675, [1412.7434].

[212] J. Byrne and P. Dawber, *A Revised Value for the Neutron Lifetime Measured Using a Penning Trap*, *Europhys. Lett.* **33** (1996) 187.

[213] A. Yue, M. Dewey, D. Gilliam, G. Greene, A. Laptev, J. Nico et al., *Improved Determination of the Neutron Lifetime*, *Phys. Rev. Lett.* **111** (2013) 222501, [1309.2623].

[214] A. Sakharov, *Violation of CP Invariance, C asymmetry, and baryon asymmetry of the universe*, *Sov. Phys. Usp.* **34** (1991) 392–393.

[215] N. Manton, *Topology in the Weinberg-Salam Theory*, *Phys. Rev. D* **28** (1983) 2019.

[216] F. R. Klinkhamer and N. Manton, *A Saddle Point Solution in the Weinberg-Salam Theory*, *Phys. Rev. D* **30** (1984) 2212.

[217] P. B. Arnold and L. D. McLerran, *Sphalerons, Small Fluctuations and Baryon Number Violation in Electroweak Theory*, *Phys. Rev. D* **36** (1987) 581.

[218] S. Khlebnikov and M. Shaposhnikov, *The Statistical Theory of Anomalous Fermion Number Nonconservation*, *Nucl. Phys. B* **308** (1988) 885–912.

[219] D. Bodeker, G. D. Moore and K. Rummukainen, *Chern-Simons number diffusion and hard thermal loops on the lattice*, *Phys. Rev. D* **61** (2000) 056003, [hep-ph/9907545].

[220] G. D. Moore, *Sphaleron rate in the symmetric electroweak phase*, *Phys. Rev. D* **62** (2000) 085011, [hep-ph/0001216].

[221] J. A. Harvey and M. S. Turner, *Cosmological baryon and lepton number in the presence of electroweak fermion number violation*, *Phys. Rev. D* **42** (1990) 3344–3349.

[222] G. Lazarides and Q. Shafi, *Origin of matter in the inflationary cosmology*, *Phys. Lett. B* **258** (1991) 305–309.

[223] K. Kumekawa, T. Moroi and T. Yanagida, *Flat potential for inflaton with a discrete R invariance in supergravity*, *Prog. Theor. Phys.* **92** (1994) 437–448, [hep-ph/9405337].

[224] G. Lazarides, *Leptogenesis in supersymmetric hybrid inflation*, *Springer Tracts Mod. Phys.* **163** (2000) 227–245, [hep-ph/9904428].

[225] G. Giudice, M. Peloso, A. Riotto and I. Tkachev, *Production of massive fermions at preheating and leptogenesis*, *JHEP* **08** (1999) 014, [hep-ph/9905242].

[226] T. Asaka, K. Hamaguchi, M. Kawasaki and T. Yanagida, *Leptogenesis in inflaton decay*, *Phys. Lett. B* **464** (1999) 12–18, [hep-ph/9906366].

[227] T. Asaka, K. Hamaguchi, M. Kawasaki and T. Yanagida, *Leptogenesis in inflationary universe*, *Phys. Rev. D* **61** (2000) 083512, [hep-ph/9907559].

[228] M. Kawasaki, M. Yamaguchi and T. Yanagida, *Natural chaotic inflation in supergravity and leptogenesis*, *Phys. Rev. D* **63** (2001) 103514, [hep-ph/0011104].

[229] K. Hamaguchi, *Cosmological baryon asymmetry and neutrinos: Baryogenesis via leptogenesis in supersymmetric theories*, other thesis, 12, 2002.

[230] L. Covi and E. Roulet, *Baryogenesis from mixed particle decays*, *Phys. Lett. B* **399** (1997) 113–118, [hep-ph/9611425].

[231] A. Pilaftsis, *Resonant CP violation induced by particle mixing in transition amplitudes*, *Nucl. Phys. B* **504** (1997) 61–107, [hep-ph/9702393].

[232] W. Buchmuller and M. Plumacher, *CP asymmetry in Majorana neutrino decays*, *Phys. Lett. B* **431** (1998) 354–362, [hep-ph/9710460].

[233] A. Pilaftsis and T. E. Underwood, *Resonant leptogenesis*, *Nucl. Phys. B* **692** (2004) 303–345, [hep-ph/0309342].

[234] A. Pilaftsis and T. E. Underwood, *Electroweak-scale resonant leptogenesis*, *Phys. Rev. D* **72** (2005) 113001, [hep-ph/0506107].

[235] A. Anisimov, A. Broncano and M. Plumacher, *The CP-asymmetry in resonant leptogenesis*, *Nucl. Phys. B* **737** (2006) 176–189, [hep-ph/0511248].

[236] B. Dev, M. Garny, J. Klaric, P. Millington and D. Teresi, *Resonant enhancement in leptogenesis*, *Int. J. Mod. Phys. A* **33** (2018) 1842003, [1711.02863].

[237] M. Flanz, E. A. Paschos and U. Sarkar, *Baryogenesis from a lepton asymmetric universe*, *Phys. Lett. B* **345** (1995) 248–252, [hep-ph/9411366].

[238] L. Covi, E. Roulet and F. Vissani, *CP violating decays in leptogenesis scenarios*, *Phys. Lett. B* **384** (1996) 169–174, [hep-ph/9605319].

[239] W. Fischler, G. Giudice, R. Leigh and S. Paban, *Constraints on the baryogenesis scale from neutrino masses*, *Phys. Lett. B* **258** (1991) 45–48.

[240] W. Buchmuller and T. Yanagida, *Baryogenesis and the scale of B-L breaking*, *Phys. Lett. B* **302** (1993) 240–244.

[241] W. Buchmuller, P. Di Bari and M. Plumacher, *Leptogenesis for pedestrians*, *Annals Phys.* **315** (2005) 305–351, [hep-ph/0401240].

[242] G. Branco, W. Grimus and L. Lavoura, *The Seesaw Mechanism in the Presence of a Conserved Lepton Number*, *Nucl. Phys. B* **312** (1989) 492–508.

[243] S. Choubey and W. Rodejohann, *A Flavor symmetry for quasi-degenerate neutrinos: L(mu) - L(tau)*, *Eur. Phys. J. C* **40** (2005) 259–268, [hep-ph/0411190].

[244] T. Araki, J. Heeck and J. Kubo, *Vanishing Minors in the Neutrino Mass Matrix from Abelian Gauge Symmetries*, *JHEP* **07** (2012) 083, [1203.4951].

[245] J. Heeck, *Neutrinos and Abelian Gauge Symmetries*, Ph.D. thesis, Heidelberg U., 2014.

[246] S. Baek, H. Okada and K. Yagyu, *Flavour Dependent Gauged Radiative Neutrino Mass Model*, *JHEP* **04** (2015) 049, [1501.01530].

[247] A. Crivellin, G. D'Ambrosio and J. Heeck, *Addressing the LHC flavor anomalies with horizontal gauge symmetries*, *Phys. Rev. D* **91** (2015) 075006, [1503.03477].

[248] R. Plestid, *Consequences of an Abelian Z' for neutrino oscillations and dark matter*, *Phys. Rev. D* **93** (2016) 035011, [1602.06651].

[249] S. Lee, T. Nomura and H. Okada, *Radiatively Induced Neutrino Mass Model with Flavor Dependent Gauge Symmetry*, *Nucl. Phys. B* **931** (2018) 179–191, [1702.03733].

[250] A. Dev, *Gauged L_μ-L_τ Model with an Inverse Seesaw Mechanism for Neutrino Masses*, 1710.02878.

[251] S. Verma, *Non-zero θ_{13} and CP-violation in inverse neutrino mass matrix*, *Nucl. Phys. B* **854** (2012) 340–349, [1109.4228].

[252] J. Liao, D. Marfatia and K. Whisnant, *Texture and Cofactor Zeros of the Neutrino Mass Matrix*, *JHEP* **09** (2014) 013, [1311.2639].

[253] X. Qian and P. Vogel, *Neutrino Mass Hierarchy*, *Prog. Part. Nucl. Phys.* **83** (2015) 1–30, [1505.01891].

[254] R. Patterson, *Prospects for Measurement of the Neutrino Mass Hierarchy*, *Ann. Rev. Nucl. Part. Sci.* **65** (2015) 177–192, [1506.07917].

[255] IceCube PINGU collaboration, M. Aartsen et al., *Letter of Intent: The Precision IceCube Next Generation Upgrade (PINGU)*, 1401.2046.

[256] KM3Net collaboration, S. Adrian-Martinez et al., *Letter of intent for KM3NeT 2.0*, *J. Phys. G* **43** (2016) 084001, [1601.07459].

[257] JUNO collaboration, F. An et al., *Neutrino Physics with JUNO*, *J. Phys. G* **43** (2016) 030401, [1507.05613].

[258] JUNO collaboration, Z. Djurcic et al., *JUNO Conceptual Design Report*, 1508.07166.

[259] L. Lavoura, *Zeros of the inverted neutrino mass matrix*, *Phys. Lett. B* **609** (2005) 317–322, [hep-ph/0411232].

[260] E. Lashin and N. Chamoun, *Zero minors of the neutrino mass matrix*, *Phys. Rev. D* **78** (2008) 073002, [0708.2423].

[261] S. Antusch, M. Drees, J. Kersten, M. Lindner and M. Ratz, *Neutrino mass operator renormalization revisited*, *Phys. Lett. B* **519** (2001) 238–242, [hep-ph/0108005].

[262] J. R. Ellis and S. Lola, *Can neutrinos be degenerate in mass?*, *Phys. Lett. B* **458** (1999) 310–321, [hep-ph/9904279].

[263] NOvA, collaboration, L. Kolupaeva, *Recent three-flavor neutrino oscillation results from the NOvA experiment*, *J. Phys. Conf. Ser.* **1690** (2020) 012172.

[264] Intensity Frontier Neutrino Working Group collaboration, A. de Gouvea et al., *Working Group Report: Neutrinos*, in *Community Summer Study 2013: Snowmass on the Mississippi*, 10, 2013, 1310.4340.

[265] F. Capozzi, E. Di Valentino, E. Lisi, A. Marrone, A. Melchiorri and A. Palazzo, *Global constraints on absolute neutrino masses and their ordering*, *Phys. Rev. D* **95** (2017) 096014, [2003.08511].

[266] Y. Ema, K. Hamaguchi, T. Moroi and K. Nakayama, *Flaxion: a minimal extension to solve puzzles in the standard model*, *JHEP* **01** (2017) 096, [1612.05492].

[267] R. Kallosh and A. Linde, *Universality Class in Conformal Inflation*, *JCAP* **07** (2013) 002, [1306.5220].

[268] S. Ferrara, R. Kallosh, A. Linde and M. Porrati, *Minimal Supergravity Models of Inflation*, *Phys. Rev. D* **88** (2013) 085038, [1307.7696].

[269] R. Kallosh, A. Linde and D. Roest, *Superconformal Inflationary α-Attractors*, *JHEP* **11** (2013) 198, [1311.0472].

[270] M. Galante, R. Kallosh, A. Linde and D. Roest, *Unity of Cosmological Inflation Attractors*, *Phys. Rev. Lett.* **114** (2015) 141302, [1412.3797].

[271] F. Takahashi, *Linear Inflation from Running Kinetic Term in Supergravity*, *Phys. Lett. B* **693** (2010) 140–143, [1006.2801].

[272] K. Nakayama and F. Takahashi, *Running Kinetic Inflation*, *JCAP* **11** (2010) 009, [1008.2956].

[273] A. R. Liddle and S. M. Leach, *How long before the end of inflation were observable perturbations produced?*, *Phys. Rev. D* **68** (2003) 103503, [astro-ph/0305263].

[274] L. Kofman, A. D. Linde and A. A. Starobinsky, *Nonthermal phase transitions after inflation*, *Phys. Rev. Lett.* **76** (1996) 1011–1014, [hep-th/9510119].

[275] R. Shannon et al., *Gravitational waves from binary supermassive black holes missing in pulsar observations*, *Science* **349** (2015) 1522–1525, [1509.07320].

[276] P. D. Lasky et al., *Gravitational-wave cosmology across 29 decades in frequency*, *Phys. Rev. X* **6** (2016) 011035, [1511.05994].

[277] L. Lentati et al., *European Pulsar Timing Array Limits On An Isotropic Stochastic Gravitational-Wave Background*, *Mon. Not. Roy. Astron. Soc.* **453** (2015) 2576–2598, [1504.03692].

[278] NANOGrav collaboration, Z. Arzoumanian et al., *The NANOGrav Nine-year Data Set: Limits on the Isotropic Stochastic Gravitational Wave Background*, *Astrophys. J.* **821** (2016) 13, [1508.03024].

[279] NANOGRAV collaboration, Z. Arzoumanian et al., *The NANOGrav 11-year Data Set: Pulsar-timing Constraints On The Stochastic Gravitational-wave Background*, *Astrophys. J.* **859** (2018) 47, [1801.02617].

[280] J. J. Blanco-Pillado, K. D. Olum and X. Siemens, *New limits on cosmic strings from gravitational wave observation*, *Phys. Lett. B* **778** (2018) 392–396, [1709.02434].

[281] C. Ringeval and T. Suyama, *Stochastic gravitational waves from cosmic string loops in scaling*, *JCAP* **12** (2017) 027, [1709.03845].

[282] A. Yung, *Vortices on the Higgs branch of the Seiberg-Witten theory*, *Nucl. Phys. B* **562** (1999) 191–209, [hep-th/9906243].

[283] P. Auclair et al., *Probing the gravitational wave background from cosmic strings with LISA*, *JCAP* **04** (2020) 034, [1909.00819].

[284] NANOGrav collaboration, Z. Arzoumanian et al., *The NANOGrav 12.5-year Data Set: Search For An Isotropic Stochastic Gravitational-Wave Background*, 2009.04496.

[285] J. Ellis and M. Lewicki, *Cosmic String Interpretation of NANOGrav Pulsar Timing Data*, 2009.06555.

[286] S. Blasi, V. Brdar and K. Schmitz, *Has NANOGrav found first evidence for cosmic strings?*, 2009.06607.

[287] W. Buchmuller, V. Domcke and K. Schmitz, *From NANOGrav to LIGO with metastable cosmic strings*, *Phys. Lett. B* **811** (2020) 135914, [2009.10649].

[288] R. Samanta and S. Datta, *Gravitational wave complementarity and impact of NANOGrav data on gravitational leptogenesis: cosmic strings*, 2009.13452.

[289] K. Asai, K. Hamaguchi, N. Nagata, J. Wada and S.-Y. Tseng, *in future work* .

[290] D. J. Chung, E. W. Kolb and A. Riotto, *Production of massive particles during reheating*, *Phys. Rev. D* **60** (1999) 063504, [hep-ph/9809453].

[291] G. F. Giudice, E. W. Kolb and A. Riotto, *Largest temperature of the radiation era and its cosmological implications*, *Phys. Rev. D* **64** (2001) 023508, [hep-ph/0005123].

[292] CMB-S4 collaboration, K. N. Abazajian et al., *CMB-S4 Science Book, First Edition*, 1610.02743.

[293] K. Abazajian et al., *CMB-S4 Science Case, Reference Design, and Project Plan*, 1907.04473.

[294] T2K collaboration, K. Abe et al., *Constraint on the matter–antimatter symmetry-violating phase in neutrino oscillations*, *Nature* **580** (2020) 339–344, [1910.03887].

[295] M. Cirelli, M. Kadastik, M. Raidal and A. Strumia, *Model-independent implications of the e+-, anti-proton cosmic ray spectra on properties of Dark Matter*, *Nucl. Phys. B* **813** (2009) 1–21, [0809.2409].

[296] S. Baek and P. Ko, *Phenomenology of U(1)(L(mu)-L(tau)) charged dark matter at PAMELA and colliders*, *JCAP* **10** (2009) 011, [0811.1646].

[297] X.-J. Bi, X.-G. He and Q. Yuan, *Parameters in a class of leptophilic models from PAMELA, ATIC and FERMI*, *Phys. Lett. B* **678** (2009) 168–173, [0903.0122].

[298] P. Foldenauer, *Light dark matter in a gauged $U(1)_{L_\mu - L_\tau}$ model*, *Phys. Rev. D* **99** (2019) 035007, [1808.03647].

[299] S. Baek, *Dark matter and muon $(g-2)$ in local $U(1)_{L_\mu - L_\tau}$-extended Ma Model*, *Phys. Lett. B* **756** (2016) 1–5, [1510.02168].

[300] A. Biswas, S. Choubey and S. Khan, *Neutrino Mass, Dark Matter and Anomalous Magnetic Moment of Muon in a $U(1)_{L_\mu - L_\tau}$ Model*, *JHEP* **09** (2016) 147, [1608.04194].

[301] A. Biswas and A. Shaw, *Reconciling dark matter, $R_{K^{(*)}}$ anomalies and $(g-2)_\mu$ in an $L_\mu - L_\tau$ scenario*, *JHEP* **05** (2019) 165, [1903.08745].

[302] A. Celis, W.-Z. Feng and M. Vollmann, *Dirac dark matter and $b \to s\ell^+\ell^-$ with U(1) gauge symmetry*, *Phys. Rev. D* **95** (2017) 035018, [1608.03894].

[303] W. Altmannshofer, S. Gori, S. Profumo and F. S. Queiroz, *Explaining dark matter and B decay anomalies with an $L_\mu - L_\tau$ model*, *JHEP* **12** (2016) 106, [1609.04026].

[304] G. Arcadi, T. Hugle and F. S. Queiroz, *The Dark $L_\mu - L_\tau$ Rises via Kinetic Mixing*, *Phys. Lett. B* **784** (2018) 151–158, [1803.05723].

[305] S. Singirala, S. Sahoo and R. Mohanta, *Exploring dark matter, neutrino mass and $R_{K^{(*)},\phi}$ anomalies in $L_\mu - L_\tau$ model*, *Phys. Rev. D* **99** (2019) 035042, [1809.03213].

[306] S. Baek, *Scalar dark matter behind $b \to s\mu\mu$ anomaly*, *JHEP* **05** (2019) 104, [1901.04761].

[307] Z.-L. Han, R. Ding, S.-J. Lin and B. Zhu, *Gauged $U(1)_{L_\mu - L_\tau}$ scotogenic model in light of $R_{K^{(*)}}$ anomaly and AMS-02 positron excess*, *Eur. Phys. J. C* **79** (2019) 1007, [1908.07192].

[308] J.-C. Park, J. Kim and S. C. Park, *Galactic center GeV gamma-ray excess from dark matter with gauged lepton numbers*, *Phys. Lett. B* **752** (2016) 59–65, [1505.04620].

[309] K. Saikawa and S. Shirai, *Precise WIMP Dark Matter Abundance and Standard Model Thermodynamics*, *JCAP* **08** (2020) 011, [2005.03544].

[310] G. Bélanger, F. Boudjema, A. Pukhov and A. Semenov, *micrOMEGAs4.1: two dark matter candidates*, *Comput. Phys. Commun.* **192** (2015) 322–329, [1407.6129].

[311] DarkSide collaboration, P. Agnes et al., *DarkSide-50 532-day Dark Matter Search with Low-Radioactivity Argon*, *Phys. Rev. D* **98** (2018) 102006, [1802.07198].

[312] G. Grilli di Cortona, A. Messina and S. Piacentini, *Migdal effect and photon Bremsstrahlung: improving the sensitivity to light dark matter of liquid argon experiments*, *JHEP* **11** (2020) 034, [2006.02453].

[313] T. R. Slatyer, *Indirect dark matter signatures in the cosmic dark ages. I. Generalizing the bound on s-wave dark matter annihilation from Planck results*, *Phys. Rev. D* **93** (2016) 023527, [1506.03811].

[314] R. K. Leane, T. R. Slatyer, J. F. Beacom and K. C. Ng, *GeV-scale thermal WIMPs: Not even slightly ruled out*, *Phys. Rev. D* **98** (2018) 023016, [1805.10305].

[315] C. Boehm, M. J. Dolan and C. McCabe, *A Lower Bound on the Mass of Cold Thermal Dark Matter from Planck*, *JCAP* **08** (2013) 041, [1303.6270].

[316] K. M. Nollett and G. Steigman, *BBN And The CMB Constrain Neutrino Coupled Light WIMPs*, *Phys. Rev. D* **91** (2015) 083505, [1411.6005].

[317] J. H. Heo and C. Kim, *Light Dark Matter and Dark Radiation*, *J. Korean Phys. Soc.* **68** (2016) 715–721, [1504.00773].

[318] N. Sabti, J. Alvey, M. Escudero, M. Fairbairn and D. Blas, *Refined Bounds on MeV-scale Thermal Dark Sectors from BBN and the CMB*, *JCAP* **01** (2020) 004, [1910.01649].

[319] CMS collaboration, A. M. Sirunyan et al., *Search for an $L_\mu - L_\tau$ gauge boson using $Z \to 4\mu$ events in proton-proton collisions at $\sqrt{s} = 13$ TeV*, *Phys. Lett. B* **792** (2019) 345–368, [1808.03684].

[320] H. Yuksel, S. Horiuchi, J. F. Beacom and S. Ando, *Neutrino Constraints on the Dark Matter Total Annihilation Cross Section*, *Phys. Rev. D* **76** (2007) 123506, [0707.0196].

[321] S. Palomares-Ruiz and S. Pascoli, *Testing MeV dark matter with neutrino detectors*, *Phys. Rev. D* **77** (2008) 025025, [0710.5420].

[322] R. Primulando and P. Uttayarat, *Dark Matter-Neutrino Interaction in Light of Collider and Neutrino Telescope Data*, *JHEP* **06** (2018) 026, [1710.08567].

[323] A. Olivares-Del Campo, C. Bœhm, S. Palomares-Ruiz and S. Pascoli, *Dark matter-neutrino interactions through the lens of their cosmological implications*, *Phys. Rev. D* **97** (2018) 075039, [1711.05283].

[324] A. Olivares-Del Campo, S. Palomares-Ruiz and S. Pascoli, *Implications of a Dark Matter-Neutrino Coupling at Hyper-Kamiokande*, in *53rd Rencontres de Moriond on Electroweak Interactions and Unified Theories*, pp. 441–444, 2018, 1805.09830.

[325] N. Klop and S. Ando, *Constraints on MeV dark matter using neutrino detectors and their implication for the 21-cm results*, *Phys. Rev. D* **98** (2018) 103004, [1809.00671].

[326] C. A. Argüelles, A. Diaz, A. Kheirandish, A. Olivares-Del-Campo, I. Safa and A. C. Vincent, *Dark Matter Annihilation to Neutrinos*, 1912.09486.

[327] N. F. Bell, M. J. Dolan and S. Robles, *Searching for Sub-GeV Dark Matter in the Galactic Centre using Hyper-Kamiokande*, *JCAP* **09** (2020) 019, [2005.01950].

[328] Borexino collaboration, G. Bellini et al., *Study of solar and other unknown anti-neutrino fluxes with Borexino at LNGS*, *Phys. Lett. B* **696** (2011) 191–196, [1010.0029].

[329] KamLAND collaboration, A. Gando et al., *A study of extraterrestrial antineutrino sources with the KamLAND detector*, *Astrophys. J.* **745** (2012) 193, [1105.3516].

[330] Super-Kamiokande collaboration, M. Malek et al., *Search for supernova relic neutrinos at SUPER-KAMIOKANDE*, *Phys. Rev. Lett.* **90** (2003) 061101, [hep-ex/0209028].

[331] Super-Kamiokande collaboration, K. Bays et al., *Supernova Relic Neutrino Search at Super-Kamiokande*, *Phys. Rev. D* **85** (2012) 052007, [1111.5031].

[332] Super-Kamiokande collaboration, H. Zhang et al., *Supernova Relic Neutrino Search with Neutron Tagging at Super-Kamiokande-IV*, *Astropart. Phys.* **60** (2015) 41–46, [1311.3738].

[333] Super-Kamiokande collaboration, E. Richard et al., *Measurements of the atmospheric neutrino flux by Super-Kamiokande: energy spectra, geomagnetic effects, and solar modulation*, *Phys. Rev. D* **94** (2016) 052001, [1510.08127].

[334] C. Garcia-Cely and J. Heeck, *Indirect searches of dark matter via polynomial spectral features*, *JCAP* **08** (2016) 023, [1605.08049].

[335] A. Ibarra, S. Lopez Gehler and M. Pato, *Dark matter constraints from box-shaped gamma-ray features*, *JCAP* **07** (2012) 043, [1205.0007].

[336] A. Ibarra, H. M. Lee, S. López Gehler, W.-I. Park and M. Pato, *Gamma-ray boxes from axion-mediated dark matter*, *JCAP* **05** (2013) 016, [1303.6632].

[337] R. Garani and J. Heeck, *Dark matter interactions with muons in neutron stars*, *Phys. Rev. D* **100** (2019) 035039, [1906.10145].

[338] A. Strumia and F. Vissani, *Precise quasielastic neutrino/nucleon cross-section*, *Phys. Lett. B* **564** (2003) 42–54, [astro-ph/0302055].

[339] E. Kolbe, K. Langanke and P. Vogel, *Estimates of weak and electromagnetic nuclear decay signatures for neutrino reactions in Super-Kamiokande*, *Phys. Rev. D* **66** (2002) 013007.

[340] S. Skadhauge and R. Zukanovich Funchal, *Determining neutrino and supernova parameters with a galactic supernova*, *JCAP* **04** (2007) 014, [hep-ph/0611194].

[341] DUNE collaboration, R. Acciarri et al., *Long-Baseline Neutrino Facility (LBNF) and Deep Underground Neutrino Experiment (DUNE): Conceptual Design Report, Volume 2: The Physics Program for DUNE at LBNF*, 1512.06148.

[342] Super-Kamiokande collaboration, K. Abe et al., *Indirect search for dark matter from the Galactic Center and halo with the Super-Kamiokande detector*, *Phys. Rev. D* **102** (2020) 072002, [2005.05109].

[343] M. Ibe, H. Murayama and T. Yanagida, *Breit-Wigner Enhancement of Dark Matter Annihilation*, *Phys. Rev. D* **79** (2009) 095009, [0812.0072].

[344] M. Ibe, Y. Nakayama, H. Murayama and T. T. Yanagida, *Nambu-Goldstone Dark Matter and Cosmic Ray Electron and Positron Excess*, *JHEP* **04** (2009) 087, [0902.2914].

[345] B. Batell, T. Han, D. McKeen and B. Shams Es Haghi, *Thermal Dark Matter Through the Dirac Neutrino Portal*, *Phys. Rev. D* **97** (2018) 075016, [1709.07001].

[346] D. McKeen and N. Raj, *Monochromatic dark neutrinos and boosted dark matter in noble liquid direct detection*, *Phys. Rev. D* **99** (2019) 103003, [1812.05102].

[347] M. Blennow, E. Fernandez-Martinez, A. Olivares-Del Campo, S. Pascoli, S. Rosauro-Alcaraz and A. Titov, *Neutrino Portals to Dark Matter*, *Eur. Phys. J. C* **79** (2019) 555, [1903.00006].

[348] S. Okawa and Y. Omura, *Light mass window of lepton portal dark matter*, 2011.04788.

[349] K. Babu, C. F. Kolda and J. March-Russell, *Implications of generalized Z - Z-prime mixing*, *Phys. Rev. D* **57** (1998) 6788–6792, [hep-ph/9710441].